Synthetic Magnetic Fields and Multi-Component BECs in Optical Lattices

A thesis submitted in partial fulfilment of

the requirements for the degree of

Doctor of Philosophy

by

Rukmani Bai

(Roll No. 13330002)

Under the supervision of

Prof. Angom Dilip Kumar Singh

Professor

Theoretical Physics Division

Physical Research Laboratory, Ahmedabad, India.

DISCIPLINE OF PHYSICS

INDIAN INSTITUTE OF TECHNOLOGY GANDHINAGAR

2018

to

My Family

Declaration

I declare that this written submission represents my ideas in my own words and where others' ideas or words have been included, I have adequately cited and referenced the original sources. I also declare that I have adhered to all principles of academic honesty and integrity and have not misrepresented or fabricated or falsified any idea/data/fact/source in my submission. I understand that any violation of the above will be cause for disciplinary action by the Institute and can also evoke penal action from the sources which have thus not been properly cited or from whom proper permission has not been taken when needed.

Signature

Name: Rukmani Bai

(Roll No: 13330002)

Date:

CERTIFICATE

It is certified that the work contained in the thesis titled **"Synthetic Magnetic Fields and Multi-Component BECs in Optical Lattices"** by Miss Rukmani Bai (Roll No. 13330002), has been carried out under my supervision and that this work has not been submitted elsewhere for a degree.

Prof. Angom Dilip Kumar Singh
Professor
Theoretical Physics Division,
Physical Research Laboratory,
Ahmedabad, India.

(Thesis Supervisor)

Date:

Thesis Approval

The thesis entitled

Synthetic Magnetic Fields and Multi-Component BECs in Optical Lattices

by

Rukmani Bai

(Roll No. 13330002)

is approved for the degree of

Doctor of Philosophy

_____	_____
Examiner	Examiner
_____	_____
Supervisor	Chairman

Date: _____

Place: _____

Acknowledgments

The five years of my PhD tenure were the years of learning. This acknowledgment is to express my sincere gratitude to the people with whom I have interacted with during this period.

I consider myself lucky to have Prof. Angom Dilip Kumar Singh as my supervisor. His insightful guidance and broad scientific knowledge have helped me to make progress in my thesis work. I thank him for teaching me the basics of physics and computer programming. Apart from science, I am deeply inspired by his attitude towards life. During my PhD years whenever I have faced any problem, be it academic or non-academic, Dilip has helped me and has given me the best possible solutions. I am extremely grateful for his patience and understanding towards me. Thank you Dilip.

I thank Arko Roy for motivating me to join the group. He has taught me the physics of ultracold atoms and helped me in the learning some of the computer skills like terminal, vi editor, gnuplot, etc. I acknowledge the help from Kuldeep Suthar at the initial stage of my PhD tenure. It was a pleasure to learn the numerical codes from him and discuss the scientific ideas. I am thankful to Sukla Pal with whom I have enjoyed many discussions that often transcended science. I express my heartfelt thanks to Soumik Bandyopadhyay for helping me everytime. I have really enjoyed his company during the time of the development of the codes and learning about the Bose Hubbard model. I thank Hrushi and Deepak for the scientific and non scientific discussions at the end of my PhD thesis.

I take this opportunity to thank my DSC members Prof. Jitesh R Bhatt, and Prof. Navinder Singh for reviewing my thesis work in the last five years. I express my gratitude to the Director, Dean, academic committee members, and the Chairperson of Theoretical Physics Division Prof. H. Mishra for providing me with the necessary facilities to carry out the research works. I am thankful to the academic chairman Prof. S. Ramachandran and the head of academic services Dr. Bhushit G. Vaishnav for their continual support. I would also like to thank other faculty members of Theoretical Physics Division, Prof. N. Mahajan, Prof. R. Rangarajan, Prof. S. Mohanty, Prof. S. Goswami, and Prof. P. Konar.

I also express my sincere thanks to Dr. S.Ganesh, Prof. G. K. Samanta, Prof. R. P. Singh, Prof. B. K. Sahoo, Prof. K. P. Subramanian, Prof. J. Banerji, Prof. R. Sekar, Prof. D. Chakrabarty, Dr. Som Kumar Sharma, Dr. Smitha Thampi, Dr. M. G. Yadava, Prof. J. S. Ray, and Prof. Bhuwan Joshi from whom I had the opportunity to learn many things during the course work. Apart from the science discussions, I have immensely enjoyed the time I have spent with Dr. Arvind Singh, Prof. K. S. Baliyan, Dr. Veeresh Singh, Dr. R. K. Kushawaha and their families.

Most of the computational works of my thesis were performed in the VIKRAM-100 High Performance Computing (HPC) cluster which is maintained by the Computer Center at Physical Research Laboratory. I am thankful to all members of the computer center, especially Mr. Jigar Raval, Mr. Samuel Johnson, Mr. Tejas Sarvaiya and Mr. H. D. Mishra for their sincere support. I am also thankful to the staff members of our division, Administration, Dispensary, Canteen, Workshop, and Maintenance section of PRL for their assistance and support. I am

grateful to the PRL and IIT-GN Library staff for all the facilities. I take this opportunity to express my gratitude to IIT Gandhinagar, and PRL for providing their research facilities.

I express my heartfelt thanks to my batch mates Navpreet, Rupa, Kuldeep, Satish, Prahlad, Jabir, Ali, Kumar, Chandan, Yasir and Hemant. They always supported me like family and made my PhD years more enjoyable. I thank my friends Aarthy, Chandni, Aashish and Sonam for their helps during the begining of the journey of PhD. I thank to my seniors Amrendra, Monojit, Priyanka, Bhayava, Anjali, Naveen, Yashpal, Dilip, Gaurav Tomar, Avdhesh, Girish Kumar, Gurava Jaiswal, Ikshu, Shradha, Manu, Dipti, Deepak, Jinia, Chandana, Lalit, Bivin, Venkey, Aproova. It was always fun to go for lunch with awesome fellas Pankaj, Newton, Nabyendu, Sudip, Shweta, Diganta, Manpreet, Luxmi, Nidhi, Soumya, Arun, Biwsajit, Arindam, Soumya(Kaka), Gauhar, Prasanna. In all of these five years, I have shared my office with Girish and Priyank, and I thank them for patiently listing to me. I thank all of my juniors cum friends Vishnu, Aman, Bhavesh, Bharti, Nijil, Niharika, Kiran, Anil, Pradeep, Archita, Sivangi, Varun, Shefali, Akansha, Richa, Subir, Kaustava, Rahul, Harsh, Ashish, Arvind, Balbeer, Surendra, Sandeep, Ayan, Abdur, Harish, Deepika, Nisha, Sivani, Anshika, Tanmoy.

Finally, I thank my father Madan Singh and my mother Chameli Devi for their support, patience and for always motivating me during the past five years of my PhD. I am lucky to have Ajeet and Satish as my younger brothers. Their love and support have always kept me going forward in life.

Rukmani Bai

Abstract

Quantum Hall states are robust and good choice for numerous potential applications and to study the physics of topological effects. These states have been observed experimentally in condensed matter systems. However, the observation of fractional quantum Hall states with high flux is difficult in these systems as they require high magnetic fields ($\approx$100 T or more). In this respect, ultracold atoms trapped in the optical lattices are clean and appropriate systems as synthetic magnetic fields equivalent to 1000 T or more can be generated using laser fields. In this thesis, I study the occurrence of quantum Hall states and competing superfluid states in optical lattices for both homogeneous and inhomogeneous systems. And, I also study the physics of multi-component ultracold atomic gases in optical lattices. For the former, I solve the Bose-Hubbard model with synthetic magnetic field referred to as the bosonic Harper-Hofstadter model, using cluster Gutzwiller mean-field and Exact diagonalization methods. The synthetic magnetic field in the optical lattices can be implemented through the Peierls phase and experimentally using laser fields. For the homogeneous case, with the inclusion of the synthetic magnetic field, we obtain the quantum Hall states as the ground state of the bosonic Harper-Hofstadter model. As a first step, the parameters of the QH states are identified based on the compressibility. We obtain the quantum Hall states for different values of synthetic magnetic field with different cluster sizes for the hard core bosons and in the neighbourhood of zero Mott lobe. For the hard core bosons, the onsite interaction energy of the atoms is much larger than the nearest neighbour tunneling energy. As a possible experimental signature, I study in detail the two-point correlation function to distinguish between the quantum Hall states and superfluid states. The states so obtained as further studied in more detail with the exact diagonalization method. I identify the quantum Hall states and superfluid states based on the Penrose-Onsager criterion and Von Neumann entropy. Then, the identification of the quantum Hall states is confirmed by computing the many-body Chern number and ground state degeneracy. For the inhomogeneous case, I do recover all the quantum Hall states for hard wall boundary and for a shallow Gaussian potential, but not with the harmonic oscillator potential. For the multi-component ultracold atomic gases, I obtain the phase diagram for the Bose-Hubbard model for two species. I get

the half-filled Mott lobes in presence of inter-species interaction strength. And, show that the width of half-filled Mott lobe varies linearly with increasing the inter-species interaction strength. I, then, consider the nearest neighbour interaction together with onsite interaction in the Bose-Hubbard model and study the phase separation for the strongly correlated phases of two-component ultracold atomic gases in optical lattices. I also study the phase diagram of the extended Bose-Hubbard model and observe the shifting of density wave lobe with the increase of the inter-species interaction strength with zero inter-species nearest neighbour interaction. While with finite inter-species nearest neighbour interaction I observe the phase separation in density wave, super-solid and superfluid phase.

Keywords: Optical lattice, Bose-Hubbard model, quantum Hall states, single-site and cluster Gutzwiller mean-field theory, exact diagonalization.

Work contribution: I was the lead person in defining and developing the ideas of the research projects which form a part of this Ph.D. thesis. I and Soumik contributed equally to the development of the codes and designing the algorithms used. I lead the preparation of the manuscripts of papers published based on the results reported in the thesis.

Contents

List of Figures

Chapter 1

Introduction

Hall effect is a phenomenon related to the motion of the electron in a 2D plane in presence of a magnetic field. If a potential difference is applied along $\mathbf{x}$ direction, and a magnetic field along $\mathbf{z}$ direction, then due to the cyclotron motion of the electrons, a Hall voltage is induced along $\mathbf{y}$ direction. This is the classical Hall effect, discovered by Edwin Hall in 1879. In the classical Hall effect, the Hall resistivity varies linearly with the applied magnetic field. Later, in 1980 the integer quantum Hall effect (IQHE) was discovered in experiments by Klitzing, Dorda and Pepper [2]. They observed plateaux in Hall resistivity of the 2D electron gas in thin films at a very low temperature and with a strong magnetic field. It is referred to as IQHE since the Hall resistivity is quantized at integer multiples of e^2/h, e electron charge and h Planck constant. This was soon followed by the discovery of fractional quantum Hall effect (FQHE) in 1982 by Tsui, Stormer, and Gossard [3]. They observed the quantization of Hall resistivity at the fractional multiples of e^2/h. The key difference between IQHE and FQHE is the role of the electron-electron correlation effects. The IQHE can be understood in terms of single-particle theory without interactions, while to explain FQHE it is essential to consider electron-electron correlation effects. A theoretical explanation of FQHE in terms of a correlated wavefunction was first given by Laughlin [4] in 1983. The Laughlin wave-function does not describe all the fractional quantum Hall states reported in the experiments but provides the essence for some of the FQHE states. Based on the theory Laughlin predicted that a quasi-particle is an anyon that has electronic charge e/m at the filling factor $\nu = 1/m$, where m is an integer number.

This implies that m flux quanta are attached to an electron, and the theory of quantum Hall (QH) states can be understood in terms of the composite particles. In the lowest Landau level, the ground state is an incompressible liquid such as QH ferromagnet which can be obtained at $\nu = 1$. While in the higher Landau levels, charge density wave such as stripe and bubbles are present.

In this chapter, I provide a brief description of the classical and quantum Hall effects, and related experimental observation of the QH effect in the context of condensed matter systems. I, then, discuss the importance of the ultracold atoms trapped in the optical lattices to study the QH states and previous studies of QH states in the optical lattices. I provide the motivation of our work on the QH states in optical lattices. At the end of the chapter, I describe previous observations related to the phase diagram, phase separation of two species BECs in the strongly interacting regime.

1.1 Classical Hall effect

It is well known that electrons moving with velocity $\mathbf{v}$ experience Lorentz force when they are placed in the magnetic field $\mathbf{B}$. The corresponding equation of motion is

$$m\dot{\mathbf{v}} = -e\left(\mathbf{E} + \mathbf{v} \times \mathbf{B}\right), \tag{1.1}$$

where m is electron mass, $\mathbf{E}$ and $\mathbf{B}$ are electric and magnetic fields, respectively. In the Hall effect as schematically shown in Fig. 1.1 the electrons are moving with velocity $\mathbf{v}$ in xy plane, a potential difference is applied along x direction and a magnetic field $B_z = -B_\perp < 0$ is applied in the $-z$ direction. For the steady state $\dot{\mathbf{v}} = 0$, as an induced potential difference along the y direction balances the deflection of the electrons due to the magnetic field $\mathbf{E} = -\mathbf{v} \times \mathbf{B}$. Thus, the current densities are

$$J = -e\rho_0\mathbf{v}, \qquad J_x = \frac{e\rho_0}{B_\perp}E_y, \qquad J_y = -\frac{e\rho_0}{B_\perp}E_x, \tag{1.2}$$

with ρ_0 equilibrium density of electron. In this, a Hall voltage is produced along $\mathbf{y}$ direction. Due to the Hall voltage the electric field E_y is present along $\mathbf{y}$ direction. Therefore, the Hall resistivity is

$$R_{xy} \equiv \frac{E_y}{J_x} = \frac{B_\perp}{e\rho_0}. \tag{1.3}$$

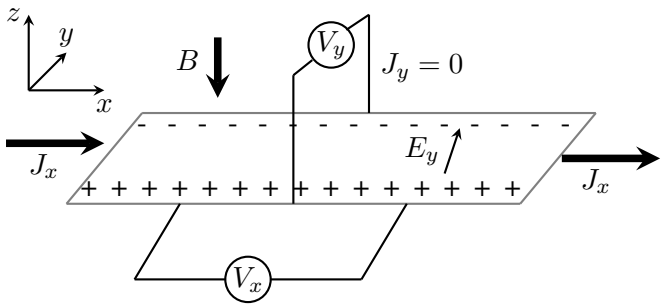

Figure 1.1: Schematic representation of Hall effect for electron in a rectangular sample. A magnetic field is applied B is applied along $-\mathbf{z}$ direction, and a current J_x is along $\mathbf{x}$ direction, a Hall voltage V_y is generated along $\mathbf{y}$ direction. Thus the Hall resistivity R_{xy} is non zero and diagonal resistivity is zero.

Here electric field along $\mathbf{x}$ direction is zero $E_x = 0$, thus the diagonal resistivity is zero $R_{xx} = E_x/J_x = 0$. In the classical Hall effect Hall resistivity is directly proportional to the applied magnetic field as in Eq. (1.3).

1.2 Quantum Hall effect

The QH effect occurs at very low temperatures and under a strong magnetic field, where the quantum nature of electrons is prominent. The electrons execute cyclotron motion in the external magnetic field and the Hamiltonian is

$$\mathbf{H} = \frac{1}{2M}\left[\left(-i\hbar\partial_x + eA_x^{\text{ext}}\right)^2 + \left(-i\hbar\partial_y + eA_y^{\text{ext}}\right)^2\right], \tag{1.4}$$

where A_k^{ext} is the vector potential, and in Landau gauge, it gives raise to the external magnetic field $\mathbf{B} = (0, 0, -B_\perp)$. The energy levels of the above Hamiltonian are quantized in terms of the cyclotron frequency $\omega_c = eB_\perp/M$. The energy levels are referred to as the Landau level and there is a large degeneracy in each level. Each of the degenerate states in a level occupies an area $2\pi l_b^2$ and is called as a Landau site. Here, $l_b = \sqrt{\hbar/(eB_\perp)}$ is the magnetic length, and this indicates that the area of a Landau site decreases with $B_\perp$. To describe the Landau level and Landau sites, consider the covariant momentum:

$$P_x \equiv -i\hbar\partial_x + eA_x^{\text{ext}}, \qquad P_y \equiv -i\hbar\partial_y + eA_y^{\text{ext}}. \tag{1.5}$$

We define the guiding center coordinate (X, Y), the center of the cyclotron motion of the electrons, in terms of the real space coordinate of the electron (x, y) as

$$X \equiv x + P_y/eB_\perp, \qquad Y \equiv y - P_x/eB_\perp \tag{1.6}$$

and their commutation relations are as follows:

$$[X, Y] = -il_B^2, \qquad [P_x, P_y] = \hbar^2/l_B^2, \tag{1.7}$$

$$[X, P_x] = [X, P_y] = [Y, P_x] = [Y, P_y] = 0, \tag{1.8}$$

where as mentioned earlier $l_B = \sqrt{\hbar/eB_\perp}$ is the magnetic length. Due to the Pauli exclusion principle one electron can occupy one quantum mechanical state or Landau site. Since X and Y do not commute, area occupied by an landau site is $\Delta X \Delta Y = 2\pi l_B^2$. Thus, in an area A, the total number of states is $A/2\pi l_B^2$. Thus each Landau level is highly degenerate as it can harbour several Landau sites. The energy of the system is

$$E_N = \Big(N + \frac{1}{2}\Big)\hbar\omega_c, \tag{1.9}$$

where $\omega_c = eB_\perp/M$ is the cyclotron frequency and N is the principal quantum number corresponding to a Landau level. Each landau levels have the same number of Landau sites. In general, the QH states are electrons occupying the lowest Landau level, and magnetic flux Φ quantized in units of the Dirac flux quanta $\Phi_D \equiv 2\pi\hbar/e$ are attached to each electron. The attached flux determine the filling factor for the QH states.

In QH effect Hall resistivity is quantized with respect to the values of the filling factor ν and can be written as

$$R_{xy} \equiv \frac{E_y}{J_x} = \frac{B_\perp}{e\rho_0} = \frac{1}{\nu}\frac{2\pi\hbar}{e^2}, \tag{1.10}$$

where

$$\nu = \frac{\text{Number of electrons}}{\text{Number of states}} = \frac{2\pi\hbar\rho_0}{eB_\perp}. \tag{1.11}$$

Furthermore, QH effect is classified as IQHE or FQHE depending on the whether ν is integer or fractional value, respectively.

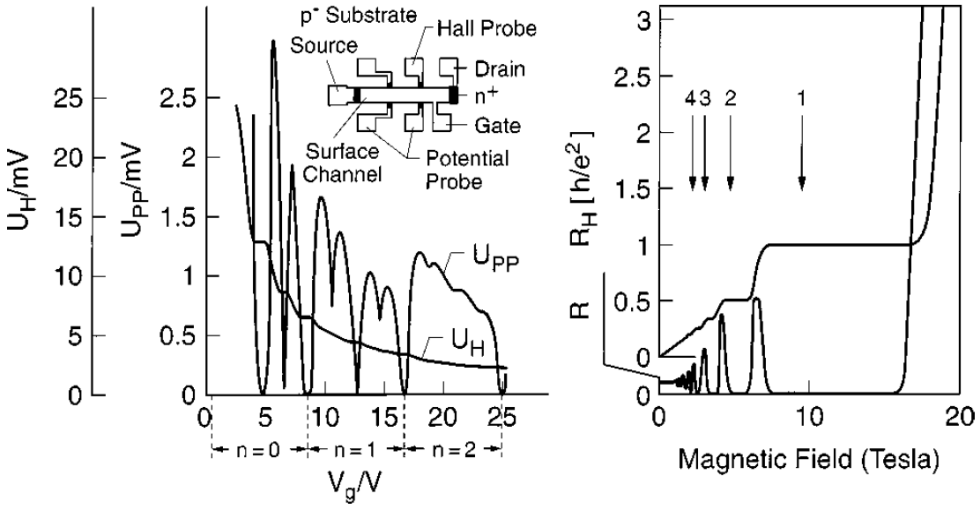

Figure 1.2: The IQHE for the electron system of a silicon MOSFET transistor in the left figure observed by K. v. Klitzing et al. in 1980. They have observed plateaus in the Hall voltage (U_H) instead of a smooth curve and a deep minima in the magnetoresistance (U_{PP}). The x axis is the gate voltage (V_g) which depends on the carrier density n. In the right figure the equivalent plot for Hall resistivity (R_H) and diagonal resistivity R with respect to the applied magnetic field for a 2D electron system on GaAs/AlGaAs. The Hall resistivity has plateaus at integer filling. Reprinted from [K. v. Klitzing et al., Phys. Rev. Lett. **45**, 494 (1980).] Copyright © 1980 by the American Physical Society.

1.2.1 Integer Quantum Hall effect

The IQHE can be understood without considering the inter-electron interactions. Thus, the single-particle states are well defined and based on this we can define the many-particle state in the presence of a magnetic field. In this scenario, although the electrons do not interact, electrons are subjected to Pauli pressure due to the Pauli exclusion principle. So, each electron experiences the presence of other electrons. In experiments, for IQH effect the Hall resistivity R_{xy} is quantized at the integer values of filling factor ν as shown in Fig. 1.2. At the same time, energy spectrum in presence of magnetic field forms Landau levels and these are identified by the principal quantum number, an integer as given in Eq. (1.9). Both of these integers are the same, that is, the IQH state with ν filling factor occupies the lowest ν Landau levels. And

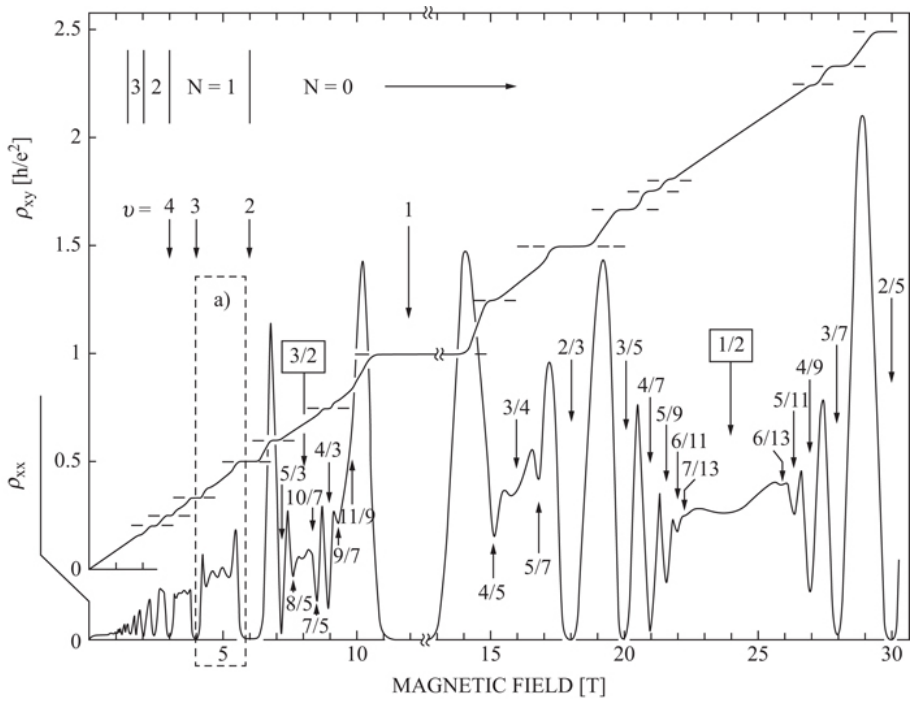

Figure 1.3: The Hall resistivity has plateaus at the fractional filling and diagonal resistivity for those plateaus is zero for fractional quantum Hall Effect. Reprinted from [R. Willett et al., Phys. Rev. Lett. **59**, 1776 (1987).] Copyright © 1987 by the American Physical Society.

the density of electrons to attain the resistivity of the ν^{th} plateau from Eq. (1.11) is $\rho_0 = (eB_\perp/2\pi\hbar)\nu = (B_\perp/\Phi_D)\nu$. This is also the electron density, which is required to fill ν Landau levels. Further, when ν landau levels are filled, there is an energy gap in the energy spectrum. An energy $\hbar\omega_c$ is required to occupy the next state. As long as the temperature is $k_BT \ll \hbar\omega_c$, these states will remain vacant. Thus, the QH states are incompressible and gaped.

1.2.2 Fractional Quantum Hall effect

In the FQH effect, Hall resistance has plateaux at the fractional value or at non-integer value of the filling factor ν. The first plateaux were observed at $\nu = 1/3$ and $2/3$, after that for $\nu = 1/5, 2/5, 3/7, 4/9, 5/9, \ldots$ in the lowest Landau levels and for $\nu = 4/3, 5/3, 7/5, 5/2, 12/5, \ldots$ in the higher Landau levels in the experiments [5]. Till date, many more plateaux for different fractional ν have been observed and are shown in

Fig. 1.3. The main difference between IQHE and FQHE is that the observation of FQHE requires strong Coulomb interactions, correlations between the electrons and presence of disorder in the system [6]. In FQHE the particles condense into a distinct quantum state, and excitations of this state can be described by fractional quantum numbers such as fractional charge and fractional statistics. The fractional statistics is intermediate between the Bose and Fermi statistics. In IQHE, ν Landau levels are occupied by the electrons and all others are vacant. In FQHE, under circumstances of a weak disorder, Hall resistivity is quantized at the fractional quantum numbers. For example, at magnetic field three times larger than the magnetic field at $\nu = 1$ for IQHE, the lowest Landau level is only $1/3$ occupied.

1.3 Ultracold atoms and FQH states

The discovery of the QH effects [2–4] in the condensed matter system has opened up the new field of topological materials. And, for a detailed understanding of the associated physics is essential to understand the properties of electrons in a magnetic field. Charged particles like electrons experience Lorentz force in the presence of magnetic fields, and in condensed matter systems, it is the essence for a host of fascinating phenomena like the integer QH effect [7, 8], fractional QH effect [9, 10], and the quantum spin Hall effect [11]. However, the dilute quantum gases of atoms, which have emerged as excellent proxies of condensed matter systems, are charge neutral and hence, there is no Lorentz force in the presence of an external magnetic field [12]. The absence of Lorentz force can, however, be remedied with the creation of artificial gauge fields through laser fields [13–15]. The atoms then experience a synthetic electromagnetic field and mimic the dynamics of charged particles in electromagnetic fields [16]. Thus, with the artificial gauge potentials, it is possible to explore phenomena such as the quantum Hall effect, and the quantum spin Hall effect [14] in dilute atomic quantum gases.

Experimental realizations of ultracold quantum gases [17–19] have provided the access to explore the physics of quantum many-body systems with controllable interactions. The experimental realization of Bose-Einstein condensates (BECs) of dilute

atomic gases in optical lattices [20–27], and consequent developments [28, 29] have opened new frontiers to explore the physics of quantum many-body systems. Most of the experiments have been performed in the weak interactions regime, the realization of Mott insulator (MI) state [26] in ultracold atoms trapped in the optical lattices take us into the strongly interacting regime with more complex many-body dynamics. This is due to the possibility of experimental control on the inter-atomic interactions, number of atoms, lattice geometry and choice of atomic species. Thus, Bose-Einstein Condensates (BEC) trapped in the optical lattices have become an essential platform to examine the many-body physics, such as quantum phase transitions [29]. The most important feature of BEC is its response towards rotation. Based on the earlier works on superfluid He, it has been studied that BEC does not rotate like normal fluid, rather rotation of superfluid He gives rise to the formation of quantized vortices [30]. The observation of the quantized vortices in the BEC has been studied by rotating the BEC [31–33], through topological phase imprinting [34, 35], or phase engineering in two-species condensates [36, 37]. In the rotating frame, the Coriolis force is analogous to the Lorentz force for charge particles moving in the uniform magnetic field. Hence, the quantized vortices can be considered as the quantized magnetic fluxes penetrating the system. Therefore, the filling factor for FQHE is $\nu = N_b/N_\phi$ number of bosons N_b divided by the number of vortices N_ϕ in the case of BEC.

Some of the strongly correlated quantum states similar to the FQH states have been realized at the high rotation in [38, 39], when the number of vortices exceeds the number of bosons in the condensate. In this method, the observed ground state is separated by an energy gap from all the other excited states. But this gap is small as interaction energy between the atoms is small due to the magnetic trap which is used in the experiments. On the other hand, in the optical lattices, the interaction energies are much larger because atoms are confined in the smaller volume. Thus, the FQH states are much more robust with a higher energy gap in the optical lattices. The Hubbard model [40] well describes the physics of particles trapped in the optical lattices. In particular, bosons in optical lattices are near ideal realizations [41] of the Bose-Hubbard model (BHM) [42]. The BHM shows two phases, MI phase in the strongly interacting regime and SF phase in the weakly interacting regime, these have

been observed in seminal work by Immanual Bloch and collaborators [26].

In the condensed matter systems, there has been enormous progress in the experimental and theoretical understanding of the QH effect [43–46], but the physics of FQH effect [3] is not yet completely understood. One of the theoretical models, the Laughlin ansatz [4] provides exact solutions for some FQH systems, but a comprehensive understating of all the states reported so far remains illusive. The main difficulty arises from the strong correlation of the electrons, but the same is essential to observe the FQH effect. Another difficulty is that the observation of FQH states requires a high magnetic field ($\approx$ 100 T) which is a major hurdle in the condensed matter systems. In this respect, ultracold atoms in the optical lattices are very clean systems with controllable parameters: inter-particle interaction, number of particles, lattice geometry, lattice depth, and temperature. Thus, these systems are ideal quantum many-body systems to study FQH states [47, 48]. The ultracold atoms are, however, charge neutral and not affected by the external magnetic fields. To overcome this, the concept of synthetic magnetic field is used to generate a force similar to Lorentz force, and it has been experimentally implemented in the optical lattices using laser field [49–56]. The synthetic magnetic field equivalent of $\approx$ 1000 T can be generated in the optical lattices. In the BHM Hamiltonian, the hopping and on-site interaction are the two competing terms. And both of these can be tuned by changing the depth of the lattice potential and employing Feshbach resonance [57, 58]. The hopping parameter J, which defines the strength of the hopping term in the BHM Hamiltonian, acquires a phase $J \rightarrow |J| \exp(i\Phi)$ in the presence of a synthetic magnetic field [59] through the Peierls substitution [60, 61] and modifies the states of BHM. So, for an atom in the optical lattice, there is a change of phase $\Phi = 2\pi\alpha$ when it hops around a unit cell or plaquette, where α is the flux quanta per plaquette. The ground state of BHM in the presence of synthetic magnetic field is the QH state.

1.3.1 Previous studies of FQH states with optical lattices

In the ultracold atoms, it has been shown that the FQH states occur as the ground state by rotating and cooling the atoms confined in the harmonic trap potential. Then, the Laughlin wave-function describes this FQH state [38, 39]. In the optical lattices, the

FQH physics is modified through the lattice. For a single particle, the optical lattice modifies the energy spectrums to the fractal structure known as Hofstadter butterfly [61] and is different from the Landau levels. In the optical lattices, described by BHM, the states are FQH type and can be obtained by melting the MI state in a superlattice potential [48] in some suitable parameter regime. It has been studied that an oscillating quadrupole potential together with a periodic modulation of the tunneling between lattice sites provides that the dynamics of the atoms in optical lattices are similar to that of the motion of the charged particle in the magnetic field [48]. In the ref. [48], the ground state was obtained by the numerical diagonalization of the lattice system and it was characterized as FQH state by considering the overlap with the Laughlin wave function. These FQH states were obtained with the low magnetic flux ($\alpha \leq 0.3$). This work was further extended in the ref. [62], where they have characterized the FQH states with the topological order of the system by calculating the Chern numbers. In the same work, features of Laughlin states were also reported in low particle density limit for $\nu = 1/2$ and $\alpha < \alpha_c = 0.4$. Here, ν is the filling factor, the number of particles per flux quanta and α_c is the critical value of the synthetic magnetic field below which FQH states exist.

In the high synthetic magnetic field, a bilayer FQH states have been reported near the rational number of magnetic flux quanta per lattice cell (α) [47]. In another work, the topological states such as Laughlin and Read-Rezayi states have been observed in the presence of a weak trapping potential [63]. The system behaves similar to the two species for the low value of α and near $\alpha = 1/2$ a stripe vortex phase of one species is obtained using Gutzwiller ansatz [63]. The same work reports, in future experimental realizations, the use of noise correlation or Hall current measurements observable signatures of the QH states. The vortex lattice states in the square and honeycomb lattices with artificial gauge potential is reported in ref. [64]. The existence of bosonic FQH states in the rotating optical lattices is predicted [65] in the vicinity of Mott plateaux using variational Monte Carlo and exact diagonalization (ED) method. The phase diagram with $\alpha = 1/4$ and $\nu = 1/2$, for Mott lobe $n = 1$ is shown in Fig.1.4. In this, the MI-SF boundary is predicted from the mean-field calculation and the FQH states are observed for low values of tunneling energy. The FQH states exist

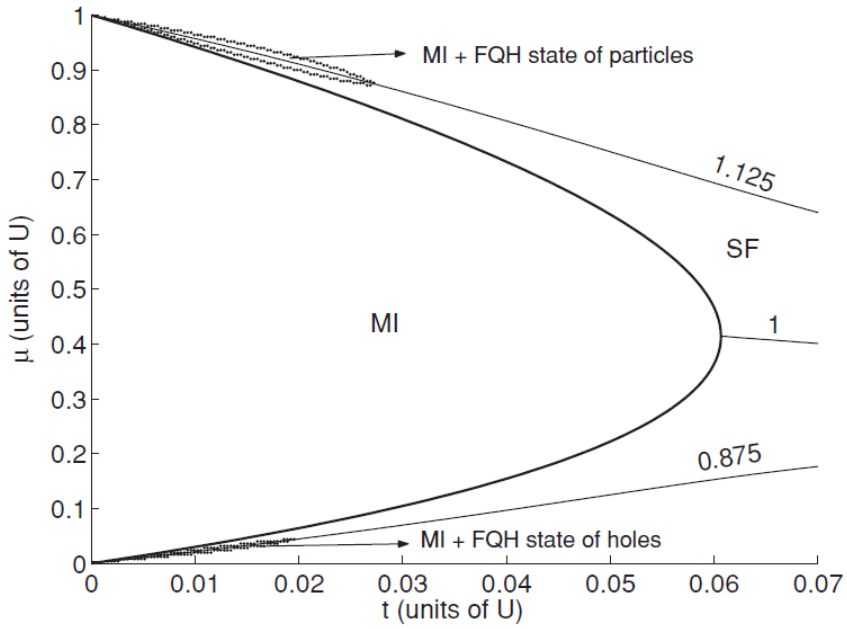

Figure 1.4: The phase diagram for $\alpha = 1/4$ and $\nu = 1/2$ Mott lobe $n = 1$. The phase transition from MI-SF is obtained from the mean-field method. The FQH states are obtained for both excess particles and holes for the low value of tunneling energy. Reprinted from [Umucalılar et al., Phys. Rev. A **81**, 053628 (2010).] Copyright © 2010 by the American Physical Society.

for the hole and particle states. The excess particles are $\epsilon = \alpha\nu = 0.125$. For hole, FQH states have the density $n = 1 - \epsilon = 0.875$ and for particle FQH states have the density $n = 1 + \epsilon = 1.125$ Fig. 1.4. Thus in our studies, we also restrict the value of J to be very low and we study the FQH states for both hole and particle excess.

Similar results for bosonic analogs of the FQH states in the vicinity of Mott lobes are reported in the recent work by considering the nearest neighbour repulsion in BHM [66]. They calculate the vortex density, energy gap, and momentum distribution by considering the effective Hamiltonian for excess particles using single-site Gutzwiller mean-field (SGMF) theory. The different states as vortex solid for small nearest neighbour repulsion and homogeneous Bose metal with the increase in nearest neighbour repulsion are reported. The Chern-Simons theory which describes the bosons with attached flux quanta [66] has been used to study the FQH state. In another recent work [67], using cluster Gutzwiller mean-field (CGMF) theory the incompressibility of the

FQH states is considered to identify these states in the numerical computations. In particular the FQH states for $\alpha = 1/5$ at $\nu = 1/2$ are discussed. The FQH states have been obtained with different filling factors and competing SF state for the same parameter regime is also obtained in this work [67]. The FQH state has the structure similar to the density wave order. The CGMF method breaks the translational invariance of the lattices system, thus a more accurate method reciprocal cluster mean-field (RCMF) H$\ddot{u}$gel et al. [68] predicted a competing FQH state as a metastable state for $\alpha = 1/4$. The ground-state phase diagram of bosonic Harper-Hofstadter model with RCMF is shown in Fig. 1.5 with anisotropic tunneling energies.

In this thesis work, I report FQH states for a square lattice at distinct νs for low and high flux. For example when $\alpha = 1/5$ low flux, we obtain QH states at $\nu = n/2$, where $n = 1, 2, \ldots, 9$ and for high flux $\alpha = 1/2$ at $\nu = 1/2$, 1, and $3/2$. In particular, I discuss the QH states for $\alpha = 1/5$, $1/4$, $1/2$ and $1/3$ in the strongly interaction domain, and in particular, choose $J/U = 0.01$ close to the Mott lobes with $n = 0$ and $n = 1$. we observe the FQH states by considering different external potential such as box potential, Gaussian potential etc.

1.4 Two species ultracold gas systems and extended BHM

The two species ultracold gas system (TUGS) is a condensate mixture of the two different atomic species [69–74], or two hyperfine states of same species [75–84] or two isotopes [85–87]. Some of the novel phenomena associated with TUGS are pattern formation [88–91], phase separation [71, 73, 74, 84, 85], nonlinear dynamical excitations [82, 92, 93], collective excitations [79], Kibble-Zurek mechanism [94], and the production of dipolar molecules [95–97]. Among all these, the most important feature of TUGS is the phase separation. The phase separation in TUGS depend on the competition of inter and intra species interaction energies. These interaction energies are controllable through the magnetic Feshbach resonance and are repulsive in nature. For the phase separation, the interspecies interaction energy must be stronger than the geometric mean of the intra-species interactions energies [98].

TUGS have been experimentally realized in two different hyperfine states of the

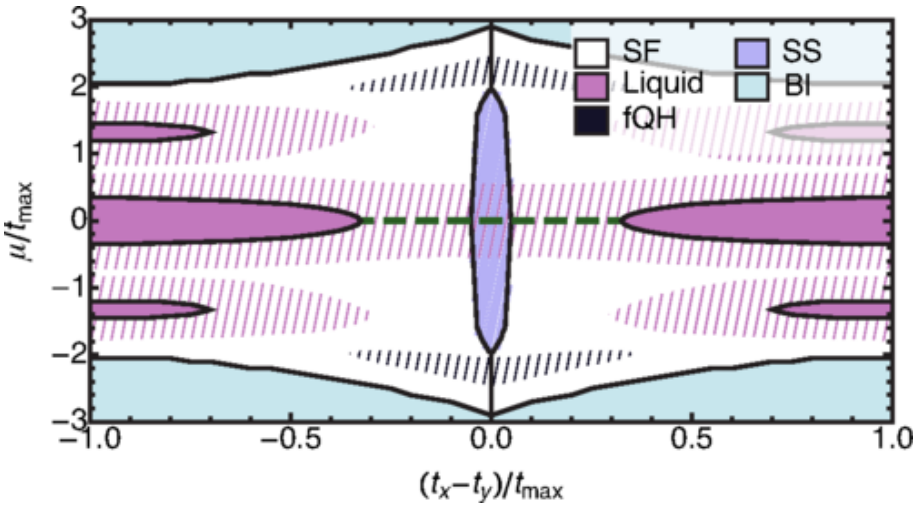

Figure 1.5: The ground state phase diagram with RCMF method in the hard core boson limit and for $\alpha = 1/4$. The the different phases are BI $\rightarrow$ band insulating (light blue), SS $\rightarrow$ supersolid (dark blue), SF $\rightarrow$ stripe superfluid (white), fQH $\rightarrow$ fractional quantum Hall (dark grey). At zero anisotropy the stripe superfluid phase undergoes a transition from vertical stripe (for $t_x > t_y$) to horizontal stripe (for $t_x < t_y$) shown through black vertical line. At zero chemical potential $\mu = 0$, the density is fixed as 1/2 and homogeneous for all phases (green dashed line). Reprinted from [Hügel et al., Phys. Rev. B **96**, 054431 (2017).] Copyright © 2017 by the American Physical Society.

^{87}Rb species [99, 100], where the presence of the second component reduces the SF coherence near to the SF-MI transition for one component. The loss of SF phase coherence is more prominent for large the admixture of the second component and tunneling rate asymmetries of the two species [99]. The coexistence of the SF and MI phases in the hexagonal lattices have also been observed [100]. The presence of second species provide an additional degree of freedom in the case of optical lattices and provide an excellent platform to study the two species BHM [41, 101–103]. The BHM for TUGS presents supercounterflow and antiferromagnetic phases in case of interspecies repulsion [104–106], density-wave instabilities and pair superfluidity in the attractive regime [107–109]. For the atomic spin mixtures, signature of Bose-glass state [110], superexchange interactions [111], antiferromagnetic ordering [112] and emergence of the twisted-superfluid ground state [113] have been observed in the

experiment.

The new techniques of adiabatic cooling [114] and thermometry [115] are results of the influence of a magnetic field the gradient to atomic spin mixtures. The phase diagram of TUGS consists the MI, SF and different combinations of mixed or phase-separated configurations of MI and SF phase [102, 116–118]. Analytical and numerical description of MI-SF phase diagram with inter-species interaction has been studied for the homogeneous system [119] and with external harmonic potential [120]. For Bose-Bose mixtures, MI-SF phase boundary is affected by the presence of the second bosonic species [121]. The quantum phases with various lattice geometries has been studied in [101, 104, 122]. The other effects which previously have been observed in the mixture of cold atomic gases in an optical lattice are demixing of bosonic atoms with increasing interspecies repulsion [123–126], non equilibrium excitations and dynamics of TUGS [82, 83, 93], quantum emulsions and coherence properties of TUGS [25, 127, 128], hydrodynamic instability in the TUGS [129]. The transport properties with the interspecies interaction has been studied [130, 131]. In the recent works at finite temperatures, multicritical behaviour of TUGS [132–134], fragmentation [135] and mixing of phase-separated states [136] have been studied.

After the study of BHM, a new direction is to study the BHM with long-range interactions. This is referred to as extended BHM (eBHM) [137], where in addition to the on-site interaction, one has to consider the interaction between atoms at the nearest neighbour sites [138]. The eBHM represents two more phases such as density wave (DW) [139–141] and supersolid (SS) [141–145] phase, apart from the MI and SF phases. The DW phase is an insulating phase, which has crystalline order in the form of staggered average occupancies at each lattice site. The SS phase shows the simultaneous existence of diagonal or crystalline order and off-diagonal or superfluid long-range orders in the system. The SS phase with striped order has been observed with spin-orbit-coupled BEC in [146, 147] and disordered supersolid with eBHM in [148]. In TUGS the eBHM has been studied with Bose-Bose mixture in a triangular lattice [149], spin-orbit coupled BEC [146, 147]. Apart from this the phase diagram and phase separation with different interaction energy strength for eBHM have not been observed and I discuss some of these results in this thesis.

1.5 Objectives of the thesis

Motivated by the recent theoretical investigations and experimental progress, we address a basic gap in our current understanding. And, that is the occurrence of QH states in optical lattices with an envelope potential. This key issue is addressed in this work. For our studies we use SGMF [150–152] and CGMF [153–157] theories, and ED. Our results, for the case of homogeneous optical lattices, agree well with the previous theoretical results. After establishing this and demonstrating that getting the geometry of QH states requires larger cluster sizes in CGMF, we provide an answer to the question: what is the nature of the QH states in optical lattices with an envelope potential? The objectives of the present studies are as follows:

- Numerical (code) development for the BHM with SGMF, CGMF, and ED methods using Gutzwiller ansatz. After establishing this, to obtain the phase diagram of BHM with SGMF and CGMF method and compare them with the previous studies.

- To obtain the QH and competing SF states with CGMF method for different values of the synthetic magnetic field and with different cluster sizes for the homogeneous system. The number of QH states depends on the cluster size and strength of the synthetic magnetic field.

- To distinguish the QH and SF states, we calculate the two-point correlation function with the CGMF method.

- To obtain the QH states with different background potential such as hard wall boundary (box potential), Gaussian potential and harmonic oscillator potential.

- To obtain the QH and SF states with the ED method. In the ED method, number of atoms are fixed based on the filling factor of the QH state.

- In ED, we compute the condensate fraction and von Neumann entropy to distinguish the QH and SF states. The condensate fraction represents the SF fraction and von Neumann entropy is a measure of correlation effect.

- To obtain the phase diagram for TUGS in the miscible and immiscible regime with extended BHM with nearest neighbour interspecies interaction.

- To study the phase separation in the strongly interacting phases as DW and SS phases.

1.6 Overview of the chapters

The overview of the chapters in the rest of the thesis is as follows:

In **Chapter 2**, I provide the details of the Bose-Hubbard model (BHM). It is a model that describes ultracold atoms trapped in the optical lattices. In this thesis, we use it to describe the physics of ultracold atoms in 2D optical lattices. We derive the mean-field Hamiltonian and use the SGMF and CGMF methods to obtain the ground state of BHM. For SGMF, the Hamiltonian is linear in the operator and contribution from NN lattice sites is considered through the mean-field. The SGMF method does not incorporate the correlations, thus we consider the CGMF method. In CGMF, we consider the exact hopping within the cluster and hopping across clusters is incorporated through the mean-field. In this chapter, I describe the Hamiltonian matrix construction in detail for both SGMF and CGMF methods. I discuss the phase diagram for finite temperature BHM at the end of the chapter.

In **Chapter 3**, I review different types of integer and fractional QH states in optical lattices such as Laughlin state, Read-Rezayi states and vortex lattice states. I, then, for completeness describe the details regarding the implementation of the synthetic magnetic field using laser fields. With the inclusion of the synthetic magnetic field, we obtain the QH states as the ground state of the bosonic Harper-Hofstadter model. These states are identified through the compressibility and two point correlation function. These Properties of the QH states are discussed in this chapter. The SGMF and CGMF methods do not capture the physics of the BHM with a synthetic magnetic field. Therefore, we solve it using the exact diagonalization (ED) method. I describe the ED method in detail and compare it with CGMF in this chapter.

In **Chapter 4**, I present the integer and fractional QH states obtained with CGMF and ED methods. We obtain the QH states for different values of the synthetic mag-

netic field with different cluster sizes for the value of $J/U = 0.01$ [65] in the vicinity of Mott lobe. I discuss about the density pattern of QH states, which can be stripe, checkerboard or homogeneous. We also observe the SF states in the same parameter regime. We compute the two-point correlation function as a characteristic property for QH state. We, then, study the QH states with different background potentials like Gaussian potential, hard wall boundary and Harmonic potential. At the end of the chapter, I present the results for the QH states obtained from the ED method and calculate the condensate fraction and von Neumann entropy to identify the QH and SF states.

In **Chapter 5**, I provide the description of BHM and extended BHM (eBHM) model for TUGS. Here, eBHM is BHM with NN interaction. The relative strength of the NN interaction is controllable in the experiments for single and two species. The eBHM shows two more phases density wave (DW) and supersolid (SS) phase as it includes long-range interactions of the atoms. A novel feature of TUGS is the phase separation. We obtain phase separation in DW and SS phases of eBHM. We obtain the phase diagram with different inter-species interaction with and without NN inter-species and discuss in this chapter.

Finally in **Chapter 6**, I present a brief summary of the results and present future directions.

Chapter 2

Bose Hubbard Model

Ultracold bosonic atoms trapped in the optical lattices are well described by the Bose-Hubbard model (BHM) [41, 42], which is the bosonic version of the Hubbard model [40]. BHM is applicable in both weak and strong interaction limits. It admits a quantum phase transition from Mott Insulator (MI) to Superfluid (SF) and, was experimentally first realized in a pioneering work by Greiner et al. in 2002 [26]. Among the two quantum phases, the MI phase corresponds to the strongly interacting regime and the SF phase corresponds to the weakly interacting regime. Our interest lies in the physics of strongly interacting regime as it is essential to observe quantum Hall states in the optical lattices. One method to study the physics of BHM is the mean-field theory with Gutzwiller ansatz [158], which was proposed by Sheshadri et al. [151]. It must, however, be emphasized that mean-field theories are not suitable to study strongly correlated states like quantum Hall states. In the present work I use mean-field results as an efficient initial theoretical tool to probe and identify parameter domains where quantum Hall states are likely to occur.

The MI-SF phase boundary of the 2D BHM with square geometry has been studied with different numerical and analytical techniques in previous works. Here, I provide a brief description of these methods and it is to be mentioned that, some of these have been used to study the MI-SF phase boundaries in other lower (1D) and higher (3D) as well. The single-site or site-decoupled mean-field theory [151] with Gutzwiller ansatz is one of the simplest methods to obtain the MI-SF phase boundary. However, as the mean-field theory tends to favour the SF phase, the mean-field theory underestimates

the location of the MI-SF transition point. In terms of accuracy, the results from quantum Monte Carlo simulations are the most reliable. And, for 2D BHM with square geometry, the results of Capogrosso-Sansone et al. [1] is considered as the benchmark in the 2D BHM literature. Analytically, it has been studied using Strong coupling expansion [159]. However, the method tends to overestimate the location of the MI-SF transition point. An improvement of the analytical methods is the work of Santos and Pelster [160], where they report results based on two different analytical approaches. First, a variational method which is based on the variational perturbation theory. And, second is the field theoretical concept of the effective potential. These methods provide better results for the MI-SF transition point than the mean-field theory and compares well with the Monte Carlo results. In a semi-analytic work [161], the effective potential in ref. [160] is considered as a starting point, and then, many-body perturbation theory based on Kato's theory is used. The other similar approaches, combination of both analytic and numerical methods, employed to calculate the MI-SF phase boundary are random-phase-approximation (RPA) [162], nonperturbative renormalization-group (RG) approach [163, 164] and bosonic dynamical mean-field theory (B-DMFT) [165]. In the case of the mean-field theory, improvement is to consider clusters of sites as a single unit. A version of the method referred to as the multi-site mean-field theory (MSMFT) [156], has been used to compute the phase diagram.

The idea of improving the single-site mean-field theory with a cluster mean-field was first suggested by Bethe [166] and Peierls [167] in the context of order-disorder transition in binary alloys. The next important development is the work of Weiss [168], who applied it to ferromagnetic systems. In the context of 2D BHM, among several works [156, 157, 169], the recent work of Lümann [157] is an important one and our work closely follows the methods mentioned in this work. In the cluster mean-field theory, by increasing cluster size the results can be improved and approaches to the quantum Monte Carlo results in the limit of infinite cluster size [157]. Besides the methods mentioned so far, the other novel approaches to identify the quantum critical region are using the ratio of compressibility to local number fluctuations [170] and parity order parameter which can be obtained by single-site resolution imaging [171]. The MI-SF phase diagram has also been studied at finite temperatures numerically

with quantum Monte Carlo simulations [170]. It must be mentioned here that, for 1D optical lattice density matrix renormalization-group (DMRG) [137, 172, 173] provide very good results, but in 2D it is restricted to cylindrical geometry. Thus, to emphasize again, the phase diagram computed with quantum Monte Carlo result [1] serves as a benchmark. However, one caveat of the method is that it is not suitable for systems with artificial gauge fields due to the sign problem associated with the phase in the hopping term.

To observe quantum Hall states in optical lattices, it is essential to introduce artificial gauge fields. So that, the neutral atoms in the optical lattices experience a force which is an analogue of the Lorentz force in charged particles. The possibility of introducing artificial gauge fields in optical lattices, first proposed in theoretical studies [15, 174, 175], have been realized in several experiments [49–55]. And, enormous progress has been made to understand the physics of the quantum Hall system in recent years. In this thesis I use SGMF [150–152] and CGMF [153–157] theories, and the ED method to study the quantum Hall physics in BHM.

In this chapter, I provide a brief description of the BHM Hamiltonian, then I derive the mean-field Hamiltonian. I use Gutzwiller ansatz to obtain the ground state solution of the mean-field Hamiltonian and obtain the MI-SF phases of the BHM using the SGMF method. The CGMF method, which is an improvement over the SGMF method, is described in detail, and in the latter part of the chapter, the BHM Hamiltonian for finite temperature is discussed.

2.1 BHM Hamiltonian

The Hamiltonian of interacting bosons confined in a potential $V(\mathbf{x})$, in second quantization, is

$$\hat{H} = \int d^3\mathbf{x}\hat{\psi}^\dagger(\mathbf{x}) \left[-\frac{\hbar^2}{2m}\nabla^2 + V(\mathbf{x}) - \mu\right] \hat{\psi}(\mathbf{x}) + \frac{1}{2}U \int d^3\mathbf{x}\hat{\psi}^\dagger(\mathbf{x})\hat{\psi}^\dagger(\mathbf{x})\hat{\psi}(\mathbf{x})\hat{\psi}(\mathbf{x}), \tag{2.1}$$

where, trapping potential $V(\mathbf{x})$ is sum of envelope potential $V_{\rm en}(\mathbf{x})$ and lattice potential $V_{\rm latt}(\mathbf{x})$, μ is the chemical potential and, $U = 4\pi\hbar^2 a_s/m$ is the inter-atomic interaction strength. Here, $a_{\rm s}$ is scattering length and m is the mass of the atom. In the lowest

band approximation, that is the relevant energy scales in the system are smaller than the excitation energy of the second band, Wannier functions can describe the system. Then, using the Wannier functions as the basis to describe the Bose field operators $\hat{\psi}(\mathbf{x})$, the above Hamiltonian is reduced to the BHM Hamiltonian [41]

$$\begin{aligned}\hat{H} &= -\sum_{p,q}\left[\left(J_x\hat{b}^\dagger_{p+1,q}\hat{b}_{p,q}+\text{H.c.}\right)+\left(J_y\hat{b}^\dagger_{p,q+1}\hat{b}_{p,q}+\text{H.c.}\right)\right] \\ &\quad+\sum_{p,q}\left[\frac{U}{2}\hat{n}_{p,q}(\hat{n}_{p,q}-1)-(\mu-\varepsilon_{p,q})\hat{n}_{p,q}\right], \end{aligned} \tag{2.2}$$

where p (q) is the lattice site index along x (y) direction, $\hat{b}_{p,q}$ $(\hat{b}^\dagger_{p,q})$ are the bosonic annihilation (creation) operators, and $\hat{n}_{p,q}$ is the occupation number operator at the (p,q)th site. The parameter, J_x (J_y) is the complex hopping strength between two nearest neighbour (NN) sites along x (y) direction. The hopping strength is defined through the overlap integral of the Wannier function at the NN lattice sites. The onsite interaction energy U between the atoms at a particular lattice site is considered as repulsive $U>0$ in this thesis. The chemical potential μ at each lattice site is modified by the envelope potential with an energy shift $\epsilon_{p,q}$, and the two can be combined as the local chemical $\tilde{\mu}_{p,q}=\mu-\epsilon_{p,q}$. It is well established that the phase diagram of BHM admits two phases, Mott-insulator (MI) and superfluid (SF) [26, 41, 42]. The strong on-site interaction limit $(J/U\ll 1)$ corresponds to the MI-phase and the opposite limit $(J/U\gg 1)$ corresponds to the SF phase. In homogeneous system, where the optical lattices do not include any background potential, the phase-boundary between MI and SF forms lobes of different fillings. On the other hand, in the presence of background harmonic potential the famous wedding cake structure appears.

2.2 Mean-Field Hamiltonian

To obtain the eigenstates of BHM in Eq. (2.2), we use the mean-field approximation [151]. In this approximation, the annihilation (creation) operators in Eq. (2.2) are decomposed as

$$\hat{b}_{p,q} = \phi_{p,q}+\delta\hat{b}_{p,q}, \tag{2.3a}$$

$$\hat{b}^\dagger_{p,q} = \phi^*_{p,q}+\delta\hat{b}^\dagger_{p,q}, \tag{2.3b}$$

where $\phi_{p,q} = \langle \hat{b}_{p,q} \rangle$ is the SF order parameter, and $\phi^*_{p,q} = \langle \hat{b}^\dagger_{p,q} \rangle$. Using these definitions in Eq. (2.2) and neglecting the terms like $\delta\hat{b}^\dagger_{p+1,q}\delta\hat{b}_{p,q}$ which are second order in the fluctuation operator, we obtain the mean-field Hamiltonian of the BHM as

$$\begin{aligned}\hat{H}^{\mathrm{MF}} &= -\sum_{p,q}\Big\{\Big[J_x\left(\hat{b}^\dagger_{p+1,q}\phi_{p,q} + \phi^*_{p+1,q}\hat{b}_{p,q} - \phi^*_{p+1,q}\phi_{p,q}\right) + \mathrm{H.c.}\Big] \\ &\quad + \Big[J_y\left(\hat{b}^\dagger_{p,q+1}\phi_{p,q} + \phi^*_{p,q+1}\hat{b}_{p,q} - \phi^*_{p,q+1}\phi_{p,q}\right) + \mathrm{H.c.}\Big]\Big\} \\ &\quad + \sum_{p,q}\left[\frac{U}{2}\hat{n}_{p,q}(\hat{n}_{p,q}-1) - \tilde{\mu}_{p,q}\hat{n}_{p,q}\right]. \end{aligned} \tag{2.4}$$

The mean-field Hamiltonian as given above is linear in terms of the bosonic operators and for a particular lattice site (p, q) the NN hopping contribution is accounted through the mean fields ($\phi_{p+1,q}$, $\phi_{p-1,q}$, $\phi_{p,q+1}$, $\phi_{p,q-1}$). Thus, the Hamiltonian in Eq. (2.4) can be considered as the sum of the single-site Hamiltonian

$$\begin{aligned}\hat{h}_{p,q} &= -\Big[J_x\left(\hat{b}^\dagger_{p,q}\phi_{p-1,q} + \phi^*_{p+1,q}\hat{b}_{p,q} - \phi^*_{p,q}\phi_{p-1,q} - \phi^*_{p+1,q}\phi_{p,q}\right) + \mathrm{H.c.}\Big] \\ &\quad - \Big[J_y\left(\hat{b}^\dagger_{p,q}\phi_{p,q+1} + \phi^*_{p,q-1}\hat{b}_{p,q} - \phi^*_{p,q}\phi_{p,q+1} - \phi^*_{p,q-1}\phi_{p,q}\right) + \mathrm{H.c.}\Big] \\ &\quad + \frac{U}{2}\hat{n}_{p,q}(\hat{n}_{p,q}-1) - \tilde{\mu}_{p,q}\hat{n}_{p,q}. \end{aligned} \tag{2.5}$$

We can, therefore, diagonalize the Hamiltonian for each site separately, and use the Gutzwiller ansatz to obtain the ground state solution of the mean field Hamiltonian in Eq. (2.4).

2.2.1 Gutzwiller ansatz

To compute the ground state of the system, we use the site dependent Gutzwiller ansatz. In this ansatz, referred to as the single site Gutzwiller mean field (SGMF) theory, the eigenstate at each site is a linear combination of Fock states and it can be written as

$$|\psi\rangle_{p,q} = \sum_{n=0}^{N_{\mathrm{b}}} c_n^{(p,q)}|n\rangle_{p,q}. \tag{2.6}$$

Here, N_b is the occupation number state with maximum number of particles and normalization condition of this wave-function is $\sum_n |c_n^{(p,q)}|^2 = 1$. The c-numbers $c_n^{(p,q)}$ are the complex coefficients of the ground state $|\psi\rangle_{p,q}$ at the (p, q)th site. Therefore, the ground state Gutzwiller wave-function of the entire system is the direct product of the

ground states of all the individual lattice sites, and it can be written in the Fock basis as

$$|\Psi_{\rm GW}\rangle = \prod_{p,q} |\psi\rangle_{p,q} = \prod_{p,q} \sum_{n=0}^{N_{\rm b}} c_n^{(p,q)} |n\rangle_{p,q}. \tag{2.7}$$

This ansatz is referred to as the single-site Gutzwiller mean-field theory and provides the exact solution of the system in the strongly interacting regime ($J \ll U$).

To obtain the ground state of the system for arbitrary values of J/U, we diagonalize the single site Hamiltonian in Eq. (2.5) and compute eigenstate at each site. The single-site Hamiltonian matrix elements in the SGMF approximation is

$$h_{mn} \quad = \quad {}_{p,q}\langle m| \hat{h}_{p,q} |n\rangle_{p,q}\,, \tag{2.8}$$

where m (n) is occupation number of the Fock space eigen basis for bra (ket) state at each lattice site (p, q). Thus, the matrix element of the term in the $\hat{h}_{p,q}$ with the operator $\hat{b}_{p,q}$ is

$$-\left(J_x\phi^*_{p+1,q} + J^*_x\phi^*_{p-1,q} + J_y\phi^*_{p,q-1} + J^*_y\phi^*_{p,q+1}\right) \langle m| \hat{b}_{p,q} |n\rangle = c_f\sqrt{n}\delta_{m,n-1}, \tag{2.9}$$

where $c_f = -(J_x\phi^*_{p+1,q} + J^*_x\phi^*_{p-1,q} + J_y\phi^*_{p,q-1} + J^*_y\phi^*_{p,q+1})$. And for the $\hat{b}^\dagger_{p,q}$ operator, matrix element is

$$-\left(J^*_x\phi_{p+1,q} + J_x\phi_{p-1,q} + J^*_y\phi_{p,q-1} + J_y\phi_{p,q+1}\right) \langle m| \hat{b}^\dagger_{p,q} |n\rangle = c^*_f\sqrt{n+1}\delta_{m,n+1}, \tag{2.10}$$

with $c^*_f = -(J^*_x\phi_{p+1,q} + J_x\phi_{p-1,q} + J^*_y\phi_{p,q-1} + J_y\phi_{p,q+1})$. Similarly, the diagonal matrix element is

$$D_{nn} = -\left[c_f\phi_{p,q} + c^*_f\phi^*_{p,q}\right] + \frac{U}{2}\left[n(n-1)\right] - \tilde{\mu}_{p,q}n. \tag{2.11}$$

Combining all the expressions, the Hamiltonian matrix can be written as

$$h = \begin{pmatrix} D_{00} & c_f & 0 & \cdots & \cdots & 0 \\ c^*_f & D_{11} & \sqrt{2}c_f & \cdots & \cdots & 0 \\ 0 & \sqrt{2}c^*_f & D_{22} & \cdots & \cdots & 0 \\ \vdots & \vdots & \vdots & \ddots & \ddots & \sqrt{N_b}c_f \\ 0 & 0 & 0 & \cdots & \sqrt{N_b}c^*_f & D_{N_bN_b} \end{pmatrix} \tag{2.12}$$

For the results presented in the thesis, I consider $N_{\rm b} = 10$ and choose an initial guess of $\phi_{p,q}$. We, then, diagonalize the Hamiltonian matrix in Eq. (2.12) for each site and

retain the lowest eigenstate. For example, for the (p, q) lattice site lowest eigenstate is the ground state $|\psi\rangle_{p,q}$ in $|\Psi_{\rm GW}\rangle$. Using this $|\psi\rangle_{p,q}$, we compute a new value of $\phi_{p,q}$

$$\phi_{p,q} = \langle\Psi_{\rm GW}|\hat{b}_{p,q}|\Psi_{\rm GW}\rangle = \sum_{n=0}^{N_{\rm b}} \sqrt{n} c_{n-1}^{(p,q)^*} c_n^{(p,q)}. \tag{2.13}$$

In an iteration, this is repeated for all the lattice sites and the direct product of the single-site ground states determine the Gutzwiller ground state $|\Psi_{\rm GW}\rangle$ of the system. After covering all the lattice sites, in the next iteration, we restart the computations again from the first lattice site. This cycle is continued till convergence is reached. Where the convergence criterion is that the change in the average value of ϕ should be smaller than a threshold value $\Delta\phi$. In this work I take $\Delta\phi = 10^{-13}$.

The phase of the ground state is determined based on the value of $\phi_{p,q}$: it is zero in the case of MI, but finite for the SF phase. This can be understood from the definition of $|\Psi_{\rm GW}\rangle$ in Eq. (2.7). For the MI state with density or occupancy $\rho = m$ the ground state is

$$|\Psi_{\rm GW}\rangle_{\rm MI}^{m} = \prod_{p,q} c_m^{(p,q)} |m\rangle_{p,q}, \tag{2.14}$$

with the condition $|c_m^{(p,q)}|^2 = 1$. Considering that only $|m\rangle_{p,q}$ contributes and it is evident that $\phi_{p,q}$ is zero from the Eq. (2.13). On the other hand, for the SF phase more than one occupation number state contributes to the ground state of each lattice site and hence $\phi_{p,q}$ is non-zero. Using the ground state of the system, I can also compute the occupancy or density at each of the lattice site as

$$\rho_{p,q} = \langle\Psi_{\rm GW}|\hat{n}_{p,q}|\Psi_{\rm GW}\rangle = \sum_{n=0}^{N_{\rm b}} n |c_n^{(p,q)}|^2. \tag{2.15}$$

For the MI phase, $\rho_{p,q}$ is integer and same for all the lattice sites. For the SF phase $\rho_{p,q}$ has non-integer value.

2.2.2 Cluster Gutzwiller mean-field theory (CGMF)

From the expression of $\hat{H}^{\rm MF}$ in Eq. (2.4), and as mentioned earlier, in the SGMF theory, the nearest-neighbour hopping or the inter-site coupling is incorporated through the SF order parameter $\phi_{p,q}$. Thus, the SGMF theory does not describe the inter-site correlation very accurately. The CGMF theory remedy this by including the hopping

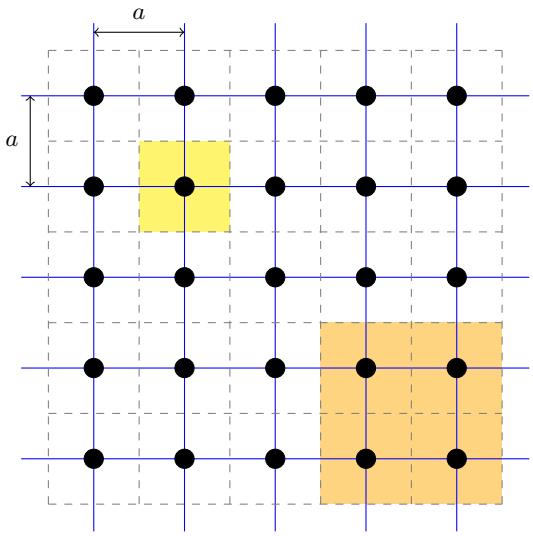

Figure 2.1: The solid blue lines between the lattice sites represent the inter-site bonds. The gray dashed lines demarcate cell around each lattice sites, which is used in representing cluster or attributing properties to each of the lattice sites. For illustration, one of the cell is highlighted in yellow and as an example of a 2×2 cluster is identified with orange color.

term exactly within the lattice sites of a cluster. To describe CGMF theory consider the system size is $K \times L$ and it is divided into W clusters of size $M \times N$, that is $W = (K \times L)/(M \times N)$. Here, K, L, M, N, $W \in \mathbb{N}$. A schematic description of the lattice, single-site and cluster is shown in Fig. 2.1. In the figure the blue lines represent the nearest-neighbour bonds and the gray dashed lines are the orthogonal bisectors of the bonds. The bisectors enclosed each lattice point within a *cell* and points of intersections of the bisectors form a *dual lattice*. For clarity one of the lattice cell is highlighted in yellow color. For the homogeneous systems, the limit of infinite extent is obtained through the periodic boundary conditions. Like in the SGMF theory, we can define a cluster Hamiltonian and then, the total Hamiltonian is the sum of all the cluster Hamiltonians [157]. To derive the Hamiltonian for the CGMF theory, we decompose the hopping part of the Hamiltonian in two terms. The first term is the exact hopping term for the inter-site coupling within the cluster and the second term defines inter-site coupling for the sites at the boundaries through the mean-field $\phi_{p,q}$. The Hamiltonian for a cluster can be written as

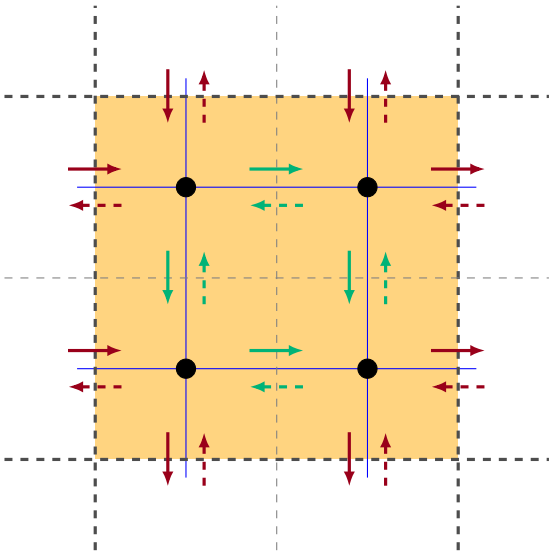

Figure 2.2: A 2×2 cluster within the lattice. The light and bold dashed lines marked boundaries of cells and cluster, respectively. The solid (dashed) green colored arrows represent the exact hopping term (Hermitian conjugate) within the cluster. Similarly, the solid (dashed) red-colored arrows represent the approximate hopping term (Hermitian conjugate) across clusters with one order of ϕ and operator.

$$\begin{aligned}\hat{H}_C \;=\; & -{\sum_{p,q\in C}}' \left[\left(J_x\hat{b}^\dagger_{p+1,q}\hat{b}_{p,q}+\text{H.c.}\right)+\left(J_y\hat{b}^\dagger_{p,q+1}\hat{b}_{p,q}+\text{H.c.}\right)\right] \\ & -\sum_{p,q\in\delta C}\left[\left(J_x\phi^*_{p+1,q}\hat{b}_{p,q}+\text{H.c.}\right)+\left(J_y\phi^*_{p,q+1}\hat{b}_{p,q}+\text{H.c.}\right)\right] \\ & +\sum_{p,q\in C}\left[\frac{U}{2}\hat{n}_{p,q}(\hat{n}_{p,q}-1)-\tilde{\mu}\hat{n}_{p,q}\right], \end{aligned} \tag{2.16}$$

where the prime in the summation of the first term is to indicate that $(p+1,q),(p,q+1)\in C$ and δC represents the lattice sites at the boundary of the cluster. The order parameter $\phi^*_{p+1,q}=\langle\hat{b}^\dagger_{p+1,q}\rangle$ with $(p+1,q)\notin C$ defines the order parameter at the boundary of the neighbouring cluster and is required to describe the inter-cluster hopping along the x direction. Similarly, $\phi^*_{p,q+1}=\langle\hat{b}^\dagger_{p,q+1}\rangle$ with $(p,q+1)\notin C$. Schematically, the clusters are conveniently represented in terms of cells. In Fig. 2.2 the cells of a 2×2 cluster and neighbouring clusters are highlighted. In this diagram, the solid (dashed) green arrow represents the exact hopping term (Hermitian conjugate) within

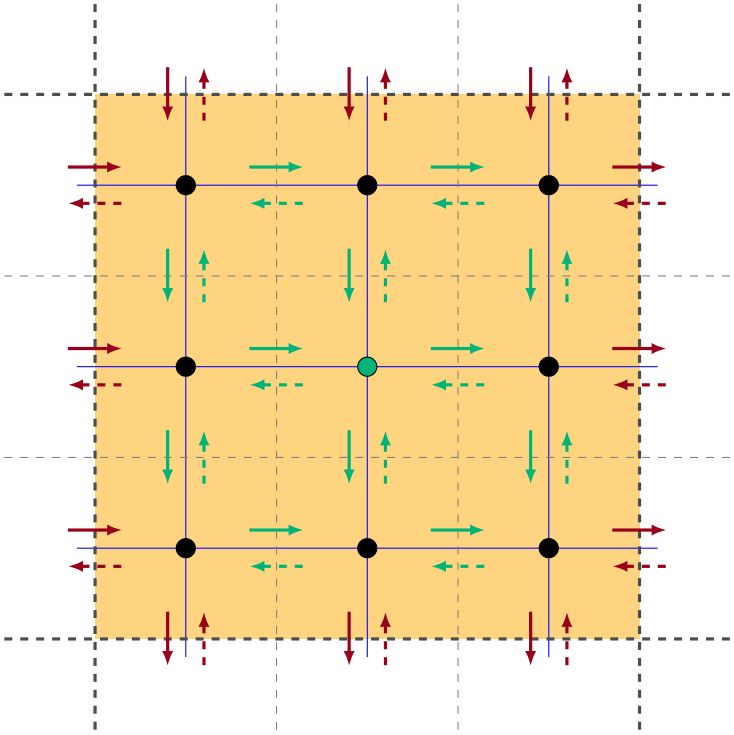

Figure 2.3: A 3×3 cluster and form of the hopping terms between the lattice sites. For clarity, each lattice site is represented in terms of cells. The light and bold dashed lines marked the boundaries of cells and cluster, respectively. The solid (dashed) green colored arrows represent the exact hopping term (Hermitian conjugate) within the cluster. Similarly, the solid (dashed) red-colored arrows represent approximate hopping term (Hermitian conjugate) across clusters with one order of ϕ and operator. The hopping terms involving the central lattice site, represented in green color, are all exact.

the cluster. The solid red (dashed) arrow represents the hopping (Hermitian conjugate) term at the boundary, which is not exact. The BHM Hamiltonian for a 2×2 cluster can be written as the sum of Hamiltonians of four lattice sites of the cluster as

$$\hat{H}_c = \hat{h}_{00} + \hat{h}_{10} + \hat{h}_{01} + \hat{h}_{11},$$

where $\hat{h}_{pq}$, $(p,q) = (0,0), (1,0), (0,1), (1,1)$ is the single-site Hamiltonian at the (p,q) lattice sites within the cluster. As mentioned earlier, I consider lattice size is $K\times L$ and the lattice sites are labeled along x (y) axis, which varies as 0, 1, . . ., and $K-1$ (0, 1, . . ., and $L-1$). The expression of the single-site Hamiltonians in terms of lattice sites

are

$$\begin{aligned}
\hat{h}_{00} &= -\left(J_x \hat{b}^{\dagger}_{1,0}\hat{b}_{0,0} + \text{H.c}\right) - \left(J_y \hat{b}^{\dagger}_{0,1}\hat{b}_{0,0} + \text{H.c}\right) \\
&\quad - \left[J_x\left(\hat{b}^{\dagger}_{0,0}\phi_{K-1,0} - \phi^{*}_{0,0}\phi_{K-1,0}\right) + \text{H.c}\right] \\
&\quad - \left[J_y\left(\hat{b}^{\dagger}_{0,0}\phi_{0,L-1} - \phi^{*}_{0,0}\phi_{0,L-1}\right) + \text{H.c}\right] \\
&\quad + \frac{U}{2}\hat{n}_{0,0}(\hat{n}_{0,0}-1) - \tilde{\mu}\hat{n}_{0,0}, \qquad (2.17) \\
\hat{h}_{10} &= -\left(J_y \hat{b}^{\dagger}_{1,1}\hat{b}_{1,0} + \text{H.c}\right) - \left[J_x\left(\phi^{*}_{2,0}\hat{b}_{1,0} - \phi^{*}_{2,0}\phi_{1,0}\right) + \text{H.c}\right] \\
&\quad - \left[J_y\left(\hat{b}^{\dagger}_{1,0}\phi_{1,L-1} - \phi^{*}_{1,0}\phi_{1,L-1}\right) + \text{H.c}\right] \\
&\quad + \frac{U}{2}\hat{n}_{1,0}(\hat{n}_{1,0}-1) - \tilde{\mu}\hat{n}_{1,0}, \qquad (2.18) \\
\hat{h}_{01} &= -\left(J_x \hat{b}^{\dagger}_{1,1}\hat{b}_{0,1} + \text{H.c}\right) - \left[J_x\left(\hat{b}^{\dagger}_{0,1}\phi_{K-1,1} - \phi^{*}_{0,1}\phi_{K-1,1}\right) + \text{H.c}\right] \\
&\quad - \left[J_y\left(\phi^{*}_{0,2}\hat{b}_{0,1} - \phi^{*}_{0,2}\phi_{0,1}\right) + \text{H.c}\right] \\
&\quad + \frac{U}{2}\hat{n}_{0,1}(\hat{n}_{0,1}-1) - \tilde{\mu}\hat{n}_{0,1}, \qquad (2.19) \\
\hat{h}_{11} &= -\left[J_x\left(\phi^{*}_{2,1}\hat{b}_{1,1} - \phi^{*}_{2,1}\phi_{1,1}\right) + \text{H.c}\right] - \left[J_y\left(\phi^{*}_{1,2}\hat{b}_{1,1} - \phi^{*}_{1,2}\phi_{1,1}\right) + \text{H.c}\right] \\
&\quad + \frac{U}{2}\hat{n}_{1,1}(\hat{n}_{1,1}-1) - \tilde{\mu}\hat{n}_{1,1}, \qquad (2.20)
\end{aligned}$$

where the operators and ϕ with index $(K-1)$ and $(L-1)$ embody the periodic boundary conditions along x and y directions, respectively. An important point is, with the 2×2 cluster none of the lattice sites have an exact representation of the hopping term. The minimal cluster size which has exact hopping terms with respect to a lattice site is 3×3, and the schematic diagram is shown in Fig. 2.3. As seen from the figure, the hopping terms involving the central lattice site are all exact.

As I have mentioned the Hamiltonian for a cluster and the full Hamiltonian for the system is the sum of all the cluster Hamiltonians. Therefore, the full Hamiltonian in the explicit form with 2×2 cluster is

$$\hat{H} = \sum_{i,j}\left[\hat{h}_{2i,2j} + \hat{h}_{2i+1,2j} + \hat{h}_{2i,2j+1} + \hat{h}_{2i+1,2j+1}\right],$$

where i (j) is cluster index along the x (y) direction. The expressions for the component Hamiltonians in the total Hamiltonian is given in the Appendix. Now to obtain the ground state solution of the cluster Hamiltonian, we calculate the matrix elements and construct the matrix of the Hamiltonian in Eq. (2.16) for each cluster. For this, I

consider the state for each cluster (i,j) in the Fock basis as

$$|\psi_c\rangle_{i,j} = \sum_{n_0,n_1...,n_{m'}} C^{(i,j)}_{n_0,n_1..,n_{m'}} |n_0,n_1...,n_{m'}\rangle\,, \tag{2.21}$$

where $m' = (M{\times}N)-1$ and n_m is the quantum number of the occupation number state of the mth lattice site within the cluster, and $C^{(i,j)}_{n_0,n_1,...,n_{m'}}$ is the amplitude of the cluster Fock state $|n_0,n_1,\ldots,n_{m'}\rangle$. The above definition can be written in a more compact form using the index quantum number $\ell \equiv \{n_0,n_1,\ldots,n_{m'}\}$ as

$$|\psi_c\rangle_{i,j} = \sum_{\ell} C^{(i,j)}_{\ell} |\phi_c\rangle_{\ell}\,, \tag{2.22}$$

where $|\phi_c\rangle_\ell$ represents the cluster basis state $|n_0,n_1...,n_{m'}\rangle$. The ground state of the entire $K\times L$ lattice, like in SGMF, is the direct product of the cluster ground states

$$|\Psi^c_{\rm GW}\rangle = \prod_k |\psi_c\rangle_k \tag{2.23}$$

where, k is the cluster index and varies from 1 to $W = (K\times L)/(M\times N)$. The SF order parameter ϕ is computed similar to Eq.(2.13) as

$$\phi_{p,q} = \langle\Psi^c_{\rm GW}|\,\hat{b}_{p,q}\,|\Psi^c_{\rm GW}\rangle\,. \tag{2.24}$$

The matrix elements of the cluster Hamiltonian are

$$H^c_{mn} =_{\ell'} \langle\phi_c|\,\hat{H}_c\,|\phi_c\rangle_\ell = \langle m_0,m_1...,m_{m'}|\,\hat{H}_c\,|n_0,n_1...,n_{n'}\rangle\,, \tag{2.25}$$

where the index quantum number $\ell' \equiv \{m_0,m_1,\ldots,m_{m'}\}$. From the cluster Hamiltonian, I find that there are thirteen unique matrix elements for any size of the cluster. Out of these twelve matrix elements arise from the hopping term and the last one from the diagonal term. Here, I describe these matrix element for the case of 2×2 cluster and for this the cluster state Fock basis are $|n_0,n_1,n_2,n_3\rangle$. Among the matrix elements arising from the hopping terms, four correspond to intra-cluster hopping, which are exact, and these are

$$\begin{aligned}
H^{\rm intra}_x &= -J_x\,\langle m_0,..,m_3|\,\hat{b}^\dagger_{2i+1,2j+k}\hat{b}_{2i,2j+k}\,|n_0,..,n_3\rangle\,,\\
H^{*\rm intra}_x &= -J^*_x\,\langle m_0,..,m_3|\,\hat{b}^\dagger_{2i,2j+k}\hat{b}_{2i+1,2j+k}\,|n_0,..,n_3\rangle\,,\\
H^{\rm intra}_y &= -J_y\,\langle m_0,..,m_3|\,\hat{b}^\dagger_{2i+l,2j+1}\hat{b}_{2i+l,2j}\,|n_0,..,n_3\rangle\,,
\end{aligned}$$

$$H_y^{*\text{intra}} = -J_y^* \langle m_0,..,m_3| \hat{b}^\dagger_{2i+l,2j} \hat{b}_{2i+l,2j+1} |n_0,..,n_3\rangle ,$$

where k $(l) = 0, 1$ for the case of 2×2. The general expression for the case of a $M\times N$ cluster is given in the Appendix. Following the cluster Hamiltonian, there are eight terms which arise from the inter-cluster hopping at the boundaries and these can be written as

$$\begin{aligned}
H_x^{\text{in}} &= -J_x \langle m_0,..,m_3| \hat{b}^\dagger_{2i,2j+k} \phi_{2i-1,2j+k} |n_0,..,n_3\rangle ,\\
H_x^{*\text{in}} &= -J_x^* \langle m_0,..,m_3| \hat{b}_{2i,2j+k} \phi^*_{2i-1,2j+k} |n_0,..,n_3\rangle ,\\
H_x^{\text{out}} &= -J_x \langle m_0,..,m_3| \hat{b}_{2i+1,2j+k} \phi^*_{2i+2,2j+k} |n_0,..,n_3\rangle ,\\
H_x^{*\text{out}} &= -J_x^* \langle m_0,..,m_3| \hat{b}^\dagger_{2i+1,2j+k} \phi_{2i+2,2j+k} |n_0,..,n_3\rangle ,\\
H_y^{\text{in}} &= -J_y \langle m_0,..,m_3| \hat{b}^\dagger_{2i+l,2j} \phi_{2i+l,2j-1} |n_0,..,n_3\rangle ,\\
H_y^{*\text{in}} &= -J_y^* \langle m_0,..,m_3| \hat{b}_{2i+l,2j} \phi^*_{2i+l,2j-1} |n_0,..,n_3\rangle ,\\
H_y^{\text{out}} &= -J_y \langle m_0,..,m_3| \hat{b}_{2i+l,2j+1} \phi^*_{2i+l,2j+2} |n_0,..,n_3\rangle ,\\
H_y^{*\text{out}} &= -J_y^* \langle m_0,..,m_3| \hat{b}^\dagger_{2i+l,2j+1} \phi_{2i+l,2j+2} |n_0,..,n_3\rangle .
\end{aligned}$$

Here, the superscript 'in' and 'out' indicate hopping from a neighbouring cluster to the cluster of interest and vice versa, respectively. Depending on the k and l these matrix elements can also be calculated. The last term, the diagonal term, is

$$\begin{aligned}
H^{\text{diag}} = \sum_{k,l} \langle m_0,..,m_3| \big(& J_x \phi^*_{2i,2j+k} \phi_{2i-1,2j+k} + \text{H.c.} \\
& + J_x \phi^*_{2i+2,2j+k} \phi_{2i+1,2j+k} + \text{H.c.} + J_y \phi^*_{2i+l,2j} \phi_{2i+l,2j-1} + \text{H.c.} \\
& + J_y \phi^*_{2i+l,2j+2} \phi_{2i+l,2j+1} + \text{H.c.}\big) + \frac{U}{2} \hat{n}_{2i+k,2j+l} \left(\hat{n}_{2i+k,2j+l} - 1\right) \\
& - \tilde{\mu} \hat{n}_{2i+k,2j+l} |n_0,..,n_3\rangle , .
\end{aligned}$$

Here it is worth to be mention that, we employ periodic boundary conditions on a toroidal geometry. For the matrix elements as I have mention earlier that there are four Fock basis for the 2×2 cluster and in general, the quantum numbers n_0, n_1, n_2 and n_3 correspond to the lattice sites $(2i, 2j)$, $(2i+1, 2j)$, $(2i, 2j+1)$, and $(2i+1, 2j+1)$, respectively. The expressions of the matrix elements for the case of the first cluster in the lattice is given in the Appendix.

2.2.3 Phase Diagram

As mentioned earlier, at zero temperature BHM admits two phases, MI and SF phases. These emerge from the competition of the kinetic energy (J) and on-site inter-atomic interaction energy (U). In the SF phase, kinetic energy dominates over the on-site interaction energy ($J \gg U$), and atoms can hop between nearest neighbour sites. The atoms are thus delocalized or itinerant and there is off-diagonal long-range order (ODLRO) in the system. Due to the phase coherence in the system, atoms exhibit interference patterns when the lattice is switched off. The phase coherence implies that the number of atoms at a lattice site or occupancy, the conjugate variable of phase, fluctuates and this leads to non-zero SF order parameter $\phi_{p,q}$. The wave-function of the SF state for $\mathcal{N}$ bosons and $K \times L$ lattice sites is

$$|\Psi_{\rm SF}\rangle \propto \left(\sum_{i=1}^{KL} \hat{b}_i^\dagger\right)^{\mathcal{N}} |0\rangle\,, \tag{2.26}$$

where $|0\rangle$ is the vacuum state. In other words, in our numerical computations the SF state is a linear combination of the coefficients c_ns and $C_{n_1,..,n_{M\times N}}$s in the SGMF and CGMF theories, respectively. In the MI phase, the on-site interaction energy dominates over the kinetic energy of the atoms ($J \ll U$) and atoms can not hop between the lattice sites. Hence, the atoms are localized and each site has commensurate integer filling. In other words, there is number coherence across the lattice but no phase coherence. As a result, there is no off-diagonal long-range order (ODLRO). The MI state with n number of atoms at each lattice site is

$$|\Psi_{\rm MI}\rangle \propto \prod_{i=1}^{KL} \left(\hat{b}_i^\dagger\right)^n |0\rangle\,. \tag{2.27}$$

In our numerical simulation, for the MI state only one of the coefficients c_n in the SGMF case and $C_{n_1,..,n_{M\times N}}$ in the CGMF case contribute. Therefore, the SF order parameter is zero. For the homogeneous system, the phase diagram for the first Mott lobe $n = 1$ is shown in the Fig. 2.5. This phase diagram is computed from the SGMF and CGMF theories. To locate the phase boundary, we compute the energy for a particular value of μ/U by varying J/U as shown in Fig. 2.4. In the SGMF case, the energy is constant in the MI phase as the SF order parameter $\phi_{p,q}$ is zero and tunneling energy does not contribute in the calculation. Therefore, energy in the strongly interacting

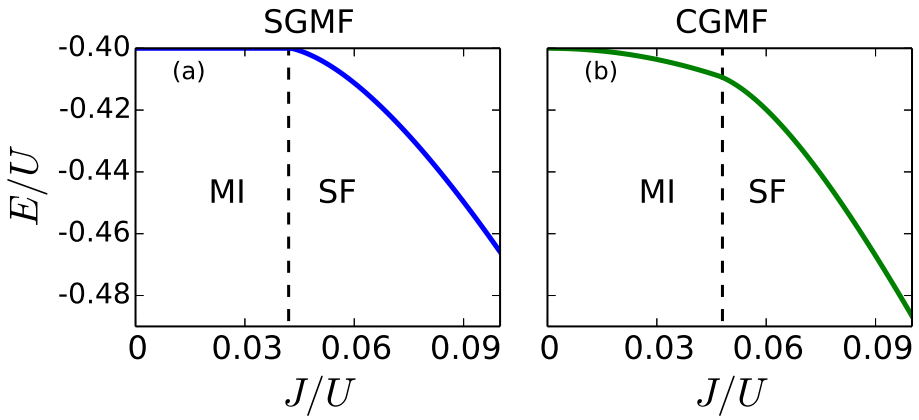

Figure 2.4: Energy of the system to obtain MI-SF phase boundary around n = 1 Mott lobe with $\mu = 0.4$ from SGMF theory in Fig. (a) and 2×2 CGMF theory in Fig.(b). The dashed line in both cases marks the phase boundary. From the CGMF calculation enhancement in the phase boundary is obtained.

regime (MI phase) with SGMF is

$$E = \frac{U}{2} n(n-1) - \mu n.$$

At the MI-SF phase boundary energy changes and depending on the value of μ it can either decrease or increase. The energy decreases across the MI-SF boundary when the phase transition is due to density fluctuations arising from holes, this corresponds to the lower part of the Mott lobe. For the upper part of the lobe, where the phase transition is due to the density fluctuations arising from particles, the energy increases. The trend in the energy for the first case is shown as an example in Fig. 2.4 (a). The dashed line in Fig. 2.4 (a) represents the phase boundary. For the CGMF computation, we consider 2×2 cluster and compute the energy for the same value of $\mu/U = 0.4$ by varying the J/U. In the CGMF, energy has variation in the MI phase as within the cluster hopping is exact. In this case, a discontinuity in the slope of the energy marks the phase boundary. The dashed line in Fig. 2.4 (b) marks the value of J/U at which the phase transition occurs with the CGMF theory.

The location of the MI-SF transition is increased to with CGMF and hence, the size of the Mott lobe is enhanced. This is due to the better description of quantum fluctuations in the system. The enhanced Mott lobes for $n = 1$ with different cluster sizes ranging from $2{\times}2$ to $4{\times}5$ are shown in the Fig. 2.5. With the SGMF method the tip

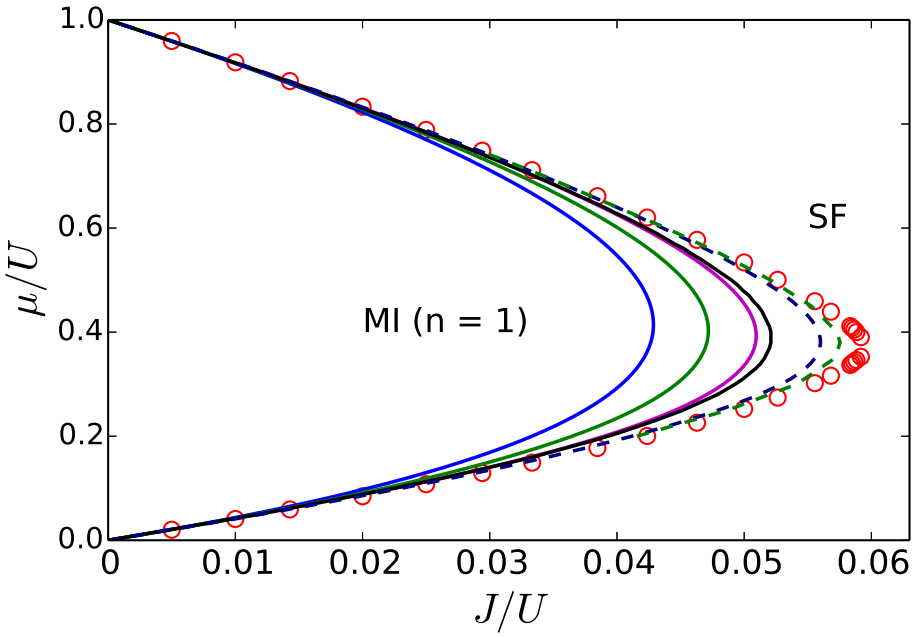

Figure 2.5: MI-SF phase boundary around n = 1 Mott lobe from SGMF theory (blue), 2×2 CGMF theory (green), 3×3 CGMF (magenta) and 4×4 CGMF (black) with open boundary condition. By considering periodic boundary condition along x direction the enhancement in the phase boundary is obtained with 4×4 CGMF (dashed Navy Blue) and 4×5 CGMF (dashed green). The Red circles are the quantum Monte Carlo results from [1] (The data are obtained from personal communication with Prof. Barbara Capogrosso-Sansone).

of the Mott lobe is located at $J/U = 0.0429$, which increases to $J/U = 0.0575$ with 4×5 cluster. Here, it is to be mentioned that at the tip of the Mott lobe the phase transition is second-order as it arises from the phase fluctuations. On the other hand below and above the tip, the phase transition is first order and arises from the density fluctuations. In general, the number of cluster states increases exponentially with cluster size and hence, for computations with large clusters it is essential to do cluster state selection based on suitable criteria. The details of the state selection and other aspects of CGMF computations with large clusters are discussed in the next section.

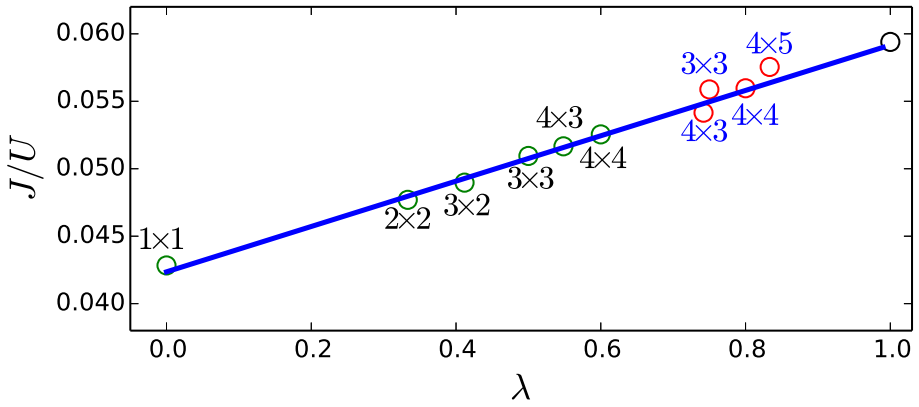

Figure 2.6: Finite size scaling plot with different cluster sizes. The scaling parameter λ is plotted with the critical value of J/U for different cluster sizes. The scaling parameter is zero for 1×1 cluster (single site) and one for infinite size cluster. In this plot green circle denote the results with open boundary condition, red circles denote the results with periodic boundary along x direction and black circle denote the result for an infinite lattice system which approaches to quantum Monte Carlo results.

2.2.4 Phase boundary and Finite-size scaling

It is well established that the mean-field theory [42] underestimates the MI-SF phase boundary. And, on the other hand, the strong coupling expansion [159, 176] overestimate the boundary when compared with the quantum Monte Carlo simulations [1]. In the literature, there has been numerous works to obtain the phase boundary of $n = 1$ Mott lobe for 2D square lattices. The multisite mean field theory predicts the tip of the lobe to be $(J/U = 0.049, \mu/U = 0.4)$ [156], with nonperturbative RG approach it is $(J/U = 0.060, \mu/U = 0.387)$ [163, 164], and with higher order many body perturbation theory it is $(J/U = 0.05909, \mu/U = 0.376)$ [161]. The finite temperature B-DMFT [165] also predict the Mott lobe boundary in agreement with the quantum Monte Carlo simulation for 2D square and 3D cubic lattices. As mentioned earlier, with SGMF, we observe the Mott lobe tip is located at $(J/U = 0.04287, \mu/U = 0.41)$. Using the CGMF method, the results improve and with large cluster sizes, the location of the tip approaches the quantum Monte Carlo result. We demonstrate this with finite-size scaling and the MI-SF phase diagram for $n = 1$ from our studies is shown in Fig. 2.5. Here, computing with a larger cluster size like $\geq 3\times3$ is computationally

expensive if we consider all the cluster states and generating a smooth phase boundary can take several weeks. To overcome this, we restrict the infinite Fock space to a limited set of Hilbert spaces. In the Hilbert space cluster states are reduced based on the number fluctuations at a single site and within the entire cluster. For $n = 1$ Mott lobe, we restrict the single site Fock basis to $n_i = \pm 2$ and total number of particles in the cluster to be N and $N \pm 1$. Here N is the number of particles in N lattice sites for Mott lobe $n = 1$. The cluster states can be further reduced for the phase boundary, where number fluctuations at each site are limited. The number fluctuations in the cluster can be restricted as $n_{cf} = \sum_i |n_i - n| \leq 7$. A similar scheme to restrict the size of the Fock space is presented in the work of Lühmann [157].

To obtain the phase boundary with large cluster size such as 3×3, 4×3, 3×4, 4×4, 4×5 we start the CGMF computations with an initial value of order parameter $\phi = 10^{-6}$. And, ϕ obtained after one iteration is used to identify the phase. The phase is MI if the new value of ϕ is smaller than the initial ϕ, and otherwise, it is SF phase. To identify the phase boundary for a specific value of μ/U we start with two values of J/U, such that the lower and higher values are in the MI and SF phases, respectively. Then, using the value of ϕ from a single iteration and bisection method we identify the phase boundary to the required accuracy. An important point is that using the periodic boundary condition improves the phase boundary results. This is to be expected as we consider the exact hopping along the direction where the periodic boundary condition is imposed. In our case, the periodic boundary condition is applied along x direction and along y direction the cluster is coupled to the neighbour through the mean-field. With this, the tip of the Mott lobe is located at $(J/U = 0.0560, \mu/U = 0.38)$ for 4×4 cluster it increases to $(J/U = 0.0575, \mu/U = 0.38)$ for 4×5 cluster .

To compare our CGMF results with the quantum Monte Carlo results, we use finite-size scaling to determine the location of the Mott lobe tip in the limit infinite size cluster. For this the scaling parameter $\lambda = B_C/(B_C + B_{\delta C})$ [157, 169] is plotted with the critical value of J/U for different cluster sizes in Fig. 2.6. Here, B_C is the number of bonds inside the cluster and $B_{\delta C}$ is the number of bonds at the boundary. In Fig. 2.6, the green circles denote the MI-SF phase transition with open boundary condition, red circles denote the MI-SF phase transition with periodic boundary condition

along x direction. We observe that in the limit of infinite sized cluster our results approaches the quantum Monte Carlo result $J/U = 0.0594$ and shown with black circle in Fig. 2.6. For comparison, in the figure, we also show the phase boundary obtained from the quantum Monte Carlo studies using the same data of the results reported in Capograsso-Sasone et al. [1].

2.3 Finite temperature BHM

The theories discussed so far are pertaining to zero temperature. These do provide important insights, however, experiments are performed at finite temperatures. So, to relate the theoretical finding with experimental realizations it is essential to incorporate the effect of thermal fluctuations arising from finite temperatures. One straight forward approach to consider $T \neq 0$ in the mean-field theory is to calculate SF order parameter $\phi_{p,q}$ ($\phi^*_{p,q}$) as thermal average of the annihilation (creation) bosonic operator [134]

$$\phi_{p,q} \equiv \langle \hat{b}_{p,q} \rangle = \frac{1}{Z} \mathrm{Tr} \left(\hat{b} e^{-\beta \hat{H}} \right),$$

where $Z = \mathrm{Tr} e^{-\beta \hat{H}}$ is the partition function, $\beta = 1/k_B T$ with T being the temperature, and $\hat{H}$ is the Hamiltonian of the system. In the finite temperature BHM, we consider ground and excited states ψ_0, ψ_1, ψ_2, ..., ψ_{N_b-1} in the single site Gutzwiller wavefunction. Therefore, the SF order parameter is

$$\phi_{p,q} = \frac{1}{Z} \sum_{i=0}^{N_b-1} \left[{}_{p,q}\langle \psi_i | \hat{b}_{p,q} | \psi_i \rangle_{p,q} \, e^{-\beta E_i} \right] \tag{2.28}$$

and the partition function is

$$Z = \sum_{i=0}^{N_b-1} e^{-\beta E_i}, \tag{2.29}$$

where, E_0, E_1, ..., E_{N_b-1} are energies of the ground state and the excited states. These energies and eigenstates are obtained by digonalizing the single site Hamiltonian. As discussed earlier, we consider N_b occupation number Fock basis states, and when we diagonalize the single-site Hamiltonian we obtain N_b eigenvalues and eigenstates. These can thus be labeled using index quantum number varying from 0 to $N_b - 1$.

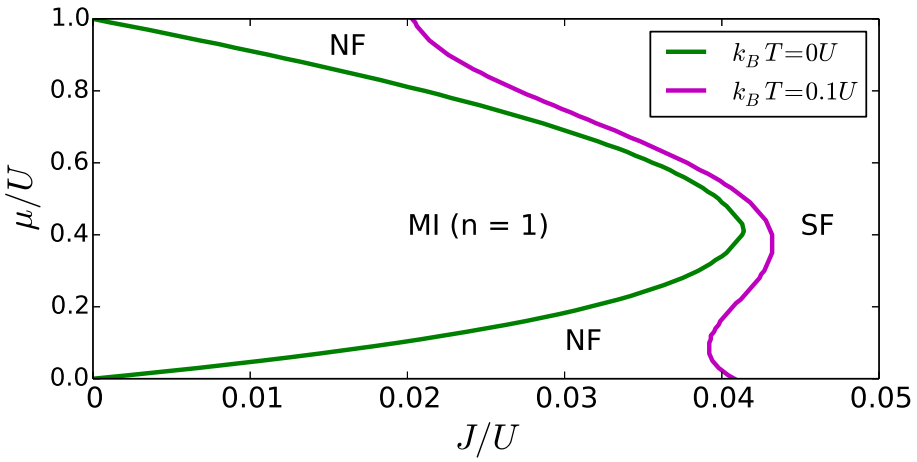

Figure 2.7: MI-SF phase boundary around n = 1 Mott lobe from SGMF theory (green) and with finite temperature theory (magenta). Melting of the Mott lobe is observed with the temperature and normal fluid (NF) phase emerges.

In short, for the finite temperature, we obtain the ground state solution by considering all the eigenstates and eigenvalues. For each computation, we start with an initial choice of $\phi_{p,q}$ and construct the single site Hamiltonian in Eq. (2.5). We diagonalize the Hamiltonian and obtain all the eigenstates and eigenenergies, and compute the new SF order parameter $\phi_{p,q}$ as in Eq. (2.28). Then, we use this new $\phi_{p,q}$ in the next iteration and repeat the process until it converges. We also compute average lattice occupancy, which is the thermal average of the number operator and can be written as

$$\rho_{p,q} = \frac{1}{Z} \sum_{i=0}^{N_b-1} \left[{}_{p,q}\langle \psi_i | \, \hat{n}_{p,q} \, | \psi_i \rangle_{p,q} \, e^{-\beta E_i} \right]. \tag{2.30}$$

The same sequence of computations is followed in the case of the CGMF theory as well. The only difference is that the thermal average is now computed in terms of the cluster states. In the CGMF the energy states are E_0, E_1, ..., $E_{N_b^{M\times N}-1}$ for the $M \times N$ cluster size. Therefore, in the case of large cluster size we apply a cut off on the eigenstates we consider in the thermal average based on the eigenenergy. After which we compute the SF order parameter for all the lattice sites within a cluster and obtain the ground state solution. We determine the finite-temperature phase diagram and at higher temperatures, we observe the melting of the MI and SF phases. As an example the phase diagram for the temperature $k_B T = 0.1U$ is shown in Fig. 2.7. At finite temperatures, a new phase referred to as normal fluid (NF) emerges. In the

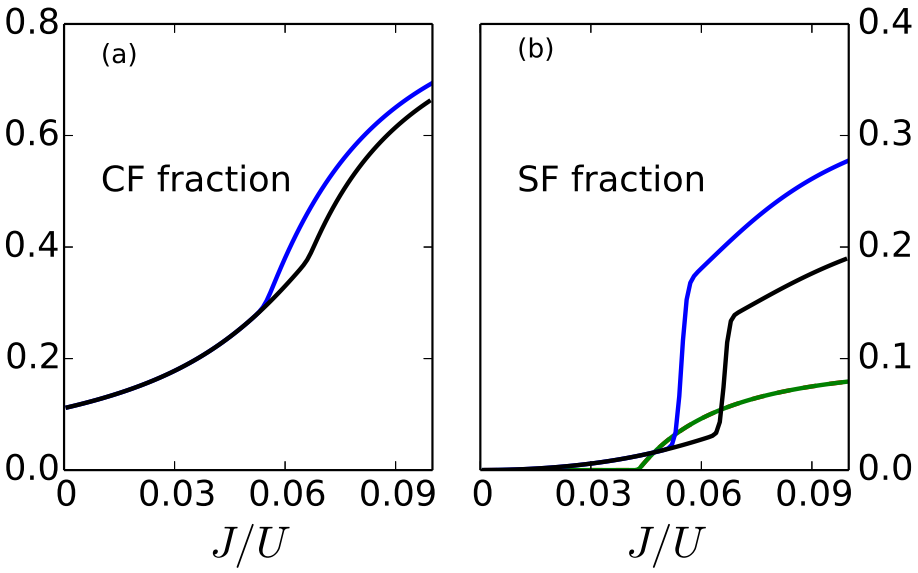

Figure 2.8: (a) Condensate (CF) fraction with 3×3 cluster with zero temperature (blue line) and at $K_BT = 0.01U$ (black line). (b) Superfluid (SF) fraction with SGMF green line and 3×3 CGMF (blue and black line). Here blue line is at zero temperature and black line is at $K_BT = 0.01U$

homogeneous case, the NF phase has real commensurate filling with zero SF order parameter. Thus, in this phase, there is no phase coherence and there is non-zero number fluctuation.

2.4 Superfluid and Condensate fractions

The condensate fraction (CF) $\rho_{\rm cf}$, for ideal bosons, is the fraction which occupies the ground state of the system. And, in the case of ideal bosons, which imply no interactions, the ground state is equivalent to the single-particle ground state. However, for interacting bosons, the general definition given by Penrose and Onsagar [177] is the appropriate definition of $\rho_{\rm cf}$. Based on which $\rho_{\rm cf}$ of a system consisting of N_a atoms is computed from the one-body density matrix (OBDM) as

$$\rho_{\rm cf} = \lambda_m^{\rm OBDM}/N_a.$$

Here, $\lambda_m^{\rm OBDM}$ is the largest eigenvalue of the OBDM and it is of the order of N_a. The OBDM of BHM can be calculated from the ground state obtained using ED and

the details are given in the next chapter. The CF obtained from above expression is shown in Fig. 2.8 (a) for a 3×3 cluster. We observe that $\rho_{\rm cf}$ is finite in the MI phase and increases as the system enters in the SF phase. From the figure, it can be seen that $\rho_{\rm cf}$ at zero temperature is higher than at finite temperature. For comparison, $\rho_{\rm cf}$ for $K_BT = 0.01U$ shown in Fig. 2.8(a). In the figure the system parameters are $\mu/U = 0.4$ and $\theta = 0.1$. The lower CF at higher temperature is expected as the thermal fluctuations deplete the condensate by exciting atoms for the condensate to higher energy states.

The superfluid fraction ρ_s, in contrast to $\rho_{\rm cf}$, is associated with the transport properties of the system. Although the term *superfluid* was coined after the famed experiments by Kapitza [178], and Allen and Misener [179] to measure the viscosity of liquid 4-He, the conceptually unambiguous signatures of superfluidity [180] are Hess-Fairbank effect [181], and existence of *metastable superflow*. Among these two, the Hess-Fairbank effect is the exact analog of Meissner effect in superconductors. And, the *metastable superflow* is often called as persistent superflow in literature. The persistent superflow has been experimentally observed in annular BECs [182] and it was shown that persistent superflow occurs even with a very low condensate fraction of 20%. Theoretically, the persistent flow arises from a phase gradient in the condensate wave-function and this can be emulated with a twisted boundary condition in the case of ultracold atoms in optical lattices [183]. In the present work, I apply a twist in the hopping along x direction. For this the hoping term in the BHM Hamiltonian is modified to $J_x = J_x e^{i(\theta/K)}$ to accommodate a twist by angle θ, where K is total no of lattice sites along x direction [184, 185]. Then, the superfluid fraction is

$$\rho_s = K^2 \frac{E_\theta - E_0}{NJ\theta^2} \tag{2.31}$$

where E_θ is the ground state energy of the system with twist θ, E_0 is the ground state energy without twist and N is total number of particles in the system. We observe that independent of the twist angle the SF fraction is zero in MI phase and finite in the SF phase this is evident from the plots in Fig. 2.8 (b). In the figure we have plotted ρ_s obtained from SGMF theory (green line) for $K_BT = 0U$ and $K_BT = 0.01U$. We observe that the two lines merge and there is no discernible finite temperature effect with SGMF. However, ρ_s is non-zero with CGMF theory and this is evident

from the results shown in Fig. 2.8 (b) based on 3×3 cluster. With CGMF theory ρ_s, in the MI phase, is finite but temperature independent. But, in the SF phase ρ_s is temperature dependent and it decreases with increasing temperature. To be specific, with 3×3 cluster for $J/U = 0.06$ where the MI tip is located in the QMC results, we get $\rho_{\rm cf} = 0.380$ at zero temperature and $\rho_{\rm cf} = 0.330$ at $K_BT = 0.01U$. On the other hand for the same value of J/U and cluster size, $\rho_s = 0.181$ at zero temperature and 0.027 at $K_BT = 0.01U$. These are also evident from the plots in the figures.

On comparing $\rho_{\rm cf}$ and ρ_s we find that $\rho_{\rm cf} > \rho_s$ and this is consistent with the previous results reported by Shams and Glyde [186]. In which they showed that the presence of external potential, like the optical lattice, lowers ρ_s. And, this is to be expected as unlike the persistent current in an annular ring, the periodic potential in an optical lattice is a barrier to the superflow.

2.5 Summary of the Chapter

In this chapter, I derive the BHM Hamiltonian for bosons in 2D optical lattices. I describe in detail the single-site and cluster mean-field theories and obtain the equilibrium solutions of BHM with Gutzwiller ansatz. The phase diagram for the $n = 1$ MI lobe is obtained with SGMF and CGMF methods. I show that the description of the MI-SF phase boundary improves with an increase in the cluster size. Through finite-size scaling, we show that in the limit of infinite cluster size our results are equivalent to QMC results. I, then, discuss BHM at finite temperatures. With the inclusion of the thermal fluctuations, arising from finite temperature, I obtain a new phase normal phase. I end the chapter with the computation of the CF and SF fractions at zero and finite temperatures. For the latter, I use twisted boundary condition by applying a twist in the hoping amplitude. I show that SF and CF fraction decrease with thermal fluctuations.

Chapter 3

Quantum Hall states in optical lattices

Quantum Hall (QH) effect is a phenomenon associated with electrons in a 2D plane under a strong magnetic field and at low temperatures. The integer QH (IQH) effect was experimentally discovered in 1980 by Klitzing, Dorda and Pepper [2], and fractional QH (FQH) effect was soon discovered in 1982 by Tsui, Stormer, and Gossard [3]. Since then it has gained much attention, both in terms of theoretical as well as experimental studies, as it is the cornerstone of topological effects in condensed matter systems [187]. One of the key theoretical breakthroughs was the work of Laughlin [4], in which he proposed a possible form of the wave-function corresponding to the QH state. The main feature of the QH effect is the Hall resistivity or the off-diagonal resistivity R_{xy} that has plateaus at particular values of the filling factor ν and it can be written as $R_{xy} = 2\pi\hbar/\nu e^2$. The diagonal resistivity $R_{xx} = 0$ for those plateaus. Here, the filling factor ν is the ratio between the number of electrons and the number of states. The IQH effect is when ν has integer values and FQH corresponds to fractional values of ν.

Despite enormous progress in the experimental and theoretical understanding of QH effect [43–46], a comprehensive understanding of the physics of the FQH effect [188] is still lacking. The main hurdle to this is the strong correlations of electrons, but the same is essential for FQH states. One of the theoretical models, the Laughlin ansatz [4] provides exact solutions for some FQH states, but not for all. One challenge to experimental efforts in condensed matter systems is the strong magnetic field required to obtain FQH states. In this respect, ultracold atoms trapped in the optical

lattices, have an advantage to study FQH states with high flux [47, 48]. In theoretical studies, features of Laughlin states in low particle density limit has been reported [62] for $\nu = 1/2$ and $\alpha < \alpha_c = 0.4$ using the Exact Diagonalization (ED) method. Here, α_c is the critical value below which FQH states exist, and α is the strength of the synthetic magnetic field. And, the existence of a striped vortex lattice phase is reported in the neighbourhood of $\alpha = 1/2$ [63]. On the other hand, based on the results of Monte Carlo and exact diagonalization (ED), the existence of bosonic FQH states is predicted [65] in the vicinity of Mott plateaus for $\alpha = 2/3$. Similar results are reported in a recent work using the Chern-Simons theory [66] in combination with single site Gutzwiller mean-field (SGMF) theory. In another recent work [67], the incompressibility of the FQH states is employed to identify these states based on the results from cluster Gutzwiller mean-field (CGMF) theory for $\alpha = 1/5$ at $\nu = 1/2$. Similarly, using reciprocal cluster mean-field (RCMF) analysis Hügel et al. [68] predicted a competing FQH state as a metastable state for $\alpha = 1/4$.

In this chapter, I review different types of QH states in optical lattices, then I provide the details about the synthetic magnetic field in optical lattice. I discuss the properties of QH states for the CGMF and ED method. I describe the ED method in great detail and compare the CGMF and ED method in this chapter.

3.1 Quantum Hall states

The QH states are the ground states of a two-dimensional electron gas at low temperatures and under a strong magnetic field. These are identified by the filling factor $\nu = N/N_\Phi$, where N is total number of electrons and N_Φ is the magnetic flux measured in units of Dirac flux quanta $\Phi_0 = 2\pi\hbar/e$. The QH states are highly entangled states which exhibit various properties such as incompressibility and charge density waves. For $\nu = 1/m$, with m as an integer, the ground state is gapped and is an incompressible quantum liquid. In the Landau gauge, this incompressible quantum liquid is described by the Laughlin wave function [4]

$$\Psi(z_1, z_2, ..., z_N) = \prod_{j>k}^{N} (z_j - z_k)^m \prod_{j=1}^{N} \mathrm{e}^{-y_i^2/2}$$

where integer m is odd to satisfy the anti-symmetrization criteria for fermions. For even m the Laughlin state corresponds to bosons, and bosonic systems with repulsive interaction can show properties similar to FQH states in electrons. In this thesis, I focus on ultracold bosons trapped in the optical lattices to study the QH states. There are other QH states such as Read-Rezayi states [189], vortex lattice state [47] and two-component states [63]. In the upper Landau level and above the filling factor $\nu = 1/2$ for weak interaction, the states with higher filling $\nu = 1, 3/2, 2, \ldots$ could be Read-Rezayi states. At higher ν, bosons can form a condensate in the lowest Landau level with the vortices in the system. Such a vortex lattice state is referred to as the mean-field QH state and is gapless and compressible. The transition from Read-Rezayi states to vortex lattice state occur at the filling $\nu \approx 2$ [63]. Two-component QH states occur when particles occupy two internal states of the system. For electrons, it is not energetically favourable, but it is possible in the bilayer systems. At lower magnetic fields, electrons occupy the higher Landau levels as degeneracy in each Landau level is decreased. For the electron system, FQH states are unstable for $N \geq 2$, where $N = 0$, $1, 2, \ldots$ are Landau levels. In this case, instead of FQH states, we observe charge density wave such as the stripe phase. In our work, I will study the QH states in the context of the bosonic system with the BH Hamiltonian in the presence of the synthetic magnetic field. We observe both IQH and FQH states with different fillings ν and for different flux values α with CGMF and exact diagonalization (ED) method.

3.2 Synthetic magnetic field in optical lattices

The wave-function of electrons in a periodic potential is periodic and referred to as the Bloch wave-functions. The corresponding energy spectrum consists of bands. In the presence of an external magnetic field, the energy spectrum split into the highly degenerate Landau levels. And, the combined effect of the periodic potential and magnetic field leads to a complex spectrum which is fractal in nature and it is called as the Hofstadter's butterfly [61].

To examine the effect of magnetic field on the electrons, consider a charge particle moving in a magnetic field $\mathbf{B} = \nabla \times \mathbf{A}$. It acquires an Aharonov-Bohm phase Φ_{AB}

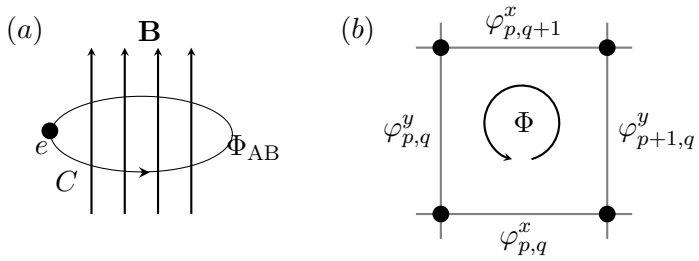

Figure 3.1: (a) Schematic diagram for an electron moving along a closed path C in presence of the magnetic field $\mathbf{B} = \nabla\times\mathbf{A}$. Electron acquire a geometric phase from the geometry of the system, and known as Aharonov-Bohm phase $\Phi_{\rm AB}$. (b) Equivalence of the geometric phase in the lattice system. Here complex tunneling amplitudes along x and y direction pick up a phase $\varphi^i_{p,q}, i = \{x, y\}$ through Peierls phases. Particle acquire a phase Φ when it tunnels across a lattice unit cell.

which depends on the closed path C traversed by the particle, which is schematically shown in Fig. 3.1(a). And, the phase can be calculated from the gauge potential as

$$\Phi_{\rm AB} = -\frac{e}{\hbar}\oint_C \mathbf{A}\cdot d\mathbf{l} = -2\pi\frac{\Phi}{\Phi_0}. \tag{3.1}$$

Here Φ is the magnetic flux enclosed by the closed path C, and $\Phi_0 = 2\pi\hbar/e$ is magnetic flux quanta. Similarly, a charge particle in a periodic lattice potential acquires a geometric phase Φ in presence of the gauge potential when it hops around a lattice unit cell as shown in Fig. 3.1(b)

$$\Phi = \varphi^x_{p,q} + \varphi^y_{p+1,q} - \varphi^x_{p,q+1} - \varphi^y_{p,q}. \tag{3.2}$$

Here $\varphi^i_{p,q} = -eA^i_{p,q}/\hbar$ is the Peierls phase with $i = \{x, y\}$ indicating the direction of hopping, and $A^i_{p,q}$ is the component of gauge potential along i^{th} direction. The Hubbard model [40] well describe the physics of the electrons in a periodic potential, and with magnetic field it is modified to the Harper-Hofstadter model [61, 190]. For the case of ultracold atoms in optical lattices, the presence of artificial gauge potential introduces Peierls phase and modifies the BHM Hamiltonian to

$$\hat{H} = -J\sum_{p,q}\left[\mathrm{e}^{i\varphi^x_{p,q}}\hat{b}^\dagger_{p+1,q}\hat{b}_{p,q} + \mathrm{e}^{i\varphi^y_{p,q}}\hat{b}^\dagger_{p,q-1}\hat{b}_{p,q} + \mathrm{H.c.}\right]. \tag{3.3}$$

This is the bosonic counterpart of the Harper-Hofstadter model. The magnetic flux per

unit cell is given by

$$\alpha = \frac{\Phi}{2\pi} = \frac{1}{2\pi}\left(\varphi^{x}_{p,q} + \varphi^{y}_{p+1,q} - \varphi^{x}_{p,q+1} - \varphi^{y}_{p,q}\right). \tag{3.4}$$

where α determines the strength of magnetic field and Φ is flux per unit cell or plaquette. Hereafter, I use plaquette instead of unit cell. In the zero field, the particles in the periodic lattice potential preserve the discrete translational symmetry, however, in presence of the magnetic field, this symmetry is broken. With the magnetic field, one has to consider the magnetic translation symmetry in which the plaquette is enlarged depending on the magnetic flux. This new plaquette is known as the magnetic unit cell, and it encloses 2π magnetic flux. So, the area of this unit cell is determined by the strength of the magnetic field. For example, in a 2D lattice $1\times4, 4\times1, 2\times2$ lattice sites are possible magnetic plaquettes for $\alpha = 1/4$. In this context, the Hofstadter's butterfly is the energy spectrum with respect to α.

As discussed in chapter 2, the BHM Hamiltonian well describes the physics of ultra-cold atoms in optical lattices. However, as atoms are charge-neutral, they are not affected by external electromagnetic fields. This can be remedied by using synthetic magnetic fields generated from artificial gauge potentials, which are created using laser fields. For bosonic atoms, this was first theoretically proposed by Jaksch and Zoller in 2003 [174] based on the method of laser-assisted tunneling. This was later refined by Mueller [191], Lim et al. [192], Gerbier and Dalibard [193], and Kolovsky [194]. Since then, there have been many other theoretical works. Most important development, however, is the experimental realizations of the artificial gauge potentials in 2D optical lattices by the Munich [53, 54] and MIT [55] groups. Inspired by these works, in this thesis, I consider a system of bosonic atoms at zero temperature in a 2D optical lattice with synthetic magnetic fields. For simplicity, I consider square lattice geometry.

In the presence of synthetic magnetic field, the atoms acquire a phase $2\pi\alpha$ upon hopping around a plaquette. Where, as defined earlier, α is the number of flux quanta per plaquette, and it has values $0 \leqslant \alpha \leqslant 1/2$. We shall also refer to α as the strength of synthetic magnetic field. Now, in the Landau gauge $\mathbf{A} = (A_x, 0, 0)$ with $A_x = 2\pi\alpha q$, such that synthetic magnetic field is along the $-z$ direction. The system is described

by the following BHM Hamiltonian [41, 47, 48, 63, 174],

$$\begin{aligned}\hat{H} &= -\sum_{p,q}\left[\left(J_x \mathrm{e}^{i2\pi\alpha q}\hat{b}^{\dagger}_{p+1,q}\hat{b}_{p,q} + \mathrm{H.c.}\right) + \left(J_y \hat{b}^{\dagger}_{p,q-1}\hat{b}_{p,q} + \mathrm{H.c.}\right)\right] \\ &\quad + \sum_{p,q}\left[\frac{U}{2}\hat{n}_{p,q}(\hat{n}_{p,q}-1) - \tilde{\mu}_{p,q}\hat{n}_{p,q}\right], \end{aligned} \tag{3.5}$$

where the NN hopping is modified through the Peierls phase [60, 61, 190]. Here, J_x (J_y) is the hopping strength along the x (y) direction. The above Hamiltonian, Eq. (3.5), is the bosonic version of the celebrated Harper-Hofstadter Hamiltonian.

In the experiments, the staggered flux in the optical lattice is created by periodic modulation of the lattice potential. As shown in Fig. 3.2, the experimental set up consists of a 2D lattice potential, created from two counter-propagating laser beams of wavelength λ. Along x direction another laser beam of wavelength 2λ is superimposed, which provides the energy offset of Δ between the neighbouring sites and forms a superlattice potential along x axis. In the superlattice potential, along the x direction the black circle denotes the low site energy and white circle denotes the sites with high energy. Along y direction the hopping is the same for all sites. Then another additional pair of running laser beams (red arrows) with wave vector $\mathbf{k}_1$, $\mathbf{k}_2$ and frequencies ω_{r1}, ω_{r2} are applied to periodically drive the system [195]. Here, $|\mathbf{k}_1| \approx |\mathbf{k}_2| \equiv k_R$, then, the phase is given by $\delta\mathbf{k}.\mathbf{R}$, where $\mathbf{R} = ma\mathbf{e}_x + na\mathbf{e}_y$ is the position vector. The phase at each lattice site is $\delta\mathbf{k}.\mathbf{R} = k_R a(m-n)$. Thus depending on the value of k_R and lattice geometry, any other phase difference can be created. Such a Peierls phase can generate the synthetic magnetic field of our interest, by including such a synthetic magnetic field in BHM we compute the phase diagram. In a homogeneous system, where the optical lattices do not include any background potential, the phase-boundary between MI and SF forms lobes of different fillings and in presence of magnetic field the MI-lobes are enhanced [196].

3.2.1 Magnetic Brollouin zone

In the condensed matter systems the lattice constant is small ($\approx$ Å) and the magnetic fields required to introduce unit magnetic flux per unit cell is very high (100 Tesla). However, that is what is required to observe some of the theoretically predicted QH

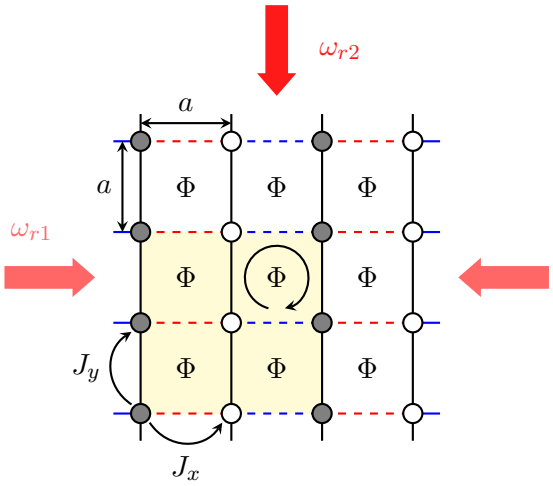

Figure 3.2: Implementation of synthetic magnetic fields in the optical lattices. Φ is the flux associated with each plaquette.

states. This limitation associated with the size of the lattice constant can be overcome in optical lattices, where the lattice constant is in multiples of 100 nm. And, as mentioned earlier, synthetic magnetic field equivalent to 100 Tesla or more can be introduced in these systems. The introduction of the magnetic field, or the synthetic magnetic field in the case of the optical lattices, modify the Brillouin zone. Without the magnetic field the BH Hamiltonian is invariant under the translation by multiples of the lattice constant. So, the corresponding translation operators are

$$\hat{T}_x = \sum_{p,q} \hat{b}^\dagger_{p+1,q} \hat{b}_{p,q}, \qquad \text{and} \qquad \hat{T}_y = \sum_{p,q} \hat{b}^\dagger_{p,q+1} \hat{b}_{p,q}. \tag{3.6}$$

The invariance under translation is manifested as these operators commute with the BH Hamiltonian $[\hat{T}_x, \hat{H}] = [\hat{T}_y, \hat{H}] = 0$ and in addition, they commute with each other $[\hat{T}_x, \hat{T}_y] = 0$ as well. Thus, one can apply the Bloch theorem to obtain the solution of this lattice system, and the Brillouin zone with lattice momenta $\mathbf{k}$ can be defined as

$$-\frac{\pi}{a} < k_x < \frac{\pi}{a}, \qquad -\frac{\pi}{a} < k_y < \frac{\pi}{a}, \tag{3.7}$$

where k_x, k_y are momenta along the x and y directions. The presence of the magnetic field or synthetic magnetic field breaks the transnational invariance of the Hamiltonian. And, the general form of the transformed translational operators are

$$\hat{T}_x = \sum_{p,q} \hat{b}^\dagger_{p+1,q} \hat{b}_{p,q} \mathrm{e}^{i\varphi^x_{p,q}}, \qquad \hat{T}_y = \sum_{p,q} \hat{b}^\dagger_{p,q+1} \hat{b}_{p,q} \mathrm{e}^{i\varphi^y_{p,q}}, \tag{3.8}$$

where, for the case of the BHM Hamiltonian with uniform synthetic magnetic field in Landau gauge, Eq. (3.5), $\varphi^x_{p,q} = 2\pi\alpha q$ and $\varphi^y_{p,q} = 0$. These operators do not commute with the BH Hamiltonian as well as with each other. The translational invariance can, however, be restored in terms of a new set of translational operators, magnetic translation operators (MTOs)

$$\hat{T}^M_x = \sum_{p,q} \hat{b}^\dagger_{p+1,q} \hat{b}_{p,q} \mathrm{e}^{i\theta^x_{p,q}}, \qquad \hat{T}^M_y = \sum_{p,q} \hat{b}^\dagger_{p,q+1} \hat{b}_{p,q} \mathrm{e}^{i\theta^y_{p,q}}, \tag{3.9}$$

where $\theta^x_{p,q}$ and $\theta^y_{p,q}$ are phases which are to be chosen such that these translation operators commute with the Hamiltonian. For the present case these phases are [197]

$$\theta^x_{p,q} = \varphi^x_{p,q} + q\Phi, \tag{3.10}$$

$$\theta^y_{p,q} = \varphi^y_{p,q} + p\Phi. \tag{3.11}$$

These translational operators redefine the size of the unit cell to magnetic unit cell.

The corresponding Brillouin zone is referred to as the magnetic Brillouin zone. If the magnetic cell is, in terms of the original lattice $m \times n$, then, the magnetic Brillouin zone can be defined as

$$-\frac{\pi}{ma} \leqslant k_x < \frac{\pi}{ma}, \qquad -\frac{\pi}{na} \leqslant k_y < \frac{\pi}{na}. \tag{3.12}$$

The schematic representation of a magnetic unit cell is shown in Fig. 3.2 by yellow shaded area for $\alpha = 1/4$. In the magnetic unit cell, the total flux enclosed is 2π. Here, as the magnetic cell is larger than the unit cell of the lattice, the magnetic Brillouin zone is smaller than the Brillouin zone.

As discussed earlier, the BH Hamiltonian is derived in the absence of the magnetic field and at zero temperature using the tight-binding approximation. In this approximation, all the particles are assumed to be in the lowest band. The BHM Hamiltonian so obtained is translationally invariant and the Bloch theorem is applicable. However, the introduction of the external magnetic field breaks the translational symmetry of the lattice. More importantly, the Bloch theorem is not applicable with the choice of a non-periodic gauge like Landau gauge for the vector potential $\mathbf{A}$. This implies that, although, we obtain the correct bosonic version of Harper-Hofstadter Hamiltonian using the Peierls substitution, the gauge needs to be chosen appropriately. Otherwise, the

vector potential is not periodic and the tight-binding approximation is not applicable. This can be resolved using singular gauge transformation [198], using which the vector potential $\mathbf{A}$ is transformed to a periodic form $\mathbf{A}_p$ in terms of magnetic flux lines, in cylindrical coordinates, as

$$\mathbf{A}_p = \mathbf{A} - \frac{\Phi_0}{2\pi\rho}\mathbf{e}_\phi, \tag{3.13}$$

where $\rho = \sqrt{x^2 + y^2}$ and Φ_0, as defined earlier, is the Dirac flux quanta. The magnetic field $\boldsymbol{\nabla} \times \mathbf{A}_p$, then, assumes the form

$$\mathbf{B} = B_0\mathbf{e}_z - \Phi_0 \sum_{mn} \delta_2(\mathbf{R} - \mathbf{R}_{mn}), \tag{3.14}$$

where, $\mathbf{R}_{mn} = ma\mathbf{e}_x + na\mathbf{e}_y$ is the position vector of the lattice points. Then, the Bloch theorem is valid for rational magnetic field strengths $\alpha = k/l$ $(k, l \in \mathbb{Z})$ and the validity of the tight binding approximation is restored. If the magnetic unit cell is of dimension $m \times n$ then the translational operators follow the relation

$$e^{-imn\Phi}(\hat{T}_x^M)^m(\hat{T}_y^M)^n = (\hat{T}_y^M)^n(\hat{T}_x^M)^m.$$

The translational operator commute if $\Phi = 2\pi k/l$ is such that mn/l is an integer. Now, with the operators $(\hat{T}_x^M)^m = \hat{M}_x^m$ and $(\hat{T}_y^M)^n = \hat{M}_y^n$ and the Hamiltonian in the presence of magnetic field as given in Eq.(3.3), we can find eigenstates $\Psi_{p,q}$ with generalized Bloch theorem as

$$\hat{M}_x^m \Psi p, q = e^{ik_x ma}\Psi p, q, \tag{3.15}$$

$$\hat{M}_y^n \Psi p, q = e^{ik_y na}\Psi p, q. \tag{3.16}$$

Based on these considerations, all results reported in this thesis are based on the computations with the system size as integral multiples of the magnetic unit cell.

3.2.2 Properties of quantum Hall states

The QH states are strongly correlated and hence, we do not get these states with the SGMF method. So, to obtain QH states we compute the ground state of the Hamiltonian in Eq. (3.5) using the CGMF method. To distinguish the ground state as either QH or SF state, we resort to an important property of the QH state: it is incompressible.

So, we compute the compressibility of the ground state as

$$\kappa = \frac{\partial \rho}{\partial \mu}. \tag{3.17}$$

Here, ρ is the density for the ground state and μ is chemical potential. The ground state is QH state if κ is zero. Thus, the presence of QH states for different filling factor ν is indicated by plateaus in the plot of density ρ as a function of μ. For the compressible SF state κ is non zero, and density ρ is linear as a function of μ.

The other important property relevant to the experimental realizations is the two-point correlation function $\langle \hat{b}_i^\dagger \hat{b}_j \rangle$. The trend in $\langle \hat{b}_i^\dagger \hat{b}_j \rangle$ is a good indicator of the presence or absence of the energy gap in the system. For a gapped system, the two-point correlation function decays exponentially [199]. Thus, in the bulk of the FQH states, which is gapped, the two-point correlation is expected to show exponential decay. On the other hand for the gapless edge of the FQH states it was shown by Wen [200] that the two-point correlation decays as power law. So, the exponential and power law decay of $\langle \hat{b}_i^\dagger \hat{b}_j \rangle$ in the bulk and edge of a state can be considered as an indication of it being a FQH state. Here, an important general conceptual point is, answering the question of whether a system is gapped or gapless is a challenging one. To put it more precisely, given a Hamiltonian, it is difficult to predict whether its spectrum is gapped or gapless [201]. This is the spectral gap problem. Where the spectral gap is the energy difference between the two lowest eigen energies of a system. It was shown by Cubitt et al. [201] that there exists no universal computational algorithm which can solve the spectral gap problem. The spectral gap problem is linked to the host of other important problems in very different branches of physics like the explanation for quark confinement in high-energy physics. To compute the two-point correlation function, we first compute the one-body density matrix (OBDM) [202, 203] and in CGMF method

$$\rho_{k,l} = \langle \Psi^c_{\mathrm{GW}} | \, \hat{b}_l^\dagger \hat{b}_k \, | \psi^c_{\mathrm{GW}} \rangle \tag{3.18}$$

where $k \equiv (p, q)$ and $l \equiv (p', q')$ are the lattice indices. This can further be written in terms of cluster states as

$$\rho_{k,l} = \prod_{jj'} {}_j \langle \psi_c | \hat{b}_l^\dagger \hat{b}_k \, | \psi_c \rangle_{j'} \,, \tag{3.19}$$

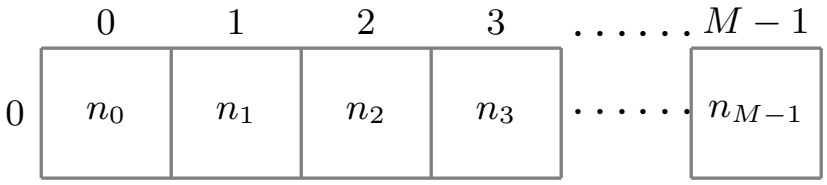

Figure 3.3: The $M \times 1$ row of a cluster with occupation number n_0, n_1, ..., n_{M-1}. Each square box represents a lattice site and each of n_i corresponds to ith lattice site in that row. Here, n_i runs from 0 to $N_b - 1$ for each lattice site.

that is, the OBDM of the entire lattice can be defined in terms of those corresponding to the cluster states. As we shall see later, in the case of ED, the expression of OBDM is equivalent to that of a single cluster. And, we use this extensively. From the above definition, the two-point correlation function along a row of lattice sites can be defined as $\langle \hat{b}^\dagger_{x,y} \hat{b}_{0,y} \rangle$, where along x axis we have fixed one lattice point as zero. For $y = 0$ and $x = 1$ the two-point correlation function for one of $M \times N$ clusters is

$$\begin{aligned} \langle \hat{b}^\dagger_{1,0} \hat{b}_{0,0} \rangle &= \sum_{m_0,..,m_{m'}} \sum_{n_0,..,n_{m'}} C^*_{m_0,..,m_{m'}} C_{n_0,..,n_{m'}} \langle m_0, .., m_{m'} | \, \hat{b}^\dagger_{1,0} \hat{b}_{0,0} \, | n_0, .., n_{m'} \rangle \,, \\ &= \sum_{m_0,..,m_{m'}} C^*_{m_0,..,m_{m'}} C_{m_0+1,m_1-1,..,m_{m'}} \sqrt{m_1(m_0+1)}. \end{aligned}$$

Here, $m' = (M \times N) - 1$, and based on the above expression, fixing $y = 0$ the general expression for any x is we get

$$\langle \hat{b}^\dagger_{x,0} \hat{b}_{0,0} \rangle = \sum_{m_0,..,m_{m'}} C^*_{m_0,..,m_{m'}} C_{m_0+1,m_1,m_2-1,..,m_{m'}} \sqrt{m_x(m_0+1)} \tag{3.20}$$

These two point correlation functions, as I have fixed $y = 0$, are for the edge of the QH state. Similarly, we can compute the two-point correlation in the bulk of the QH states by choosing $y = (N-1)/2$. In general, for QH states, two point correlation function has power law behaviour at the edge. In the bulk, it is non-monotonic, initially it decays exponentially and then increases.

3.3 Exact Diagonalization Method

The CGMF method incorporates correlation effects better than the SGMF method, but it still uses the mean-field ϕ to account for the hopping terms at the boundaries between

two clusters. The use of the mean-field can, however, be avoided entirely with the ED method. For a $M \times N$ lattice the BHM Hamiltonian to be used in the ED method is

$$\begin{aligned} \hat{H} &= -\sum_{\substack{0\leqslant p<M \\ 0\leqslant q<N}} \left[\left(J_x \mathrm{e}^{i2\pi\alpha q} \hat{b}^\dagger_{p+1,q} \hat{b}_{p,q} + J_y \hat{b}^\dagger_{p,q+1} \hat{b}_{p,q} \right) + \mathrm{H.c.} \right] \\ &\quad + \sum_{\substack{0\leqslant p<M \\ 0\leqslant q<N}} \frac{U}{2} \hat{n}_{p,q}(\hat{n}_{p,q} - 1). \end{aligned} \tag{3.21}$$

The key difference of the above BHM Hamiltonian from those in the SGMF and CGMF methods is the absence of the term with the chemical potential. In the ED method, we fix the number of atoms in the system, and hence, the Hamiltonian is diagonalized using many-particle states in a Hilbert space. So, the computation is in the micro-canonical ensemble and the chemical potential is not required. Except for the fixed number of particles, the generation or identification of states is similar to the case of a single cluster in CGMF. So, we can consider that the Hilbert space is spanned by the states $|\psi_c\rangle$ of one $M \times N$ cluster. As we had noted earlier, in the context of CGMF, the number of cluster states increases exponentially with the size. So, to enable computations with the ED method for larger lattice sizes, we define the cluster states or the basis states of the Hilbert space based on a hierarchy of many-body states. The most basic many-body state in this scheme is the occupation number states $|n_i\rangle$ of the ith lattice site. Then, in the next step using these single-site basis we define a *row state* consisting of M lattice sites as

$$|\phi\rangle_m = \prod_{i=0}^{M-1} |n_i\rangle \,, \tag{3.22}$$

where, $0 \leqslant i \leqslant M-1$ are lattice sites along x direction, and $m \equiv \{n_0, n_1, \ldots, n_{M-1}\}$ is an index quantum number which identifies each of the row states uniquely. The schematic representation of a row state is shown in Fig. 3.3. A basis state of the $M \times N$ lattice or cluster state is a direct product of N row states and can be written as

$$|\Phi_c\rangle_\ell = \prod_{j=0}^{N-1} |\phi^j\rangle_{m^j} = \prod_{j=0}^{N-1} \prod_{i=0}^{M-1} |n_i^j\rangle \,, \tag{3.23}$$

here, $0 \leqslant j \leqslant N-1$ identifies the row states and a schematic representation is shown in Fig. 3.4. In the above definition we have introduced the index quantum number ℓ to

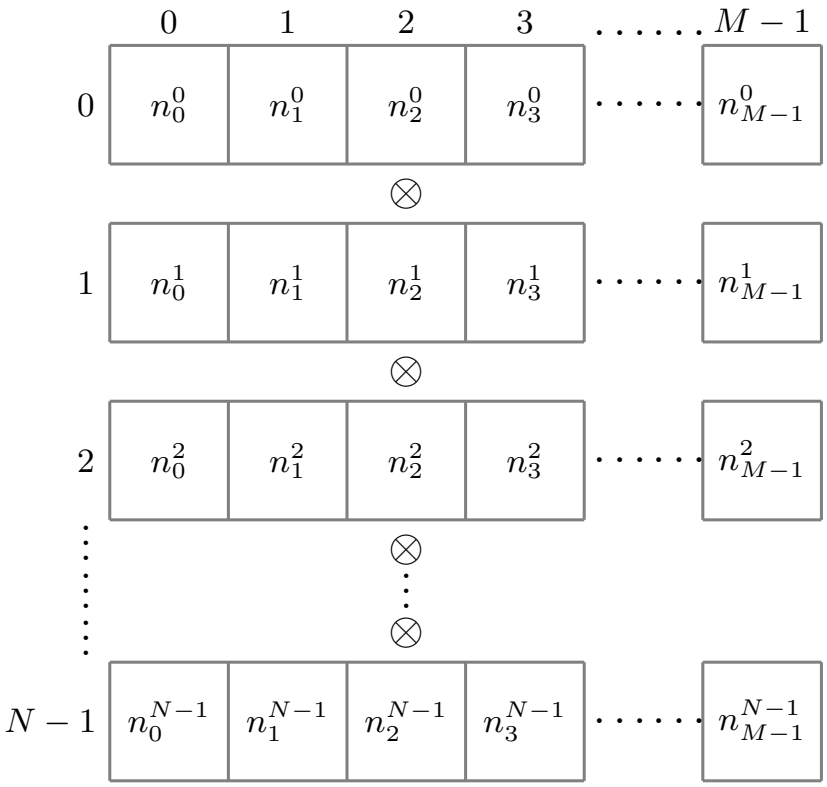

Figure 3.4: The $M \times N$ cluster with occupation number n_0^j, n_1^j,. . .,n_{M-1}^j for jth row of the cluster. Each square box represents a lattice site and each of n_i^j corresponds to each jth row of cluster and ith lattice site in that row. Here, n_i^j runs from 0 to $N_b - 1$ for each lattice site.

identify each of the basis states uniquely, that is

$$\ell \equiv \{n_0^0, n_1^0, \ldots, n_{M-1}^0, n_0^1, n_1^1, \ldots, n_{M-1}^1, \ldots, n_0^{N-1}, n_1^{N-1}, .., n_{M-1}^{N-1}\}. \tag{3.24}$$

From the definition of the index quantum number of row states, this is also equivalent to writing as

$$\ell \equiv \{m^0, m^1, .., m^{N-1}\}. \tag{3.25}$$

To reiterate, as shown in Fig. 3.4 there is a hierarchy of states, the single-site occupation number states $|n_i^j\rangle$, the row states $|\phi\rangle_m$ and cluster states $|\Phi_c\rangle_\ell$.

3.3.1 Hilbert space and Hamiltonian matrix

To construct the Hilbert space within which the Hamiltonian is diagonalized, consider the total number of atoms to be N_a. This number can be arbitrary, but to give a concrete

example and relevant to the present work, I consider low density $N_a \ll M \times N$. Here, the QH states are obtained for parameters which lie in the domain between the $n = 0$ and $n = 1$ Mott lobes. We can, therefore, consider the occupation number states $|0\rangle$ and $|1\rangle$ for the computations and the average occupancy lies between 0 and 1. Then, the total number of atoms in the row states $|\phi\rangle_m$ is $0 \leqslant \sum_i n_i^j \leqslant \min(M, N_a)$. As the cluster states $|\Phi_c\rangle_\ell$ are direct product of $|\phi\rangle_m$, the total number of atoms in a basis $|\Phi_c\rangle_\ell$ must satisfy the condition

$$\sum_{i=0}^{M-1} \sum_{j=0}^{N-1} n_i^j = N_a. \tag{3.26}$$

For illustration, consider $N_a = 4$ and the size of the lattice as 4×4. Then, the number of atoms in $|\phi\rangle_m$ can range from 0 to 4, and considering that occupation number states at each lattice sites are either $|0\rangle$ or $|1\rangle$, the possible row states are

$$|0,0,0,0\rangle\,,\ |0,0,0,1\rangle\,,\ \ldots,\ |1,1,1,1\rangle\,.$$

In total there are sixteen $|\phi\rangle_m$ and an example of $|\Phi_c\rangle_\ell$ defined as direct product of four $|\phi\rangle_m$s is

$$|\Phi_c\rangle_\ell = |0,0,0,0\rangle \otimes |0,1,1,0\rangle \otimes |0,0,0,1\rangle \otimes |1,0,0,0\rangle\,.$$

Thus, the number of $|\Phi_c\rangle_\ell$ is

$${}^{MN}C_{N_a} = {}^{16}C_4 = 1820,$$

which is much less than the number of states $2^{16} = 65536$ required for computation with 4×4 cluster in CGMF. The essence of the ED method is then to compute the Hamiltonian matrix elements between the cluster states as

$${}_{\ell'}\langle\Phi_c'|\,\hat{H}\,|\Phi_c\rangle_\ell = \prod_{k=0}^{M-1}\prod_{l=0}^{N-1}\prod_{i=0}^{M-1}\prod_{j=0}^{N-1} \langle n_k^l|\,\hat{H}\,|n_i^j\rangle\,, \tag{3.27}$$

and then, diagonalize the Hamiltonian matrix to obtain the eigenvalues and eigenvectors. Considering that the sequence of $|\Phi_c\rangle_\ell$ is not based on symmetries, but rather based on the combinatorics of $|\phi\rangle_m$, the row wise computation of Hamiltonian matrix is more efficient. In this regard, for example, the matrix element of hopping term along x-axis $J_x \mathrm{e}^{i2\pi\alpha q}\hat{b}^\dagger_{p+1,q}\hat{b}_{p,q}$ can proceed in a sequence of steps. And one of the efficient approach is to compare the row states and identify if the ${}_{\ell'}\langle\Phi_c'|$ and $|\Phi_c\rangle_\ell$ have right

combinations of occupation number states to have non-zero matrix element. This can be done in the following steps:

1. Compare the row states ${}_{m'}\langle\phi|$ and $|\phi\rangle_m$ of ${}_{\ell'}\langle\Phi'_c|$ and $|\Phi_c\rangle_\ell$, respectively. Proceed to the next step if ${}_{\ell'}\langle\Phi_c|$ and $|\Phi_c\rangle_\ell$ only differ in one of the row states, say the 1st row.

2. Consider ${}_{m'^1}\langle\phi^1|$ and $|\phi^1\rangle_{m^1}$, and compare the single site occupation number states. Proceed to the next step if the difference in these two row states arise from the difference in the occupation number states of two neighbouring lattice sites, say 3rd and 4th lattice sites.

3. The matrix element is nonzero and value is $\sqrt{n'_2(n'_3+1)}$ if $n'_2 = n_2 + 1$ and $n'_3 = n_3 - 1$. For the example considered, we have nonzero matrix element for the term $p = 2$ and $q = 1$.

In a similar way, for the example considered, the matrix element of the Hermitian conjugate term $J_x^* \mathrm{e}^{-i2\pi\alpha q}\hat{b}^\dagger_{p,q}\hat{b}_{p+1,q}$ is nonzero when the first two conditions are met and the last is modified to $n'_2 = n_2 - 1$ and $n'_3 = n_3 + 1$. With slight modifications, the same approach can be applied to compute the matrix elements of the hopping term along y-axis. For this case, two neighbouring row states should be different, and at the level of the lattice sites, the difference should be on the same column. Then, to have a nonzero matrix element the occupation numbers should satisfy conditions equivalent to the condition in the third in the above chain of steps. The computation of the on-site interaction Hamiltonian matrix elements is trivial as it is diagonal and does not require a comparison of the basis states. After diagonalizing the Hamiltonian, we can get the ground state as

$$|\Psi_c\rangle = \sum_\ell C_\ell \, |\Phi_c\rangle_\ell \,, \tag{3.28}$$

where, C_ℓ is the coefficient of the cluster state and the normalization condition of the state is $\sum_\ell |C_\ell|^2 = 1$. The normalization, however, is guaranteed as the Hamiltonian is Hermitian.

3.3.2 Calculation of properties

Using the ED method with the basis set defined as a hierarchy of states, we could diagonalize lattice sizes up to 4×12. As the computations with the ED method are in the micro canonical ensemble, the SF order parameter $\phi_{p,q}$ at a lattice site can not be calculated as $\langle \hat{b}_{p,q} \rangle$. So, the SF order parameter can not be used as a property to distinguish SF ground state. The suitable method to differentiate the QH states and SF states is based on the Penrose-Onsager criterion [177] and von Neumann entropy. For this, we construct the OBDM, Eq. (3.18), as

$$\rho = \begin{pmatrix} \langle \hat{b}^\dagger_{0,0} \hat{b}_{0,0} \rangle & \langle \hat{b}^\dagger_{1,0} \hat{b}_{0,0} \rangle & \dots & \langle \hat{b}^\dagger_{0,1} \hat{b}_{0,0} \rangle & \dots & \langle \hat{b}^\dagger_{M',N'} \hat{b}_{0,0} \rangle \\ \langle \hat{b}^\dagger_{0,0} \hat{b}_{1,0} \rangle & \langle \hat{b}^\dagger_{1,0} \hat{b}_{1,0} \rangle & \dots & \langle \hat{b}^\dagger_{0,1} \hat{b}_{1,0} \rangle & \dots & \langle \hat{b}^\dagger_{M',N'} \hat{b}_{1,0} \rangle \\ \vdots & \vdots & \vdots & \vdots & \ddots & \vdots \\ \langle \hat{b}^\dagger_{0,0} \hat{b}_{M',N'} \rangle & \langle \hat{b}^\dagger_{1,0} \hat{b}_{M',N'} \rangle & \dots & \langle \hat{b}^\dagger_{0,1} \hat{b}_{M',N} \rangle & \dots & \langle \hat{b}^\dagger_{M',N'} \hat{b}_{M',N'} \rangle \end{pmatrix},$$

with $M' = M - 1$ and $N' = N - 1$. In OBDM the diagonal elements are the number operators at that lattice site, and off diagonal matrix elements are similar to the matrix elements of the hopping term. The computation of the OBDM involves all the basis states and we can follow a scheme similar to that of the Hamiltonian matrix elements as outlined in the previous Section. The dimension of the OBDM matrix is $M \times N$ and we obtain the eigenstates and eigenvalues by diagonalizing it. If $\lambda_m^{\mathrm{OBDM}}$ is the largest eigenvalue of the OBDM and it is of the order of N_a, following the Penrose-Onsagar criterion, the condensate fraction in the system is

$$\rho_{\mathrm{cf}} = n_m^{\mathrm{OBDM}} / N_a.$$

Here, N_a as defined earlier is the total number of atoms in the system. The ground state is a QH state if the largest eigenvalue of the OBDM is much less than N_a. From the scaled eigenvalues p_i we can compute the von Neumann entropy as

$$S = -\sum_i^{M \times N} p_i \ln(p_i), .$$

In general, the von Neumann entropy is higher for a strongly correlated state like the QH states than the SF states.

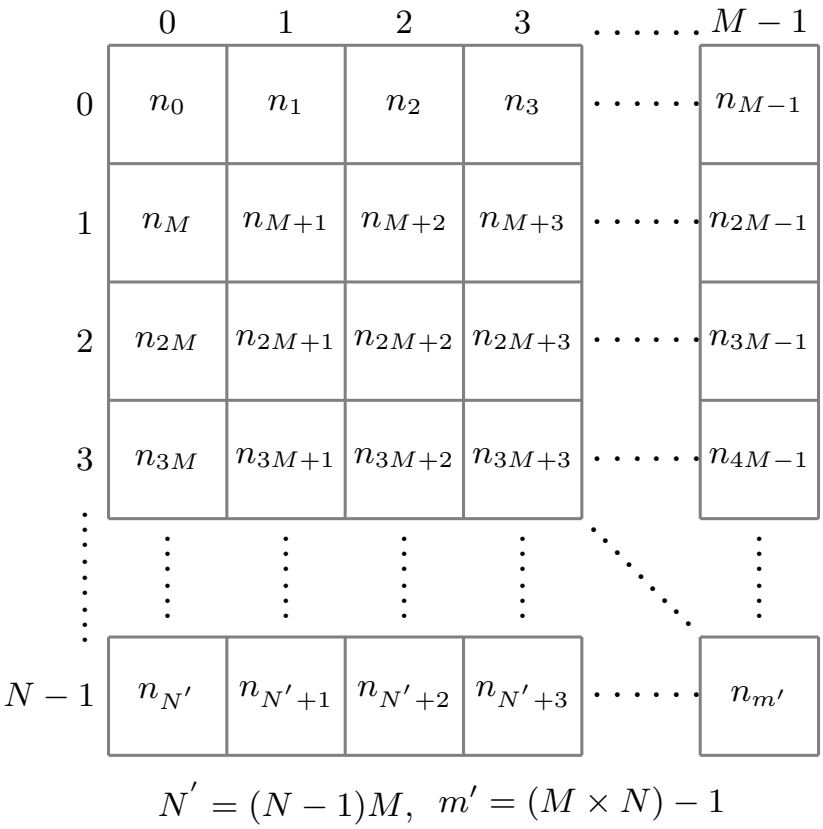

Figure 3.5: The $M \times N$ cluster with occupation number $n_0, n_1, .., n_{m'}$ at each lattice site for CGMF. Each square box represents a lattice site and each of n_i corresponds to each i lattice site. Here, n_i runs from 0 to $N_b - 1$ for each lattice site.

3.3.3 Comparison of ED and CGMF

The general features of the hierarchical definition of states and the approach to compute the Hamiltonian matrix elements can also be adapted to the CGMF theory as well. As discussed earlier, in the CGMF theory, hopping is exact within the cluster but hopping at the boundary is considered via the mean-field ϕ. Thus, for clusters of size $M \times N$, the cluster state defined in Eq. (2.21) is the direct product of the occupation number states at each lattice site and can be written as

$$|\Phi_c\rangle_\ell = \prod_{i=0}^{m'} |n_i\rangle \,, \tag{3.29}$$

where $m' = (M \times N) - 1$ and $i = 0, 1, \ldots, m'$ are the lattice site index, with M (N) as number of lattice sites along x (y) direction, $\ell \equiv \{n_0, n_1, \ldots, n_{m'}\}$ as defined earlier is the index quantum number to identify each of the cluster states uniquely. For

illustration, the correspondence between quantum numbers and lattice sites is shown in Fig. 3.5. The ground state of the CGMF Hamiltonian in Eq. (2.16) is obtained by using the cluster wave-function in Eq. (3.29). The Hamiltonian matrix element can be written as

$$\begin{aligned} {}_{\ell'}\langle \Phi_c | \hat{H} | \Phi_c \rangle_{\ell} &= \prod_{j=0}^{m'} \prod_{i=0}^{m'} \langle n'_j | \hat{H} | n_i \rangle \\ &= \langle n'_0, n'_1, \ldots, n'_{m'} | \hat{H} | n_0, n_1, \ldots, n_{m'} \rangle . \end{aligned} \tag{3.30}$$

The definition of the states and computation of the matrix elements can, however, be cast in terms of the row and cluster states as in ED. With this modification, we can implement constraints on the number of atoms in the row and cluster states, thereby reducing the dimension of the Hamiltonian matrix in the CGMF. The only difference from ED is, in CGMF the inter-cluster hopping terms are linear in order parameter ϕ and hence, connect states in Hilbert spaces with the different total number of atoms. In other words, the Hamiltonian matrix in CGMF is defined with respect to Fock space. Another difference is, the diagonal terms have a contribution from μ. With this adaptation, we can consider larger clusters in the CGMF.

3.3.4 Limitations of ED

The ED method provides the exact solution of the BH Hamiltonian. The limitation of this method is that it restricts the computation for large system size, due to the exponential increase in the dimension of Hamiltonian matrix. We perform our computation at the most for 4×12 lattice which has the matrix dimension of 12271512 for synthetic magnetic field $\alpha = 1/4$ and $\nu = 1/2$. Thus, we can not perform the computation for lattice size higher than this. Another limitation of ED is to incorporate the envelope potential. In the CGMF, the incorporation of the envelope potential is simple for large system size, like 40×40 in our case, while with ED we can not go for such a large lattice system.

3.4 Summary of the chapter

In this chapter, I provide a brief description of different QH states which can occur either as ground or excited state in the BHM model with the introduction of synthetic magnetic fields. The model is the bosonic version of the celebrated Harper-Hofstadter model in fermionic systems. I, then, discuss the properties of QH states and, in particular, I focus on the two-point correlation function. After that, I discuss the ED method in great detail. In the context of ED, the use of Penrose-Onsager criterion to compute the condensate fraction is discussed. We also compare the CGMF and ED method, and limitations of the ED method in this chapter.

Chapter 4

Quantum Hall states from CGMF and ED methods

We have studied QH states in the homogeneous BHM with the synthetic magnetic field and inhomogeneous case with confining potentials such as box and harmonic potentials. In this chapter, I discuss the QH states which we obtain with different flux values of $\alpha = 1/5$, $1/4$, $1/3$, and $1/2$, and by varying the cluster sizes in the CGMF theory. Here, as mentioned earlier, it is to be emphasized that we do not get QH states with SGMF theory as it does not encapsulate the correlation effects accurately. The QH states obtained from the CGMF method are identified based on the compressibility $\kappa = \partial\rho/\partial\mu$. For the QH states $\kappa = 0$ or incompressible, and it is finite for the SF states. As a result, $\rho(\mu)$ of QH states has plateaus at different ν and it is linear for the SF phase Fig. 4.1. In our study, similar to the experimental realizations we consider isotropic hopping, $J_x = J_y = J$, and repulsive on-site interaction, $U > 0$. In the case of an inhomogeneous system, the QH states are sensitive to the confining envelope potential. We do observe QH states with the box potential for all the cases but that is not the case for the harmonic potential. However, shallow the harmonic potential is we do not get QH state. Using the ED method we also observe the QH states for different flux values and filling factors. In the case of the ED method, we differentiate the QH and SF states based on the Penrose-Onsager criterion and von Neumann entropy. With the ED method, the largest lattice size we consider is 4×12. Although the computational scheme used in the ED method is applicable to CGMF, considering clusters of size

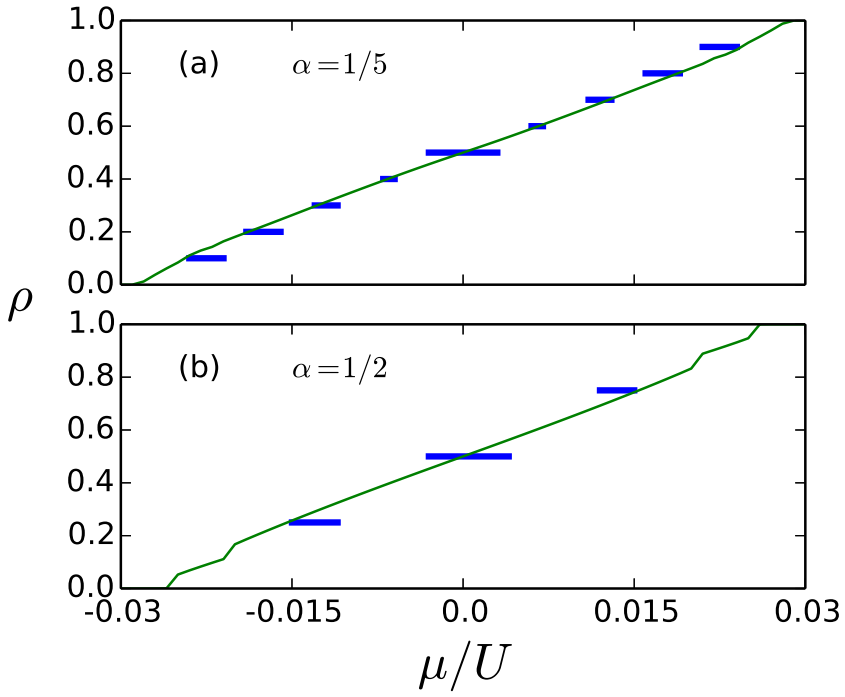

Figure 4.1: The variation in the number density ρ in the presence of synthetic magnetic field with $\alpha = 1/5$ in Fig. (a) and for $\alpha = 1/2$ in Fig. (b). The states in SF phase are compressible and have non-zero SF order parameter ϕ. As a result, ρ varies linearly with μ and the green curve represents the SF solutions. For specific values of filling factor ν there are states with constant ρ, represented by the blue lines, and these correspond to the existence of QH states. In Fig. (a), the plateaus or the constant ρ values correspond to $\nu = n/2$, $n = 1, 2, \ldots, 9$. In Fig. (b), the plateaus correspond to $\nu = 1/2$, 1, and $3/2$

.

4×12 is computationally not feasible with the CGMF computation due to the large matrix dimension. To relate with experimental observations we also compute the two-point correlation functions which can serve to distinguish the QH and SF states.

4.1 QH states in the Homogeneous system

The QH states are one of the possible ground state candidates of the BHM Hamiltonian in Eq. (3.5) in presence of the synthetic magnetic field. The other is the SF state, and for the parameter range of our interest, these two are the competing states for the ground

state. To obtain the ground state, I use CGMF and ED methods. We construct the BHM Hamiltonian matrix as described in chapter 2, and diagonalize it and the lowest energy eigenstate is the ground state of the system. As reported in previous works [65], the QH states are present in the strongly interacting regime and in the vicinity of the Mott lobe. We also consider our studies in this domain and fix the hopping strength as $J_x = J_y = 0.01U$ for all of our studies. Further more, our studies are near in parameter domain close to the $n = 0$ and $n = 1$ Mott lobes. So the occupancy at each lattice site is either 0 or 1. Accordingly, we consider $|0\rangle$ and $|1\rangle$ as the occupation number basis states at each lattice site. In the case of computations with the CGMF method, we vary the chemical potential from $-0.03U$ to $0.03U$ and compute the compressibility κ.

The CGMF computations are done with clusters which are integer multiple of the magnetic unit cell. As we consider uniform flux of Φ for $\alpha = 1/N$, a $1 \times N$ cluster forms a magnetic unit cell. We, however, find that except for a $\pi/2$ rotation the results are identical to $N\times1$ cluster. This is due to the coupling of atomic motions along x and y directions through the interparticle interaction. We find that the QH states are very sensitive to the initial condition and to improve convergence, we use a successive over-relaxation method with a very low value of ϕ as initial guess. For the SF states, the use of the relaxation method is not required. To mimic the infinite system or thermodynamic limit, we employ periodic boundary condition along x and along y direction. The QH states of different values of α are discussed in the next few subsections.

4.1.1 Synthetic magnetic field $\alpha = 1/5$

For the low flux $\alpha = 1/5$, we consider a single cluster of size 2×5, such that it is integer multiple of the magnetic unit cell 1×5 lattice unit cell. We consider the system size as 20×20 lattice sites, which encloses 10×4 clusters. In each iteration, we diagonalize the Hamiltonian matrix for each of the clusters in a sequence and obtain the ground state (in terms of $C_{n_0,n_1,\ldots,n_9}$) for each of the clusters. For each of the clusters, we also compute the SF order parameter ϕ at each lattice site of the cluster. As mentioned earlier, the coupling between two neighbouring clusters is incorporated through ϕ. We repeat the computations for μ in steps of $\Delta\mu = 0.001U$ for $\mu \in [-0.03U, 0.03U]$ and compute κ. This is done for both QH and SF states, and the plot of ρ as a function

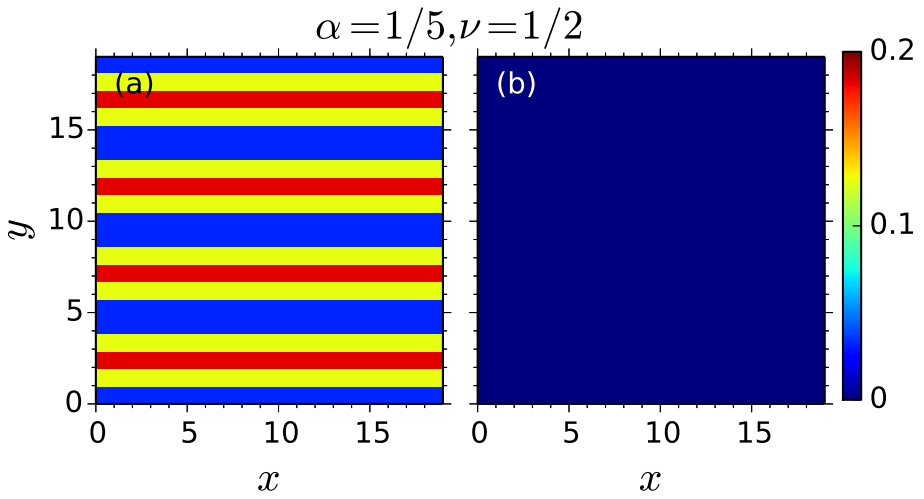

Figure 4.2: (a) Hall state with stripe phase for $\alpha = 1/5, \nu = 1/2$ with average number $\rho = 0.1$. (b) Zero SF order parameter ϕ for the same.

of μ is shown in Fig. 4.1(a). In the figures the horizontal lines (blue) corresponding to constant ρ indicate the presence of QH states, and linear (green) line corresponds to the SF states. The QH states are obtained at the fillings $\nu = n/2$, $n = 1, 2, \ldots, 9$, and corresponding density for these states are $\rho = n/10$, $n = 1, 2, \ldots, 9$. For low density ($\rho < 1$) our CGMF results with 2×5 cluster for $\nu = 1/2$ are consistent with the results reported in Natu et al. [67]. The plots of ρ and ϕ for this FQH state are shown in Fig. 4.2 (a), and (b), respectively. The FQH state has a stripe pattern in ρ and as to be expected ϕ is zero. Similarly, we observe that the FQH states with $\nu = 3/2$, $7/2$, and $9/2$ are also striped, whereas it is homogeneous for $\nu = 5/2$. In addition, we obtain striped integer QH (IQH) states for $\nu = 1, 2, 3$ and 4. As an example one of the IQH states for $\nu = 2$ is shown in Fig. 4.3 (a). As described earlier, we also obtain the competing SF states for the same value of μ and J corresponding to the QH state. For the present case of $\alpha = 1/5$ the SF state is always the ground state and QH state is a metastable state. The energy difference between these two competing states is $\approx 10^{-3}U$. The SF states have zigzag pattern in ρ and ϕ. The competing SF state corresponding to $\nu = 2$ IQH state is shown in Fig. 4.3 (b).

To examine the stability of the patterns, we analyze our results with increasing cluster sizes. As the CGMF approach breaks the translation symmetry of the lattice, we observe the effect of different cluster sizes on the QH states. Here, to maintain the

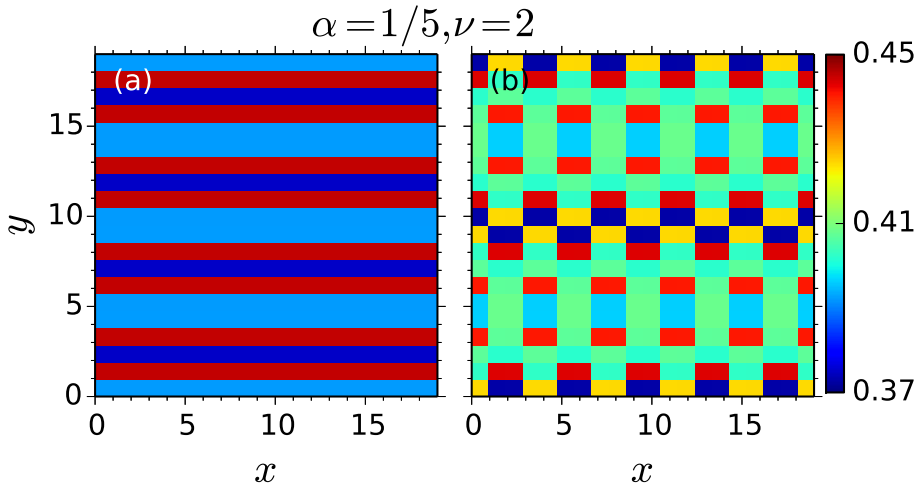

Figure 4.3: (a) Hall state with stripe phase for $\alpha = 1/5, \nu = 2$ with average number $\rho = 0.4$. (b) The superfluid state with density wave order which is similar to supersolid. For the Hall states SF order parameter ϕ is zero, while there are large fluctuation in the ϕ for the superfluid state (not shown here).

magnetic translation of the system along the y axis, we consider clusters consisting of 5 lattice sites along y direction. But, along x axis, we vary the number of lattice sites in the cluster. To show the dependence of the ρ on the cluster size, we show one of the IQH states for $\nu = 1$ with different cluster sizes in Fig. 4.4. On increasing the cluster size to 3×5 the IQH states with stripe geometry are transformed to checkerboard pattern as shown in Fig. 4.4 (a). Further, IQH state has reduced density variations with 4×5 cluster in Fig. 4.4 (b).

It is to be noted that we obtain the same IQH states but rotated by $\pi/2$, when the cluster sizes are 5×2, 5×3 and 5×4. For example with 5×2 cluster the stripe pattern is horizontal while it is vertical for 2×5 cluster. Considering this property of QH states, and noting that 1×5 is the magnetic unit cell, an accurate description of the FQH state is possible with 5×5 cluster. With this cluster size the operator part of the hopping term in the BHM Hamiltonian is exact along x and y axis within the cluster symmetrically. For example, with 2×5 cluster, hopping along x axis has contribution through mean-field after $2a$ while it is $5a$ for 5×5 cluster, where a is lattice constant. The IQH state with 5×5 cluster is shown in Fig. 4.4 (c). The density pattern is still checkerboard with higher density variation. Another important observation with different cluster sizes is

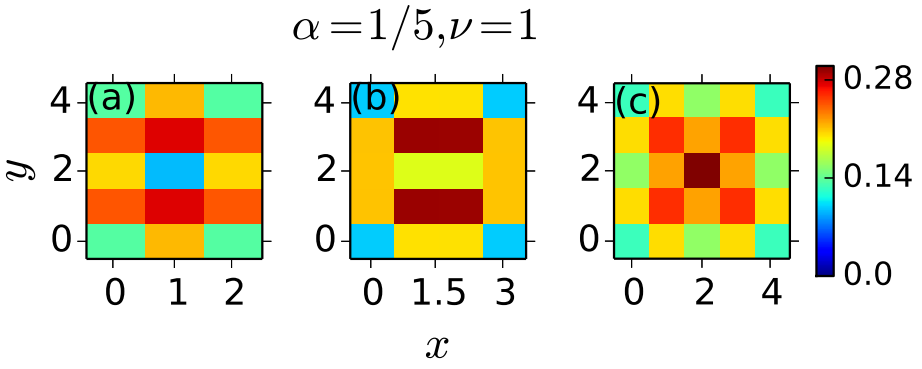

Figure 4.4: The variations in ρ for IQH state of $\alpha = 1/5$ and $\nu = 1$ for a single cluster of different sizes. (a) The result from 3×5 cluster has checkerboard pattern. (b) 4×5 cluster has less variations in ρ compared to 3×5. (c) 5×5 cluster shows a rich variation in ρ and unlike in (a) and (b) the central lattice site has maxima in density.

that central lattice site has a lower density with 3×5 cluster and it has a maximum density with 5×5 cluster. For this case, we consider a single cluster, in the context of inhomogeneous system, and results are discussed in the later part of the thesis. We also obtain the IQH state for 5×5 lattice through ED calculations.

4.1.2 Synthetic magnetic field $\alpha = 1/4$

For the case of $\alpha = 1/4$, we obtain QH states for $\nu = n/2$, where $n = 1, 2, \ldots, 7$, with 2×4 and 4×4 clusters. The FQH states for $\nu = 1/2, 3/2, 5/2$ are striped with 2×4 cluster, however, like in the case of $\alpha = 1/5$ is transformed into checkerboard with 4×4 cluster. That is, the pattern depends on the cluster size. Furthermore, as we increase the cluster size to 4×8, the FQH state with $\nu = 1/2$ filling remain qualitatively unchanged. For the IQH states the $\nu = 1$ and 3 are striped with 2×4 cluster and checkerboard with 4×4 cluster. But, the IQH state corresponding to $\nu = 2$ has homogeneous density. It must be mentioned that the thermodynamic limit, due to the coupling of neighbouring clusters through ϕ, does not apply to CGMF description of QH states where $\phi = 0$. However, this does limit the applicability of the theory to finite size systems relevant to experimental realizations in optical lattices. On the other hand for the competing SF state, a large lattice size in essence of finite ϕ corresponds to the thermodynamic limit.

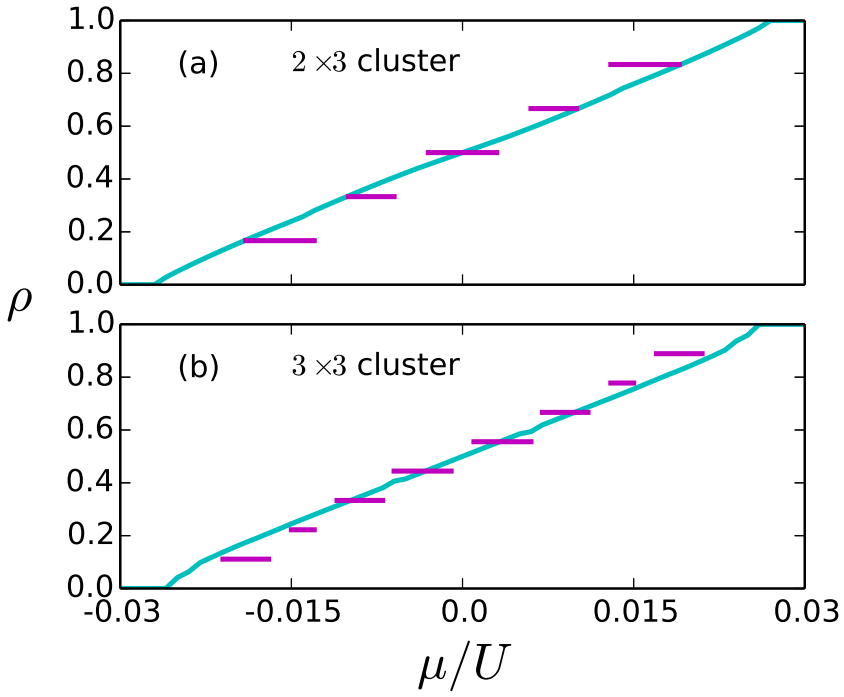

Figure 4.5: The variation in the number density ρ for $\alpha = 1/3$ as a function of μ. The states in SF phase are compressible and have non-zero superfluid order parameter ϕ. As a result, ρ varies linearly with μ and the green curve represents the SF states. For specific values of filling factor ν there are states with constant ρ, represented by the blue lines, and these correspond to the QH states. (a) Results from 2×3 cluster, the plateaus or the constant ρ values correspond to $\nu = n/2$, $n = 1, 2, \ldots, 5$ and the corresponding ρ values are $n/6$. (b) Results from 3×3, the plateaus correspond to $\nu = n/3$, $n = 1, 2, \ldots, 8$ and the corresponding ρ values are $n/9$.

4.1.3 Synthetic magnetic field $\alpha = 1/3$

In the Fig. 4.5, the plateaus corresponding to constant ρ indicate the presence of QH states. Our computations, as mentioned earlier, are for low value of $J/U = 0.01$ and in the vicinity of $n = 0$ and 1 Mott lobes where $\rho < 1$. We obtain the QH states for $\nu = n/2$, with $n = 1, 2, \ldots, 5$ by taking the 2×3 cluster, and at $\nu = n/3$, with $n = 1, 2, \ldots, 8$ by taking the 3×3 cluster. Here, the results from CGMF with 3×3 cluster are close to the ED results as the contributions from the nearest neighbour hopping from the central lattice is exact. And, indeed, the diagonalization of the cluster in the CGMF can be transformed into ED with minor modifications in the computations of

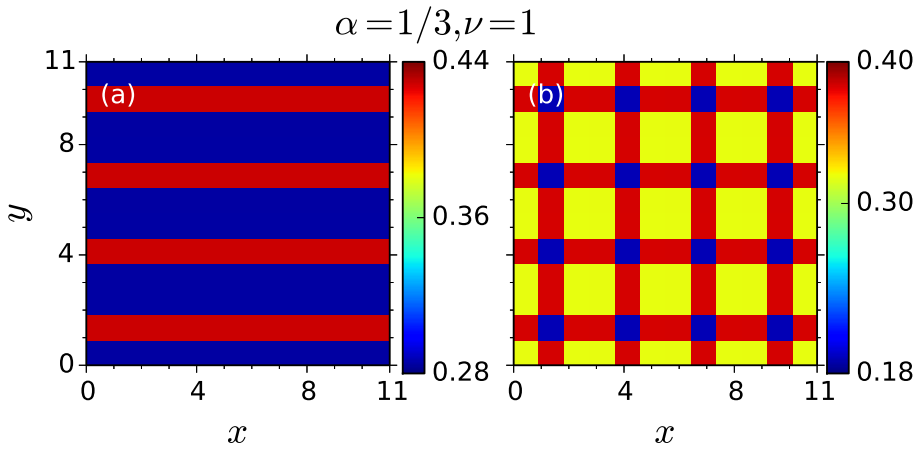

Figure 4.6: The IQH state for $\alpha = 1/3$ and $\nu = 1$ with (a) 2×3 cluster and (b) with 3×3 cluster. The IQH state switches from stripe to checkerboard geometry with the mentioned cluster sizes.

the Hamiltonian matrix elements.

As an example the IQH state for $\nu = 1$, and $\mu/U = -0.008$ with density $\rho = 1/3$ is shown in Fig. 4.6. It is striped with 2×3 cluster and transforms into checkerboard with 3×3 cluster. The transformation from the stripe to the checkerboard pattern is observed for the other IQH state of $\nu = 2$ as well. We observe that all the IQH and FQH states have stripe pattern except the $\nu = 3/2$ state, which has homogeneous density with $\rho = 0.5$ with 2×3 cluster. And the corresponding SF states have a zigzag pattern in the density ρ and in the SF order parameter ϕ. As an example, the FQH state for $\nu = 5/2$ and the corresponding SF state are shown in the Fig. 4.7. As discussed earlier, we do not observe the half-integer FQH states with 3×3 cluster, but do observe the FQH states at the one-third fillings. One of the FQH and SF state with 3×3 cluster for $\nu = 1/3$ is shown in the Fig. 4.8. Here, with 3×3 cluster, we observe that all the FQH states have a checkerboard pattern and all the SF states have diagonal stripe patterns. We find that in all the cases SF state is the ground state and QH state is a metastable state.

4.1.4 Synthetic magnetic field $\alpha = 1/2$

For the high flux $\alpha = 1/2$, we consider 2×4 and 4×4 clusters in the CGMF computations. Compressibility $\rho(\mu)$ for $\alpha = 1/2$ is shown in Fig. 4.1. It must be emphasized

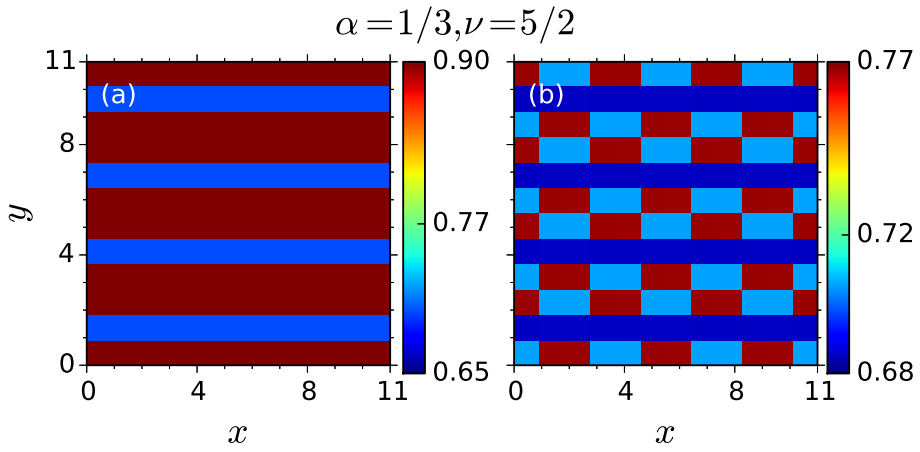

Figure 4.7: (a) The FQH state with $\alpha = 1/3$ and $\nu = 5/2$ with 2×3 cluster, it has a stripe pattern in the density with vanishing SF order parameter. (b) The analogous SF state with zigzag pattern in the density as well as in the SF order parameter.

that $\alpha = 1/2$ is relevant to the recent experimental realizations of synthetic magnetic field in optical lattices [54, 55]. For this value of α, we obtain the QH states for $\nu = 1/2$, 1, and $3/2$ from both the clusters. Like in the case of $\alpha = 1/5$, the $\nu = 1/2$ and $3/2$ FQH states are in the vicinity of MI lobes, and the FQH and SF states are stripe and homogeneous phases, respectively, in the results obtained with 4×2 cluster. However, as shown in Fig. 4.9, the structure of the FQH state is transformed into checkerboard with 4×4 cluster. The latter is more reliable as the operator part of the hopping term in the cluster Hamiltonian is exact along x and y axis within the cluster. For $\nu = 1$ the IQH and SF states are homogeneous for both the cluster sizes.

4.1.5 Comparison of the QH states

Based on our results, only the QH states for $\alpha = 1/4$ and $\nu = 1/2$, 1, $3/2$ and 2 are ground states with $J/U \approx 0.01$, and the competing SF state is metastable. For the mentioned values of ν the QH states are the ground state over a small range of μ centered around $-0.019U$, $-0.014U$, $-0.007U$ and $0.000U$ respectively. For the other combinations of α and ν, the SF and QH states are ground and metastable states, respectively. In general, for different αs, the energy difference between the SF and QH state is $\Delta E \approx 10^{-3}$U. For the parameters of experimental interest $U/\hbar$ = 130

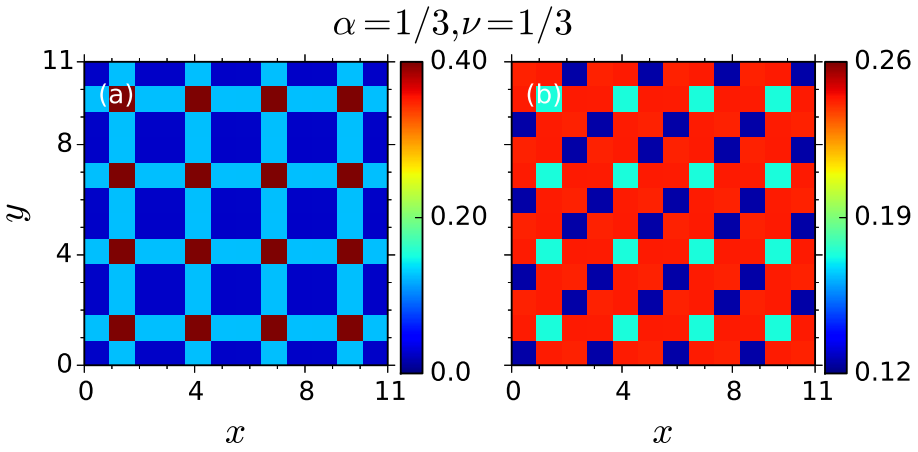

Figure 4.8: (a) The represents FQH state with $\alpha = 1/3$ and $\nu = 1/3$ with 3×3 cluster with a checkerboard pattern in the density and vanishing SF order parameter. (b) The analogous SF state with diagonal stripe pattern in the density as well as in the SF order parameter.

Hz [204] and we get $\Delta E \approx 10^{-2}$nK. This implies stringent bounds on the thermal excitations during the state preparation to obtain QH states. One feature of the CGMF results which distinguishes the QH states from the SF states is the energy. For the QH state, the energy decreases with increasing cluster size. For example the QH state of $\alpha = 1/4$ with $\nu = 1/2$ and $\mu = -0.02U$ has energy $-0.0031U$ and $-0.0046U$ with 2×4, and 4×4 clusters, respectively. Whereas for the SF state, the energy remains almost unchanged as it is $-0.0042U$ and $-0.0045U$, respectively. Thus, the QH state emerges as the ground state with the 4×4 cluster. Here, the key point is not the values of the energies per se, but the importance of having better correlation effects to obtain QH states. These trends arise from a better description of the hopping term with larger cluster size.

4.2 QH states in inhomogeneous system

The simplest modification to the homogeneous system for comparison with the experimental realizations is to impose hard-wall or open boundary conditions. This corresponds to the 2D optical lattice realization similar to the case of homogeneous BEC in a box potential [205]. With the hard-wall boundary we recover the QH states for

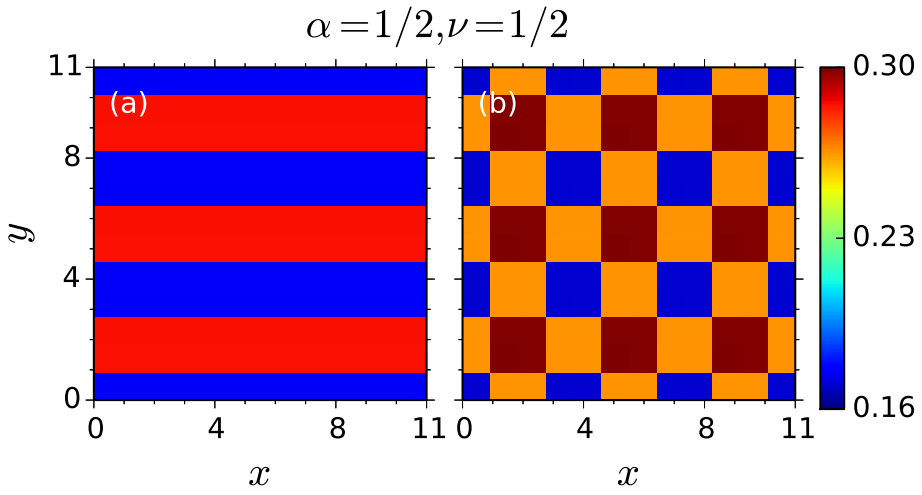

Figure 4.9: The variation in the lattice occupancy ρ of the FQH states with stripe and checkerboard geometry for high flux $\alpha = 1/2$ obtained using CGMF for the filling factor $\nu = 1/2$. This is a metastable state, and the ground state is in the SF phase. (a) The FQH state has average number density $\rho = 0.25$ with stripe pattern and it is obtained from 2×4 cluster. (b) The checkerboard FQH state with the same number density obtained from CGMF theory with 4×4 cluster. In both the cases the ground states, SF phase, like the FQH state has stripe and checkerboard geometries with 2×4 and 4×4 cluster, respectively.

all αs described earlier, and energies remain unchanged. The competing SF states, on the other hand, have higher energies with the hard-wall boundary. In the present work, the largest size of the cluster in the CGMF computations required to encapsulate one magnetic unit cell along y-axis and have the similar representation of hopping terms along x axis is 5×5 for $\alpha = 1/5$. For this reason, we focus on the properties of the QH states of $\alpha = 1/5$. The other QH states are qualitatively similar but computationally less demanding. It is also to be emphasized that the results of a single cluster with hard-wall boundary is equivalent to ED.

The IQH state for $\nu = 1$ with different cluster sizes are shown in Fig. 4.10, which has stripe geometry. Like in the homogeneous case, the stripe geometry is transformed into checkerboard geometry with 3×5 cluster. However, the most important observation is that $\rho(x, y)$ obtained from 5×5 cluster, although checkerboard in structure, is very different from that of 3×5 and 4×5, which are shown in Fig. 4.4. The other envelope

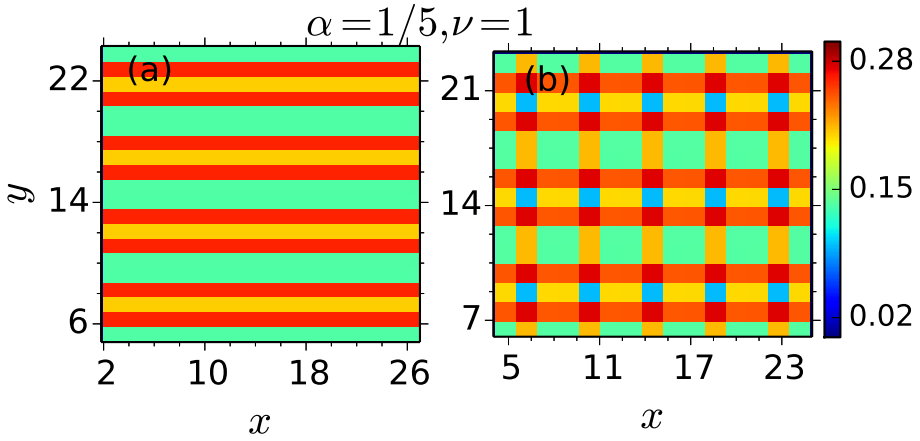

Figure 4.10: Density distribution of the IQH state for $\alpha = 1/5$ and $\nu = 1$ with hard-wall boundary. The average density of atoms in this state is $\rho = 0.2$. (a) The IQH state has stripe geometry in the CGMF results with 2×5 clusters. (b) It is, however, transformed to checkerboard geometry when $3{\times}5$ clusters are considered in the CGMF computations.

potential which is of experimental relevance is the harmonic oscillator potential. Then, the energy offset $\varepsilon_j = \Omega j^2 = \Omega(p^2 + q^2)$, Ω is the strength of the potential. To encompass the envelope potential, we consider a larger lattice size ranging from $40{\times}40$ to 80×80. We, however, find no QH states with the harmonic oscillator envelope potential. This is due to the nature of $\partial\varepsilon_j/\partial j$, it monotonically increases and does not favour the incompressible phase like QH state. One possible modification is that the beam waist w of the laser beam generating the envelope potential is large. So that, the effective envelope potential is still a Gaussian $V_G = U_0 e^{-(x^2+y^2)/w}$. Here, the amplitude of the Gaussian potential U_0 is proportional to the intensity of the laser beam. With this potential, $\partial\varepsilon_j/\partial j$ also decays exponentially and we find that the QH states exist for $U_0 \leqslant 10^{-3}U$. At higher values of U_0 only the SF state is obtained from the CGMF computations

4.3 Two point correlation function

An observable property to identify the QH states is the two-point correlation function $\langle \hat{b}_x^\dagger(y)\hat{b}_0(y)\rangle$, where the expectation is computed with respect to $|\psi_c\rangle$, and the results

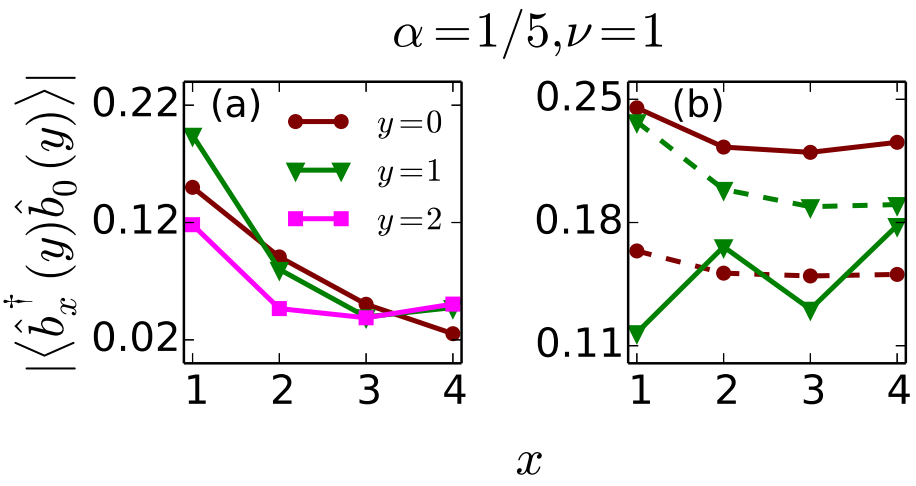

Figure 4.11: Two-point correlation function for low flux $\alpha = 1/5$ with the 5×5 and 5×3 clusters for the QH and SF states, respectively. The correlation is calculated along the x direction for the single cluster. Here $y = 0$ and 1 represent the edge and bulk, respectively. (a) As a characteristic feature of QH state, the correlation function of the $\nu = 1$ IQH state decays non-monotonically in the bulk, and there is no difference between the hard-wall and periodic boundary conditions. (b) For the corresponding SF state there is no trend in the bulk correlation function with hard-wall boundary (solid green line), but it decays monotonically at the edge (solid brown line). With periodic boundary condition (dashed lines), the range of values change, and both the bulk and edge exhibit monotonic decay in correlation.

from the 5×5 cluster are shown in Fig. 4.11(a). As mentioned in the previous chapter, the two-point correlation function is closely related to the OBDM [202, 203]. From the OBDM one can compute the condensate fraction based on Penrose-Onsagar criterion [177] and von Neumann entropy [206]. The correlation function, as recently proposed, could be measured with quantum probes [207, 208]. As reported in a recent work [209], it can be seen from the figure that $\langle \hat{b}_x^\dagger(y)\hat{b}_0(y)\rangle$ decays as inverse power law at the edge. However, in the bulk, as it is gaped, it initially shows exponential decay $\langle \hat{b}_x^\dagger(y)\hat{b}_0(y)\rangle \propto e^{-x/\xi}$ but it is power law when $x > K/2$ or on reaching the opposite edge. Here, ξ is the correlation length of the system and as mentioned earlier, K is the size of the cluster along x. For the SF state with 5×3 cluster, as seen from Fig. 4.11(b), the correlation through the bulk does not show any nonmonotonicity. Here, we have

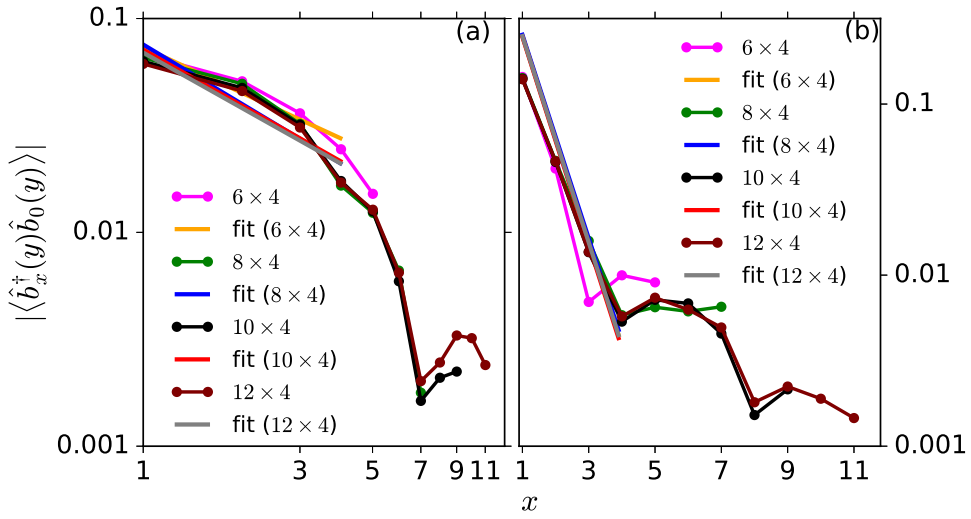

Figure 4.12: Two point correlation function for $\alpha = 1/4$ and $\nu = 1/2$ with increasing cluster size. (a) Log-log plot for power law decay of two point correlation function at edges $y = 0$. (b) Log-linear plot for exponential behaviour of two point correlation function in the bulk $y = 1$.

considered 5×3 cluster as the correlation in the bulk is not sensitive to the size of the cluster.

To verify the trends in the two-point correlation function we compute it for increasing cluster sizes. As an example we consider the case of $\alpha = 1/4$, and $\nu = 1/2$ FQH state by considering cluster sizes of 6×4, 8×4, 10×4 and 12×4. As mentioned earlier, in chapter 3, the two-point correlation function of QH states has power law decay at the edges. For the present case, as shown in Fig 4.12 (a), the fitting function $\propto 1/x^a$ for the edges $y = 0$ gives a value of $a = 0.86$. While in the bulk it decays exponentially as $\propto e^{-x/\xi}$ with $\xi = 1.6$ and the relevant plots are shown in Fig 4.12 (b). In general, this type of detailed study on the trends of two-point correlation function is difficult with ED as the matrix size increases exponentially with system size.

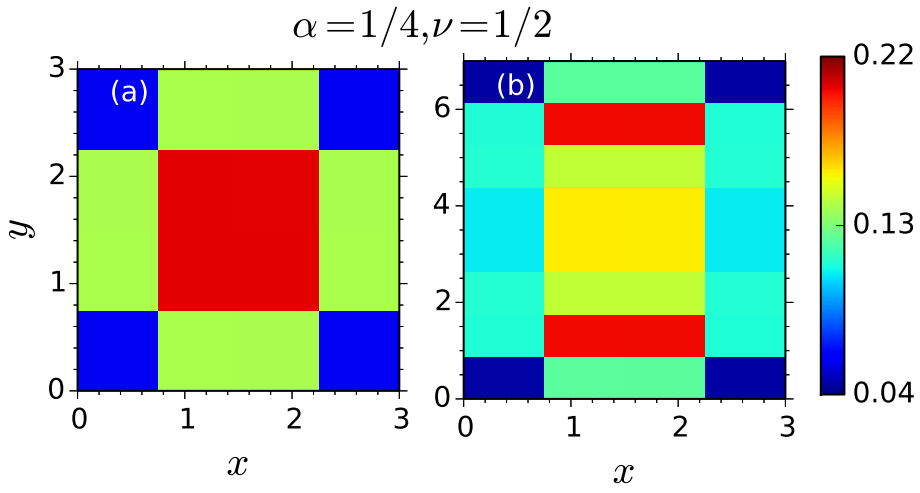

Figure 4.13: (a) Hall state with checkerboard pattern for $\alpha = 1/4, \nu = 1/2$ with 4×4 cluster. (b) Same Hall state with checkerboard pattern with 4×8 cluster.

4.4 ED Results

In using the ED method [202, 203], we focus our attention on the $\alpha = 1/4$, which have QH states as a ground state. For this we, in particular, consider $\nu = 1/2$ FQH state with cluster sizes 4×4, 4×8, and 4×12. Here, as alluded earlier, we distinguish the QH states and SF states based on the Penrose-Onsager criterion [177] and von Neumann entropy [206]. For this, we compute OBDM in Eq. (3.18), and then diagonalize it and obtain the energy eigenvalues. Following the Penrose-Onsager criterion, the state is SF if the condensate fraction $\rho_{\rm cf} = \lambda_m^{\rm OBDM}/N_a \approx 1$, where $\lambda_m^{\rm OBDM}$ is the largest eigenvalue of the OBDM, and N_a is the total number of atoms. In contrast, for the QH states $\rho_{\rm cf} < 1$. Our results are in agreement with this, for example, with 4×4 cluster, the values of $\rho_{\rm cf}$ are 0.56 and 0.89 for the FQH and SF states, respectively. Once the OBDM is diagonalized, we calculate the von Neumann entropy

$$S = -\sum_{i}^{M\times N} p_i \ln(p_i),$$

where $p_i = \lambda_i^{\rm OBDM}/N_a$ and $M\times N$ are eigenvalues of the OBDM. As the von Neumann entropy is a measure of correlation effect, it is higher for the more correlated states like QH states compared to the SF states. For the states considered the values of S are 1.0 and 0.53 for the FQH and SF states, respectively. These values indicate that the FQH state, as expected, is more correlated than the SF state. When the cluster size is

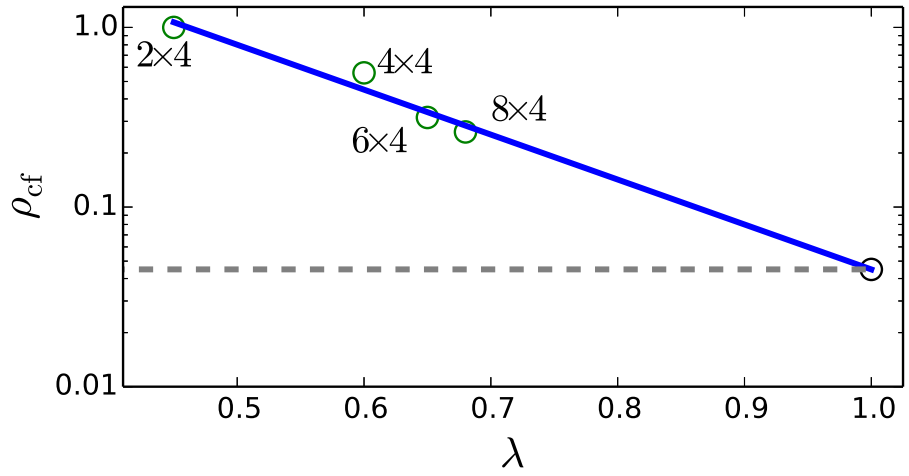

Figure 4.14: Condensate fraction $\rho_{\rm cf}$ of the QH state with $\alpha = 1/4$, and $\nu = 1/2$ as a function of system size. The thermodynamic limit of $\rho_{\rm cf} = 0.04$ is obtained from the finite size scaling by fitting a line.

increased to $4{\times}8$ the value of $\rho_{\rm cf}$ is modified to 0.26 and 0.80 for the FQH and SF states, respectively. And, the corresponding values of S are 1.84 and 0.95, respectively. We also obtain similar results for the other QH and SF states, for example, $\rho_{\rm cf}$ is 0.33 and 0.75 for the QH and SF states respectively with 5×5 cluster for $\alpha = 1/5$, and $\nu = 1$. The corresponding value of S is 1.89 and 1.20, respectively. It is to be mentioned here that the QH and SF states obtained from the ED method have the same features, ρ and ϕ, as in CGMF results.

With ED, we obtain QH states for 4×4, 5×5, 4×8 and 4×12 cluster and identify them based on the Penrose-Onsager criterion. Here, it must be mentioned that the QH states obtained from 4×4 and 5×5, 4×8 agree with the CGMF results. One of the FQH states with $\alpha = 1/4$ and $\nu = 1/2$ is shown in Fig. 4.13. For this case the total number of atoms with 4×4 cluster is $N_a = 2$, and the number of cluster states is 120. Similarly, for 4×8 and 4×12 the number of atoms and cluster states are $N_a = 4$ & 35960 and $N_a = 6$ and 12271512, respectively. To obtain the thermodynamic limit of $\rho_{\rm cf}$ we do a finite size scaling analysis using clusters of different size. As an example, we compute the thermodynamic limit of $\rho_{\rm cf}$ for $\alpha = 1/4$ and $\nu = 1/2$ QH state. For this we choose $2{\times}4$, $4{\times}4$, $6{\times}4$ and $8{\times}4$ clusters and finite scaling analysis is done with the parameter λ. Based on the results, the plot of the $\rho_{\rm cf}$ as a function of λ is shown

in Fig 4.14. From the fitting function we obtain the $\rho_{\rm cf}$ in the thermodynamic limit ($\lambda = 1$) as 0.04. The small value indicates that the ground state is not SF and hence, consistent with our identification as a FQH state.

4.5 Numerical validation of FQH states

To confirm that the states we identify as FQH states are indeed true, we investigate further by computing other properties of the states. For this, to be specific, let us consider the $\nu = 1/2$ FQH state with $\alpha = 1/4$ obtained from 8×4 cluster. This state is identified as Laughlin state in the literature [62, 210]. We examine the ground state degeneracy and compute the many-body Chern number (MBCN) for this state by imposing twist angles with periodic boundary conditions. The Hamiltonian with twist angle on the boundary is [62, 210, 211]

$$\begin{aligned}\hat{H} &= -\sum_{p,q}\left[\left(J_x \mathrm{e}^{i2\pi(\alpha q-\delta_{xK}\theta_x)}\hat{b}^\dagger_{p+1,q}\hat{b}_{p,q} + \mathrm{H.c.}\right) + \left(J_y \mathrm{e}^{-i2\pi\delta_{yL}\theta_y}\hat{b}^\dagger_{p,q-1}\hat{b}_{p,q} + \mathrm{H.c.}\right)\right] \\ &\quad + \sum_{p,q}\frac{U}{2}\hat{n}_{p,q}(\hat{n}_{p,q}-1) \qquad (4.1)\end{aligned}$$

where θ_x and θ_y are the twist angles along x and y directions, respectively. And, these have finite values at the boundary for $K \times L$ system size.

4.5.1 Ground state degeneracy

An important property of the FQH state is the ground state degeneracy. It was shown by Wen and Niu [212] that the FQH state with $\nu = p/q$, where p and q are mutually prime integers, on a Riemann surface of genus g is q^g fold degenerate. In our case, topologically, a torus in 2D has $g = 1$. Thus, for the present case of $\nu = 1/2$ on the torus geometry, the ground state should be doubly degenerate if it is an FQH state. This is indeed the case and can be considered as an evidence of the ground being FQH state. Further, we vary the twist angles θ_x and θ_y compute the ground state energy. And, find that the double degeneracy is independent of the twist angles. This is to be expected as the ground state degeneracy is determined by the integer denominator of ν and not dependent on the twist angles. There is a finite energy gap as the first excited state

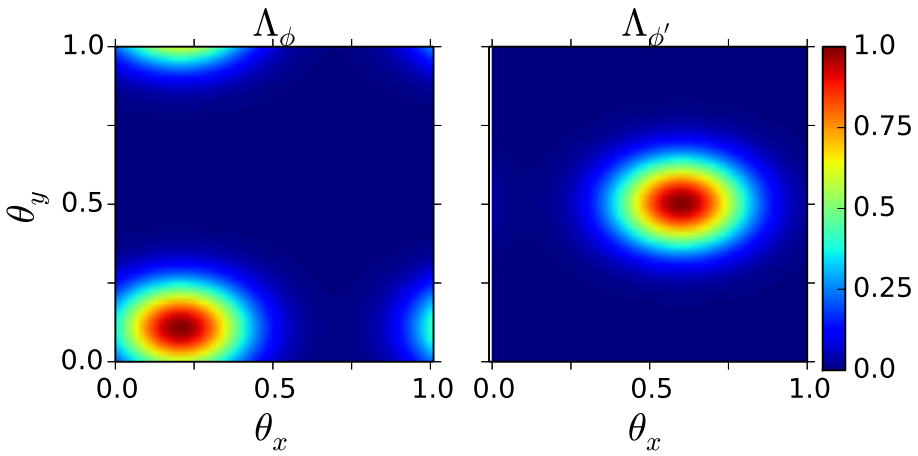

Figure 4.15: Plot for Λ_ϕ and $\Lambda_{\phi'}$ where the reference degenerate ground states ϕ and $\phi^{'}$ are considered at the twist angles $(\theta_x, \theta_y) = (0.2, 0.1), (0.6, 0.5)$.

is separated from the ground state by $0.0021U$. The ground state degeneracy should be lifted with open boundary condition as it depends on the topology of the system. Indeed, we find that with open boundary condition, the ground state is non-degenerate.

The results, for the ground state degeneracy, is dependent on the system size. For example, with a system size of 4×4, the three lowest eigenvalues are $-0.0586U$, $-0.0556U$ and $-0.0552U$. Thus, relatively, we consider the lowest two as non-degenerate as the energy difference is $0.0020U$. The first two excited states, which have an energy difference of 0.0003, could be considered as quasi-degenerate. The results change significantly when we consider a larger system size of 6×4. The three lowest eigenvalues are then $-0.0854U$, $-0.0854U$ and $-0.0833U$. And, double degeneracy of the ground state is self-evident. With an even larger system size of 8×4 these three lowest eigen energies decrease to $-0.1129U$, $-0.1129U$ and $-0.1108U$. However, an important point is that in both results the separation of the first excited state from the ground state remains unchanged at $0.0021U$. Although, we have given the details of only the $\nu = 1/2$ and $\alpha = 1/4$ state, we find that the ground state of $\nu = 3/2$ and $\alpha = 1/4$ is double degenerate. And, our results with different system sizes show similar trends.

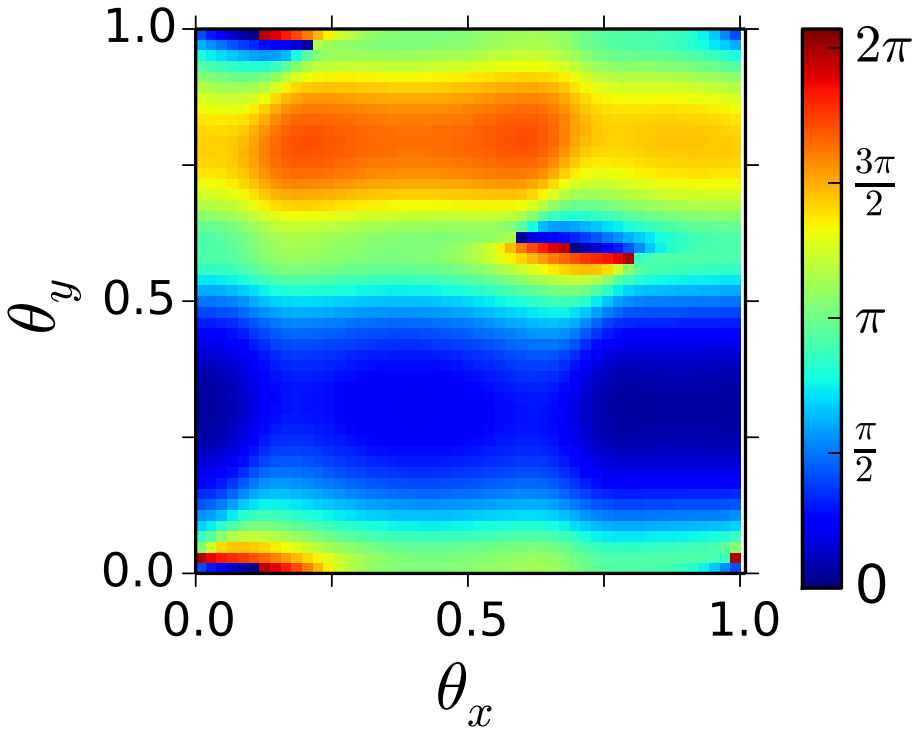

Figure 4.16: The argument field Ω for the FQH states which shows the phase change for the vortex.

4.5.2 Many-body Chern number

The QH states are topological in nature and do not have a local order parameter. The MBCN is one of the approaches to identify the topological order of a many-body system. To compute MBCN, in our studies, we do a series of computations by varying the twist angles θ_x and θ_y And, we give detailed results for the MBCN of the $\nu = 1/2$ FQH states. For providing a general description of MBCN, take $\Psi^{(\alpha)}(x, y)$ as the non-degenerate wave-function of the QH state for magnetic flux α. And, let $\Psi^{(\alpha)}(\theta_x, \theta_y)$ be the wave-function of the same state with twist angles θ_x and θ_y. Then, we can define a vector field with components

$$\mathcal{A}_j^{(\alpha)}(\theta_x, \theta_y) = i\langle\Psi^{(\alpha)}(\theta_x, \theta_y)|\frac{\partial}{\partial\theta_j}|\Psi^{(\alpha)}(\theta_x, \theta_y)\rangle, \tag{4.2}$$

and, in terms of this vector field the MBCN is

$$C(\alpha) = \frac{1}{2\pi}\int_0^{2\pi} d\theta_x \int_0^{2\pi} d\theta_y \left[\partial_x \mathcal{A}_y^{(\alpha)} - \partial_y \mathcal{A}_x^{(\alpha)}\right]. \tag{4.3}$$

The definition of the MBCN can be extended to the case of degenerate states as well. However, the definition given above is a continuum description. For discrete systems

like optical lattices we use the method, applicable to numerical results, as discussed by Hatsugai et al. [213, 214], and as implemented by Hazezi et al. [62, 211] and Gerster et al. [210] for BHM with synthetic magnetic fields. In which case the twist angles are varied in the range of $(\theta_x, \theta_y) \in [0,1] \times [0,1]$ for the torus geometry. This method of computing MBCN is based on the computation of overlaps. We consider the two reference degenerate ground state ϕ and $\phi^{'}$ at different twist angles which are not parallel to each other and these can be arbitrary. For our computation we take these states at $(\theta_x, \theta_y) = (0.2, 0.1)$ and $(0.6, 0.5)$. These two states correspond to two different gauge references, and then, we compute the overlaps

$$\Lambda_{\phi} = \det \langle \phi_i | \, P(\theta_x, \theta_y) \, | \phi_j \rangle \,, \tag{4.4}$$

$$\Lambda_{\phi'} = \det \langle \phi_i^{'} | \, P(\theta_x, \theta_y) \, | \phi_j^{'} \rangle \,, \tag{4.5}$$

where i, j varies from 0 to 1. And, here 0 and 1 identify the degenerate ground states of the reference states. In the above definition, $P(\theta_x, \theta_y)$ is the projector on the degenerate ground state and is defined as

$$P(\theta_x, \theta_y) = |\psi_0(\theta_x, \theta_y)\rangle \langle \psi_0(\theta_x, \theta_y)| + |\psi_1(\theta_x, \theta_y)\rangle \langle \psi_1(\theta_x, \theta_y)| \,, \tag{4.6}$$

where $|\psi_0(\theta_x, \theta_y)\rangle$ and $|\psi_1(\theta_x, \theta_y)\rangle$ are the two degenerate ground state eigenstates defined for twist angles θ_x and θ_y. In the Fig.4.15, we show the scalar fields Λ_{ϕ} and $\Lambda_{\phi'}$ as a function of the twist angles. In the figure we observe regions where Λ_{ϕ} is nonzero but $\Lambda_{\phi'}$ is zero and vice versa. This is due to the choice of reference states which are almost orthogonal to each other. Thus the MBCN is equal to one for the $\nu = 1/2$ FQH state that to $1/2$ for each states. We also calculate the argument field $\Omega_{\phi \to \phi'} = \det \langle \phi_i^{'} | \, P(\theta_x, \theta_y) \, | \phi_j \rangle$ and observe a phase change from $-\pi$ to π shown in the Fig. 4.16

4.6 Summary of the chapter

In this chapter, I discuss QH states obtained from a combination of CGMF and ED methods. We get QH states for different value of synthetic magnetic field α = $1/5$, $1/4$, $1/3$ and $1/2$, and for different filling factors. I, then study these QH states with background potential and find that for shallow Gaussian potential, we do recover the QH states but not for harmonic potential. I provide further evidence for the QH states by calculating the two-point correlation function in the CGMF method. With the ED results we examine the properties of these QH states in terms of the Penrose-Onsager criterion and von Neumann entropy. And, as a validation, we compute MBCN, which is a topological invariant. As an example, I discuss in detail the computation of MBCN for the $\nu = 1/2$ Laughlin states which has MBCN equal to unity.

Chapter 5

Two species ultracold gas systems

Two species ultracold gas system (TUGS) is the condensates which consists condensate mixture of two different atomic species or two isotopes of the same element or two different hyperfine states of the atomic species. I study the TUGS which is trapped in the optical lattices, and can be described by BH Hamiltonian in this thesis. After the first experimental realization of TUGS in the two hyperfine states $|F = 2, m_F = 2\rangle$ and $|F = 2, m_F = -1\rangle$ of ^{87}Rb atom [75], this field has become important to study the experimental and theoretical rich physics, which is not accessible in the single species BEC. In two different hyperfine states of the same species TUGS has been realized in [75–84]. On the other hand the TUGS in two different atomic species [69–74], two different isotopes [85–87] have been reported. Using the TUGS, interesting phenomena such as pattern formation [88–91], phase separation [71, 73, 74, 84, 85], nonlinear dynamical excitations [82, 92, 93], collective excitations [79], Kibble-Zurek mechanism [94], and the production of dipolar molecules [95–97] have been studied. The phases separation, among all the phenomena is a unique property of TUGS. The experimental realization of TUGS in optical lattices has been observed in [99, 215] and theoretical studies are presented in [104, 119, 216, 217]. The essential feature associated with the TUGS is phase separation [124, 125, 218] which has not been fully studied in the strongly interacting regime of BHM. The BHM for TUGS [41, 101–103] has been studied and phase diagram of TUGS [102, 116–118] shows the different combinations of mixed MI-SF phases apart from the MI and SF phase. The phase diagram with TUGS has been studied with inter-species interactions for homogeneous system [119],

with external potential [120], and the presence of second species have been studied in [121]. After the study of BHM with TUGS, new direction to study the BHM is by considering nearest neighbour (NN) interaction in the BHM which is known as extended BHM (eBHM) [137]. The eBHM shows two more phases density wave (DW) [139–141] and supersolid (SS) phase [141–145] apart from the MI and SF phases. The DW phase is an insulating phase similar to the MI phase but with the crystalline order, and the SS phase is a compressible phase with both diagonal and off diagonal order and has a crystalline structure. The eBHM and phase separation associated with eBHM is the main focus of the current study.

In this chapter, I describe the BH Hamiltonian for TUGS and Obtain the ground state solution with the Gutzwiller ansatz. Then, I discuss the BH Hamiltonian of TUGS by considering the nearest neighbour intra and inter-species interaction, which is referred as eBHM for TUGS. I obtain the phase diagram of BHM and eBHM for TUGS with different inter species interactions. In the end, I provide the phase separation density profile for different phases such as DW, SS, and SF.

5.1 BH Hamiltonian for TUGS

We consider TUGS confined in square optical lattices. At zero temperature, the BH Hamiltonian for this system can be expressed as [101, 102, 104, 117, 129, 219–221]

$$\begin{aligned}\hat{H}^{\mathrm{TUGS}} &= -\sum_{k=1,2}\sum_{p,q}\left[\left(J_x^k \hat{b}_{p+1,q}^{\dagger k}\hat{b}_{p,q}^k + \mathrm{H.c.}\right) + \left(J_y^k \hat{b}_{p,q+1}^{\dagger k}\hat{b}_{p,q}^k + \mathrm{H.c.}\right)\right] \\ &\quad + \sum_{k=1,2}\sum_{p,q}\left[\frac{U_{kk}}{2}\hat{n}_{p,q}^k(\hat{n}_{p,q}^k - 1) - \tilde{\mu}_{p,q}^k \hat{n}_{p,q}^k\right] + \sum_{p,q} U_{12}\hat{n}_{p,q}^1\hat{n}_{p,q}^2, \quad (5.1)\end{aligned}$$

where $k = 1, 2$ represents the 1st and 2nd species, J_x^k (J_y^k) is the hopping strength along x (y) directions for these two species, U_{kk} is the intra-species interaction, and U_{12} is the inter-species interaction between the two species. It is to be mentioned that in the above and following discussions, all the interactions are repulsive in nature $U > 0$. The local chemical potential at each lattice site for each of the species is $\tilde{\mu}^k = \mu^k - \varepsilon_{p,q}^k$. To obtain the ground state solution of the above Hamiltonian, we use single-site Gutzwiller mean field theory. For this, like in the case of single species, we derive the mean-field Hamiltonian by partitioning ${\hat{b}_{p,q}^k}^\dagger$ and $\hat{b}_{p,q}^k$ into a mean-field

and fluctuation operator part. Then, the mean-field Hamiltonian for TUGS in optical lattices is

$$\begin{aligned}\hat{H}^{\mathrm{TUGS}} &= -\sum_{k=1,2}\sum_{p,q}\Bigg\{\left[J_x^k\left(\hat{b}^{\dagger k}_{p+1,q}\phi^k_{p,q}+\phi^{k*}_{p+1,q}\hat{b}^k_{p,q}-\phi^{k*}_{p+1,q}\phi^k_{p,q}\right)+\mathrm{H.c.}\right]\\ &\quad+\left[J_y^k\left(\hat{b}^{\dagger k}_{p,q+1}\phi^k_{p,q}+\phi^{k*}_{p,q+1}\hat{b}^k_{p,q}-\phi^{k*}_{p,q+1}\phi^k_{p,q}\right)+\mathrm{H.c.}\right]\Bigg\}\\ &\quad+\sum_{k=1,2}\sum_{p,q}\left[\frac{U_{kk}}{2}\hat{n}^k_{p,q}(\hat{n}^k_{p,q}-1)-\tilde{\mu}^k_{p,q}\hat{n}^k_{p,q}\right]+\sum_{p,q}U_{12}\hat{n}^1_{p,q}\hat{n}^2_{p,q}, \quad (5.2)\end{aligned}$$

here, $\phi^k_{p,q}$ ($\phi^{k*}_{p,q}$) is SF order parameter of the kth species. As mentioned earlier, in the SGMF method, the total Hamiltonian of the system is written as the sum of the single-site Hamiltonians. And, from the above Hamiltonian we can identify the single-site mean field Hamiltonian for the TUGS as

$$\begin{aligned}\hat{h}^{\mathrm{TUGS}}_{p,q} &= -\sum_{k=1,2}\Bigg\{\left[J_x^k\left(\hat{b}^{\dagger k}_{p,q}\phi^k_{p-1,q}+\phi^{k*}_{p+1,q}\hat{b}^k_{p,q}-\phi^{k*}_{p,q}\phi^k_{p-1,q}-\phi^{k*}_{p+1,q}\phi^k_{p,q}\right)+\mathrm{H.c.}\right]\\ &\quad+\left[J_y^k\left(\hat{b}^{\dagger k}_{p,q}\phi^k_{p,q+1}+\phi^{k*}_{p,q-1}\hat{b}^k_{p,q}-\phi^{k*}_{p,q}\phi^k_{p,q+1}-\phi^{k*}_{p,q-1}\phi^k_{p,q}\right)+\mathrm{H.c.}\right]\Bigg\}\\ &\quad+\sum_{k=1,2}\left[\frac{U_{kk}}{2}\hat{n}^k_{p,q}(\hat{n}^k_{p,q}-1)-\tilde{\mu}^k_{p,q}\hat{n}^k_{p,q}\right]+U_{12}\hat{n}^1_{p,q}\hat{n}^2_{p,q}. \quad (5.3)\end{aligned}$$

We can now diagonalize the above Hamiltonian at each lattice site and obtain the ground state. The ground state Gutzwiller wave-function for TUGS at (p,q)th site is

$$|\psi\rangle_{p,q}=\sum_{n_1,n_2}c^{(p,q)}_{n_1,n_2}|n_1,n_2\rangle_{p,q}. \quad (5.4)$$

Here n_1 and n_2 are Fock states for 1st and 2nd species respectively, and with N_b occupation number states, both can have values 0, 1, ..., N_b-1. The c-number $c^{p,q}_{n_1,n_2}$ is the complex co-efficients for the ground state $|\psi\rangle_{p,q}$ and satisfies the normalization condition $\sum_{n_1,n_2}|c^{(p,q)}_{n_1,n_2}|^2=1$. For compact notation we combine the two quantum numbers n_1 and n_2 of the occupation number states of the two species into a single index quantum number n. With this notation $|n\rangle\equiv|n_1,n_2\rangle$ and the above equations can be rewritten as

$$|\psi\rangle_{p,q}=\sum_n c^{(p,q)}_n\,|n\rangle_{p,q}\,, \quad (5.5)$$

and, the normalization condition is $\sum_n|c^{(p,q)}_n|^2=1$. Hereafter, we use this compact notation, and we resort to the notation of n_1 and n_2 where there is a need of clarity.

5.1.1 Hamiltonian Matrix

To apply the single-site Gutzwiller mean-field theory to the TUGS, the first step is to construct the matrix of the single-site Hamiltonian in Eq. (5.3). For this, we use the Gutzwiller wave-function in Eq. (5.4) and the matrix element can be written as

$$h_{n'n} =_{p,q} \langle n'|\, \hat{h}^{\mathrm{TUGS}}_{p,q}\, |n\rangle_{p,q}\,. \tag{5.6}$$

Here, the combined quantum numbers n' (n), in terms of n'_1, n'_2 (n_1, n_2) these are $n' = n'_2 N_b + n'_1$ and $n = n_2 N_b + n_1$. The Hamiltonian in Eq. (5.3) can be partitioned into five terms

$$\hat{h}^{\mathrm{TUGS}}_{p,q} = \hat{h}^1_{p,q} + \hat{h}^2_{p,q} + \hat{h}^3_{p,q} + \hat{h}^4_{p,q} + \hat{h}^5_{p,q}.$$

The full form of the first four terms are

$$\begin{aligned}
\hat{h}^1_{p,q} &= -\left(J^1_x \phi^{1*}_{p+1,q} + J^{1*}_x \phi^{1*}_{p-1,q} + J^1_y \phi^{1*}_{p,q-1} + J^{1*}_y \phi^{1*}_{p,q+1}\right) \hat{b}^1_{p,q}, && (5.7)\\
\hat{h}^2_{p,q} &= -\left(J^2_x \phi^{2*}_{p+1,q} + J^{2*}_x \phi^{2*}_{p-1,q} + J^2_y \phi^{2*}_{p,q-1} + J^{2*}_y \phi^{2*}_{p,q+1}\right) \hat{b}^2_{p,q}, && (5.8)\\
\hat{h}^3_{p,q} &= -\left(J^{1*}_x \phi^1_{p+1,q} + J^1_x \phi^1_{p-1,q} + J^{1*}_y \phi^1_{p,q-1} + J^1_y \phi^1_{p,q+1}\right) \hat{b}^{\dagger 1}_{p,q}, && (5.9)\\
\hat{h}^4_{p,q} &= -\left(J^{2*}_x \phi^2_{p+1,q} + J^2_x \phi^2_{p-1,q} + J^{2*}_y \phi^2_{p,q-1} + J^2_y \phi^2_{p,q+1}\right) \hat{b}^{\dagger 2}_{p,q}, && (5.10)
\end{aligned}$$

and the fifth term consists of all the diagonal terms in Eq. (5.3). Like in the case of single species, the Hamiltonian matrix is sparse due to the selection rules arising from the orthogonality of the occupation number states. To illustrate the non-zero matrix elements we consider the matrix elements of the terms in the Hamiltonian for a fixed state $|n\rangle$. For the first term the non-zero matrix elements are of the form

$$\begin{aligned}
\langle n'|\, \hat{h}^1_{p,q}\, |n\rangle &= -\left(J^1_x \phi^{1*}_{p+1,q} + J^{1*}_x \phi^{1*}_{p-1,q} + J^1_y \phi^{1*}_{p,q-1} + J^{1*}_y \phi^{1*}_{p,q+1}\right) \langle n'|\, \hat{b}^1_{p,q}\, |n\rangle\\
&= c^1_f \sqrt{n_1}\, \delta_{n'_1, n_1 - 1} \delta_{n'_2, n_2} = c^1_f \sqrt{n_1}, && (5.11)
\end{aligned}$$

where $c^1_f = -\left(J^1_x \phi^{1*}_{p+1,q} + J^{1*}_x \phi^{1*}_{p-1,q} + J^1_y \phi^{1*}_{p,q-1} + J^{1*}_y \phi^{1*}_{p,q+1}\right)$, with $n' = n_2 N_b + n_1 - 1$ and $n = n_2 N_b + n_1$. In the matrix elements of the remaining terms, as mentioned earlier, the value n remains unchanged. But, depending on the term of the Hamiltonian there is a change in the value of n'. Similarly, for the second term $\hat{h}^2_{p,q}$, the non-zero matrix elements are of the form

$$\langle n'|\, \hat{h}^2_{p,q}\, |n\rangle = -\left(J^2_x \phi^{2*}_{p+1,q} + J^{2*}_x \phi^{2*}_{p-1,q} + J^2_y \phi^{2*}_{p,q-1} + J^{2*}_y \phi^{2*}_{p,q+1}\right) \langle n'_1, n'_2|\, \hat{b}^2_{p,q}\, |n_1, n_2\rangle$$

$$= c_f^2\sqrt{n_2}\delta_{n_1',n_1}\delta_{n_2',n_2-1} = c_f^2\sqrt{n_2}, \tag{5.12}$$

where $c_f^2 = -\left(J_x^2\phi_{p+1,q}^{2*} + J_x^{2*}\phi_{p-1,q}^{2*} + J_y^2\phi_{p,q-1}^{2*} + J_y^{2*}\phi_{p,q+1}^{2*}\right)$, with $n' = (n_2-1)N_b+ n_1$ and $n = n_2N_b + n_1$. For the third term $\hat{h}_{p,q}^3$, the non-zero matrix elements are of the form

$$\begin{aligned}\langle n'|\,\hat{h}_{p,q}^3\,|n\rangle &= -\left(J_x^{1*}\phi_{p+1,q}^1 + J_x^1\phi_{p-1,q}^1 + J_y^{1*}\phi_{p,q-1}^1 + J_y^1\phi_{p,q+1}^1\right)\langle n_1'n_2'|\,\hat{b}_{p,q}^{\dagger 1}\,|n_1,n_2\rangle \\ &= c_f^{1*}\sqrt{n_1+1}\delta_{n_1',n_1+1}\delta_{n_2',n_2} = c_f^{1*}\sqrt{n_1+1},\end{aligned} \tag{5.13}$$

where $c_f^{1*} = -\left(J_x^{1*}\phi_{p+1,q}^1 + J_x^1\phi_{p-1,q}^1 + J_y^{1*}\phi_{p,q-1}^1 + J_y^1\phi_{p,q+1}^1\right)$, with $n' = n_2N_b + n_1 + 1$ and $n = n_2N_b + n_1$. And, for the fourth term $\hat{h}_{p,q}^4$, the non-zero matrix element is of the form

$$\begin{aligned}\langle n'|\,\hat{h}_{p,q}^4\,|n\rangle &= -\left(J_x^{2*}\phi_{p+1,q}^2 + J_x^2\phi_{p-1,q}^2 + J_y^{2*}\phi_{p,q-1}^2 + J_y^2\phi_{p,q+1}^2\right)\langle n_1'n_2'|\,\hat{b}_{p,q}^{\dagger 2}\,|n_1,n_2\rangle \\ &= c_f^{2*}\sqrt{n_2+1}\delta_{n_1',n_1}\delta_{n_2',n_2+1} = c_f^2\sqrt{n_2+1},\end{aligned} \tag{5.14}$$

where $c_f^{2*} = -\left(J_x^{2*}\phi_{p+1,q}^2 + J_x^2\phi_{p-1,q}^2 + J_y^{2*}\phi_{p,q-1}^2 + J_y^2\phi_{p,q+1}^2\right)$, with $n' = (n_2+1)N_b+ n_1$ and $n = n_2N_b + n_1$. Finally, the matrix element of the diagonal term $\hat{h}_{p,q}^5$ is

$$\begin{aligned}D_{nn} &= \sum_{k=1,2}\left\{-\left[c_f^k\phi_{p,q}^k + c_f^{k*}\phi_{p,q}^{k*}\right] + \frac{U_{kk}}{2}\left[n_{p,q}^k(n_{p,q}^k-1)\right] - \tilde{\mu}^k n_{p,q}^k\right\} \\ &\quad + U_{12}n_{p,q}^1n_{p,q}^2.\end{aligned} \tag{5.15}$$

Once the Hamiltonian matrix is diagonalized, considering only the lowest energy eigenstate, we obtain the coefficients $c_n^{(p,q)}$. From these the SF order parameters for both the species at the lattice site (p,q) can be computed as

$$\phi_{p,q}^1 = {}_{p,q}\langle\psi|\hat{b}_{p,q}^1|\psi\rangle_{p,q} = \sum_{n_1,n_2}\sqrt{n_1}c_{n_1-1,n_2}^{(p,q)*}c_{n_1,n_2}^{(p,q)}, \tag{5.16}$$

$$\phi_{p,q}^2 = {}_{p,q}\langle\psi|\hat{b}_{p,q}^2|\psi\rangle_{p,q} = \sum_{n_1,n_2}\sqrt{n_2}c_{n_1,n_2-1}^{(p,q)*}c_{n_1,n_2}^{(p,q)}, \tag{5.17}$$

and the corresponding occupancy of the two species are

$$n_{p,q}^1 = {}_{p,q}\langle\psi|\hat{n}_{p,q}^1|\psi\rangle_{p,q} = \sum_{n_1,n_2}n_1|c_{n_1,n_2}^{(p,q)}|^2, \tag{5.18}$$

$$n_{p,q}^2 = {}_{p,q}\langle\psi|\hat{n}_{p,q}^2|\psi\rangle_{p,q} = \sum_{n_1,n_2}n_2|c_{n_1,n_2}^{(p,q)}|^2. \tag{5.19}$$

Using these values, we can do the computations for the next lattice site and continue this till the last lattice site. This completes one iteration, and then, like in the case of the single species repeat the iteration till convergence.

5.1.2 Extended BHM for TUGS

The BHM Hamiltonian with NN interaction is referred to as the extended BHM Hamiltonian. In the case of TUGS, we consider the addition of the NN interaction to study the effect of long-range interaction on the density distribution in the immiscible domain. The extended BH Hamiltonian for TUGS is

$$\begin{aligned}\hat{H}^{\mathrm{Ext}} &= \hat{H}^{\mathrm{TUGS}} + \sum_{k=1,2}\sum_{p,q} V_k \hat{n}^k_{p,q}\left(\hat{n}^k_{p-1,q} + \hat{n}^k_{p+1,q} + \hat{n}^k_{p,q-1} + \hat{n}^k_{p,q+1}\right) \\ &\quad + \sum_{p,q}\Big[V_{12}\hat{n}^1_{p,q}\left(\hat{n}^2_{p-1,q} + \hat{n}^2_{p+1,q} + \hat{n}^2_{p,q-1} + \hat{n}^2_{p,q+1}\right) \\ &\quad + V_{21}\hat{n}^2_{p,q}\left(\hat{n}^1_{p-1,q} + \hat{n}^1_{p+1,q} + \hat{n}^1_{p,q-1} + \hat{n}^1_{p,q+1}\right)\Big], \end{aligned} \tag{5.20}$$

here, V_k is the intra NN interaction strength for both the species, and V_{12} (V_{21}) is the inter NN interaction between the two species. And, in the present work, all of these are repulsive, $V_k > 0$ and $V_{12} > 0$. The NN interaction is non-zero in the experiments with dipolar atomic species. And, more importantly, the relative effect of the long-range interaction can be enhanced by suppressing the contact interaction through magnetic Feshbach resonance. To obtain the ground state of the extended BH Hamiltonian, we use SGMF method, that is total Hamiltonian is the sum of single-site Hamiltonians

$$\begin{aligned}\hat{h}^{\mathrm{Ext}}_{p,q} &= \hat{h}^{\mathrm{TUGS}}_{p,q} + \sum_{k=1,2} V_k \hat{n}^k_{p,q}\left(\hat{n}^k_{p-1,q} + \hat{n}^k_{p+1,q} + \hat{n}^k_{p,q-1} + \hat{n}^k_{p,q+1}\right) \\ &\quad + V_{12}\hat{n}^1_{p,q}\left(\hat{n}^2_{p-1,q} + \hat{n}^2_{p+1,q} + \hat{n}^2_{p,q-1} + \hat{n}^2_{p,q+1}\right) \\ &\quad + V_{21}\hat{n}^2_{p,q}\left(\hat{n}^1_{p-1,q} + \hat{n}^1_{p+1,q} + \hat{n}^1_{p,q-1} + \hat{n}^1_{p,q+1}\right). \end{aligned} \tag{5.21}$$

For extended BH Hamiltonian also, we diagonalize the Hamiltonian at each site separately, and NN interaction terms contribute to the diagonal matrix element.

5.2 Phase diagram of TUGS

For the SGMF, like in the case of single species, we start the computations with the initial choice of SF order parameter ϕ, and construct the matrix of the Hamiltonian in Eq. (5.3) by using Gutzwiller state in Eq. (5.4). We diagonalize it, iterate and repeat till convergence to obtain the ground state. We identify the MI-SF phase boundary based

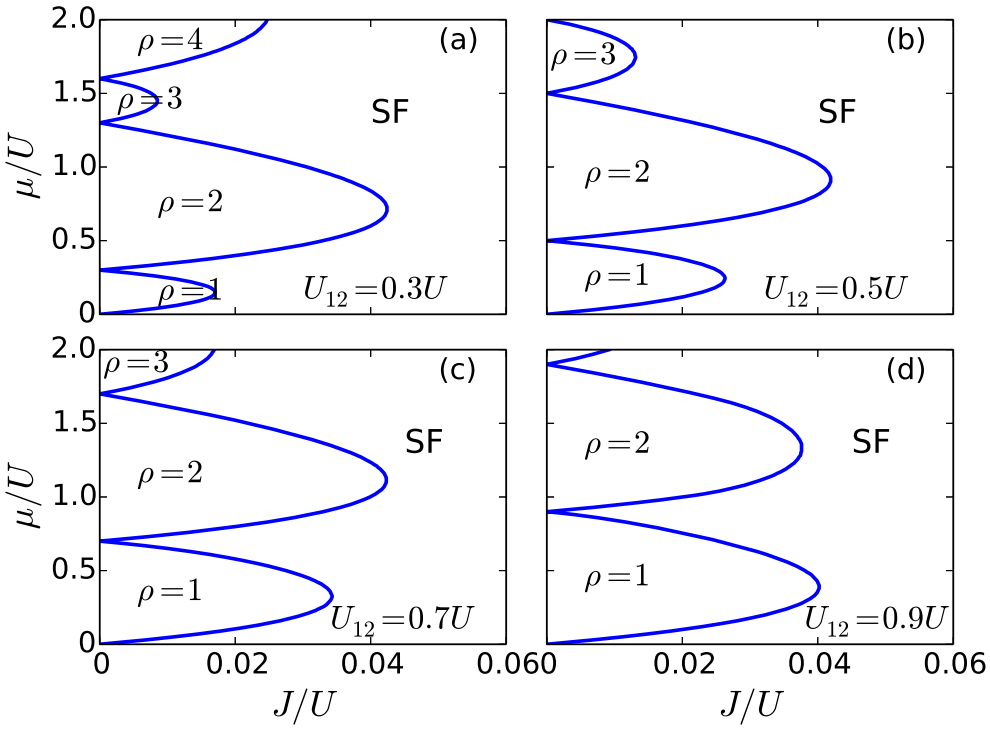

Figure 5.1: Phase diagram of TUGS by varying the inter-species interaction strength U_{12}. A half filling ($\rho^1 = \rho^2 = 0.5$, $\rho = 1$) MI lobe emerges with the introduction of interspecies interaction (U_{12}) for low value of μ. This lobe further enhances with the higher values of U_{12}. The similar behaviour is observed for the ($\rho^1 = \rho^2 = 1.5$, $\rho = 3$) MI lobe.

on the SF order parameter and the lattice occupancy at each site. For the MI phase, SF order parameter is zero with integer commensurate filling at each site. While for the SF phase occupancy is commensurate but real with non-zero SF order parameter. The phase diagrams of the BH Hamiltonian of TUGS in Eq. (5.3) for different values of U_{12} are shown in Fig. 5.1. For simplicity, we consider $J_x^1 = J_y^1 = J_x^2 = J_y^2 = J$, $\mu^1 = \mu^2 = \mu$ and $U_{11} = U_{22} = U$. These considerations may quantitatively modify the location of phase transition in the phase diagram, but do not alter the physics of interest in a qualitative way. We scale all the energies with U, and plot the phase diagram with respect to μ/U and J/U.

The phase diagrams consists of lobes of incompressible MI phase in which the average lattice occupancy $\rho = \rho^1 + \rho^2$ is integer at each site. In absence of interaction strength $U_{12} = 0$, the phase diagram of the two species is identical to the case of single

species. With the introduction of inter-species interaction, with $U_{12} = 0.3U$, the half filled lobe having $\rho^1 = \rho^2 = 0.5$, $\rho = 1$ for each species appears in the phase diagram for $\mu \approx 0.4U$. This is shown in Fig. 5.1(a). For the range of $0.4 \leq \mu \leq 1.4U$, we obtain the MI phase with $\rho^1 = \rho^2 = 1$, $\rho = 2$ for both the species, the location of the Mott lobe tip ($J \approx 0.042U$) is similar to that of the single species. On increasing μ further we obtain the MI lobe of $\rho^1 = \rho^2 = 1.5$, $\rho = 3$ for small range of μ. And MI lobe for $\rho^1 = \rho^2 = 2$, $\rho = 4$ is also obtained for large value of μ. The half-filled lobes arise due to the presence of two species and characteristics of TUGS in optical lattices. Next, when we increase the inter-species interaction energy to $U_{12} = 0.5U$. We observe that the MI lob of $\rho = 4$ is shifted beyond the range of μ and J considered. With the increase in U_{12} the MI lobes corresponding to half fillings $\rho = 1$ and $\rho = 3$ are increased as shown in Fig. 5.1 (b). As shown in Fig. 5.1 (c), we observe that these half-filled MI lobes are further enhanced for $U_{12} = 0.7U$. In the last subfigure Fig. 5.1 (d), we show that the MI lobe for $\rho = 3$ is shifted beyond the range of the μ and J considered for $U_{12} = 0.9U$.

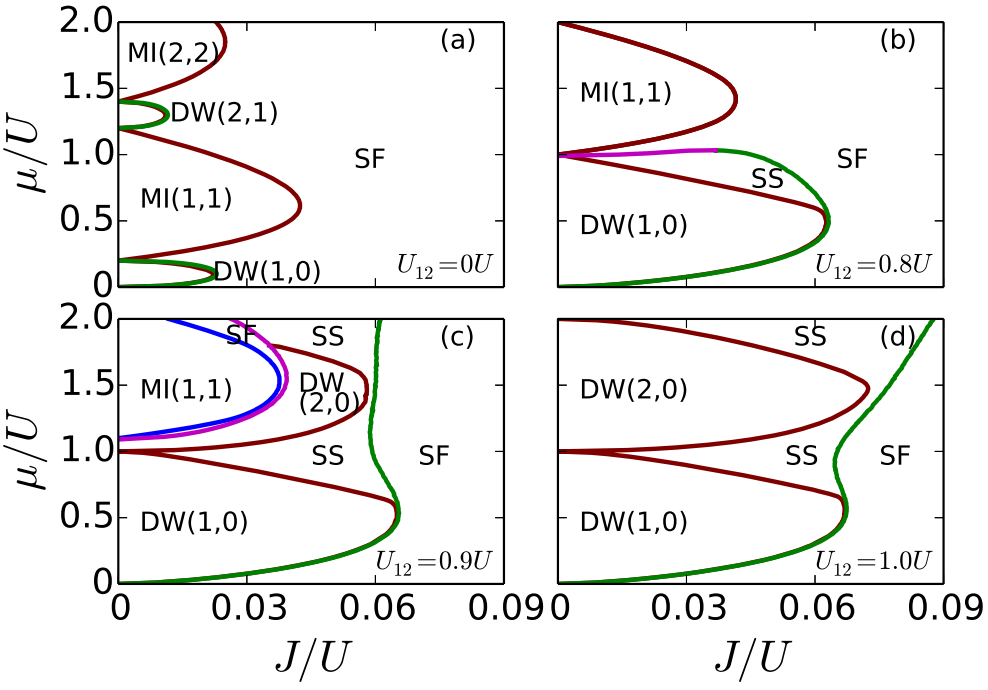

Figure 5.2: Phase diagram of extended BHM for TUGS at the different inter-species interaction strength U_{12} and for inter-species NN interaction $V_{12} = V_{21} = 0$, $V_1 = V_2 = 0.05U$. The MI(1,1) lobe transforms into the DW(2,0) by increasing the U_{12}.

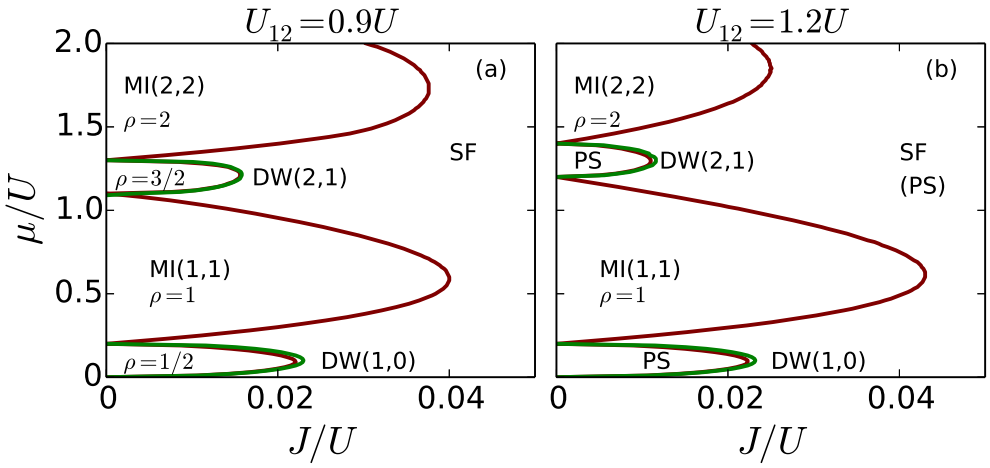

Figure 5.3: Phase diagram of extended BHM for TUGS at the different inter-species interaction strength U_{12} and for inter-species NN interaction $V_{12} = V_{21} = 0.05U$, $V_1 = V_2 = 0.05U$. Phase separated (PS) domain are shown in the DW and SF phases.

5.2.1 Phase diagram of TUGS extended BHM

We obtain the ground state solution of extended BHM in Eq. (5.21) by using Gutzwiller ansatz as described earlier. The extended BHM shows two more phases: DW and SS. To study effect of the NN interaction, we consider $V_{12} = V_{21} = 0$ and $V_1 = V_2 = 0.05U$. The phase diagram is, then, obtained by varying the inter species interaction strength U_{12}. Like in the BHM case, we consider $J_x^1 = J_y^1 = J_x^2 = J_y^2 = J$, $\mu^1 = \mu^2 = \mu$ and $U_{11} = U_{22} = U$. The phase diagram for extended BHM at $U_{12} = 0$ for TUGS is shown in Fig. 5.2 (a). As shown in the figure, we observe DW(1,0), MI(1,1), DW(2,1), SS (green line) and SF phases with the introduction of NN interaction V_k. In the phase diagram, the DW and MI phase lobes appear for both species. As to be expected, the SS phase appears near to the DW(1,0) and DW (2,1) lobes. It has been shown in earlier studies that the DW and SS lobes are enhanced with the stronger V_k and for $V_k \geq U$ only the checkerboard DW and SS phases exist for the single species [141].

For $U_{12} = 0$, as mentioned earlier, the two species phase diagram is reduced to that of the single species phase diagram. With finite inter-species interaction $U_{12} = 0.8U$, the corresponding phase diagram is as shown in Fig. 5.2 (b). The inter-species interaction effectively enhances the NN intra-species interaction V_k, therefore DW(1,0)

and SS lobes are enhanced in Fig. 5.2 (b), and at the same time the lobes are shifted to higher values of μ. On further increasing the inter-species interaction to $U_{12} = 0.9U$, DW(1,0) lobe is enhanced, and region of the SS phase is also increased. Another important feature is that the MI(1,1) phase is transformed into the DW(2,0) phase. The transformation from an incompressible MI phase to another incompressible phase DW passes through the compressible SF phase as an intermediate phase. The MI-SF-DW transition is discernible in the phase diagram in Fig. 5.2 (c). Here, we also observe that the area of the SS phase also increased. On increasing U_{12}, the DW lobe is enhanced, MI and SF lobe start to vanish and DW(2,0) lobe replaces these MI and SF phases. At $U_{12} = U$, within the range of the parameters considered, the MI phase vanishes, and we observe DW(1,0) and DW(2,0) lobes with enhanced SS regime. In short, there are two observable effects of increasing the inter-species interaction strength U_{12}: the DW and SS regimes are enhanced due to larger effective V_{kk}; and the MI-DW transition through SF phase is observed. The latter has not been observed in previous works.

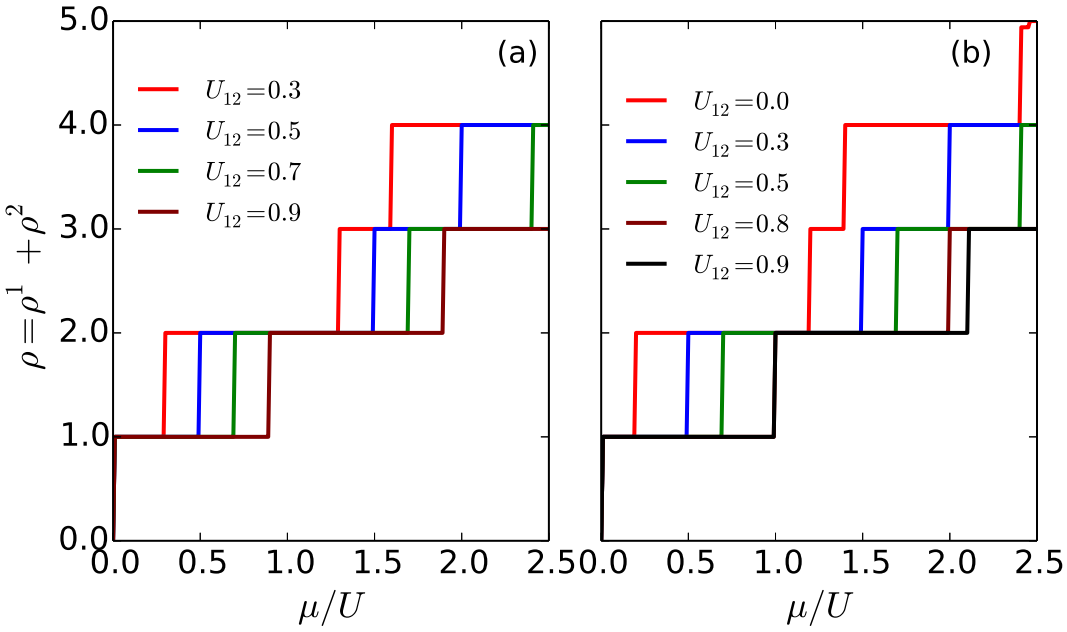

Figure 5.4: (a) Shifting of half filled ($\rho = 1, 3, ..$) MI lobes for BHM with inter-species interaction strength U_{12}/U. (b) Shifting of DW lobe ($\rho = 1, 3, ..$) with U_{12} in the case of eBHM for $V_{12} = 0$. Here in both cases, we have fixed $J/U = 0$.

To show the changes in the half filled MI lobes ($\rho = 1, 3, 5, \ldots$) of the BHM with increasing U_{12}, the value of ρ at $J/U = 0$ is plotted as a function of μ/U in Fig 5.4 (a).

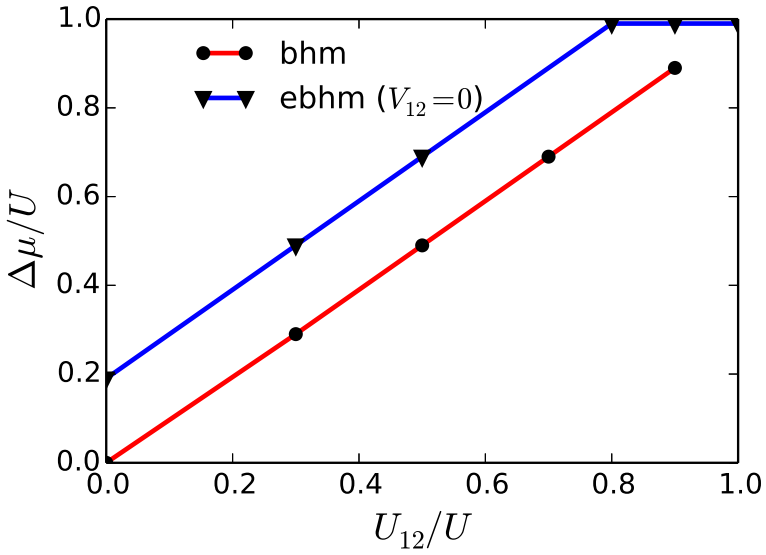

Figure 5.5: Plot for width of $\rho = 1$ in terms of μ/U for half filed MI lobe for BHM and DW lobe for eBHM with inter-species interaction strength U_{12}.

From the figure it is clear that the width of the half filled MI lobes increase but the MI lobes for both the species ($\rho = 2, 4, \ldots$) remain unchanged with increasing U_{12}. Similarly, in the case of eBHM too, as shown in Fig 5.4 (b), the width of the DW lobes ($\rho = 1, 3, 5, \ldots$) increase with the increase in U_{12}. And, the width of the MI lobes ($\rho = 2, 4, \ldots$) remain unchanged. The plots in the Fig 5.4 (b) correspond to $J/U = 0$ and $V_{12} = 0$. This implies that we consider intra-species long-range interactions but not for the inter-species interaction. For a better representation of the increase in the width of the MI lobes, as an example, the width of the $\rho = 1$ is plotted as a function of U_{12} in Fig 5.5 for both BHM and eBHM. The width for $\rho = 1$ vary linearly with interaction strength for BHM. There is key difference in the case of eBHM, initially the width vary linearly but after $U_{12} = 0.8$ the width remains unchanged.

5.3 Miscible and Immiscible phases

A feature unique to TUGS is the phenomenon of phase separation, which occurs when the inter-species interaction exceeds a critical value. This phenomenon, in general, is associated with several novel phenomena in nonlinear dynamics, pattern formation, and phase transitions in condensed matter systems, etc. In the case of TUGS, phase

separation in the weakly interacting regime or the SF regime is very well studied. However, it is yet to be explored in the strongly interacting regimes such as the DW and SS phases, and yet to achieve experimentally. Here, I discuss our results related to the phase-separated domain in the strongly interacting regime.

We observe like reported in previous works, phase separation in the SF phase with the BHM, but there is no phase separation in the MI phase. We find that to observe phase separation in the strongly interacting regime, we need to incorporate NN interactions. With NN interactions, we do get different geometries in the phase-separated regime. For this, we solve the Eq. (5.21) with finite long-range interactions. We first consider finite intra-species long-range interactions, but with no long-range inter-species interactions $V_{12} = 0$. In this case, we do not observe the phase separation. In the next step, we consider finite V_{12}. We, then, observe the phase separation. For our present study, we take $V_1 = V_2 = V_{12} = 0.05U$. With these values of long-range interaction, we have studied the phase diagram in the two regimes corresponding to the contact interactions: miscible phase $U_{12}^2 \ll U_{11}U_{22}$; and immiscible phase $U_{12}^2 \gg U_{11}U_{22}$. As mentioned earlier, the interactions considered are all repulsive $U, V > 0$, and this is essential to observe the phase separation in the system.

5.3.1 Miscible phase

In the miscible phase, we consider $U_{12} = 0.9U$ and the corresponding phase diagram in Fig. 5.3 (a). The phase diagram supports DW, SS and SF phases. The DW(1,0) lobe is defined with respect to the total site occupancy $n_{p,q}^1 + n_{p,q}^2$, such that $n_{p,q}^k$ are either zero or one. Most importantly, the distributions of the zero and one of $n_{p,q}^k$ is random, but the total $n_{p,q}^1 + n_{p,q}^2$ exhibit DW(1,0). This implies that the average number densities of the two species are $\rho^1 = \rho^2 = 1/4$ and thus the total number density is $\rho = \rho^1 + \rho^2 = 1/2$. The SS phase, which circumscribes the DW(1,0) lobe, is an intervening phase between the DW and SF phases. The SS phase is checkerboard in ρ as well as ϕ. In the SF phase ρ is homogeneous with finite ϕ, and species are in the miscible phase.

At higher values of μ Mott lobe $\rho = \rho^1 + \rho^2 = 1$ appears in the phase diagram. In this phase too, the site occupancy of each species $n_{p,q}^k$ are either zero or one, but the

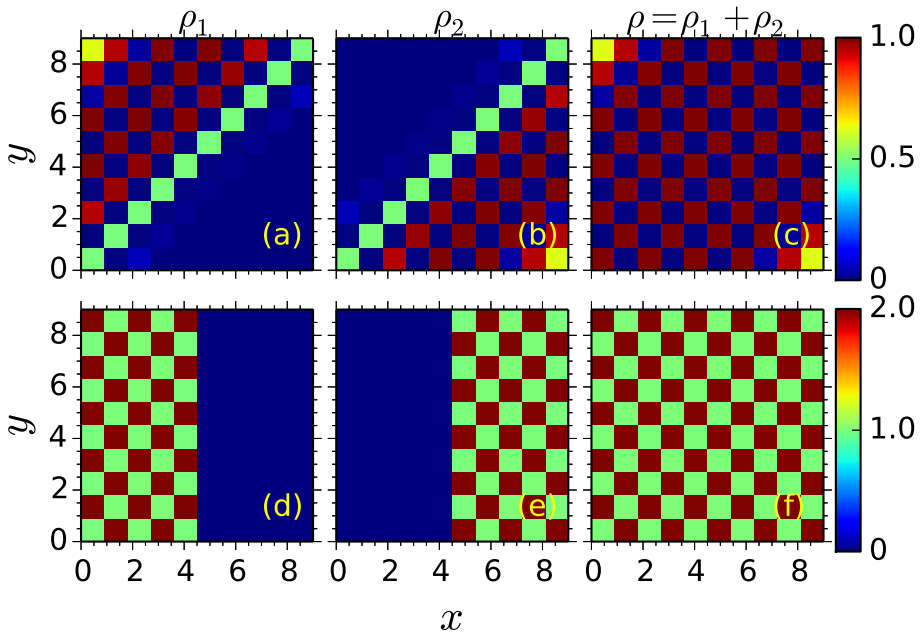

Figure 5.6: (a-c) Phase separation in the DW(1,0) phase without periodic boundary condition with diagonal pattern. (d-e) Phase separation in the DW(2,1) phase with periodic boundary condition with side by side pattern.

distribution of the values is random. However, the total site occupancy $n^1_{p,q} + n^2_{p,q}$ is one. On further increasing μ we get the DW(2,1) phase with $\rho = \rho^1 + \rho^2 = 3/2$, and like in the case of DW(1,0), SS phase circumscribes it. We, then, observe the MI(2,2) lobe with $\rho = \rho^1 + \rho^2 = 2$ at still higher μ. Here, it is to be emphasized that with $V_{12} \neq 0$, we define the lobes in terms of the total average density ρ. While we had use ρ^1 and ρ^2 to identify the phases for $V_{12} = 0$.

5.3.2 Immiscible phase

For the immiscible regime, we consider $U_{12} = 1.2U$, and the corresponding phase diagram is shown in Fig. 5.3 (b). The phase diagram is similar to the $V_{12} = 0$ case, but here it is identified with the total density ρ. The important feature of this phase diagram is that we obtain the phase separation near the DW-SS and SS-SF phase transitions. In the SF phase, we observe the phase separation in the entire domain. In the DW(1,0) lobe, we obtain the phase separation without periodic boundary condition, and we obtain the diagonally phase separation geometry as shown in Fig. 5.6 (a-c). In this

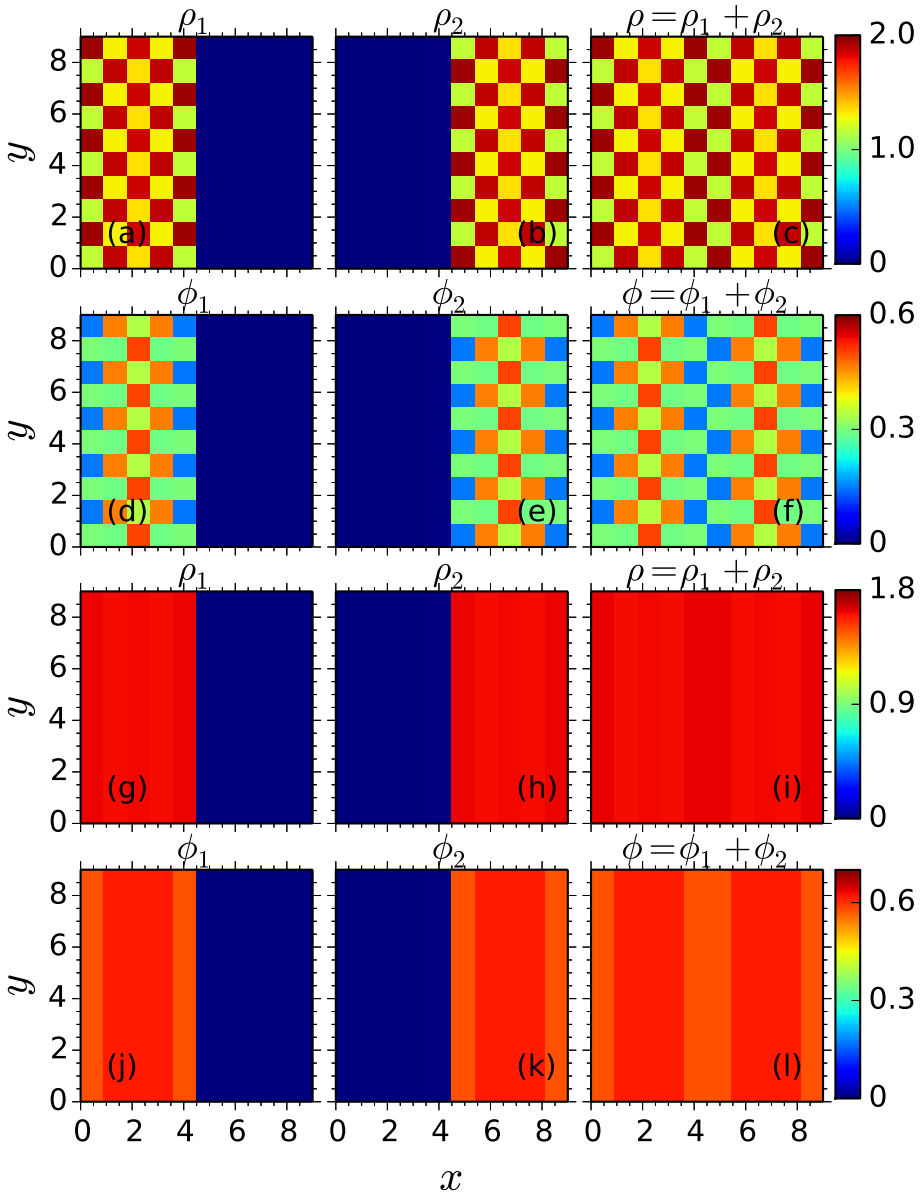

Figure 5.7: (a-f) Phase separation in the SS phase with periodic boundary condition with side by side pattern.(g-l) Phase separation in the SF phase with periodic boundary condition with side by side pattern.

regime, we do not observe the side by side phase separation. The DW(2,1) shows rich physics. We observe the side by side phase separation in the DW, SS and SF phases. Phase separation in DW(2,1) phase is shown in Fig. 5.6 (d-e), in SS phase Fig. 5.7 (a-f), and in SF phase Fig. 5.7 (g-l). We do not observe the phase separation in the MI phase.

5.4 Summary of the chapter

In this chapter, I describe the BH Hamiltonian for TUGS. I then, discuss the nearest neighbour intra and inter-species interaction in the BH Hamiltonian, which is known as eBHM for TUGS. We obtain the ground state solution with the Gutzwiller ansatz for both BHM and eBHM TUGS. For BHM, I show that the phase diagram has half-filled MI lobes in presence of inter-species interaction U_{12} of the system. The width of half-filled MI lobes increase linearly with U_{12}. While for eBHM we obtain the shifting in the DW lobe with increasing inter-species interaction strength. In the end, I provide the phase separation density profile for different phases such as DW, SS, and SF.

Chapter 6

Summary and future directions

Summary

In summary, I have studied bosonic Harper-Hofstadter model for 2D square lattice, for different values of synthetic magnetic field α and filling factor ν. I have used the SGMF, CGMF and ED methods to obtain the ground state solution of the system. We obtain the QH and competing SF states. We obtain QH states for $\alpha = 1/5$ with $\nu = n/2$ where $n = 1, 2, \ldots, 9$. The QH states are checker board in density for all νs except for $\nu = 5/2$, which is homogeneous. For $\alpha = 1/3$ with $\nu = n/3$ where $n = 1, 2, \ldots, 8$, all the QH states are checker board in nature. For $\alpha = 1/4$ with $\nu = n/2$ where $n = 1, 2, \ldots, 7$. All the states have checker board density, and are consistent with the previous RCMF results [68]. For $\alpha = 1/2$ with $\nu = 1/2, 1$ and $3/2$, the QH states for $\nu = 1/2$ and $3/2$ are Checker board but homogeneous for $\nu = 1$.

Based on our results with CGMF and ED, the $\alpha = 1/4$ with $\nu = 1/2, 1, 3/2$ and 2 are the QH states which occur as the ground state of the BHM with synthetic magnetic field, and these states exist within a narrow range of chemical potential μ. For other combinations of α and ν, the SF state is the ground state and the QH states exist as a metastable state. The experimental observation of a pure QH state needs tight control on the thermal excitations as the two competing states, QH and SF states, are nearly degenerate. The energy separation between these states is $\approx 10^{-2}$nK. Furthermore, the QH state is sensitive to the nature of the envelope potential of the optical lattice. The QH states exist for very shallow Gaussian envelope potentials but cease to exist

for harmonic oscillator potential. The case of a box potential is the most promising experimentally realizable envelope potential to observe a pure QH state of BHM with a synthetic magnetic field.

The two-point correlation function for the QH state is non-monotonic. It decays exponentially in the bulk and it has power law behaviour at the edges. These are signatures of the gaped bulk and gapless edges for QH state. We obtain all the QH states with the ED method and identify them based on the Penrose-Onsager criterion and von Neumann entropy. The Penrose-Onsager criterion provides the condensate fraction ($\rho_{\rm cf}$) for the ground states obtained from the ED method. The condensate fraction is less than one ($\rho_{\rm cf} < 1$) for QH state and for SF state ($\rho_{\rm cf} \approx 1$). The von Neumann entropy is a measure of entanglement of the state, and QH states have a higher von Neumann entropy than the SF states. This serves as an additional measure to distinguish the QH and SF states. We have studied the physics of two species BEC in the strongly interacting regime. After obtaining the phase diagram for BHM of TBEC, I have presented the results for extended BHM. For the extended BHM, we have obtained phase separation in the strongly correlated phases such as density wave and supersolid phases as well as in the superfluid phase. We do not obtain the phase separation in the MI phase.

For the studies reported in the thesis I have used SGMF, CGMF, and ED methods. The results of CGMF for MI-SF phase diagram approaches the QMC results with a large cluster size. That justifies the use of CGMF in our studies as QMC results are considered as the benchmark for the MI-SF phase diagram. However, to study the QH states, the CGMF and ED method are more appropriate as QMC based methods suffer sign problems. The other method to study the QH states is DMRG but it is applicable in one dimensional systems. The other method which is appropriate for studying strongly correlated systems in the Tensor Networks (TN). It provides more reliable results as the correlations between lattice sites are represented in vector form. In our future works, we have plans of using the TN method.

Future directions

We have studied ultracold bosonic atoms with onsite (short-range) interaction in the BHM. In the future, we plan to study the effect of long-range interaction with single and two-species BECs in optical lattices. For these systems two more phases density wave (DW) and supersolid (SS), apart from the Mott insulator (MI) and superfluid (SF) phase emerge. The long-range dipole-dipole interaction decays as the inverse cubic power of the distance, and have emerged as promising systems to examine magnetic ordering. The dipolar interaction is characterized by the long-range and anisotropic properties, in which the dipole forces modify the ground state and collective excitations of the system. Due to the interplay of short-range and long-range interactions, interesting phenomena such as the ferromagnetic order and spin waves emerge in the dipolar system. We shall use the SGMF and CGMF methods to study the BHM with long-range interaction and plan to study the different phases for single species BEC. Then, depending on the orientation of the dipole, we shall study the quantum phases. The physics of TBEC, which I describe in this thesis have been carried out for some of the specific values of interspecies interaction. In the near future, we shall study the phase diagram with the variation of the interspecies nearest neighbour interaction. The most important issue is the stabilization of the SS phase in these systems, that I shall try to address in our future works.

Another promising direction of study is the real-time dynamics of BHM with and without the synthetic magnetic field. The real-time dynamics will be carried out with all possible interactions. The study of QH states in the TBEC is our other interest. In this thesis, I have used von Neumann entropy as a measure of correlation for the QH states. But, a more accurate measure of correlation for topological states like the QH states is the topological entanglement γ [222, 223]. The computation of topological entanglement, however, requires partitioning the system and then, computing the von Neumann entropy of the sub-systems. Such computations of γ have been done for QH states using tensor networks [185]. But, with the ED method, the system partition involves Singular Value Decomposition of large matrix and this is numerically challenging for larger system sizes. In the near future our plan is to calculate γ for the QH states I have discussed in this thesis.

Appendix A

Matrix Elements And Numerical Details

The expression of cluster Hamiltonians in terms of cluster sites are

$$\begin{aligned}
\hat{h}_{2i,2j} &= -\left(J_x\hat{b}^{\dagger}_{2i+1,2j}\hat{b}_{2i,2j}+\mathrm{H.c}\right)-\left(J_y\hat{b}^{\dagger}_{2i,2j+1}\hat{b}_{2i,2j}+\mathrm{H.c}\right)\\
&\quad-\left[J_x\left(\hat{b}^{\dagger}_{2i,2j}\phi_{2i-1,2j}-\phi^{*}_{2i,2j}\phi_{2i-1,2j}\right)+\mathrm{H.c}\right]\\
&\quad-\left[J_y\left(\hat{b}^{\dagger}_{2i,2j}\phi_{2i,2j-1}-\phi^{*}_{2i,2j}\phi_{2i,2j-1}\right)+\mathrm{H.c}\right]\\
&\quad+\frac{U}{2}\hat{n}_{2i,2j}(\hat{n}_{2i,2j}-1)-\tilde{\mu}\hat{n}_{2i,2j}, \qquad \text{(A.1)}\\
\hat{h}_{2i+1,2j} &= -\left(J_y\hat{b}^{\dagger}_{2i+1,2j+1}\hat{b}_{2i+1,2j}+\mathrm{H.c}\right)\\
&\quad-\left[J_x\left(\phi^{*}_{2i+2,2j}\hat{b}_{2i+1,2j}-\phi^{*}_{2i+2,2j}\phi_{2i+1,2j}\right)+\mathrm{H.c}\right]\\
&\quad-\left[J_y\left(\hat{b}^{\dagger}_{2i+1,2j}\phi_{2i+1,2j-1}-\phi^{*}_{2i+1,2j}\phi_{2i+1,2j-1}\right)+\mathrm{H.c}\right]\\
&\quad+\frac{U}{2}\hat{n}_{2i+1,2j}(\hat{n}_{2i+1,2j}-1)-\tilde{\mu}\hat{n}_{2i+1,2j}, \qquad \text{(A.2)}\\
\hat{h}_{2i,2j+1} &= -\left(J_x\hat{b}^{\dagger}_{2i+1,2j+1}\hat{b}_{2i,2j+1}+\mathrm{H.c}\right)\\
&\quad-\left[J_x\left(\hat{b}^{\dagger}_{2i,2j+1}\phi_{2i-1,2j+1}-\phi^{*}_{2i,2j+1}\phi_{2i-1,2j+1}\right)+\mathrm{H.c}\right]\\
&\quad-\left[J_y\left(\phi^{*}_{2i,2j+2}\hat{b}_{2i,2j+1}-\phi^{*}_{2i,2j+2}\phi_{2i,2j+1}\right)+\mathrm{H.c}\right]\\
&\quad+\frac{U}{2}\hat{n}_{2i,2j+1}(\hat{n}_{2i,2j+1}-1)-\tilde{\mu}\hat{n}_{2i,2j+1}, \qquad \text{(A.3)}\\
\hat{h}_{2i+1,2j+1} &= -\left[J_x\left(\phi^{*}_{2i+2,2j+1}\hat{b}_{2i+1,2j+1}-\phi^{*}_{2i+2,2j+1}\phi_{2i+1,2j+1}\right)+\mathrm{H.c}\right]\\
&\quad-\left[J_y\left(\phi^{*}_{2i+1,2j+2}\hat{b}_{2i+1,2j+1}-\phi^{*}_{2i+1,2j+2}\phi_{2i+1,2j+1}\right)+\mathrm{H.c}\right]\\
&\quad+\frac{U}{2}\hat{n}_{2i+1,2j+1}(\hat{n}_{2i+1,2j+1}-1)-\tilde{\mu}\hat{n}_{2i+1,2j+1}. \qquad \text{(A.4)}
\end{aligned}$$

Let us consider only one cluster ($i = j = 0$) and find the matrix elements. For this single cluster $n_0 = (0,0)$, $n_1 = (1,0)$, $n_2 = (0,1)$, $n_3 = (1,1)$. Here, we are working in the Fock basis such that $n_0, .., n_3$ runs from $0, 1, .., N_b - 1$ and the bra (K) and ket (L) state for the matrix elements in term of $m(n)$ can be written as

$$\begin{aligned} K &= m_3 N_b^3 + m_2 N_b^2 + m_1 N_b + m_0 \\ L &= n_3 N_b^3 + n_2 N_b^2 + n_1 N_b + n_0. \end{aligned}$$

Now, for H_x^{intra} term with $i = j = k = 0$, the matrix element is

$$\begin{aligned} H_x^{\text{intra}} &= -J_x \left\langle m_0, .., m_3 \right| \hat{b}_{1,0}^\dagger \hat{b}_{0,0} \left| n_0, .., n_3 \right\rangle, \\ &= -J_x \sqrt{m_1}\sqrt{n_0}\delta_{m_0,n_0-1}\delta_{m_1-1,n_1}\delta_{m_2,n_2}\delta_{m_3,n_3} \\ &= -J_x \sqrt{m_1}\sqrt{m_0+1}, \end{aligned} \tag{A.5}$$

where the locations for the matrix element are

$$\begin{aligned} K &= m_3 N_b^3 + m_2 N_b^2 + m_1 N_b + m_0 \\ L &= m_3 N_b^3 + m_2 N_b^2 + (m_1 - 1) N_b + (m_0 + 1). \end{aligned} \tag{A.6}$$

We calculate the matrix elements for a single 2×2 cluster in terms of the single site Fock basis m_0, m_1, m_2, m_3. In compact form, for a single cluster thirteen elements are

$$\begin{aligned} H_x^{\text{intra}}(K,L) &= -J_x \left\langle m_0, .., m_3 \right| \hat{b}_{2i+1,2j+k}^\dagger \hat{b}_{2i,2j+k} \left| n_0, .., n_3 \right\rangle, \\ H_x^{\text{intra}}(K,L) &= \begin{cases} -J_x \sqrt{m_1}\sqrt{m_0+1} & \text{for } k = 0 \\ -J_x \sqrt{m_3}\sqrt{m_2+1} & \text{for } k = 1 \end{cases} \end{aligned}$$

where K is the row location as $K = m_3 N_b^3 + m_2 N_b^2 + m_1 N_b + m_0$ for the matrix and L is the column location as

$$L = \begin{cases} m_3 N_b^3 + m_2 N_b^2 + (m_1 - 1) N_b + (m_0 + 1) & \text{for } k = 0 \\ (m_3 - 1) N_b^3 + (m_2 + 1) N_b^2 + m_1 N_b + m_0 & \text{for } k = 1 \end{cases}$$

Here, we fix the bra state such as K and calculate the corresponding ket state L for all the matrix elements in terms of Fock basis. The matrix element $H_x^{*\text{intra}}$ is

$$H_x^{*\text{intra}}(K,L) = \begin{cases} -J_x^* \sqrt{m_0}\sqrt{m_1+1} & \text{for } k = 0 \\ -J_x^* \sqrt{m_2}\sqrt{m_3+1} & \text{for } k = 1 \end{cases}$$

with

$$L = \begin{cases} m_3 N_b^3 + m_2 N_b^2 + (m_1+1) N_b + (m_0 - 1) & \text{for } k = 0 \\ (m_3+1) N_b^3 + (m_2 - 1) N_b^2 + m_1 N_b + m_0 & \text{for } k = 1 \end{cases}$$

The matrix element H_y^{intra} is

$$H_y^{\text{intra}}(K,L) \;\; = \;\; \begin{cases} -J_y \sqrt{m_2}\sqrt{m_0+1} & \text{for } k = 0 \\ -J_y \sqrt{m_3}\sqrt{m_1+1} & \text{for } k = 1 \end{cases}$$

with location

$$L = \begin{cases} m_3 N_b^3 + (m_2 - 1) N_b^2 + m_1 N_b + (m_0 + 1) & \text{for } k = 0 \\ (m_3 - 1) N_b^3 + m_2 N_b^2 + (m_1+1) N_b + m_0 & \text{for } k = 1 \end{cases}$$

The matrix element $H_y^{*\text{intra}}$ is

$$H_y^{*\text{intra}}(K,L) \;\; = \;\; \begin{cases} -J_y^* \sqrt{m_0}\sqrt{m_2+1} & \text{for } k = 0 \\ -J_y^* \sqrt{m_1}\sqrt{m_3+1} & \text{for } k = 1 \end{cases}$$

with location

$$L = \begin{cases} m_3 N_b^3 + (m_2 + 1) N_b^2 + m_1 N_b + (m_0 - 1) & \text{for } k = 0 \\ (m_3+1) N_b^3 + m_2 N_b^2 + (m_1 - 1) N_b + m_0 & \text{for } k = 1 \end{cases}$$

The matrix element H_x^{in} is

$$H_x^{\text{in}}(K,L) \;\; = \;\; \begin{cases} -J_x \sqrt{m_0}\phi_{2i-1,2j} & \text{for } k = 0 \\ -J_x \sqrt{m_2}\phi_{2i-1,2j+1} & \text{for } k = 1 \end{cases}$$

with location

$$L = \begin{cases} m_3 N_b^3 + m_2 N_b^2 + m_1 N_b + (m_0 - 1) & \text{for } k = 0 \\ m_3 N_b^3 + (m_2 - 1) N_b^2 + m_1 N_b + m_0 & \text{for } k = 1 \end{cases}$$

The matrix element $H_x^{*\text{in}}$ is

$$H_x^{*\text{in}}(K,L) \;\; = \;\; \begin{cases} -J_x^* \sqrt{m_0+1}\phi^*_{2i-1,2j} & \text{for } k = 0 \\ -J_x^* \sqrt{m_2+1}\phi^*_{2i-1,2j+1} & \text{for } k = 1 \end{cases}$$

with location

$$L = \begin{cases} m_3 N_b^3 + m_2 N_b^2 + m_1 N_b + (m_0 + 1) & \text{for } k = 0 \\ m_3 N_b^3 + (m_2 + 1) N_b^2 + m_1 N_b + m_0 & \text{for } k = 1 \end{cases}$$

The matrix element H_y^{in} is

$$H_y^{\text{in}}(K, L) \;=\; \begin{cases} -J_y \sqrt{m_0}\, \phi_{2i,2j-1} & \text{for } k = 0 \\ -J_y \sqrt{m_1}\, \phi_{2i+1,2j-1} & \text{for } k = 1 \end{cases}$$

with location

$$L = \begin{cases} m_3 N_b^3 + m_2 N_b^2 + m_1 N_b + (m_0 - 1) & \text{for } k = 0 \\ m_3 N_b^3 + m_2 N_b^2 + (m_1 - 1) N_b + m_0 & \text{for } k = 1 \end{cases}$$

The matrix element $H_y^{*\text{in}}$ is

$$H_y^{*\text{in}}(K, L) \;=\; \begin{cases} -J_y^* \sqrt{m_0 + 1}\, \phi^*_{2i,2j-1} & \text{for } k = 0 \\ -J_y^* \sqrt{m_1 + 1}\, \phi^*_{2i+1,2j-1} & \text{for } k = 1 \end{cases}$$

with location

$$L = \begin{cases} m_3 N_b^3 + m_2 N_b^2 + m_1 N_b + (m_0 + 1) & \text{for } k = 0 \\ m_3 N_b^3 + m_2 N_b^2 + (m_1 + 1) N_b + m_0 & \text{for } k = 1 \end{cases}$$

The matrix element H_x^{out} is

$$H_x^{\text{out}}(K, L) \;=\; \begin{cases} -J_x \sqrt{m_1 + 1}\, \phi^*_{2i+2,2j} & \text{for } k = 0 \\ -J_x \sqrt{m_3 + 1}\, \phi^*_{2i+2,2j+1} & \text{for } k = 1 \end{cases}$$

with location

$$L = \begin{cases} m_3 N_b^3 + m_2 N_b^2 + (m_1 + 1) N_b + m_0 & \text{for } k = 0 \\ (m_3 + 1) N_b^3 + m_2 N_b^2 + m_1 N_b + m_0 & \text{for } k = 1 \end{cases}$$

The matrix element $H_x^{*\text{out}}$ is

$$H_x^{*\text{out}}(K, L) \;=\; \begin{cases} -J_x^* \sqrt{m_1}\, \phi_{2i+2,2j} & \text{for } k = 0 \\ -J_x^* \sqrt{m_3}\, \phi_{2i+2,2j+1} & \text{for } k = 1 \end{cases}$$

with location

$$L = \begin{cases} m_3 N_b^3 + m_2 N_b^2 + (m_1 - 1) N_b + m_0 & \text{for } k = 0 \\ (m_3 - 1) N_b^3 + m_2 N_b^2 + m_1 N_b + m_0 & \text{for } k = 1 \end{cases}$$

The matrix element H_y^{out} is

$$H_y^{\text{out}}(K, L) \;=\; \begin{cases} -J_y \sqrt{m_2 + 1}\, \phi^*_{2i,2j+2} & \text{for } k = 0 \\ -J_y \sqrt{m_3 + 1}\, \phi^*_{2i+1,2j+2} & \text{for } k = 1 \end{cases}$$

with location

$$L = \begin{cases} m_3 N_b^3 + (m_2 + 1) N_b^2 + m_1 N_b + m_0 & \text{for } k = 0 \\ (m_3 + 1) N_b^3 + m_2 N_b^2 + m_1 N_b + m_0 & \text{for } k = 1 \end{cases}$$

The matrix element $H_y^{*\text{out}}$ is

$$H_y^{*\text{out}}(K, L) \;=\; \begin{cases} -J_y^* \sqrt{m_2}\, \phi_{2i,2j+2} & \text{for } k = 0 \\ -J_y^* \sqrt{m_3}\, \phi_{2i+1,2j+2} & \text{for } k = 1 \end{cases}$$

with location

$$L = \begin{cases} m_3 N_b^3 + (m_2 - 1) N_b^2 + m_1 N_b + m_0 & \text{for } k = 0 \\ (m_3 + 1) N_b^3 + m_2 N_b^2 + m_1 N_b + m_0 & \text{for } k = 1 \end{cases}$$

Diagonal element is

$$\begin{aligned} H^{\text{diag}} \;=\; & \sum\nolimits_{k,l} \big(J_x \phi^*_{2i,2j+k} \phi_{2i-1,2j+k} + \text{H.c.} + J_x \phi^*_{2i+2,2j+k} \phi_{2i+1,2j+k} + \text{H.c.} \\ & + J_y \phi^*_{2i+l,2j} \phi_{2i+l,2j-1} + \text{H.c.} + J_y \phi^*_{2i+l,2j+2} \phi_{2i+l,2j+1} + \text{H.c.} \big) \\ & + \frac{U}{2} \hat{n}_{2i+k,2j+l} \left(\hat{n}_{2i+k,2j+l} - 1 \right) - \tilde{\mu} \hat{n}_{2i+k,2j+l} \end{aligned}$$

with location $L = m_3 N_b^3 + m_2 N_b^2 + m_1 N_b + m_0$.

For the numerical computation, we take the initial value of SF order parameter to calculate the matrix elements. After that we diagonalize the Hamiltonian and obtain the lowest eigenvector which is the new cluster wave-function for the next iteration. With this new wave-function, we calculate the SF order parameter ϕ at each lattice site in the cluster as

$$\phi_{0,0} \;=\; \sum_{m_0,..,m_3} \sum_{n_0,..,n_3} C^{*(0,0)}_{m_0,..,m_3} C^{(0,0)}_{n_0,..,n_3} \left\langle m_0, .., m_3 \right| \hat{b}_{0,0} \left| n_0, .., n_3 \right\rangle$$

$$\phi_{0,0} = \sum_{m_0,..,m_3} \sum_{n_0,..,n_3} C^{*(0,0)}_{m_0,..,m_3} C^{(0,0)}_{n_0,..,n_3} \sqrt{n_0} \delta_{m_0,n_0-1} \delta_{m_1,n_1} \delta_{m_2,n_2} \delta_{m_3,n_3}$$
$$\phi_{0,0} = \sum_{m_0,..,m_3} \sqrt{m_0+1} C^{*(0,0)}_{m_0,m_1,m_2,m_3} C^{(0,0)}_{m_0+1,m_1,m_2,m_3}.$$

And similarly

$$\phi_{1,0} = \sum_{m_0,..,m_3} \sqrt{m_1+1} C^{*(0,0)}_{m_0,m_1,m_2,m_3} C^{(0,0)}_{m_0,m_1+1,m_2,m_3}$$
$$\phi_{0,1} = \sum_{m_0,..,m_3} \sqrt{m_2+1} C^{*(0,0)}_{m_0,m_1,m_2,m_3} C^{(0,0)}_{m_0,m_1,m_2+1,m_3}$$
$$\phi_{1,1} = \sum_{m_0,..,m_1} \sqrt{m_3+1} C^{*(0,0)}_{m_0,m_1,m_2,m_3} C^{(0,0)}_{m_0,m_1,m_2,m_3+1},$$

and use these ϕ in the next iteration and repeat the process till the convergence in the ϕ is order of 10^{-6} in the successive two iteration. We also calculate lattice occupancy at each lattice sites within the cluster as

$$\rho_{0,0} = \sum_{m_0,..,m_3} m_0 |C^{(0,0)}_{m_0,m_1,m_2,m_3}|^2, \ \rho_{1,0} = \sum_{m_0,..,m_3} m_1 |C^{(0,0)}_{m_0,m_1,m_2,m_3}|^2$$
$$\rho_{0,1} = \sum_{m_0,..,m_3} m_2 |C^{(0,0)}_{m_0,m_1,m_2,m_3}|^2, \ \rho_{1,1} = \sum_{m_0,..,m_3} m_3 |C^{(0,0)}_{m_0,m_1,m_2,m_3}|^2$$

Bibliography

[1] B. Capogrosso-Sansone, S. G. Söyler, N. Prokof'ev, and B. Svistunov, *Monte carlo study of the two-dimensional Bose-Hubbard model,* Phys. Rev. A **77**, 015602 (2008).

[2] K. v. Klitzing, G. Dorda, and M. Pepper, *New method for high-accuracy determination of the fine-structure constant based on quantized Hall resistance,* Phys. Rev. Lett. **45**, 494–497 (1980).

[3] D. C. Tsui, H. L. Stormer, and A. C. Gossard, *Two-dimensional magnetotransport in the extreme quantum limit,* Phys. Rev. Lett. **48**, 1559 (1982).

[4] R. B. Laughlin, *Anomalous Quantum Hall effect: An incompressible quantum fluid with fractionally charged excitations,* Phys. Rev. Lett. **50**, 1395 (1983).

[5] R. Willett, J. P. Eisenstein, H. L. Störmer, D. C. Tsui, A. C. Gossard, and J. H. English, *Observation of an even-denominator quantum number in the fractional Quantum Hall effect,* Phys. Rev. Lett. **59**, 1776–1779 (1987).

[6] J. K. Jain, *Composite-fermion approach for the fractional Quantum Hall effect,* Phys. Rev. Lett. **63**, 199–202 (1989).

[7] K. von Klitzing, *The quantized Hall effect,* Rev. Mod. Phys. **58**, 519–531 (1986).

[8] D. R. Yennie, *Integral Quantum Hall effect for nonspecialists,* Rev. Mod. Phys. **59**, 781–824 (1987).

[9] H. L. Stormer, D. C. Tsui, and A. C. Gossard, *The fractional Quantum Hall effect,* Rev. Mod. Phys. **71**, S298–S305 (1999).

[10] H. L. Stormer, *Nobel lecture: The fractional Quantum Hall effect,* Rev. Mod. Phys. **71**, 875–889 (1999).

[11] M. König, H. Buhmann, L. W. Molenkamp, T. Hughes, C.-X. Liu, X.-L. Qi, and S.-C. Zhang, *The Quantum Spin Hall effect: Theory and experiment,* J. Phys. Soc. Japan **77**, 031007 (2008).

[12] N. Goldman, G. Juzeliūnas, P. Öhberg, and I. B. Spielman, *Light-induced gauge fields for ultracold atoms,* Rep. Prog. Phys. **77**, 126401 (2014).

[13] G. Juzeliūnas and P. Öhberg, *Slow light in degenerate fermi gases,* Phys. Rev. Lett. **93**, 033602 (2004).

[14] S.-L. Zhu, H. Fu, C.-J. Wu, S.-C. Zhang, and L.-M. Duan, *Spin Hall effects for cold atoms in a light-induced gauge potential,* Phys. Rev. Lett. **97**, 240401 (2006).

[15] I. B. Spielman, *Raman processes and effective gauge potentials,* Phys. Rev. A **79**, 063613 (2009).

[16] K. Jim´enez-Garc´ıa, *Artificial Gauge Fields for Ultracold Neutral Atoms,* Ph.D. thesis, National Institute of Standards and Technology, and the University of Maryland Gaithersburg, Maryland (2012).

[17] M. H. Anderson, J. R. Ensher, M. R. Matthews, C. E. Wieman, and E. A. Cornell, *Observation of Bose-Einstein condensation in a dilute atomic vapor,* Science **269**, 198–201 (1995).

[18] K. B. Davis, M. O. Mewes, M. R. Andrews, N. J. van Druten, D. S. Durfee, D. M. Kurn, and W. Ketterle, *Bose-Einstein condensation in a gas of sodium atoms,* Phys. Rev. Lett. **75**, 3969–3973 (1995).

[19] C. C. Bradley, C. A. Sackett, J. J. Tollett, and R. G. Hulet, *Evidence of Bose-Einstein condensation in an atomic gas with attractive interactions,* Phys. Rev. Lett. **75**, 1687–1690 (1995).

[20] B. P. Anderson and M. A. Kasevich, *Macroscopic quantum interference from atomic tunnel arrays,* Science **282**, 1686 (1998).

[21] M. Kozuma, L. Deng, E. W. Hagley, J. Wen, R. Lutwak, K. Helmerson, S. L. Rolston, and W. D. Phillips, *Coherent splitting of Bose-Einstein condensed atoms with optically induced Bragg diffraction,* Phys. Rev. Lett. **82**, 871 (1999).

[22] J. Stenger, S. Inouye, A. P. Chikkatur, D. M. Stamper-Kurn, D. E. Pritchard, and W. Ketterle, *Bragg spectroscopy of a Bose-Einstein condensate,* Phys. Rev. Lett. **82**, 4569 (1999).

[23] Y. B. Ovchinnikov, J. H. Müller, M. R. Doery, E. J. D. Vredenbregt, K. Helmerson, S. L. Rolston, and W. D. Phillips, *Diffraction of a released Bose-Einstein condensate by a pulsed standing light wave,* Phys. Rev. Lett. **83**, 284 (1999).

[24] E. W. Hagley, L. Deng, M. Kozuma, M. Trippenbach, Y. B. Band, M. Edwards, M. Doery, P. S. Julienne, K. Helmerson, S. L. Rolston, and W. D. Phillips, *Measurement of the coherence of a Bose-Einstein condensate,* Phys. Rev. Lett. **83**, 3112 (1999).

[25] M. Greiner, I. Bloch, O. Mandel, T. W. Hänsch, and T. Esslinger, *Exploring phase coherence in a 2D lattice of Bose-Einstein condensates,* Phys. Rev. Lett. **87**, 160405 (2001).

[26] M. Greiner, O. Mandel, T. Esslinger, T. W. Hänsch, and I. Bloch, *Quantum phase transition from a superfluid to a Mott insulator in a gas of ultracold atoms,* Nature (London) **415**, 39 (2002).

[27] M. Lewenstein, A. Sanpera, V. Ahufinger, B. Damski, A. Sen(De), and U. Sen, *Ultracold atomic gases in optical lattices: mimicking condensed matter physics and beyond,* Adv. Phys. **56**, 243 (2007).

[28] O. Morsch and M. Oberthaler, *Dynamics of Bose-Einstein condensates in optical lattices,* Rev. Mod. Phys. **78**, 179 (2006).

[29] I. Bloch, J. Dalibard, and W. Zwerger, *Many-body physics with ultracold gases,* Rev. Mod. Phys. **80**, 885 (2008).

[30] E. J. Yarmchuk, M. J. V. Gordon, and R. E. Packard, *Observation of stationary vortex arrays in rotating superfluid helium,* Phys. Rev. Lett. **43**, 214–217 (1979).

[31] K. W. Madison, F. Chevy, W. Wohlleben, and J. Dalibard, *Vortex formation in a stirred Bose-Einstein condensate,* Phys. Rev. Lett. **84**, 806–809 (2000).

[32] J. R. Abo-Shaeer, C. Raman, J. M. Vogels, and W. Ketterle, *Observation of vortex lattices in Bose-Einstein condensates,* Science **292**, 476–479 (2001).

[33] P. C. Haljan, I. Coddington, P. Engels, and E. A. Cornell, *Driving Bose-Einstein-condensate vorticity with a rotating normal cloud,* Phys. Rev. Lett. **87**, 210403 (2001).

[34] T. Isoshima, M. Nakahara, T. Ohmi, and K. Machida, *Creation of a persistent current and vortex in a Bose-Einstein condensate of alkali-metal atoms,* Phys. Rev. A **61**, 063610 (2000).

[35] A. E. Leanhardt, A. Görlitz, A. P. Chikkatur, D. Kielpinski, Y. Shin, D. E. Pritchard, and W. Ketterle, *Imprinting vortices in a Bose-Einstein condensate using topological phases,* Phys. Rev. Lett. **89**, 190403 (2002).

[36] J. E. Williams and M. J. Holland, *Preparing topological states of a Bose-Einstein condensate,* Nature **401**, 568–572 (1999).

[37] M. R. Matthews, B. P. Anderson, P. C. Haljan, D. S. Hall, C. E. Wieman, and E. A. Cornell, *Vortices in a Bose-Einstein condensate,* Phys. Rev. Lett. **83**, 2498–2501 (1999).

[38] N. K. Wilkin and J. M. F. Gunn, *Condensation of "composite bosons" in a rotating bec,* Phys. Rev. Lett. **84**, 6–9 (2000).

[39] B. Paredes, P. Fedichev, J. I. Cirac, and P. Zoller, $\frac{1}{2}$*-anyons in small atomic Bose-Einstein condensates,* Phys. Rev. Lett. **87**, 010402 (2001).

[40] J. Hubbard, *Electron correlations in narrow energy bands,* Proc. Royal Soc. A **276**, 238 (1963).

[41] D. Jaksch, C. Bruder, J. I. Cirac, C. W. Gardiner, and P. Zoller, *Cold bosonic atoms in optical lattices,* Phys. Rev. Lett. **81**, 3108 (1998).

[42] M. P. A. Fisher, P. B. Weichman, G. Grinstein, and D. S. Fisher, *Boson localization and the superfluid-insulator transition,* Phys. Rev. B **40**, 546 (1989).

[43] Z. F. Ezawa, *Quantum Hall Effects: Recent Theoretical and Experimental Developments* (World Scientific, Singapore, 2013), 3rd ed.

[44] X.-G. Wen, *Theory of the edge states in fractional Quantum Hall effects,* Int. J. Mod. Phys. B **06**, 1711 (1992).

[45] G. Murthy and R. Shankar, *Hamiltonian theories of the fractional Quantum Hall effect,* Rev. Mod. Phys. **75**, 1101 (2003).

[46] T. H. Hansson, M. Hermanns, S. H. Simon, and S. F. Viefers, *Quantum Hall physics: Hierarchies and conformal field theory techniques,* Rev. Mod. Phys. **89**, 025005 (2017).

[47] R. N. Palmer and D. Jaksch, *High-field fractional Quantum Hall effect in optical lattices,* Phys. Rev. Lett. **96**, 180407 (2006).

[48] A. S. Sørensen, E. Demler, and M. D. Lukin, *Fractional Quantum Hall states of atoms in optical lattices,* Phys. Rev. Lett. **94**, 086803 (2005).

[49] Y.-J. Lin, R. L. Compton, A. R. Perry, W. D. Phillips, J. V. Porto, and I. B. Spielman, *Bose-Einstein condensate in a uniform light-induced vector potential,* Phys. Rev. Lett. **102**, 130401 (2009).

[50] Y.-J. Lin, R. L. Compton, K. Jimenez-Garcia, J. V. Porto, and I. B. Spielman, *Synthetic magnetic fields for ultracold neutral atoms,* Nature (London) **462**, 628 (2009).

[51] J. Dalibard, F. Gerbier, G. Juzeliūnas, and P. Öhberg, *Colloquium: Artificial gauge potentials for neutral atoms,* Rev. Mod. Phys. **83**, 1523 (2011).

[52] Y.-J. Lin, R. L. Compton, K. Jimenez-Garcia, W. D. Phillips, J. V. Porto, and I. B. Spielman, *A synthetic electric force acting on neutral atoms,* Nat. Phys. **7**, 531 (2011).

[53] M. Aidelsburger, M. Atala, S. Nascimbène, S. Trotzky, Y.-A. Chen, and I. Bloch, *Experimental realization of strong effective magnetic fields in an optical lattice,* Phys. Rev. Lett. **107**, 255301 (2011).

[54] M. Aidelsburger, M. Atala, M. Lohse, J. T. Barreiro, B. Paredes, and I. Bloch, *Realization of the Hofstadter Hamiltonian with ultracold atoms in optical lattices,* Phys. Rev. Lett. **111**, 185301 (2013).

[55] H. Miyake, G. A. Siviloglou, C. J. Kennedy, W. C. Burton, and W. Ketterle, *Realizing the Harper Hamiltonian with laser-assisted tunneling in optical lattices,* Phys. Rev. Lett. **111**, 185302 (2013).

[56] N. Goldman, J. C. Budich, and P. Zoller, *Topological quantum matter with ultracold gases in optical lattices,* Nat. Phys. **12**, 639 (2016).

[57] S. Inouye, M. R. Andrews, J. Stenger, H.-J. Miesner, D. M. Stamper-Kurn, and W. Ketterle, *Observation of Feshbach resonances in a Bose-Einstein condensate,* Nature (London) **392**, 151 (1998).

[58] C. Chin, R. Grimm, P. Julienne, and E. Tiesinga, *Feshbach resonances in ultracold gases,* Rev. Mod. Phys. **82**, 1225 (2010).

[59] K. Jiménez-García, L. J. LeBlanc, R. A. Williams, M. C. Beeler, A. R. Perry, and I. B. Spielman, *Peierls substitution in an engineered lattice potential,* Phys. Rev. Lett. **108**, 225303 (2012).

[60] R. E. Peierls, *On the theory of diamagnetism of conduction electrons,* Z. Phys. **80**, 763 (1933).

[61] D. R. Hofstadter, *Energy levels and wave functions of Bloch electrons in rational and irrational magnetic fields,* Phys. Rev. B **14**, 2239 (1976).

[62] M. Hafezi, A. S. Sørensen, E. Demler, and M. D. Lukin, *Fractional Quantum Hall effect in optical lattices,* Phys. Rev. A **76**, 023613 (2007).

[63] R. N. Palmer, A. Klein, and D. Jaksch, *Optical lattice Quantum Hall effect,* Phys. Rev. A **78**, 013609 (2008).

[64] Y. Kuno, T. Nakafuji, and I. Ichinose, *Phase diagrams of the Bose-Hubbard model and the Haldane-Bose-Hubbard model with complex hopping amplitudes,* Phys. Rev. A **92**, 063630 (2015).

[65] R. O. Umucalilar and E. J. Mueller, *Fractional Quantum Hall states in the vicinity of Mott plateaus,* Phys. Rev. A **81**, 053628 (2010).

[66] Y. Kuno, K. Shimizu, and I. Ichinose, *Bosonic analogs of the fractional Quantum Hall state in the vicinity of mott states,* Phys. Rev. A **95**, 013607 (2017).

[67] S. S. Natu, E. J. Mueller, and S. Das Sarma, *Competing ground states of strongly correlated bosons in the Harper-Hofstadter-Mott model,* Phys. Rev. A **93**, 063610 (2016).

[68] D. Hügel, H. U. R. Strand, P. Werner, and L. Pollet, *Anisotropic Harper-Hofstadter-Mott model: Competition between condensation and magnetic fields,* Phys. Rev. B **96**, 054431 (2017).

[69] G. Modugno, M. Modugno, F. Riboli, G. Roati, and M. Inguscio, *Two atomic species superfluid,* Phys. Rev. Lett. **89**, 190404 (2002).

[70] A. Lercher, T. Takekoshi, M. Debatin, B. Schuster, R. Rameshan, F. Ferlaino, R. Grimm, and H.-C. Nägerl, *Production of a dual-species Bose-Einstein condensate of* Rb *and* Cs *atoms,* Eur. Phys. J. D **65**, 3 (2011).

[71] D. J. McCarron, H. W. Cho, D. L. Jenkin, M. P. Köppinger, and S. L. Cornish, *Dual-species Bose-Einstein condensate of* ^{87}Rb *and* ^{133}Cs*,* Phys. Rev. A **84**, 011603 (2011).

[72] B. Pasquiou, A. Bayerle, S. M. Tzanova, S. Stellmer, J. Szczepkowski, M. Parigger, R. Grimm, and F. Schreck, *Quantum degenerate mixtures of strontium and rubidium atoms,* Phys. Rev. A **88**, 023601 (2013).

[73] L. Wacker, N. B. Jørgensen, D. Birkmose, R. Horchani, W. Ertmer, C. Klempt, N. Winter, J. Sherson, and J. J. Arlt, *Tunable dual-species Bose-Einstein condensates of* ^{39}K *and* ^{87}Rb*,* Phys. Rev. A **92**, 053602 (2015).

[74] F. Wang, X. Li, D. Xiong, and D. Wang, *A double species* $^{23}\mathrm{Na}$ *and* $^{87}\mathrm{Rb}$ *Bose-Einstein condensate with tunable miscibility via an interspecies Feshbach resonance,* J. Phys. B **49**, 015302 (2016).

[75] C. J. Myatt, E. A. Burt, R. W. Ghrist, E. A. Cornell, and C. E. Wieman, *Production of two overlapping Bose-Einstein condensates by sympathetic cooling,* Phys. Rev. Lett. **78**, 586 (1997).

[76] D. S. Hall, M. R. Matthews, J. R. Ensher, C. E. Wieman, and E. A. Cornell, *Dynamics of component separation in a binary mixture of Bose-Einstein condensates,* Phys. Rev. Lett. **81**, 1539 (1998).

[77] D. M. Stamper-Kurn, M. R. Andrews, A. P. Chikkatur, S. Inouye, H.-J. Miesner, J. Stenger, and W. Ketterle, *Optical confinement of a Bose-Einstein condensate,* Phys. Rev. Lett. **80**, 2027 (1998).

[78] J. Stenger, S. Inouye, D. M. Stamper-Kurn, H.-J. Miesner, A. P. Chikkatur, and W. Ketterle, *Spin domains in ground-state Bose-Einstein condensates,* Nature (London) **396**, 345 (1998).

[79] P. Maddaloni, M. Modugno, C. Fort, F. Minardi, and M. Inguscio, *Collective oscillations of two colliding Bose-Einstein condensates,* Phys. Rev. Lett. **85**, 2413 (2000).

[80] G. Delannoy, S. G. Murdoch, V. Boyer, V. Josse, P. Bouyer, and A. Aspect, *Understanding the production of dual Bose-Einstein condensation with sympathetic cooling,* Phys. Rev. A **63**, 051602 (2001).

[81] L. E. Sadler, J. M. Higbie, S. R. Leslie, M. Vengalattore, and D. M. Stamper-Kurn, *Spontaneous symmetry breaking in a quenched ferromagnetic spinor Bose-Einstein condensate,* Nature (London) **443**, 312 (2006).

[82] K. M. Mertes, J. W. Merrill, R. Carretero-González, D. J. Frantzeskakis, P. G. Kevrekidis, and D. S. Hall, *Nonequilibrium dynamics and superfluid ring excitations in binary Bose-Einstein condensates,* Phys. Rev. Lett. **99**, 190402 (2007).

[83] R. P. Anderson, C. Ticknor, A. I. Sidorov, and B. V. Hall, *Spatially inhomogeneous phase evolution of a two-component Bose-Einstein condensate,* Phys. Rev. A **80**, 023603 (2009).

[84] S. Tojo, Y. Taguchi, Y. Masuyama, T. Hayashi, H. Saito, and T. Hirano, *Controlling phase separation of binary Bose-Einstein condensates via mixed-spin-channel Feshbach resonance,* Phys. Rev. A **82**, 033609 (2010).

[85] S. B. Papp, J. M. Pino, and C. E. Wieman, *Tunable miscibility in a dual-species Bose-Einstein condensate,* Phys. Rev. Lett. **101**, 040402 (2008).

[86] S. Händel, T. P. Wiles, A. L. Marchant, S. A. Hopkins, C. S. Adams, and S. L. Cornish, *Magnetic merging of ultracold atomic gases of* $^{85}\mathrm{Rb}$ *and* $^{87}\mathrm{Rb}$*,* Phys. Rev. A **83**, 053633 (2011).

[87] S. Sugawa, R. Yamazaki, S. Taie, and Y. Takahashi, *Bose-Einstein condensate in gases of rare atomic species,* Phys. Rev. A **84**, 011610 (2011).

[88] S. Ronen, J. L. Bohn, L. E. Halmo, and M. Edwards, *Dynamical pattern formation during growth of a dual-species Bose-Einstein condensate,* Phys. Rev. A **78**, 053613 (2008).

[89] M. A. Hoefer, J. J. Chang, C. Hamner, and P. Engels, *Dark-dark solitons and modulational instability in miscible two-component Bose-Einstein condensates,* Phys. Rev. A **84**, 041605 (2011).

[90] C. Hamner, J. J. Chang, P. Engels, and M. A. Hoefer, *Generation of dark-bright soliton trains in superfluid-superfluid counterflow,* Phys. Rev. Lett. **106**, 065302 (2011).

[91] S. De, D. L. Campbell, R. M. Price, A. Putra, B. M. Anderson, and I. B. Spielman, *Quenched binary Bose-Einstein condensates: Spin-domain formation and coarsening,* Phys. Rev. A **89**, 033631 (2014).

[92] Y. Eto, M. Takahashi, K. Nabeta, R. Okada, M. Kunimi, H. Saito, and T. Hirano, *Bouncing motion and penetration dynamics in multicomponent Bose-Einstein condensates,* Phys. Rev. A **93**, 033615 (2016).

[93] Y. Eto, M. Takahashi, M. Kunimi, H. Saito, and T. Hirano, *Nonequilibrium dynamics induced by miscible-immiscible transition in binary Bose-Einstein condensates,* New J. Phys. **18**, 073029 (2016).

[94] E. Nicklas, M. Karl, M. Höfer, A. Johnson, W. Muessel, H. Strobel, J. Tomkovič, T. Gasenzer, and M. K. Oberthaler, *Observation of scaling in the dynamics of a strongly quenched quantum gas,* Phys. Rev. Lett. **115**, 245301 (2015).

[95] P. K. Molony, P. D. Gregory, Z. Ji, B. Lu, M. P. Köppinger, C. R. Le Sueur, C. L. Blackley, J. M. Hutson, and S. L. Cornish, *Creation of ultracold* $^{87}\mathrm{Rb}^{133}\mathrm{Cs}$ *molecules in the rovibrational ground state,* Phys. Rev. Lett. **113**, 255301 (2014).

[96] M. Guo, B. Zhu, B. Lu, X. Ye, F. Wang, R. Vexiau, N. Bouloufa-Maafa, G. Quéméner, O. Dulieu, and D. Wang, *Creation of an ultracold gas of ground-state dipolar* $^{23}\mathrm{Na}^{87}\mathrm{Rb}$ *molecules,* Phys. Rev. Lett. **116**, 205303 (2016).

[97] S. A. Will, J. W. Park, Z. Z. Yan, H. Loh, and M. W. Zwierlein, *Coherent microwave control of ultracold* $^{23}\mathrm{Na}^{40}\mathrm{K}$ *molecules,* Phys. Rev. Lett. **116**, 225306 (2016).

[98] T.-L. Ho and V. B. Shenoy, *Binary mixtures of Bose condensates of alkali atoms,* Phys. Rev. Lett. **77**, 3276 (1996).

[99] B. Gadway, D. Pertot, R. Reimann, and D. Schneble, *Superfluidity of interacting bosonic mixtures in optical lattices,* Phys. Rev. Lett. **105**, 045303 (2010).

[100] P. Soltan-Panahi, J. Struck, P. Hauke, A. Bick, W. Plenkers, G. Meineke, C. Becker, P. Windpassinger, M. Lewenstein, and K. Sengstock, *Multi-component quantum gases in spin-dependent hexagonal lattices,* Nat. Phys. **7**, 434 (2011).

[101] L.-M. Duan, E. Demler, and M. D. Lukin, *Controlling spin exchange interactions of ultracold atoms in optical lattices,* Phys. Rev. Lett. **91**, 090402 (2003).

[102] E. Altman, W. Hofstetter, E. Demler, and M. D. Lukin, *Phase diagram of two-component bosons on an optical lattice,* New Journal of Physics **5**, 113 (2003).

[103] W. Wang, V. Penna, and B. Capogrosso-Sansone, *Analysis and resolution of the ground-state degeneracy of the two-component Bose-Hubbard model,* Phys. Rev. E **90**, 022116 (2014).

[104] A. B. Kuklov and B. V. Svistunov, *Counterflow superfluidity of two-species ultracold atoms in a commensurate optical lattice,* Phys. Rev. Lett. **90**, 100401 (2003).

[105] U. Shrestha, *Antiferromagnetism in a bosonic mixture of rubidium* $(^{87}\mathrm{Rb})$ *and potassium* $(^{41}\mathrm{K})$*,* Phys. Rev. A **82**, 041603 (2010).

[106] M. Guglielmino, V. Penna, and B. Capogrosso-Sansone, *Ising antiferromagnet with ultracold bosonic mixtures confined in a harmonic trap,* Phys. Rev. A **84**, 031603 (2011).

[107] L. Mathey, *Commensurate mixtures of ultracold atoms in one dimension,* Phys. Rev. B **75**, 144510 (2007).

[108] A. Hu, L. Mathey, I. Danshita, E. Tiesinga, C. J. Williams, and C. W. Clark, *Counterflow and paired superfluidity in one-dimensional Bose mixtures in optical lattices,* Phys. Rev. A **80**, 023619 (2009).

[109] C. Menotti and S. Stringari, *Detection of pair-superfluidity for bosonic mixtures in optical lattices,* Phys. Rev. A **81**, 045604 (2010).

[110] B. Gadway, D. Pertot, J. Reeves, M. Vogt, and D. Schneble, *Glassy behavior in a binary atomic mixture,* Phys. Rev. Lett. **107**, 145306 (2011).

[111] S. Trotzky, P. Cheinet, S. Fölling, M. Feld, U. Schnorrberger, A. M. Rey, A. Polkovnikov, E. A. Demler, M. D. Lukin, and I. Bloch, *Time-resolved observation and control of superexchange interactions with ultracold atoms in optical lattices,* Science **319**, 295 (2008).

[112] B. Gadway, D. Pertot, J. Reeves, and D. Schneble, *Probing an ultracold-atom crystal with matter waves,* Nat. Phys. **8**, 544 (2012).

[113] P. Soltan-Panahi, D.-S. Luhmann, J. Struck, P. Windpassinger, and K. Sengstock, *Quantum phase transition to unconventional multi-orbital superfluidity in optical lattices,* Nat. Phys. **8**, 71 (2012).

[114] P. Medley, D. M. Weld, H. Miyake, D. E. Pritchard, and W. Ketterle, *Spin gradient demagnetization cooling of ultracold atoms,* Phys. Rev. Lett. **106**, 195301 (2011).

[115] D. M. Weld, P. Medley, H. Miyake, D. Hucul, D. E. Pritchard, and W. Ketterle, *Spin gradient thermometry for ultracold atoms in optical lattices,* Phys. Rev. Lett. **103**, 245301 (2009).

[116] A. Isacsson, M.-C. Cha, K. Sengupta, and S. M. Girvin, *Superfluid-insulator transitions of two-species bosons in an optical lattice,* Phys. Rev. B **72**, 184507 (2005).

[117] M. Iskin, *Strong-coupling expansion for the two-species Bose-Hubbard model,* Phys. Rev. A **82**, 033630 (2010).

[118] D. Benjamin and E. Demler, *Variational polaron method for Bose-Bose mixtures,* Phys. Rev. A **89**, 033615 (2014).

[119] G.-H. Chen and Y.-S. Wu, *Quantum phase transition in a multicomponent Bose-Einstein condensate in optical lattices,* Phys. Rev. A **67**, 013606 (2003).

[120] R. V. Pai, J. M. Kurdestany, K. Sheshadri, and R. Pandit, *Bose-Hubbard models in confining potentials: Inhomogeneous mean-field theory,* Phys. Rev. B **85**, 214524 (2012).

[121] M. Guglielmino, V. Penna, and B. Capogrosso-Sansone, *Mott-insulator–to–superfluid transition in Bose-Bose mixtures in a two-dimensional lattice,* Phys. Rev. A **82**, 021601 (2010).

[122] L. He, Y. Li, E. Altman, and W. Hofstetter, *Quantum phases of Bose-Bose mixtures on a triangular lattice,* Phys. Rev. A **86**, 043620 (2012).

[123] O. E. Alon, A. I. Streltsov, and L. S. Cederbaum, *Demixing of bosonic mixtures in optical lattices from macroscopic to microscopic scales,* Phys. Rev. Lett. **97**, 230403 (2006).

[124] T. Mishra, R. V. Pai, and B. P. Das, *Phase separation in a two-species Bose mixture,* Phys. Rev. A **76**, 013604 (2007).

[125] F. Zhan and I. P. McCulloch, *Comment on "Phase separation in a two-species Bose mixture",* Phys. Rev. A **89**, 057601 (2014).

[126] F. Lingua, M. Guglielmino, V. Penna, and B. Capogrosso Sansone, *Demixing effects in mixtures of two bosonic species,* Phys. Rev. A **92**, 053610 (2015).

[127] T. Roscilde and J. I. Cirac, *Quantum emulsion: A glassy phase of bosonic mixtures in optical lattices,* Phys. Rev. Lett. **98**, 190402 (2007).

[128] P. Buonsante, S. M. Giampaolo, F. Illuminati, V. Penna, and A. Vezzani, *Mixtures of strongly interacting bosons in optical lattices,* Phys. Rev. Lett. **100**, 240402 (2008).

[129] E. Lundh and J.-P. Martikainen, *Kelvin-helmholtz instability in two-component bose gases on a lattice,* Phys. Rev. A **85**, 023628 (2012).

[130] S. Hooley and K. A. Benedict, *Dynamical instabilities in a two-component Bose-Einstein condensate in a one-dimensional optical lattice,* Phys. Rev. A **75**, 033621 (2007).

[131] J. Ruostekoski and Z. Dutton, *Dynamical and energetic instabilities in multicomponent Bose-Einstein condensates in optical lattices,* Phys. Rev. A **76**, 063607 (2007).

[132] G. Ceccarelli, J. Nespolo, A. Pelissetto, and E. Vicari, *Bose-Einstein condensation and critical behavior of two-component bosonic gases,* Phys. Rev. A **92**, 043613 (2015).

[133] G. Ceccarelli, J. Nespolo, A. Pelissetto, and E. Vicari, *Phase diagram and multicritical behaviors of mixtures of three-dimensional bosonic gases,* Phys. Rev. A **93**, 033647 (2016).

[134] S. Anufriiev and T. A. Zaleski, *Multicriticality and interaction-induced first-order phase transitions in mixtures of ultracold bosons in an optical lattice,* Phys. Rev. A **94**, 043613 (2016).

[135] H. Shim and T. Bergeman, *Phase coherence and fragmentation of two-component Bose-Einstein condensates loaded in state-dependent optical lattices,* Phys. Rev. A **94**, 043631 (2016).

[136] P. N. Galteland, E. Babaev, and A. Sudbø, *Thermal remixing of phase-separated states in two-component bosonic condensates,* New J. Phys. **17**, 103040 (2015).

[137] T. D. Kühner, S. R. White, and H. Monien, *One-dimensional Bose-Hubbard model with nearest-neighbor interaction,* Phys. Rev. B **61**, 12474–12489 (2000).

[138] L. Santos, G. V. Shlyapnikov, and M. Lewenstein, *Roton-maxon spectrum and stability of trapped dipolar Bose-Einstein condensates,* Phys. Rev. Lett. **90**, 250403 (2003).

[139] B. Capogrosso-Sansone, C. Trefzger, M. Lewenstein, P. Zoller, and G. Pupillo, *Quantum phases of cold polar molecules in 2d optical lattices,* Phys. Rev. Lett. **104**, 125301 (2010).

[140] T. Flottat, L. d. F. de Parny, F. Hébert, V. G. Rousseau, and G. G. Batrouni, *Phase diagram of bosons in a two-dimensional optical lattice with infinite-range cavity-mediated interactions,* Phys. Rev. B **95**, 144501 (2017).

[141] M. Iskin, *Route to supersolidity for the extended Bose-Hubbard model,* Phys. Rev. A **83**, 051606 (2011).

[142] K.-K. Ng and Y.-C. Chen, *Supersolid phases in the bosonic extended hubbard model,* Phys. Rev. B **77**, 052506 (2008).

[143] D. Yamamoto and I. Danshita, *Stability of superflow in supersolid phases of lattice bosons with dipole-dipole interaction,* Journal of Physics: Conference Series **273**, 012020 (2011).

[144] M. Boninsegni and N. V. Prokof'ev, *Colloquium: Supersolids: What and where are they?* Rev. Mod. Phys. **84**, 759–776 (2012).

[145] L. Julian, M. Andrea, Z. Philip, E. Tilman, and D. Tobias, *Supersolid formation in a quantum gas breaking a continuous translational symmetry,* Nature **543**, 87 (2017).

[146] L. Jun-Ru, L. Jeongwon, H. Wujie, B. Sean, S. Boris, T. F. Çağrı, J. A. O., and K. Wolfgang, *A stripe phase with supersolid properties in spin–orbit-coupled bose–einstein condensates,* Nature **543**, 91 (2017).

[147] M. Yan, Y. Qian, H.-Y. Hui, M. Gong, C. Zhang, and V. W. Scarola, *Spin-orbit-driven transitions between mott insulators and finite-momentum superfluids of bosons in optical lattices,* Phys. Rev. A **96**, 053619 (2017).

[148] L. Fei, M. T. A., and S. V. W., *Disordered supersolids in the extended Bose-Hubbard model,* Scientific Reports **7**, 12752 (2017).

[149] F. Trousselet, P. Rueda-Fonseca, and A. Ralko, *Competing supersolids of bose-bose mixtures in a triangular lattice,* Phys. Rev. B **89**, 085104 (2014).

[150] D. S. Rokhsar and B. G. Kotliar, *Gutzwiller projection for bosons,* Phys. Rev. B **44**, 10328 (1991).

[151] K. Sheshadri, H. R. Krishnamurthy, R. Pandit, and T. V. Ramakrishnan, *Superfluid and insulating phases in an interacting-boson model: Mean-field theory and the RPA,* EPL **22**, 257 (1993).

[152] U. Bissbort and W. Hofstetter, *Stochastic mean-field theory for the disordered Bose-Hubbard model,* EPL **86**, 50007 (2009).

[153] P. Buonsante, V. Penna, and A. Vezzani, *Fractional-filling loophole insulator domains for ultracold bosons in optical superlattices,* Phys. Rev. A **70**, 061603 (2004).

[154] D. Yamamoto, *Correlated cluster mean-field theory for spin systems,* Phys. Rev. B **79**, 144427 (2009).

[155] P. Pisarski, R. M. Jones, and R. J. Gooding, *Application of a multisite mean-field theory to the disordered Bose-Hubbard model,* Phys. Rev. A **83**, 053608 (2011).

[156] T. McIntosh, P. Pisarski, R. J. Gooding, and E. Zaremba, *Multisite mean-field theory for cold bosonic atoms in optical lattices,* Phys. Rev. A **86**, 013623 (2012).

[157] D.-S. Lühmann, *Cluster Gutzwiller method for bosonic lattice systems,* Phys. Rev. A **87**, 043619 (2013).

[158] M. C. Gutzwiller, *Effect of correlation on the ferromagnetism of transition metals,* Phys. Rev. Lett. **10**, 159–162 (1963).

[159] J. K. Freericks and H. Monien, *Strong-coupling expansions for the pure and disordered bose- hubbard model,* Phys. Rev. B **53**, 2691–2700 (1996).

[160] F. E. A. dos Santos and A. Pelster, *Quantum phase diagram of bosons in optical lattices,* Phys. Rev. A **79**, 013614 (2009).

[161] N. Teichmann, D. Hinrichs, M. Holthaus, and A. Eckardt, *Bose-Hubbard phase diagram with arbitrary integer filling,* Phys. Rev. B **79**, 100503 (2009).

[162] N. Dupuis and K. Sengupta, *Superfluid to mott-insulator transition of cold atoms in optical lattices,* Physica B: Condensed Matter **404**, 517 – 520 (2009).

[163] A. Rançon and N. Dupuis, *Nonperturbative renormalization group approach to the Bose-Hubbard model,* Phys. Rev. B **83**, 172501 (2011).

[164] A. Rançon and N. Dupuis, *Nonperturbative renormalization group approach to strongly correlated lattice bosons,* Phys. Rev. B **84**, 174513 (2011).

[165] P. Anders, E. Gull, L. Pollet, M. Troyer, and P. Werner, *Dynamical mean-field theory for bosons,* New Journal of Physics **13**, 075013 (2011).

[166] H. A. Bethe, *Statistical theory of superlattices,* Proc. R. Soc. Lond. A **150**, 552–575 (1935).

[167] R. E. Peierls, *Statistical theory of superlattices with unequal concentrations of the components,* Proc. Cambridge Philos. Soc. **32**, 477 (1936).

[168] P. R. Weiss, *The application of the bethe-peierls method to ferromagnetism,* Phys. Rev. **74**, 1493–1504 (1948).

[169] D. Yamamoto, A. Masaki, and I. Danshita, *Quantum phases of hardcore bosons with long-range interactions on a square lattice,* Phys. Rev. B **86**, 054516 (2012).

[170] E. Duchon and N. Trivedi, *Fluctuations and quantum criticality in the two-dimensional bose hubbard model,* Annalen der Physik **525**, L35–L39 (2013).

[171] S. P. Rath, W. Simeth, M. Endres, and W. Zwerger, *Non-local order in mott insulators, duality and wilson loops,* Annals of Physics (New York) pp. 256–271 (2013).

[172] C. Kollath, U. Schollwöck, J. von Delft, and W. Zwerger, *Spatial correlations of trapped one-dimensional bosons in an optical lattice,* Phys. Rev. A **69**, 031601 (2004).

[173] C. Kollath, A. M. Läuchli, and E. Altman, *Quench dynamics and nonequilibrium phase diagram of the Bose-Hubbard model,* Phys. Rev. Lett. **98**, 180601 (2007).

[174] D. Jaksch and P. Zoller, *Creation of effective magnetic fields in optical lattices: the Hofstadter butterfly for cold neutral atoms,* New J. Phys. **5**, 56 (2003).

[175] K. Osterloh, M. Baig, L. Santos, P. Zoller, and M. Lewenstein, *Cold atoms in non-abelian gauge potentials: From the hofstadter "moth" to lattice gauge theory,* Phys. Rev. Lett. **95**, 010403 (2005).

[176] N. Elstner and H. Monien, *Dynamics and thermodynamics of the Bose-Hubbard model,* Phys. Rev. B **59**, 12184–12187 (1999).

[177] O. Penrose and L. Onsager, *Bose-Einstein condensation and liquid helium,* Phys. Rev. **104**, 576–584 (1956).

[178] P. Kapitza, *Viscosity of liquid helium below the λ-point,* Nature **141**, 74–74 (1938).

[179] J. F. Allen and A. D. Misener, *Flow of liquid helium ii,* Nature **141**, 75–75 (1938).

[180] A. J. Leggett, *Superfluidity,* Rev. Mod. Phys. **71**, S318–S323 (1999).

[181] G. B. Hess and W. M. Fairbank, *Measurements of angular momentum in superfluid helium,* Phys. Rev. Lett. **19**, 216–218 (1967).

[182] C. Ryu, M. F. Andersen, P. Cladé, V. Natarajan, K. Helmerson, and W. D. Phillips, *Observation of persistent flow of a Bose-Einstein condensate in a toroidal trap,* Phys. Rev. Lett. **99**, 260401 (2007).

[183] A. M. Rey, K. Burnett, R. Roth, M. Edwards, C. J. Williams, and C. W. Clark, *Bogoliubov approach to superfluidity of atoms in an optical lattice,* J. Phys. B **36**, 825–841 (2003).

[184] R. Roth and K. Burnett, *Superfluidity and interference pattern of ultracold bosons in optical lattices,* Phys. Rev. A **67**, 031602 (2003).

[185] M. Gerster, M. Rizzi, F. Tschirsich, P. Silvi, R. Fazio, and S. Montangero, *Superfluid density and quasi-long-range order in the one-dimensional disordered bose–hubbard model,* New Journal of Physics **18**, 015015 (2016).

[186] A. A. Shams and H. R. Glyde, *Superfluidity and Bose-Einstein condensation in optical lattices and porous media: A path integral monte carlo study,* Phys. Rev. B **79**, 214508 (2009).

[187] D. J. Thouless, M. Kohmoto, M. P. Nightingale, and M. den Nijs, *Quantized Hall conductance in a two-dimensional periodic potential,* Phys. Rev. Lett. **49**, 405–408 (1982).

[188] D. C. Tsui, H. L. Stormer, and A. C. Gossard, *Two-dimensional magnetotransport in the extreme quantum limit,* Phys. Rev. Lett. **48**, 1559 (1982).

[189] N. Read and E. Rezayi, *Beyond paired Quantum Hall states: Parafermions and incompressible states in the first excited landau level,* Phys. Rev. B **59**, 8084–8092 (1999).

[190] P. G. Harper, *Single band motion of conduction electrons in a uniform magnetic field,* Proc. Phys. Soc. A **68**, 874 (1955).

[191] E. J. Mueller, *Artificial electromagnetism for neutral atoms: Escher staircase and laughlin liquids,* Phys. Rev. A **70**, 041603 (2004).

[192] L.-K. Lim, C. M. Smith, and A. Hemmerich, *Staggered-vortex superfluid of ultracold bosons in an optical lattice,* Phys. Rev. Lett. **100**, 130402 (2008).

[193] F. Gerbier and J. Dalibard, *Gauge fields for ultracold atoms in optical superlattices,* New J. Phys. **12**, 033007 (2010).

[194] A. R. Kolovsky, *Creating artificial magnetic fields for cold atoms by photon-assisted tunneling,* EPL (Europhysics Letters) **93**, 20003 (2011).

[195] M. Aidelsburger, *Artificial gauge fields and topology with ultracold atoms in optical lattices,* Journal of Physics B: Atomic, Molecular and Optical Physics **51**, 193001 (2018).

[196] M. O. Oktel, M. Niţ ă, and B. Tanatar, *Mean-field theory for Bose-Hubbard model under a magnetic field,* Phys. Rev. B **75**, 045133 (2007).

[197] B. Bernevig and T. Hughes, *Topological Insulators and Topological Superconductors* (Princeton University Press, 2013).

[198] A. Trellakis, *Nonperturbative solution for bloch electrons in constant magnetic fields,* Phys. Rev. Lett. **91**, 056405 (2003).

[199] M. Hastings and T. Koma, *Spectral gap and exponential decay of correlations,* Commun. Math. Phys. **265**, 781–804 (2006).

[200] X.-G. WEN, *Theory of the edge states in fractional Quantum Hall effects,* International Journal of Modern Physics B **06**, 1711–1762 (1991).

[201] T. S. Cubitt, D. Perez-Garcia, and M. M. Wolf, *Undecidability of the spectral gap,* Nature **528**, 207–211 (2015).

[202] J. M. Zhang and R. X. Dong, *Exact diagonalization: the Bose-Hubbard model as an example,* European Journal of Physics **31**, 591 (2010).

[203] D. Raventós, T. Graß, M. Lewenstein, and B. Juliá-Díaz, *Cold bosons in optical lattices: a tutorial for exact diagonalization,* Journal of Physics B: Atomic, Molecular and Optical Physics **50**, 113001 (2017).

[204] M. E. Tai, A. Lukin, M. Rispoli, R. Schittko, T. Menke, D. Borgnia, P. M. Preiss, F. Grusdt, A. M. Kaufman, and M. Greiner, *Microscopy of the interacting Harper-Hofstadter model in the two-body limit,* Nature (London) **546**, 519 (2017).

[205] A. L. Gaunt, T. F. Schmidutz, I. Gotlibovych, R. P. Smith, and Z. Hadzibabic, *Bose-Einstein condensation of atoms in a uniform potential,* Phys. Rev. Lett. **110**, 200406 (2013).

[206] J. von Neumann, *Mathematical Foundations of Quantum Mechanics: New Edition* (Princeton University Press, 2018), new edition ed.

[207] T. J. Elliott and T. H. Johnson, *Nondestructive probing of means, variances, and correlations of ultracold-atomic-system densities via qubit impurities,* Phys. Rev. A **93**, 043612 (2016).

[208] M. Streif, A. Buchleitner, D. Jaksch, and J. Mur-Petit, *Measuring correlations of cold-atom systems using multiple quantum probes,* Phys. Rev. A **94**, 053634 (2016).

[209] Y.-C. He, F. Grusdt, A. Kaufman, M. Greiner, and A. Vishwanath, *Realizing and adiabatically preparing bosonic integer and fractional Quantum Hall states in optical lattices,* Phys. Rev. B **96**, 201103 (2017).

[210] M. Gerster, M. Rizzi, P. Silvi, M. Dalmonte, and S. Montangero, *Fractional Quantum Hall effect in the interacting hofstadter model via tensor networks,* Phys. Rev. B **96**, 195123 (2017).

[211] M. Hafezi, A. S. Sørensen, M. D. Lukin, and E. Demler, *Characterization of topological states on a lattice with chern number,* Europhysics Letters (EPL) **81**, 10005 (2007).

[212] X. G. Wen and Q. Niu, *Ground-state degeneracy of the fractional Quantum Hall states in the presence of a random potential and on high-genus riemann surfaces,* Phys. Rev. B **41**, 9377–9396 (1990).

[213] Y. Hatsugai, *Explicit gauge fixing for degenerate multiplets: A generic setup for topological orders,* Journal of the Physical Society of Japan **73**, 2604–2607 (2004).

[214] Y. Hatsugai, *Characterization of topological insulators: Chern numbers for ground state multiplet,* Journal of the Physical Society of Japan **74**, 1374–1377 (2005).

[215] J. Catani, L. De Sarlo, G. Barontini, F. Minardi, and M. Inguscio, *Degenerate Bose-Bose mixture in a three-dimensional optical lattice,* Phys. Rev. A **77**, 011603 (2008).

[216] A. Kuklov, N. Prokof'ev, and B. Svistunov, *Commensurate two-component bosons in an optical lattice: Ground state phase diagram,* Phys. Rev. Lett. **92**, 050402 (2004).

[217] M.-C. CHA, *Asymmetric two-component hard-core boson mixtures in a one-dimensional optical lattice,* International Journal of Modern Physics B **27**, 1362002 (2013).

[218] Y.-C. Kuo and S.-F. Shieh, *Phase separation of multi-component bose–einstein condensates in optical lattices,* Journal of Mathematical Analysis and Applications **347**, 521 – 533 (2008).

[219] B. Damski, L. Santos, E. Tiemann, M. Lewenstein, S. Kotochigova, P. Julienne, and P. Zoller, *Creation of a dipolar superfluid in optical lattices,* Phys. Rev. Lett. **90**, 110401 (2003).

[220] S. Powell, *Magnetic phases and transitions of the two-species Bose-Hubbard model,* Phys. Rev. A **79**, 053614 (2009).

[221] P. P. Hofer, C. Bruder, and V. M. Stojanović, *Superfluid drag of two-species Bose-Einstein condensates in optical lattices,* Phys. Rev. A **86**, 033627 (2012).

[222] A. Kitaev and J. Preskill, *Topological entanglement entropy,* Phys. Rev. Lett. **96**, 110404 (2006).

[223] M. Levin and X.-G. Wen, *Detecting topological order in a ground state wave function,* Phys. Rev. Lett. **96**, 110405 (2006).

List of Publications

Thesis related Publications

1. **R. Bai**, S. Bandyopadhyay, S. Pal, K. Suthar and D. Angom,
   Bosonic quantum Hall states in single-layer two-dimensional optical lattices
   Phys. Rev. A **98**, 023606 (2018). arXiv:1802.07988

2. **R. Bai**, A. Roy, D. Angom, P. Muruganandam
   Condensates in double-well potential with synthetic gauge potentials and vortex seeding
   Phys. Lett. A **382**, 2376 - 2381 (2018). arXiv:1705.06493

3. **R. Bai**, S. Bandyopadhyay, S. Pal, K. Suthar and D. Angom,
   Quantum Hall states for $\alpha = 1/3$ in optical lattices,
   Quantum Collisions and Confinement of Atomic and Molecular Species, and Photons, Springer Proceedings, 211–221 (2019)

4. **R. Bai**, S. Bandyopadhyay, K. Suthar and D. Angom,
   Quantum phases of two component BECs with extended Bose-Hubbard Model
   under preparation.

Other Publication

5. S. Pal, **R. Bai**, S. Bandyopadhyay, K. Suthar and D. Angom,
   Enhancement of Bose glass phase in presence of artificial gauge field,
   Phys. Rev. A **99**, 053610 (2019). arXiv:1807.00269

6. K. Suthar, **R. Bai**, S. Bandyopadhyay, S. Pal, and D. Angom,
   Supersolid phase of extended Bose-Hubbard model with artificial gauge field,
   arXiv:1904.12649 (under review)

7. S. Bandyopadhyay, **R. Bai**, S. Pal, K. Suthar, R. Nath and D. Angom,
   Quantum phases of canted dipolar bosons in a two-dimensional square optical lattice,
   Phys. Rev. A **100**, 053623 (2019). arXiv:1906.07483

Publications attached with thesis

1. **R. Bai**, S. Bandyopadhyay, S. Pal, K. Suthar and D. Angom,
   Bosonic quantum Hall states in single-layer two-dimensional optical lattices
   Phys. Rev. A **98**, 023606 (2018).
   doi: 10.1103/PhysRevA.98.023606

2. **R. Bai**, A. Roy, D. Angom, P. Muruganandam
   Condensates in double-well potential with synthetic gauge potentials and vortex seeding
   Phys. Lett. A **382**, 2376 - 2381 (2018).
   doi: 10.1016/j.physleta.2018.05.051

Bosonic quantum Hall states in single-layer two-dimensional optical lattices

Rukmani Bai,[1,2] Soumik Bandyopadhyay,[1,2] Sukla Pal,[1] K. Suthar,[1] and D. Angom[1]
[1]*Physical Research Laboratory, Ahmedabad 380009, Gujarat, India*
[2]*Indian Institute of Technology Gandhinagar, Palaj, Gandhinagar 382355, Gujarat, India*

(Received 27 February 2018; published 7 August 2018)

Quantum Hall (QH) states of two-dimensional (2D) single-layer optical lattices are examined using the Bose-Hubbard model (BHM) in the presence of an artificial gauge field. We study the QH states of both the homogeneous and inhomogeneous systems. For the homogeneous case, we use cluster Gutzwiller mean-field (CGMF) theory with cluster sizes ranging from 2×2 to 5×5. We then consider the inhomogeneous case, which is relevant to experimental realization. In this case, we use CGMF and exact diagonalization (ED). The ED studies are using lattice sizes ranging from 3×3 to 4×12. Our results show that the geometries of the QH states are sensitive to the magnetic flux α and cluster sizes. For homogeneous systems, among various combinations of $1/5 \leqslant \alpha \leqslant 1/2$ and filling factor ν, only the QH state of $\alpha = 1/4$ with $\nu = 1/2,\ 1,\ 3/2$, and 2 occur as ground states. For other combinations, the competing superfluid (SF) state is the ground state and QH state is metastable. For BHM with envelope potential, all the QH states observed in homogeneous systems exist for box potentials, but none exist for the harmonic potential. The QH states also persist for very shallow Gaussian envelope potential. As a possible experimental signature, we study the two-point correlations of the QH and SF states.

DOI: 10.1103/PhysRevA.98.023606

I. INTRODUCTION

The experimental realization of Bose-Einstein condensates (BECs) of dilute atomic gases in optical lattices [1–4] and consequent developments [5,6] have opened new frontiers to explore the physics of quantum many-body systems. This is due to the possibility of experimental control on the interatomic interactions, number of atoms, lattice geometry, and choice of atomic species. In particular, bosons in optical lattices are near ideal realizations [7] of the Bose-Hubbard model (BHM) [8,9]. The recent experimental implementations of artificial gauge potential [10–16] in optical lattices have introduced an important parameter and made these systems excellent testing ground for QH physics [17]. Despite enormous progress in experimental and theoretical understanding of the QH effect [18–21], a basic understanding of the fractional quantum Hall (FQH) effect [22] is still missing. The major difficulty arises from the strong correlations of electrons, but which is also the origin of FQH states. Although the Laughlin ansatz [23] provides exact solutions for some FQH systems, it is not yet observed in experiments. The strong magnetic field required to obtain FQH states is the major hurdle to observe these many-body states. Optical lattices, in this respect, have the advantage as various topological states, such as FQH states, are predicted to occur within the range of parameters achieved in experiments [24,25].

In the BHM Hamiltonian, the hopping and on-site interaction are the two competing terms. And both of these can be tuned by changing the depth of the lattice potential and employing Feshbach resonance [26,27]. The hopping parameter J, which defines the strength of the hopping term in the BHM Hamiltonian, acquires a phase $J \to |J| \exp(i\Phi)$ in the presence of an artificial gauge potential [28] through the Peierls substitution [29,30] and modifies the states of BHM. So, for an atom in the optical lattice, there is a change of phase $\Phi = 2\pi\alpha$ when it hops around a unit cell or plaquette, where α is the flux quanta per plaquette. In theoretical studies, features of Laughlin states in low particle density limit have been reported [31] for $\nu = 1/2$ and $\alpha < \alpha_c = 0.4$. Here, ν is the filling factor, the number of particles per flux quanta, and α_c is the critical value below which FQH states exist. For $\alpha > \alpha_c$, the equilibrium ground-state properties start to change, and the existence of a striped vortex lattice phase is reported in the neighborhood of $\alpha = 1/2$ [32]. On the other hand, based on the results of Monte Carlo and exact diagonalization (ED), the existence of bosonic FQH states is predicted [33] in the vicinity of Mott plateaus for $\alpha = 2/3$. Similar results are reported in a recent work using the Chern-Simons theory [34] in combination with single-site Gutzwiller mean-field (SGMF) theory. In another recent work [35], the incompressibility of the FQH states is employed to identify these states in computations using cluster Gutzwiller mean-field (CGMF) theory for $\alpha = 1/5$ at $\nu = 1/2$. On the other hand, using reciprocal cluster mean-field (RCMF) analysis, Hügel *et al.* [36] predicted a competing FQH state as a metastable state for $\alpha = 1/4$. In this work, we report FQH states at distinct νs for low and high flux. For example, when $\alpha = 1/5$, we obtain QH states at $\nu = n/2$, where $n = 1, 2, \ldots, 9$ and for $\alpha = 1/2$ at $\nu = 1/2,\ 1$, and $3/2$. In particular, we discuss the QH states for $\alpha = 1/5,\ 1/4$, and $1/2$ in the hard-core boson limit. We also obtain QH states for the $\alpha = 1/3$ case; however, we have not provided the details as the general trend is similar to $\alpha = 1/5$.

Motivated by the recent theoretical investigations and experimental progress, we address a basic gap in our current understanding, that is, the occurrence of QH states in optical lattices with an envelope potential. This key issue is addressed in this work. For our studies, we use SGMF [37–39] and CGMF [40–44] theories and ED. Our results, for the case of homogeneous optical lattices, agree well with the previous theoretical observations. After establishing this and demonstrating that

getting the geometry of QH states requires larger cluster sizes in CGMF, we provide an answer to the following question: What is the nature of the QH states in optical lattices with an envelope potential?

II. THEORETICAL METHODS

We consider bosonic atoms at zero temperature confined in a two-dimensional (2D) square optical lattice with an envelope potential in the presence of synthetic magnetic field [14–16,45]. In the Landau gauge, the system is well described by the BHM [7,24,25,32,45] with Peierls substitution in the nearest-neighbor (NN) hopping [29,30,46], and the Hamiltonian is

$$\begin{aligned}\hat{H} = &-\sum_{p,q}[(J_x e^{i2\pi\alpha q}\hat{b}^{\dagger}_{p+1,q}\hat{b}_{p,q} + \text{H.c.}) \\ &+ (J_y \hat{b}^{\dagger}_{p,q+1}\hat{b}_{p,q} + \text{H.c.})] \\ &+ \sum_{p,q}\left[\frac{U}{2}\hat{n}_{p,q}(\hat{n}_{p,q}-1) - (\mu - \varepsilon_{p,q})\hat{n}_{p,q}\right], \quad (1)\end{aligned}$$

where p (q) is the lattice site index along x (y) direction, $\hat{b}_{p,q}$ ($\hat{b}^{\dagger}_{p,q}$) is the bosonic annihilation (creation) operator, and $\hat{n}_{p,q}$ is the number operator. The parameter J_x (J_y) is the complex hopping strength between two NN sites along the x (y) direction, and U is the on-site interaction strength. Here, μ is the chemical potential and $\varepsilon_{p,q}$ is the energy offset of the envelope potential. The envelope or confining potential, in the case of harmonic potential, modifies μ by the energy offset $\varepsilon_{p,q} = \Omega(p^2 + q^2)$, where Ω is the strength of the harmonic confining potential. The phase $2\pi\alpha$ in J_x arises from the synthetic magnetic field and $0 \leqslant \alpha \leqslant 1/2$. It is well established that for $\alpha = 0$ the phase diagram of BHM admits two phases, Mott insulator (MI) and superfluid (SF) phases [3,7,8]. The strong on-site interaction limit ($J/U \ll 1$) corresponds to the MI phase, whereas the opposite limit ($J/U \gg 1$) corresponds to the SF phase. The phase diagram in the μ-J plane consists of Mott lobes with increasing commensurate integer filling. It has been shown in previous studies that MI lobes are enlarged for $\alpha \neq 0$ [47].

A. Gutzwiller mean-field theory

To obtain the eigenstates of BHM, we use the mean-field approximation [38]. For the mean-field Hamiltonian, the annihilation (creation) operators in Eq. (1) are decomposed as

$$\hat{b}_{p,q} = \phi_{p,q} + \delta\hat{b}_{p,q}, \quad (2a)$$

$$\hat{b}^{\dagger}_{p,q} = \phi^{*}_{p,q} + \delta\hat{b}^{\dagger}_{p,q}, \quad (2b)$$

where $\phi_{p,q} = \langle\hat{b}_{p,q}\rangle$ is the SF order parameter and $\phi^{*}_{p,q} = \langle\hat{b}^{\dagger}_{p,q}\rangle$. Using these definitions in Eq. (1) and neglecting the second-order term in fluctuations like $\delta\hat{b}^{\dagger}_{p+1,q}\delta\hat{b}_{p,q}$, we obtain the mean-field Hamiltonian of the BHM as

$$\begin{aligned}\hat{H}^{\text{MF}} = &-\sum_{p,q}\{[J_x e^{i2\pi\alpha q}(\hat{b}^{\dagger}_{p+1,q}\phi_{p,q} + \phi^{*}_{p+1,q}\hat{b}_{p,q} \\ &- \phi^{*}_{p+1,q}\phi_{p,q}) + \text{H.c.}] + [J_y(\hat{b}^{\dagger}_{p,q+1}\phi_{p,q} + \phi^{*}_{p,q+1}\hat{b}_{p,q} \\ &- \phi^{*}_{p,q+1}\phi_{p,q}) + \text{H.c.}]\} \\ &+ \sum_{p,q}\left[\frac{U}{2}\hat{n}_{p,q}(\hat{n}_{p,q}-1) - (\mu - \varepsilon_{p,q})\hat{n}_{p,q}\right]. \quad (3)\end{aligned}$$

The order parameter $\phi_{p,q}$ is zero for the MI phase and finite for the SF phase. The Hamiltonian in Eq. (3) can be considered as the sum of the single-site Hamiltonian

$$\begin{aligned}\hat{h}_{p,q} = &-[J_x e^{i2\pi\alpha q}(\phi^{*}_{p+1,q}\hat{b}_{p,q} - \phi^{*}_{p+1,q}\phi_{p,q}) + \text{H.c.}] \\ &- [J_y(\phi^{*}_{p,q+1}\hat{b}_{p,q} - \phi^{*}_{p,q+1}\phi_{p,q}) + \text{H.c.}] \\ &+ \frac{U}{2}\hat{n}_{p,q}(\hat{n}_{p,q}-1) - (\mu - \varepsilon_{p,q})\hat{n}_{p,q}. \quad (4)\end{aligned}$$

We can therefore diagonalize the Hamiltonian for each site separately. To compute the ground state of the system, we use the site-dependent Gutzwiller ansatz. That is, the ground state of the system is the direct product of the ground states of all the sites,

$$|\Psi_{\text{GW}}\rangle = \prod_{p,q}|\psi\rangle_{p,q} = \prod_{p,q}\sum_{n=0}^{N_{\text{b}}} c_n^{(p,q)}|n\rangle_{p,q}, \quad (5)$$

where N_b is the highest occupation number basis state and $c_n^{(p,q)}$ are the complex coefficients of the ground state $|\psi\rangle_{p,q}$ at the site (p, q) with the normalization condition $\sum_n |c_n^{(p,q)}|^2 = 1$. Then, the SF order parameter at the lattice site (p, q) is

$$\phi_{p,q} = \langle\Psi_{\text{GW}}|\hat{b}_{p,q}|\Psi_{\text{GW}}\rangle = \sum_{n=0}^{N_{\text{b}}}\sqrt{n}\,c_{n-1}^{(p,q)*}c_n^{(p,q)}. \quad (6)$$

Based on the definition of $|\Psi_{\text{GW}}\rangle$ in Eq. (5), the MI state with density or occupancy $\rho = m$ is

$$|\Psi_{\text{GW}}\rangle_{\text{MI}}^{m} = \prod_{p,q} c_m^{(p,q)}|m\rangle_{p,q}, \quad (7)$$

with the condition $|c_m^{(p,q)}|^2 = 1$. Considering the above expression, it is evident that $\phi_{p,q}$ is zero in the MI phase of the system. But $\phi_{p,q}$ is finite for the SF phase as more than one occupation number state contribute to $|\psi\rangle_{p,q}$. As the intersite coupling is through $\phi_{p,q}$, it cannot describe strongly correlated FQH states. For this reason, previous works have relied on CGMF [35] and RCMF [36] to obtain FQH states in BHM. In the present work, to obtain the ground state, the mean-field Hamiltonian is diagonalized for each lattice site with $N_{\text{b}} = 10$ using initial guess of $\phi_{p,q}$. After diagonalization, the ground state is retained as the state $|\psi\rangle_{p,q}$ of the site in $|\Psi_{\text{GW}}\rangle$. In addition, using $|\psi\rangle_{p,q}$, a new $\phi_{p,q}$ is computed and this cycle is continued until convergence.

B. Cluster Gutzwiller mean-field theory

From the expression of $\hat{H}^{\text{MF}}$ in Eq. (3), and as mentioned earlier, it is evident that the nearest-neighbor hopping or the intersite coupling is incorporated through the order parameter $\phi_{p,q}$. Thus, the SGMF theory does not describe the intersite correlation very accurately. The CGMF remedy this by including the hopping term exactly within the lattice sites of a cluster. For this, consider that the system size is $K \times L$ and it is divided into W clusters of size $M \times N$, that

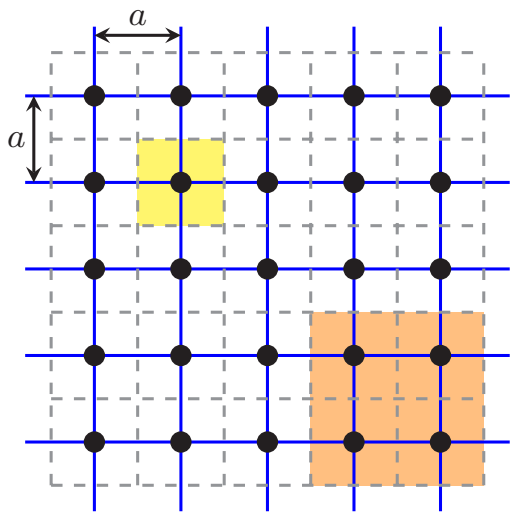

FIG. 1. The solid blue lines between the lattice sites represent the intersite bonds. The gray dashed lines demarcate cells around each lattice site, which are used in representing cluster or attributing properties to each of the lattice sites. For illustration, one of the cells is highlighted in yellow and as an example a 2×2 cluster is identified with orange color.

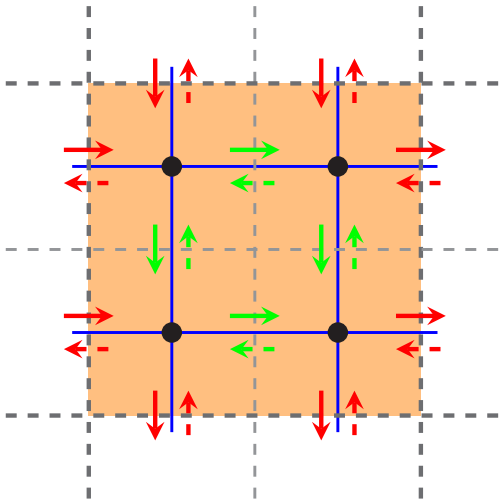

FIG. 2. A 2×2 cluster within the lattice. The light and bold dashed lines marked boundaries of cells and cluster, respectively. The solid (dashed) green (light gray) arrows represent the exact hopping term (Hermitian conjugate) within the cluster. Similarly, the solid (dashed) red (gray) arrows represent approximate hopping term (Hermitian conjugate) across clusters with one order of ϕ and operator.

is, $W = (K \times L)/(M \times N)$. Here, K, L, M, N, $W \in \mathbb{N}$. A schematic description of a cluster or a representation of a cell around a lattice site used while representing ρ are shown in Fig. 1. Then, for the homogeneous systems, the limit of infinite extent is obtained through the periodic boundary conditions. Like in the SGMF theory, we can define a cluster Hamiltonian and total Hamiltonian is the sum of all the cluster Hamiltonians [44]. To derive the Hamiltonian for CGMF, we decompose the hopping part of the Hamiltonian in two terms. The first term is the exact hopping term for intersite coupling within the cluster and the second term defines intersite coupling for the sites at the boundary through mean field $\phi_{p,q}$. The Hamiltonian for a cluster can be written as

$$\begin{aligned}\hat{H}_C = &- {\sum_{p,q\in C}}' [(e^{i2\pi\alpha q} J_x \hat{b}^\dagger_{p+1,q} \hat{b}_{p,q} + \text{H.c.}) \\ &+ (J_y \hat{b}^\dagger_{p,q+1} \hat{b}_{p,q} + \text{H.c.})] \\ &- \sum_{p,q\in\delta C} [(e^{i2\pi\alpha q} J_x \phi^*_{p+1,q} \hat{b}_{p,q} + \text{H.c.}) \\ &+ (J_y \phi^*_{p,q+1} \hat{b}_{p,q} + \text{H.c.})] \\ &+ \sum_{p,q\in C} \left[\frac{U}{2} \hat{n}_{p,q}(\hat{n}_{p,q} - 1) - (\mu - \varepsilon_{p,q})\hat{n}_{p,q} \right], \quad (8)\end{aligned}$$

where the prime in the summation of the first term is to indicate that $(p+1, q), (p, q+1) \in C$ and δC represents the lattice sites at the boundary of the cluster. The order parameter $\phi^*_{p+1,q} = \langle \hat{b}^\dagger_{p+1,q} \rangle$ with $(p+1, q) \notin C$ defines the order parameter at the boundary of the neighboring cluster and is required to describe the intercluster hopping along the x direction. Similarly, $\phi^*_{p,q+1} = \langle \hat{b}^\dagger_{p,q+1} \rangle$ with $(p, q+1) \notin C$. Schematically, the clusters are conveniently represented in terms of cells. In Fig. 2, the cells of a 2×2 cluster and neighboring clusters are highlighted.

To obtain the ground state with CGMF, we diagonalize the cluster Hamiltonian and the ground state of the cluster in the Fock basis is

$$|\Psi_c\rangle = \sum_{n_0,n_1\ldots,n_{m'}} C_{n_0,n_1,\ldots,n_{m'}} |n_0, n_1, \ldots, n_{m'}\rangle, \quad (9)$$

where $m' = (M \times N) - 1$ and n_i is the index of the occupation number state of ith lattice site within the cluster, and $C_{n_0,n_1,\ldots,n_{m'}}$ is the amplitude of the cluster Fock state $|n_0, n_1, \ldots, n_{m'}\rangle$. The above definition can be written in a more compact form using the index quantum number $\ell \equiv \{n_0, n_1, \ldots, n_{m'}\}$ as

$$|\Psi_c\rangle = \sum_\ell C_\ell |\Phi_c\rangle_\ell, \quad (10)$$

where $|\Phi_c\rangle_\ell$ represents the cluster basis state $|n_0, n_1 \ldots, n_{m'}\rangle$. The ground state of the entire $K \times L$ lattice, like in SGMF, is the direct product of the cluster ground states

$$\left|\Psi^c_{\text{GW}}\right\rangle = \prod_k |\Psi_c\rangle_k, \quad (11)$$

where k is the cluster index and varies from 1 to $W = (K \times L)/(M \times N)$. The SF order parameter ϕ is computed similarly to Eq. (6) as

$$\phi_{p,q} = \left\langle \Psi^c_{\text{GW}} \right| \hat{b}_{p,q} \left| \Psi^c_{\text{GW}} \right\rangle. \quad (12)$$

As mentioned in the previous works [34,35], the convergence is very sensitive to the initial conditions, and to accelerate

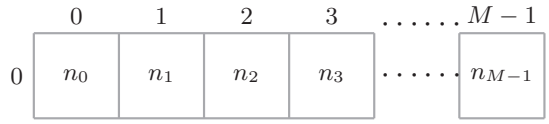

FIG. 3. The $M \times 1$ row of a cluster with occupation number $n_0, n_1, \ldots, n_{M-1}$. Each square box represents a lattice site and each of n_i corresponds to ith lattice site in that row. Here, n_i runs from 0 to $N_b - 1$ for each lattice site.

convergence we use the method of successive overrelaxation [48].

C. Exact diagonalization method

For an $M \times N$ lattice, the computations with ED method are done with the BH Hamiltonian

$$\hat{H} = -\sum_{\substack{0\leqslant p<M \\ 0\leqslant q<N}} [(J_x e^{i2\pi\alpha q}\hat{b}^{\dagger}_{p+1,q}\hat{b}_{p,q} + J_y \hat{b}^{\dagger}_{p,q+1}\hat{b}_{p,q}) + \text{H.c.}] + \sum_{\substack{0\leqslant p<M \\ 0\leqslant q<N}} \frac{U}{2}\hat{n}_{p,q}(\hat{n}_{p,q} - 1). \quad (13)$$

Here, μ is not required as, unlike the mean-field theories, the number of atoms is fixed and the computations are in the corresponding Hilbert space. The Hilbert space is spanned by the states $|\Psi_c\rangle$, which like in CGMF can be considered as states of one $M \times N$ cluster, and the ground state is obtained by diagonalizing the Hamiltonian matrix. For compact notation, we consider each $|\Psi_c\rangle$ is a direct product of N row states, and each row state is represented as

$$|\phi\rangle_m = \prod_{i=0}^{M-1} |n_i\rangle, \quad (14)$$

where $0 \leqslant i \leqslant M-1$ are lattice sites along x direction, $|n_i\rangle$ is the occupation number state at ith lattice site, and $m \equiv \{n_0, n_1, \ldots, n_{M-1}\}$ is an index quantum number of the row state. The schematic representation of a row state is shown in Fig. 3. Thus, one of the cluster states can be written as

$$|\Phi_c\rangle_\ell = \prod_{j=0}^{N-1} |\phi^j\rangle_{m^j} = \prod_{j=0}^{N-1}\prod_{i=0}^{M-1} |n_i^j\rangle, \quad (15)$$

where $0 \leqslant j \leqslant N-1$ represent a row of the cluster as shown in Fig. 4, and we have introduced cluster state index quantum number $\ell \equiv \{n_0^0, n_1^0, \ldots, n_{M-1}^0, n_0^1, n_1^1, \ldots, n_{M-1}^1, \ldots, n_0^{N-1}, n_1^{N-1}, \ldots, n_{M-1}^{N-1}\}$, which is essentially equivalent to writing $\ell \equiv \{m^0, m^1, \ldots, m^{N-1}\}$. In short, as shown in Fig. 4 there is a hierarchy of states: the single-site occupation number states $|n_i^j\rangle$, the row states $|\phi\rangle_m$, and cluster states $|\Phi_c\rangle_\ell$.

Now to construct the Hilbert space, consider the total number of atoms to be N_a, and for the present work, we consider low density $N_a \ll M \times N$. We can therefore consider the occupation number state at each lattice site to vary from say $|0\rangle$ to $|1\rangle$, and consider the total number of atoms in the row states $|\phi\rangle_m$ as $0 \leqslant \sum_i n_i^j \leqslant \min(M, N_a)$. However, the cluster states $|\Phi_c\rangle_\ell$ are direct product states of $|\phi\rangle_m$ such that the total number of atoms in $|\Phi_c\rangle_\ell$ is N_a, that is,

$$\sum_{i=0}^{M-1}\sum_{j=0}^{N-1} n_i^j = N_a. \quad (16)$$

After diagonalizing the Hamiltonian in Eq. (13) (for details, see the appendix), we can get the ground state as

$$|\Psi_c\rangle = \sum_\ell C_\ell |\Phi_c\rangle_\ell, \quad (17)$$

where C_ℓ is the coefficient of the cluster state and normalization of the state is ensured through the condition $\sum_\ell |C_\ell|^2 = 1$. The normalization, however, is guaranteed as the Hamiltonian is Hermitian. As explained in the appendix, the general features of the ED method described here can be extended to the CGMF theory to compactify the Fock space used in the computations.

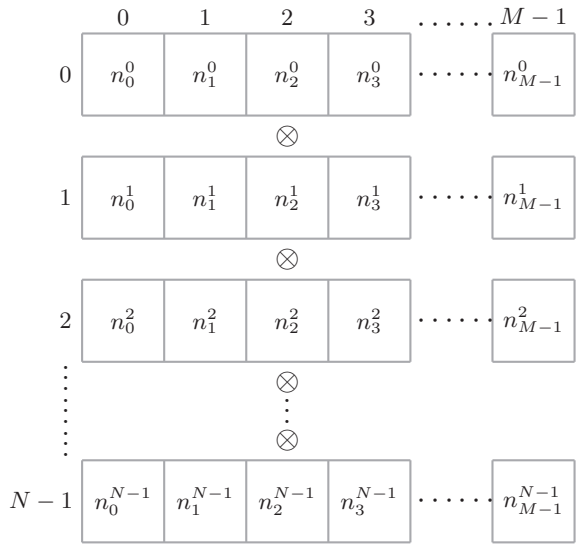

FIG. 4. The $M \times N$ cluster with occupation number $n_0^j, n_1^j, \ldots, n_{M-1}^j$ for jth row of the cluster. Each square box represents a lattice site and each of n_i^j corresponds to each jth row of cluster and ith lattice site in that row. Here, n_i^j runs from 0 to $N_b - 1$ for each lattice site.

III. RESULTS AND DISCUSSIONS

To examine the effect of additional correlation in the CGMF compared to SGMF, we compute the phase diagram using the two methods in the presence of an artificial gauge field. For the SGMF, we choose the basis size $N_b = 10$, that is, the basis set of each lattice site is $\{|0\rangle_{p,q}, |1\rangle_{p,q}, \ldots, |9\rangle_{p,q}\}$. For the CGMF computations, we consider a cluster basis consisting of single-site occupation number states $\{|0\rangle, |1\rangle\}$. As an example, the $\rho = 1$ Mott lobe obtained from SGMF and CGMF with 3×2 clusters for $\alpha = 1/3$ is shown in Fig. 5. Based on the figure, the Mott lobe obtained from the CGMF is larger than the SGMF. This indicates that the CGMF provides a better description of the strongly correlated state like the MI phase better. The other important observation from the figure is

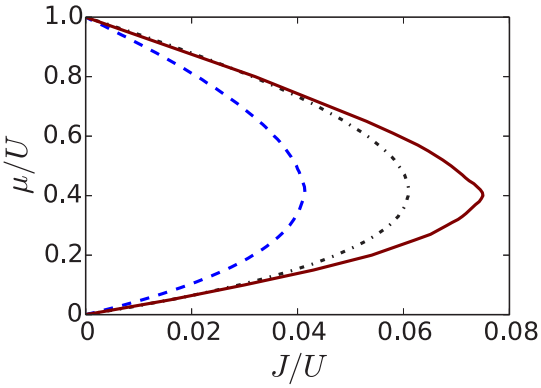

FIG. 5. MI-SF phase boundary around $\rho = 1$ Mott lobe with $\alpha = 0$ from SGMF theory (blue dashed line). For $\alpha = 1/3$, from SGMF (black dot-dashed line) and from 3×2 CGMF theory (brown solid line). From the CGMF calculation enhancement in the phase boundary is obtained.

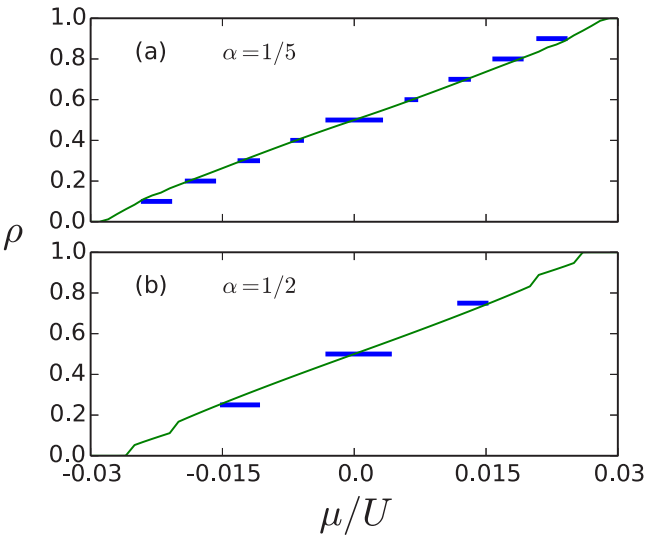

FIG. 6. The number density ρ with synthetic magnetic field $\alpha > 0$. The SF states are compressible; as a result, ρ varies linearly with μ, which correspond to the green curves. The incompressible QH states correspond to constant ρ (blue lines) or plateaus for specific values of filling factor ν. (a) $\alpha = 1/5$ and the plateaus correspond to $\nu = n/2, n = 1, 2, \ldots, 9$. (b) $\alpha = 1/2$ and the plateaus correspond to $\nu = 1/2,\ 1$, and $3/2$.

that the artificial gauge field enhances the Mott lobe. This is expected as the synthetic magnetic field induced cyclotron motion suppresses the itinerant character of atoms in the SF phase and supports the MI phase due to the localization effect [49]. Our phase diagram from the SGMF theory is consistent with the results of Ref. [34].

The CGMF computations are done with clusters which are integer multiple of the magnetic unit cell. As we consider a system where the flux Φ is staggered along the y axis, for $\alpha = 1/N$, a $1 \times N$ cluster forms a magnetic unit cell. We, however, find that except for a $\pi/2$ rotation the results are identical to $N \times 1$ cluster. This is due to the coupling of motion along x and y through the interparticle interaction. The states obtained are classified based on the compressibilty $\kappa = \partial\rho/\partial\mu$, where the density $\rho = \sum_j \langle\psi_c|\,\hat{n}_j\,|\psi_c\rangle\,/(K \times L)$. For the QH states, $\kappa = 0$ or it is incompressible, and $\kappa > 0$ for the SF states. As a result, QH states manifest as plateaus in $\rho(\mu)$ for different ν and it is linear for the SF phase. Thus, in Fig. 6 the horizontal lines indicating constant ρ define the existence of QH states. Here, for simplicity and to be consistent with the experimental realizations we consider isotropic hopping, $J_x = J_y = J$, and repulsive on-site interaction, $U > 0$.

A. Homogeneous system

Based on our results, only the QH states for $\alpha = 1/4$ and $\nu = 1/2,\ 1,\ 3/2$, and 2 are ground states when $J/U \approx 0.01$, and the competing SF state is metastable. For the mentioned values, the QH state is the ground state over a small range of μ centered around $-0.019U$, $-0.014U$, $-0.007U$, and $0.000U$, respectively. For the other combination of α and ν, the SF and QH states are ground and metastable states, respectively. In general, for different αs, the energy difference between the SF and QH states $\Delta E \approx 10^{-3}\,U$. For the parameters of experimental interest $U/\hbar = 130$ Hz [50] and we get $\Delta E \approx 10^{-2}$ nK. This implies stringent bounds on the thermal excitations during the state preparation to obtain QH states. One feature of the CGMF results which distinguishes the QH states from the SF states is the energy. For the QH state, the energy decreases with increasing cluster size. For example, the QH state of $\alpha = 1/4$ with $\nu = 1/2$ and $\mu = -0.02U$ has energy $-0.0031U$ and $-0.0046U$ with 2×4 and 4×4 clusters, respectively. Whereas for the SF state, the energy remains almost unchanged, as it is $-0.0042U$ and $-0.0045U$, respectively. Thus, the QH state emerges as the ground state with the 4×4 cluster. Here, the key point is not the values of the energies per se, but the importance of having better correlation effects to obtain QH states. These trends arise from the better description of the hopping term with larger cluster size. Besides $\alpha = 1/4$, the other values of α we have studied in detail are $1/5$ and $1/2$. Results for each of the α considered are described.

1. $\alpha = 1/5$

For the hard-core boson limit, where $\rho < 1$, with $\alpha = 1/5$, we obtain QH states for $\nu = n/2$, where $n = 1,\ 2,\ \ldots,\ 9$ with 2×5 cluster. The case of $\nu = 1/2$ was reported by Natu *et al.* [35] and as shown in Fig. 7 our results are consistent. Among the new FQH states, we have identified $\nu = 3/2,\ 7/2$, and $9/2$ as stripe phase, whereas it is homogeneous for $\nu = 5/2$. In addition, we obtain stripe phase integer QH (IQH) states for $\nu = 1,\ 2,\ 3$, and 4 fillings. The other distinguishing feature of $\nu = 2$ and $5/2$ is that the competing SF states have zigzag order in ρ and ϕ. On increasing the cluster size to 3×5, the QH states with stripe geometry are transformed to checkerboard, and the density contrast is reduced on increasing the cluster size to 4×5. We also obtain the same QH states but rotated by $\pi/2$ when the cluster sizes are 5×2, 5×3, and 5×4. For example, with 5×2 cluster, the stripe order is horizontal, while it is vertical for 2×5 cluster. Considering this property of QH states, and noting that 1×5 is the magnetic unit cell for $\alpha = 1/5$, an accurate description of the FQH state is possible

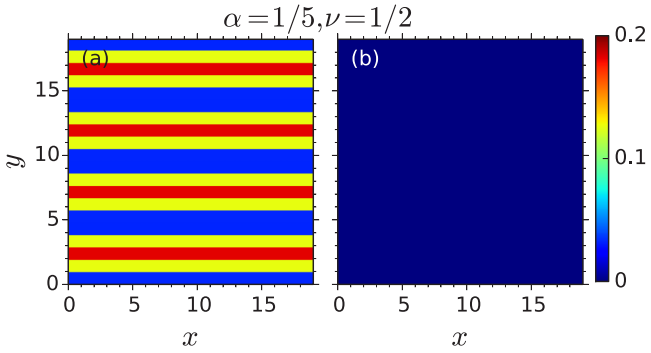

FIG. 7. (a) Hall state with stripe phase for $\alpha = 1/5$, $\nu = 1/2$ with average number $\rho = 0.1$. (b) Zero SF order parameter ϕ for the same.

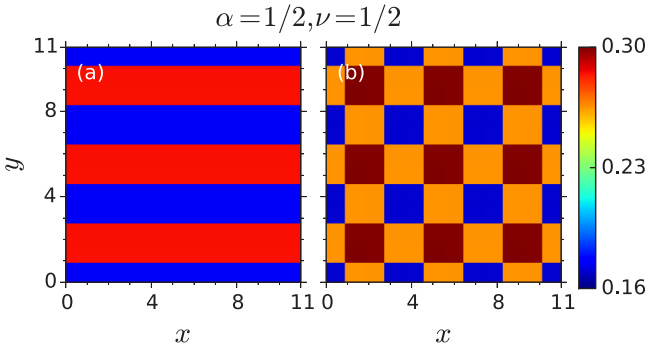

FIG. 8. The variation in the lattice occupancy ρ of the FQH states with stripe and checkerboard geometry for high flux $\alpha = 1/2$ obtained using CGMF for the filling factor $\nu = 1/2$. This is a metastable state, and the ground state is in SF phase. (a) The FQH state has average number density $\rho = 0.25$ with stripe pattern and it is obtained from the 2×4 cluster. (b) The checkerboard FQH state with the same number density obtained from CGMF theory with the 4×4 cluster. In both the cases, the ground states, SF phase, like the FQH state, have stripe and checkerboard geometries with 2×4 and 4×4 clusters, respectively.

with 5×5 cluster. With this cluster size, the operator part of the hopping term in Eq. (1) is exact along the x and y axes within the cluster symmetrically. For example, with the 2×5 cluster, hopping along the x axis has a contribution through the mean field after $2a$ while it is $5a$ for the 5×5 cluster, where a is lattice constant.

2. $\alpha = 1/4$

For the case of $\alpha = 1/4$, we obtain QH states for $\nu = n/2$, where $n = 1, 2, \ldots, 7$, with 2×4 and 4×4 clusters. The FQH states for $\nu = 1/2, 3/2, 5/2$ have stripe order with the 2×4 cluster; however, like in the case of $\alpha = 1/5$ they are transformed into checkerboard order with the 4×4 cluster. That is, the geometry depends on the cluster size. Furthermore, as we increase the cluster size to 4×8, the FQH state with $\nu = 1/2$ filling remains qualitatively unchanged. For the IQH states, the $\nu = 1$ and 3 have stripe order with the 2×4 cluster and checkerboard order with the 4×4 cluster. But, the IQH state corresponding to $\nu = 2$ has homogeneous density order. It must be mentioned that the thermodynamic limit, due to the coupling of neighbouring clusters through ϕ, does not apply to CGMF description of QH states where $\phi = 0$. This limits the applicability of the theory to finite-size systems relevant to experimental realizations in optical lattices. On the other hand, for the competing SF state, a large lattice size, due to the finite ϕ, corresponds to the thermodynamic limit.

3. $\alpha = 1/2$

For the high flux $\alpha = 1/2$, we again consider 2×4 and 4×4 clusters in the CGMF computations. It must be emphasized that $\alpha = 1/2$ is relevant to the recent experimental realizations [15,16]. For this value of α, we obtain the QH states for $\nu = 1/2$, 1, and $3/2$ from both the clusters. Like in $\alpha = 1/5$ and $1/4$ cases, the $\nu = 1/2$ and $3/2$ FQH and SF states are stripe and homogeneous phases, respectively, with the 2×4 cluster. The structure of the FQH state is transformed into checkerboard with the 4×4 cluster. This transformation is visible from the variation in ρ for the case of $\nu = 1/2$ as shown in Fig. 8. For $\nu = 1$ the IQH and SF states are homogeneous for both the cluster sizes. An important observation is that the homogeneous QH state is generic to $\rho = 0.5$ for the values of α considered in the present work.

B. Inhomogeneous system

The simplest modification to the homogeneous system for comparison with experimental realizations is to impose hard-wall boundary conditions. This corresponds to the 2D optical lattice realization similar to the case of homogeneous BEC in a box potential [51]. With the hard-wall boundary we recover the QH states for all αs described earlier, and energies remain unchanged. The competing SF states, on the other hand, have higher energies with hard-wall boundary. In the present work, the largest cluster size in the CGMF computations required to encapsulate one magnetic unit cell along the y axis and maintain symmetry in the exact description of hopping term is 5×5 for $\alpha = 1/5$. For this reason, we focus on the properties of the QH states of $\alpha = 1/5$. The other QH states are qualitatively similar but computationally less demanding. It is also to be emphasized that the results of single cluster with hard-wall boundary is equivalent to ED. Because with the hard-wall boundary, we do not employ the periodic boundary condition, thus the mean-field part vanishes and the Hamiltonian becomes exact.

The IQH state for $\nu = 1$ with different cluster sizes are shown in Fig. 9, which has stripe geometry. Like in the homogeneous case, the stripe geometry is transformed into checkerboard geometry with the 3×5 cluster. However, the most important observation is that $\rho(x, y)$ obtained from the 5×5 cluster, although checkerboard in structure, is very different from that of the 3×5 and 4×5 clusters, which are shown in Fig. 10. An observable property to identify the QH states is the two-point correlation function $\langle \hat{b}_x^\dagger(y)\hat{b}_0(y)\rangle$, where the expectation is computed with respect to $|\psi_c\rangle$, and the results from the 5×5 cluster are as shown in Fig. 11(a). The two-point correlation function is closely related to another important property, the one-body density matrix (OBDM) [52,53]

$$\rho_{k,l} = \langle \psi_c | \hat{b}_l^\dagger \hat{b}_k | \psi_c \rangle, \tag{18}$$

where $k \equiv (x, y)$ and $l \equiv (x', y')$ are lattice indices. From the OBDM, one can compute the condensate fraction based on

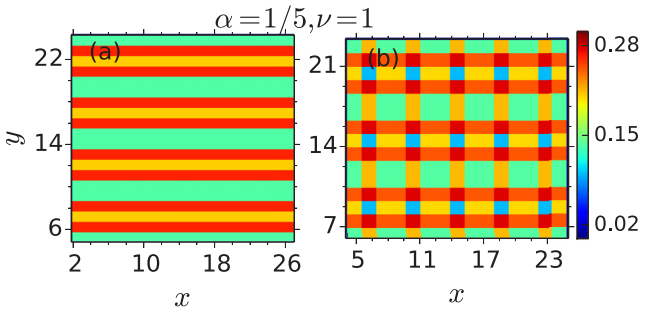

FIG. 9. Density distribution of the IQH state for $\alpha = 1/5$ and $\nu = 1$ with hard-wall boundary. The average density of atoms in this state is $\rho = 0.2$. (a) The IQH state has stripe geometry in the CGMF results with 2×5 clusters. (b) It is, however, transformed to checkerboard geometry when 3×5 clusters are considered in the CGMF computations.

the Penrose-Onsagar criterion [54] and von Neumann entropy [55–57]. These measures are particularly relevant to the ED method and are described while discussing the ED results. The correlation function, as recently proposed, could be measured with quantum probes [58,59]. As reported in a recent work [60], it can be seen from the figure that $\langle \hat{b}_x^\dagger(y)\hat{b}_0(y)\rangle$ decays as inverse power law at the edge. However, in the bulk, as it is gaped, it initially shows exponential decay $\langle \hat{b}_x^\dagger(y)\hat{b}_0(y)\rangle \propto e^{-x/\xi}$ but it is power law when $x > K/2$ or on reaching the opposite edge. Here, ξ is the correlation length of the system and as mentioned earlier, K is the size of the cluster along x. For the SF state with the 5×3 cluster, as seen from Fig. 11(b), the correlation through the bulk does not show any nonmonotonicity. Here, we have considered the 5×3 cluster as the correlation in the bulk is not sensitive to the size of the cluster.

The other envelope potential which is of experimental relevance is the harmonic oscillator potential. Then, the energy offset $\varepsilon_j = \Omega j^2 = \Omega(p^2 + q^2)$, where Ω is the strength of the potential. To encapsulate the envelope potential, we consider a larger lattice size ranging from 40×40 to 80×80. We, however, find that the QH states are absent. This is due to the nature of $\partial\varepsilon_j/\partial j$: It monotonically increases and does not favor incompressible phase like QH state. One possible modification

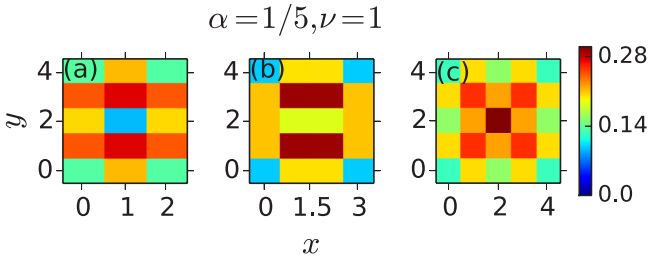

FIG. 10. The variations in ρ for IQH state of $\alpha = 1/5$ and $\nu = 1$ for a single cluster of different sizes. (a) The result from 3×5 cluster has checkerboard pattern, and is the unit cell of the large lattice shown in Fig. 9. (b) 4×5 cluster has less variations in ρ compared to 3×5. (c) 5×5 cluster shows a rich variation in ρ and unlike in panels (a) and (b) the central lattice site has maxima in density.

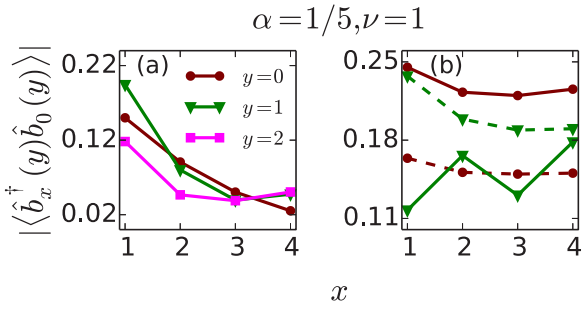

FIG. 11. Two-point correlation function for low flux $\alpha = 1/5$ with the 5×5 and 5×3 clusters for the QH and SF states, respectively. The correlation is calculated along the x direction for the single cluster. Here $y = 0$ and 1 represent the edge and bulk, respectively. (a) As a characteristic feature of QH state, the correlation function of the $\nu = 1$ IQH state decays nonmonotonically in the bulk, and there is no difference between the hard-wall and periodic boundary conditions. (b) For the corresponding SF state, there is no trend in the bulk correlation function with hard-wall boundary (solid green line with down triangle symbol), but it decays monotonically at the edge (solid brown line with circle symbol). With periodic boundary condition (dashed lines), the range of values change, and both the bulk and edge exhibit monotonic decay in correlation.

is that the beam waist w of the laser beam generating the envelope potential is large, so that the effective envelope potential is still a Gaussian $V_G = U_0 e^{-(x^2+y^2)/w}$. Here, the amplitude of the Gaussian potential U_0 is proportional to the intensity of the laser beam. With this potential, $\partial\varepsilon_j/\partial j$ also decays exponentially and we find that the QH states exist for $U_0 \leqslant 10^{-3}U$. At higher values of U_0, only the SF state is obtained from the CGMF computations.

C. ED results

With the ED computations [52,53], we focus our attention on the $\alpha = 1/4$, which have QH states as ground state. For this, we in particular consider $\nu = 1/2$ FQH state with cluster sizes 4×4, 4×8, and 4×12. Here, as alluded earlier, we distinguish the QH states and SF states based on the Penrose-Onsager criterion [54] and von Neumann entropy [55–57]. For this, we compute OBDM in Eq. (18) and then digonalize it. Following the Penrose-Onsager criterion, the state is SF if $p_m = \lambda_m^{\mathrm{OBDM}}/N \approx 1$, where $\lambda_m^{\mathrm{OBDM}}$ is the largest eigenvalue of the OBDM, and N is the total number of atoms. In contrast, for the QH states $p_m < 1$. Our results are in agreement with this; for example, with the 4×4 cluster, the values of p_m are 0.56 and 0.89 for the FQH and SF states, respectively. Once the OBDM is diagonalized, the von Neumann entropy is defined as

$$S = -\sum_i^M p_i \ln(p_i), \tag{19}$$

where $p_i = \lambda_i^{\mathrm{OBDM}}/N$ and M is dimension of the OBDM. As the von Neumann entropy is a measure of entanglement, it is higher for the more correlated states like QH states compared to the SF states. For the states considered, the values of S are 1.0 and 0.53 for the FQH and SF states, respectively. These values

indicate that the FQH state, as expected, is more entangled than the SF state. When the cluster size is increased to 4×8, the value of p_m is modified to 0.26 and 0.80 for the FQH and SF states, respectively, and the corresponding values of S are 1.84 and 0.95, respectively. We also obtain similar results for the other QH and SF states; for example, p_m is 0.33 and 0.75 for the QH and SF states respectively with the 5×5 cluster for $\alpha = 1/5$, $\nu = 1$. The corresponding value of S is 1.89 and 1.20 respectively. It is to be mentioned here that the QH and SF states obtained from the ED method have the same features, ρ and ϕ, as in CGMF results.

IV. CONCLUSIONS

Based on the results of our studies with CGMF and ED, the $\alpha = 1/4$ with $\nu = 1/2,\ 1,\ 3/2$, and 2 are the QH states which occur as ground states of the BHM with synthetic magnetic fields, and these states exist within a narrow range of μ. For other combinations of α and ν, the SF state is the ground state and the QH state exist as a metastable state. The experimental observation of a pure QH state needs tight control on the thermal excitations as the two competing states, QH and SF states, are nearly degenerate. The separation is only $\approx 10^{-2}$ nK. Furthermore, the QH state is sensitive to the nature of the envelope potential of the optical lattice. The QH states exist for very shallow Gaussian envelope potentials but cease to exist when the envelope potential is harmonic. The case of a box potential is the most promising experimentally realizable envelope potential to observe a pure QH state of BHM with a synthetic magnetic field.

ACKNOWLEDGMENTS

The results presented in the paper are based on the computations using Vikram-100, the 100TFLOP HPC Cluster at Physical Research Laboratory, Ahmedabad, India. We thank Arko Roy, S. Gautam, and S. A. Silotri for valuable discussions.

APPENDIX

To illustrate the form of the Hamiltonian in CGMF, consider the BHM Hamiltonian for a 2×2 cluster located at the bottom right of the lattice in Fig. 1 is

$$\hat{h}_c = \hat{h}_{00} + \hat{h}_{10} + \hat{h}_{01} + \hat{h}_{11},$$

where $\hat{h}_{pq}$ is the single-site Hamiltonian at the (p, q) lattice sites within the cluster. In general, if the lattice considered is $K \times L$, then the lattice sites are labeled along x (y) axis as 0, 1, ..., and $K-1$ (0, 1, ..., and $L-1$). The expressions of the single-site Hamiltonians are

$$\begin{aligned}\hat{h}_{00} = &-(J_x \hat{b}^\dagger_{1,0}\hat{b}_{0,0} + \text{H.c.}) - (J_y \hat{b}^\dagger_{0,1}\hat{b}_{0,0} + \text{H.c.}) \\ &- [J_x(\hat{b}^\dagger_{0,0}\phi_{K-1,0} - \phi^*_{0,0}\phi_{K-1,0}) + \text{H.c.}] \\ &- [J_y(\hat{b}^\dagger_{0,0}\phi_{0,L-1} - \phi^*_{0,0}\phi_{0,L-1}) + \text{H.c.}] \\ &+ \frac{U}{2}\hat{n}_{0,0}(\hat{n}_{0,0} - 1) - \tilde{\mu}\hat{n}_{0,0}, \end{aligned} \tag{A1}$$

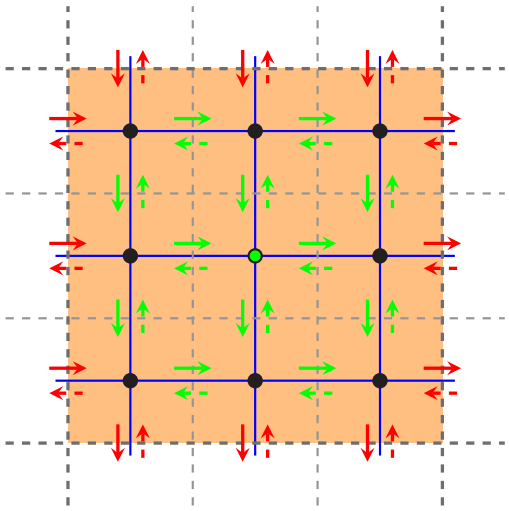

FIG. 12. A 3×3 cluster and form of the hopping terms between the lattice sites. For clarity, each lattice site is represented in terms of cells. The light and bold dashed lines mark boundaries of cells and cluster, respectively. The solid (dashed) light gray arrows represent the exact hopping term (Hermitian conjugate) within the cluster. Similarly, the solid (dashed) gray arrows represent approximate hopping term (Hermitian conjugate) across clusters with one order of ϕ and operator. The hopping terms involving the central lattice site, represented in green color, are all exact.

$$\begin{aligned}\hat{h}_{10} = &-(J_y \hat{b}^\dagger_{1,1}\hat{b}_{1,0} + \text{H.c.}) \\ &- [J_x(\phi^*_{2,0}\hat{b}_{1,0} - \phi^*_{2,0}\phi_{1,0}) + \text{H.c.}] \\ &- [J_y(\hat{b}^\dagger_{1,0}\phi_{1,L-1} - \phi^*_{1,0}\phi_{1,L-1}) + \text{H.c.}] \\ &+ \frac{U}{2}\hat{n}_{1,0}(\hat{n}_{1,0} - 1) - \tilde{\mu}\hat{n}_{1,0}, \end{aligned} \tag{A2}$$

$$\begin{aligned}\hat{h}_{01} = &-(J_x \hat{b}^\dagger_{1,1}\hat{b}_{0,1} + \text{H.c.}) \\ &- [J_x(\hat{b}^\dagger_{0,1}\phi_{K-1,1} - \phi^*_{0,1}\phi_{K-1,1}) + \text{H.c.}] \\ &- [J_y(\phi^*_{0,2}\hat{b}_{0,1} - \phi^*_{0,2}\phi_{0,1}) + \text{H.c.}] \\ &+ \frac{U}{2}\hat{n}_{0,1}(\hat{n}_{0,1} - 1) - \tilde{\mu}\hat{n}_{0,1}, \end{aligned} \tag{A3}$$

$$\begin{aligned}\hat{h}_{11} = &-[J_x(\phi^*_{2,1}\hat{b}_{1,1} - \phi^*_{2,1}\phi_{1,1}) + \text{H.c.}] \\ &- [J_y(\phi^*_{1,2}\hat{b}_{1,1} - \phi^*_{1,2}\phi_{1,1}) + \text{H.c.}] \\ &+ \frac{U}{2}\hat{n}_{1,1}(\hat{n}_{1,1} - 1) - \tilde{\mu}\hat{n}_{1,1}, \end{aligned} \tag{A4}$$

where the operators and ϕ with index $(K-1)$ and $(L-1)$ embody the periodic boundary conditions along x and y directions, respectively. An important point is that with the 2×2 cluster, none of the lattice sites have an exact representation of the hopping term. The minimal cluster size which has exact hopping terms with respect to a lattice site is 3×3, and the schematic diagram is shown in Fig. 12. As seen from the figure, the hopping terms involving the central lattice site are all exact.

For illustration of ED, consider $N_a = 4$ and the size of the lattice as 4×4. Then, the number of atoms in $|\phi\rangle_m$ can range from 0 to 4, and considering that occupation number states at

each lattice sites are either $|0\rangle$ or $|1\rangle$, the possible row states are

$$|0,0,0,0\rangle, |0,0,0,1\rangle, \ldots, |1,1,1,1\rangle.$$

In total, there are 16 $|\phi\rangle_m$, and an example of $|\Phi_c\rangle_\ell$ defined as direct product of four $|\phi\rangle_m$ s is

$$|\Phi_c\rangle_\ell = |0,0,0,0\rangle \otimes |0,1,1,0\rangle \otimes |0,0,0,1\rangle \otimes |1,0,0,0\rangle.$$

Thus, the number of $|\Phi_c\rangle_\ell$ is

$${}^{M\times N}C_{N_a} = {}^{16}C_4 = 1820,$$

which is much less than the number of states $2^{16} = 65536$ required for computation with 4×4 cluster in CGMF.

The essence of ED is then to compute the Hamiltonian matrix elements between the cluster states as

$${}_{\ell'}\langle\Phi_c'|\,\hat{H}\,|\Phi_c\rangle_\ell = \prod_{k=0}^{M-1}\prod_{l=0}^{N-1}\prod_{i=0}^{M-1}\prod_{j=0}^{N-1}\langle m_k^l|\hat{H}|n_i^j\rangle, \tag{A5}$$

and then diagonalize the Hamiltonian matrix to obtain the eigenvalues and eigenvectors. Considering that the sequence of $|\Phi_c\rangle_\ell$ is not based on symmetries but rather based on the combinatorics of $|\phi\rangle_m$, the row-wise computation of Hamiltonian matrix is more efficient. In this regard, the matrix element of the hopping term along the x axis $J_x e^{i2\pi\alpha q}\hat{b}^\dagger_{p+1,q}\hat{b}_{p,q}$ can be done in the following steps:

(1) Compare the row states ${}_{m'}\langle\phi|$ and $|\phi\rangle_m$ of ${}_{\ell'}\langle\Phi_c'|$ and $|\Phi_c\rangle_\ell$, respectively. Proceed to the next step if ${}_{\ell'}\langle\Phi_c|$ and $|\Phi_c\rangle_\ell$ only differ in one of the row states, say, the first row.

(2) Consider ${}_{m'^1}\langle\phi^1|$ and $|\phi^1\rangle_{m^1}$, and compare the single-site occupation number states. Proceed to the next step if the difference in these two row states arises from the difference in the occupation number states of two neighboring lattice sites, say, the third and fourth lattice sites.

(3) The matrix element is nonzero and value is $\sqrt{n_2'(n_3'+1)}$ if $n_2' = n_2 + 1$ and $n_3' = n_3 - 1$. For the example considered, we have nonzero matrix element for the term $p = 2$ and $q = 1$.

In a similar way, for the example considered, the matrix element of the Hermitian conjugate term $J_x^* e^{-i2\pi\alpha q}\hat{b}^\dagger_{p,q}\hat{b}_{p+1,q}$ is nonzero when the first two conditions are met and the last is modified to $n_2' = n_2 - 1$ and $n_3' = n_3 + 1$. With slight modifications, the same approach can be applied to compute the matrix elements of the hopping term along the y axis. For this case, two neighboring row states should be different, and at the level of the lattice sites, the difference should be on the same column. Then, to have nonzero matrix element, the occupation numbers should satisfy conditions equivalent to the third condition in the above chain of steps. The computation of the interaction Hamiltonian matrix elements is trivial as it is diagonal and does not require comparison of states.

The general features of the hierarchical definition of states and the approach to compute the Hamiltonian matrix elements can also be adapted to the CGMF theory as well. As discussed earlier, in the CGMF theory, hopping is exact within the cluster but hopping at the boundary is considered via the mean field ϕ. Thus, for cluster of size $M \times N$, the cluster state defined in Eq. (9) is the direct product of the occupation number states at each lattice site and can be written as

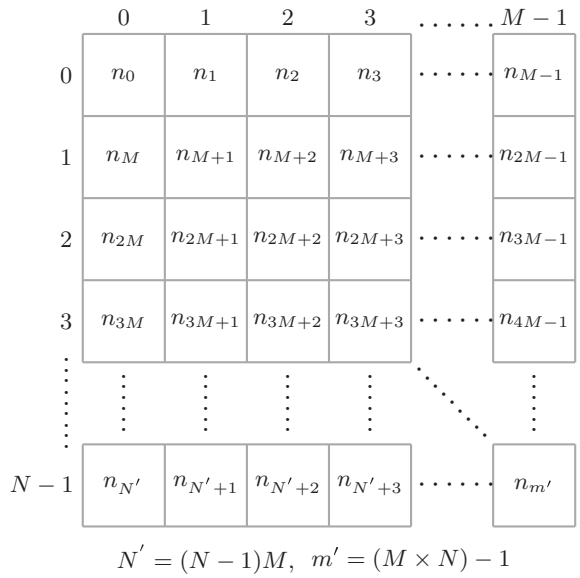

FIG. 13. The $M \times N$ cluster with occupation number $n_0, n_1, \ldots, n_{m'}$ at each lattice site for CGMF. Each square box represents a lattice site and each n_i corresponds to each i lattice site. Here, n_i runs from 0 to $N_b - 1$ for each lattice site.

$$|\Phi_c\rangle_\ell = \prod_{i=0}^{m'}|n_i\rangle, \tag{A6}$$

where $m' = (M \times N) - 1$, $i = 0, 1, \ldots, m'$ are the lattice site index, with M (N) as number of lattice sites along x (y) direction and $\ell = \{n_0, n_1, \ldots, n_{m'}\}$ as defined earlier is the index quantum number to identify each of the cluster states uniquely. For illustration, the correspondence between quantum numbers and lattice sites is shown in Fig. 13. The ground state of the CGMF Hamiltonian in Eq. (8) is obtained by using the cluster state in Eq. (A6). The Hamiltonian matrix element can be written as

$$\begin{aligned}{}_{\ell'}\langle\Phi_c|\,\hat{H}\,|\Phi_c\rangle_\ell &= \prod_{j=0}^{m'}\prod_{i=0}^{m'}\langle n_j'|\,\hat{H}\,|n_i\rangle \\ &= \langle n_0', n_1', \ldots, n_{m'}'|\,\hat{H}|n_0, n_1, \ldots, n_{m'}\rangle.\end{aligned} \tag{A7}$$

The definition of the states and computation of the matrix elements can, however, be cast in terms of the row and cluster states as in ED. With this modification, we can implement constraints on the number of atoms in the row and cluster states, thereby reducing the dimension of the Hamiltonian matrix in the CGMF. The only difference from ED is that in CGMF the intercluster hopping terms are linear in order parameter ϕ and hence connect states in Hilbert spaces with different total number of atoms. In other words, the Hamiltonian matrix in CGMF is defined with respect to Fock space. Another difference is that the diagonal terms have contribution from μ.

[1] B. P. Anderson and M. A. Kasevich, Macroscopic quantum interference from atomic tunnel arrays, Science **282**, 1686 (1998).

[2] M. Greiner, I. Bloch, O. Mandel, T. W. Hänsch, and T. Esslinger, Exploring Phase Coherence in a 2D Lattice of Bose-Einstein Condensates, Phys. Rev. Lett. **87**, 160405 (2001).

[3] M. Greiner, O. Mandel, T. Esslinger, T. W. Hänsch, and I. Bloch, Quantum phase transition from a superfluid to a Mott insulator in a gas of ultracold atoms, Nature (London) **415**, 39 (2002).

[4] M. Lewenstein, A. Sanpera, V. Ahufinger, B. Damski, A. Sen(De), and U. Sen, Ultracold atomic gases in optical lattices: Mimicking condensed matter physics and beyond, Adv. Phys. **56**, 243 (2007).

[5] O. Morsch and M. Oberthaler, Dynamics of Bose-Einstein condensates in optical lattices, Rev. Mod. Phys. **78**, 179 (2006).

[6] I. Bloch, J. Dalibard, and W. Zwerger, Many-body physics with ultracold gases, Rev. Mod. Phys. **80**, 885 (2008).

[7] D. Jaksch, C. Bruder, J. I. Cirac, C. W. Gardiner, and P. Zoller, Cold Bosonic Atoms in Optical Lattices, Phys. Rev. Lett. **81**, 3108 (1998).

[8] M. P. A. Fisher, P. B. Weichman, G. Grinstein, and D. S. Fisher, Boson localization and the superfluid-insulator transition, Phys. Rev. B **40**, 546 (1989).

[9] J. Hubbard, Electron correlations in narrow energy bands, Proc. R. Soc. London, Ser. A **276**, 238 (1963).

[10] Y.-J. Lin, R. L. Compton, A. R. Perry, W. D. Phillips, J. V. Porto, and I. B. Spielman, Bose-Einstein Condensate in a Uniform Light-Induced Vector Potential, Phys. Rev. Lett. **102**, 130401 (2009).

[11] Y.-J. Lin, R. L. Compton, K. Jimenez-Garcia, J. V. Porto, and I. B. Spielman, Synthetic magnetic fields for ultracold neutral atoms, Nature (London) **462**, 628 (2009).

[12] J. Dalibard, F. Gerbier, G. Juzeliūnas, and P. Öhberg, Colloquium: Artificial gauge potentials for neutral atoms, Rev. Mod. Phys. **83**, 1523 (2011).

[13] Y.-J. Lin, R. L. Compton, K. Jimenez-Garcia, W. D. Phillips, J. V. Porto, and I. B. Spielman, A synthetic electric force acting on neutral atoms, Nat. Phys. **7**, 531 (2011).

[14] M. Aidelsburger, M. Atala, S. Nascimbène, S. Trotzky, Y.-A. Chen, and I. Bloch, Experimental Realization of Strong Effective Magnetic Fields in an Optical Lattice, Phys. Rev. Lett. **107**, 255301 (2011).

[15] M. Aidelsburger, M. Atala, M. Lohse, J. T. Barreiro, B. Paredes, and I. Bloch, Realization of the Hofstadter Hamiltonian with Ultracold Atoms in Optical Lattices, Phys. Rev. Lett. **111**, 185301 (2013).

[16] H. Miyake, G. A. Siviloglou, C. J. Kennedy, W. C. Burton, and W. Ketterle, Realizing the Harper Hamiltonian with Laser-Assisted Tunneling in Optical Lattices, Phys. Rev. Lett. **111**, 185302 (2013).

[17] N. Goldman, J. C. Budich, and P. Zoller, Topological quantum matter with ultracold gases in optical lattices, Nat. Phys. **12**, 639 (2016).

[18] Z. F. Ezawa, *Quantum Hall Effects: Recent Theoretical and Experimental Developments*, 3rd ed. (World Scientific, Singapore, 2013).

[19] X.-G. Wen, Theory of the edge states in fractional quantum Hall effects, Int. J. Mod. Phys. B **06**, 1711 (1992).

[20] G. Murthy and R. Shankar, Hamiltonian theories of the fractional quantum Hall effect, Rev. Mod. Phys. **75**, 1101 (2003).

[21] T. H. Hansson, M. Hermanns, S. H. Simon, and S. F. Viefers, Quantum Hall physics: Hierarchies and conformal field theory techniques, Rev. Mod. Phys. **89**, 025005 (2017).

[22] D. C. Tsui, H. L. Stormer, and A. C. Gossard, Two-Dimensional Magnetotransport in the Extreme Quantum Limit, Phys. Rev. Lett. **48**, 1559 (1982).

[23] R. B. Laughlin, Anomalous Quantum Hall Effect: An Incompressible Quantum Fluid with Fractionally Charged Excitations, Phys. Rev. Lett. **50**, 1395 (1983).

[24] R. N. Palmer and D. Jaksch, High-Field Fractional Quantum Hall Effect in Optical Lattices, Phys. Rev. Lett. **96**, 180407 (2006).

[25] A. S. Sørensen, E. Demler, and M. D. Lukin, Fractional Quantum Hall States of Atoms in Optical Lattices, Phys. Rev. Lett. **94**, 086803 (2005).

[26] S. Inouye, M. R. Andrews, J. Stenger, H.-J. Miesner, D. M. Stamper-Kurn, and W. Ketterle, Observation of Feshbach resonances in a Bose-Einstein condensate, Nature (London) **392**, 151 (1998).

[27] C. Chin, R. Grimm, P. Julienne, and E. Tiesinga, Feshbach resonances in ultracold gases, Rev. Mod. Phys. **82**, 1225 (2010).

[28] K. Jiménez-García, L. J. LeBlanc, R. A. Williams, M. C. Beeler, A. R. Perry, and I. B. Spielman, Peierls Substitution in an Engineered Lattice Potential, Phys. Rev. Lett. **108**, 225303 (2012).

[29] R. E. Peierls, On the theory of diamagnetism of conduction electrons, Z. Phys. **80**, 763 (1933).

[30] D. R. Hofstadter, Energy levels and wave functions of Bloch electrons in rational and irrational magnetic fields, Phys. Rev. B **14**, 2239 (1976).

[31] M. Hafezi, A. S. Sørensen, E. Demler, and M. D. Lukin, Fractional quantum Hall effect in optical lattices, Phys. Rev. A **76**, 023613 (2007).

[32] R. N. Palmer, A. Klein, and D. Jaksch, Optical lattice quantum Hall effect, Phys. Rev. A **78**, 013609 (2008).

[33] R. O. Umucalilar and E. J. Mueller, Fractional quantum Hall states in the vicinity of Mott plateaus, Phys. Rev. A **81**, 053628 (2010).

[34] Y. Kuno, K. Shimizu, and I. Ichinose, Bosonic analogs of the fractional quantum Hall state in the vicinity of Mott states, Phys. Rev. A **95**, 013607 (2017).

[35] S. S. Natu, E. J. Mueller, and S. Das Sarma, Competing ground states of strongly correlated bosons in the Harper-Hofstadter-Mott model, Phys. Rev. A **93**, 063610 (2016).

[36] D. Hügel, H. U. R. Strand, P. Werner, and L. Pollet, Anisotropic Harper-Hofstadter-Mott model: Competition between condensation and magnetic fields, Phys. Rev. B **96**, 054431 (2017).

[37] D. S. Rokhsar and B. G. Kotliar, Gutzwiller projection for bosons, Phys. Rev. B **44**, 10328 (1991).

[38] K. Sheshadri, H. R. Krishnamurthy, R. Pandit, and T. V. Ramakrishnan, Superfluid and insulating phases in an interacting-boson model: Mean-field theory and the RPA, EPL **22**, 257 (1993).

[39] U. Bissbort and W. Hofstetter, Stochastic mean-field theory for the disordered Bose-Hubbard model, EPL **86**, 50007 (2009).

[40] P. Buonsante, V. Penna, and A. Vezzani, Fractional-filling loophole insulator domains for ultracold bosons in optical superlattices, Phys. Rev. A **70**, 061603 (2004).

[41] D. Yamamoto, Correlated cluster mean-field theory for spin systems, Phys. Rev. B **79**, 144427 (2009).
[42] P. Pisarski, R. M. Jones, and R. J. Gooding, Application of a multisite mean-field theory to the disordered Bose-Hubbard model, Phys. Rev. A **83**, 053608 (2011).
[43] T. McIntosh, P. Pisarski, R. J. Gooding, and E. Zaremba, Multisite mean-field theory for cold bosonic atoms in optical lattices, Phys. Rev. A **86**, 013623 (2012).
[44] D.-S. Lühmann, Cluster Gutzwiller method for bosonic lattice systems, Phys. Rev. A **87**, 043619 (2013).
[45] D. Jaksch and P. Zoller, Creation of effective magnetic fields in optical lattices: The Hofstadter butterfly for cold neutral atoms, New J. Phys. **5**, 56 (2003).
[46] P. G. Harper, Single band motion of conduction electrons in a uniform magnetic field, Proc. Phys. Soc. A **68**, 874 (1955).
[47] M. Ö. Oktel, M. Niţă, and B. Tanatar, Mean-field theory for Bose-Hubbard model under a magnetic field, Phys. Rev. B **75**, 045133 (2007).
[48] R. Barrett, M. Berry, T. Chan, J. Demmel, J. Donato, J. Dongarra, V. Eijkhout, R. Pozo, C. Romine, and H. van der Vorst, *Templates for the Solution of Linear Systems: Building Blocks for Iterative Methods* (SIAM, Philadelphia, PA, 1994).
[49] M. Niemeyer, J. K. Freericks, and H. Monien, Strong-coupling perturbation theory for the two-dimensional Bose-Hubbard model in a magnetic field, Phys. Rev. B **60**, 2357 (1999).
[50] M. E. Tai, A. Lukin, M. Rispoli, R. Schittko, T. Menke, D. Borgnia, P. M. Preiss, F. Grusdt, A. M. Kaufman, and M. Greiner, Microscopy of the interacting Harper-Hofstadter model in the two-body limit, Nature (London) **546**, 519 (2017).
[51] A. L. Gaunt, T. F. Schmidutz, I. Gotlibovych, R. P. Smith, and Z. Hadzibabic, Bose-Einstein Condensation of Atoms in a Uniform Potential, Phys. Rev. Lett. **110**, 200406 (2013).
[52] J. M. Zhang and R. X. Dong, Exact diagonalization: The Bose-Hubbard model as an example, Eur. J. Phys. **31**, 591 (2010).
[53] D. Raventós, T. G., M. Lewenstein, and B. Juliá-Díaz, Cold bosons in optical lattices: A tutorial for exact diagonalization, J. Phys. B **50**, 113001 (2017).
[54] O. Penrose and L. Onsager, Bose-Einstein condensation and liquid helium, Phys. Rev. **104**, 576 (1956).
[55] G. Vidal, J. I. Latorre, E. Rico, and A. Kitaev, Entanglement in Quantum Critical Phenomena, Phys. Rev. Lett. **90**, 227902 (2003).
[56] A. Kitaev and J. Preskill, Topological Entanglement Entropy, Phys. Rev. Lett. **96**, 110404 (2006).
[57] M. Levin and X.-G. Wen, Detecting Topological Order in a Ground State Wave Function, Phys. Rev. Lett. **96**, 110405 (2006).
[58] T. J. Elliott and T. H. Johnson, Nondestructive probing of means, variances, and correlations of ultracold-atomic-system densities via qubit impurities, Phys. Rev. A **93**, 043612 (2016).
[59] M. Streif, A. Buchleitner, D. Jaksch, and J. Mur-Petit, Measuring correlations of cold-atom systems using multiple quantum probes, Phys. Rev. A **94**, 053634 (2016).
[60] Y.-C. He, F. Grusdt, A. Kaufman, M. Greiner, and A. Vishwanath, Realizing and adiabatically preparing bosonic integer and fractional quantum Hall states in optical lattices, Phys. Rev. B **96**, 201103 (2017).

Physics Letters A 382 (2018) 2376–2381

Contents lists available at ScienceDirect

Physics Letters A

www.elsevier.com/locate/pla

Condensates in double-well potential with synthetic gauge potentials and vortex seeding

Rukmani Bai [a,b,*], Arko Roy [a,c], D. Angom [a], P. Muruganandam [d,e]

[a] Physical Research Laboratory, Navrangpura, Ahmedabad 380009, Gujarat, India
[b] Indian Institute of Technology, Gandhinagar, Ahmedabad 382424, Gujarat, India
[c] Max-Planck-Institut für Physik komplexer Systeme, Nöthnitzer Straße 38, 01187 Dresden, Germany
[d] Department of Physics, Bharathidasan University, Tiruchirappalli 620024, India
[e] Department of Medical Physics, Bharathidasan University, Tiruchirappalli 620024, India

ARTICLE INFO

Article history:
Received 1 December 2017
Received in revised form 17 April 2018
Accepted 29 May 2018
Available online 1 June 2018
Communicated by V.A. Markel

Keywords:
Bose–Einstein condensate
Artificial gauge potential
Mean-field theory
Ultra-cold atoms

ABSTRACT

We demonstrate an enhancement in the vortex generation when artificial gauge potential is introduced to condensates confined in a double well potential. This is due to the lower energy required to create a vortex in the low condensate density region within the barrier. Furthermore, we study the transport of vortices between the two wells, and show that the traverse time for vortices is longer for the lower height of the well. We also show that the critical value of synthetic magnetic field to inject vortices into the bulk of the condensate is lower in the double-well potential compared to the harmonic confining potential.

1. Introduction

Charged particles experience Lorentz force in the presence of magnetic fields, and in condensed matter systems, it is the essence for a host of fascinating phenomena like the integer quantum Hall effect [1,2], fractional quantum Hall effect [3,4], and the quantum spin Hall effect [5]. In contrast, the dilute quantum gases of atoms, which have emerged as excellent proxies of condensed matter systems, do not experience Lorentz force as these are charge neutral. This can, however, be remedied with the creation of artificial gauge fields through laser fields [6–10]. Thus, with the artificial gauge potentials it is possible to explore phenomena such as the quantum Hall effect, and the quantum spin Hall effect [7] in dilute atomic quantum gases. The introduction of synthetic magnetic field arising from artificial gauge field is also an efficient approach to generate quantized vortices in Bose–Einstein condensates (BEC) of dilute atomic gases. This method has the advantage of having time-independent trapping potentials over the other methods like rotation [11–13], topological phase imprinting [14,15], or phase engineering in two-species condensates [16,17]. In addition, it has the possibility to inject large ensembles of vortices, and an efficient scheme to nucleate vortices with synthetic magnetic fields was demonstrated in a recent work [18]. The method relies on the creation of an inhomogeneous synthetic magnetic field, which has its maxima coincident with the low density region of a spatially separated pair of BECs.

In this work we examine a scheme to nucleate vortices in BECs through synthetic magnetic field by employing the density gradient associated with a double well trapping potential. The advantages of the scheme are: vortices are generated in the bulk of the condensate; shorter relaxation time after nucleation; and higher density of vortices. In contrast, the other methods like rotating traps and phase imprinting nucleates vortices at the periphery. These then migrate to the bulk and as the process is diabatic, the relaxation times are long. Hence, the present scheme is better suited to explore phenomena associated with high vortex densities like quantum turbulence [19,20]. BECs in double well potentials were first theoretically studied to examine the physics of Josephson currents [21–23], latter observed in experiments [24–27], and studied numerically in a recent work [28]. For our study, we theoretically consider the case of a double well potential which is engineered from a harmonic potential by introducing a Gaussian barrier. For alkali metal atoms, the barrier is a blue-detuned light sheet obtained from a laser beam, and such setups have been used in experiments to observe the matter wave interference [29], Josephson effects [26], and collision of matter-wave solitons [30]. The artificial gauge potential is introduced through Raman coupling [8], and as a case study we consider the case of ^{87}Rb BEC.

* Corresponding author.
E-mail address: rukmani@prl.res.in (R. Bai).

https://doi.org/10.1016/j.physleta.2018.05.051
0375-9601/

We use Gross–Pitaevskii (GP) equation for a mean-field description of the BEC with the artificial gauge potential. In this work we quench the artificial gauge potential by increasing the Raman detuning, and simultaneously increase the height of the barrier potential. It is found that the extended low density region associated with the barrier promotes the formation of vortices. However, the quench imparts energy to the BEC and transfer it to an excited state. For comparison, we also examine the vortex generation in the case of uniform BEC [31]. Such a system, devoid of trap induced inhomogeneities, is better for quantitative comparison of experimental results with theory. This was demonstrated in a recent study on wave turbulence in uniform BECs [32]. To induce relaxation of the condensate to the ground state, we use the standard approach of introducing a dissipative term [33–35]. The presence of the dissipative term in the GP equation is consistent with the experimental observations of dissipation or damping [36, 37], which arises from the interaction between the condensate and non-condensate atoms.

The paper is organized as follows. In Section 2 we provide a description of the theory on how to generate artificial gauge potential in BECs using Raman coupling. Then, we incorporate the gauge potential in the Gross–Pitaevskii equation to arrive at a mean field description of BEC. In Section 3, we present the results of numerical computations, and discuss the implications. We, then, conclude with the key observations.

2. BEC in artificial gauge potentials

To study the vortex formation in double well with synthetic magnetic field in BECs theoretically, we consider the scheme based on light induced gauge potential proposed in Ref. [8]. In particular, we consider a quasi-2D BEC along the xy-plane of two level atoms, which in the present work is taken as the $F = 1$ ground state of ^{87}Rb atoms. To generate spatial inhomogeneity an external magnetic field $B(y) = B_0 + \Delta B(y)$ is applied along the y direction. Here B_0 is the static magnetic field which introduces a linear Zeeman splitting of the ground state manifold. The energy levels are separated by $\Delta_z = g\mu_B B_0$, and $\delta(y) = g\mu_B \Delta B(y)$ is the measure of detuning from Raman resonance. The constants g and μ_B are the atomic Landé factor and Bohr magneton, respectively. The two levels in the ground state are Raman coupled through two counter-propagating laser beams passing through the BEC along $\pm x$ directions [38]. The momentum transferred to the atoms through interactions with the Raman lasers induces a change in the kinetic energy part of the Hamiltonian through the vector potential term A_x. The modified Hamiltonian, however, remains gauge invariant, and there is a corresponding synthetic magnetic field $B_z = -\partial A_x/\partial x$.

2.1. Modified Gross–Pitaevskii equation

In the absence of Raman coupling, the Hamiltonian of the quasi-2D BEC confined in a harmonic trapping potential $\hat{V}_{\rm trap}$ is

$$\hat{H} = \hat{H}_x + \hat{H}_y + \hat{V}_{\rm trap} + \hat{H}_{\rm int}, \tag{1}$$

where $\hat{H}_x$, $\hat{H}_y$ represent the kinetic energy part of the Hamiltonian term along x, y directions respectively, and $\hat{H}_{\rm int}$ denotes the interaction energy between the atoms. Let $|1\rangle = |1, 0\rangle$ and $|2\rangle = |1, -1\rangle$ denote the two states in the ground state manifold of the atoms. The Raman lasers are along the x direction, and hence, the addition of the atom-light coupling term modifies H_x to

$$\hat{H}_x = E_{\rm r} \begin{pmatrix} \left(\tilde{k}_x + 1\right)^2 - \frac{\hbar\delta}{2E_{\rm r}} & \frac{\hbar\Omega}{2E_{\rm r}} \\ \frac{\hbar\Omega}{2E_{\rm r}} & \left(\tilde{k}_x - 1\right)^2 + \frac{\hbar\delta}{2E_{\rm r}} \end{pmatrix}, \tag{2}$$

where $E_{\rm r} = \left(\hbar^2 k_{\rm r}^2/2m\right)$ is the recoil energy, and $\tilde{k}_x = (k_x/k_{\rm r})$ with k_x as the x-component of the wave-vector, Ω is the Raman coupling between two levels, and δ is the Raman detuning.

To derive the modified Gross–Pitaevskii (GP) equation, we diagonalize $\hat{H}_x$ and obtain the dispersion relation for the two levels in the limit of strong Rabi coupling, $\hbar\Omega \gg 4E_r$. This ensures that there is single energy minima of the system and leads to the following: there is a change in the momentum along the x direction which provides a gauge potential $eA_x/\hbar k_{\rm r} = \tilde{\delta}/(\tilde{\Omega} \pm 4)$ in the system; and from the light-atom coupling the atoms acquires an effective mass m^* defined by $m^*/m = \tilde{\Omega}/(\tilde{\Omega} \pm 4)$. Here $\pm$ denotes the two energy levels in the system and $\tilde{\delta} = \hbar\delta/E_r$, $\tilde{\Omega} = \hbar\Omega/E_r$. Based on this Hamiltonian and restricting the dynamics to only the lowest dressed state, the behaviour of such a condensate in the presence of artificial gauge fields is governed by the following dimensionless modified Gross–Pitaevskii (GP) equation

$$\begin{aligned} i\frac{\partial\phi(x,y,t)}{\partial t} = \Bigg[& -\frac{1}{2}\frac{m}{m^*}\frac{\partial^2}{\partial x^2} - \frac{1}{2}\frac{\partial^2}{\partial y^2} + \frac{i2\pi\delta'}{\lambda_{\rm L}\Omega E_{\rm r}} y\frac{\partial}{\partial x} \\ & + \frac{1}{2}x^2 + \frac{1}{2}y^2\left(1 + \frac{2C_{\rm rab}\delta'^2}{E_{\rm r}}\right) + g_{\rm 2D}|\phi(x,y,t)|^2 \\ & - \left(\frac{\Omega - 2}{2}\right)E_{\rm r}\Bigg]\phi(x,y,t). \end{aligned} \tag{3}$$

In the above equation, all the parameters having the dimensions of length, energy, and time have been scaled with respect to the oscillator length $a_{\rm osc} = \sqrt{\hbar/m\omega_x}$, energy $\hbar\omega_x$ and time $\omega_x t$ respectively. For simplicity of notations, from here on we will represent the transformed quantities $(\Omega, \delta', E_{\rm r}, \lambda_{\rm L})$ without tilde. The condensate wavefunction is represented by $\phi(x, y, t)$, $C_{\rm rab} = \left(1/\Omega(\Omega - 4) + (4 - \Omega)/4(\Omega + 4)^2\right)$, $\delta = \delta' y$, δ' is defined to be the detuning gradient, Ω is the Rabi frequency, $E_{\rm r} = \left(2\pi^2/\lambda_{\rm L}^2\right)$ is the recoil energy of electrons, $g_{\rm 2D} = 2a_s N\sqrt{2\pi\lambda}/a_{\rm osc}$ is the interaction energy with N as the total number of atoms in the condensate, and $\lambda \gg 1$ is the trap anisotropy parameter along the z direction.

2.2. Double well (DW) potential

For the present work, we consider quasi-2D BEC confined in a double well potential

$$V_{\rm dw} = V_{\rm trap} + U_0 \exp(-2y^2/\sigma^2), \tag{4}$$

where U_0 and σ are the depth and width of the double well potential respectively and $V_{\rm trap} = (1/2)m\omega_\perp^2(x^2 + y^2)$ is the harmonic potential along x and y directions, and we have considered the symmetric case $\omega_\perp = \omega_x = \omega_y$.

The presence of the double well potential modifies the density distribution, breaks the rotational symmetry of the condensate, and brings about novel effects in the dynamical evolution of the condensate which forms the main topic of the present study.

2.3. Thomas Fermi correction in the condensates density

The focus of the present work, as mentioned earlier, is to examine the formation of vortices in the quasi-2D BEC with the introduction of artificial gauge potential. It has been shown in previous works on rotated condensates that vortices are seeded at the periphery of the condensate cloud, where the low density of the condensate is energetically favourable for the formation of vortices [39]. This is due to the presence of nodeless surface excitations [40], which create instabilities in the condensate and lead to the nucleation of vortices [41]. At later times the vortices migrate and

enter the bulk of the condensate. To analyse the density distribution and optimal conditions for generation of vortices, consider a BEC with large number of particles. The condensate is then well described with the Thomas–Fermi (TF) approximation as the interaction energy dominates in the GP equation, and the kinetic energy can be neglected in the bulk of the condensates as the spatial gradient is negligible. In this approximation the density in the bulk is $|\phi_{\rm TF}|^2 = (\mu - V_{\rm trap})/(2g_{2D})$, where μ is the chemical potential of the condensate. The TF approximation, however, fails at the periphery of condensate as the $\phi_{\rm TF}$ is discontinuous at the boundary [42]. However, vortices are seeded at the peripheral regions where the TF approximation may break down. Similar conditions are applicable to the densities at the edges of the double well potential considered in the present work. For this we take μ in terms of TF radius R and trapping potential in term of radial distance r. The correction to the TF density at the edges, similar to the harmonic trapping potential, is

$$|\phi^c_{\rm TF}|^2 = \frac{R^2 - r^2}{2g_{2D}}\left[1 - \frac{R^2}{2(R^2 - r^2)^3}\right]^2. \tag{5}$$

In the above equation, first term is TF density in the bulk of condensate and second term is correction to the TF density. Now, the density at the boundary is calculated as $n_c = |\phi_{\rm TF}|^2 - |\phi^c_{\rm TF}|^2$, and for the region within the barrier of the double well, TF approximation is valid as the barrier potential decays exponentially. Accordingly, the density distribution is

$$|\phi^b_{\rm TF}|^2 = \frac{R^2 - r^2 - U_0 \exp(-2y^2/\sigma^2)}{2g_{2D}}, \tag{6}$$

here U_0 and σ are depth and width of the double well potential. The above density distribution is symmetric about the x-axis, and hence, the low density region is more extended compared to the peripheral region of a harmonic trapping potential. So, the density variation arising from the potential barrier enhances the formation of vortices.

3. Results and discussion

3.1. Numerical details

For the present study, we numerically solve the Gross–Pitaevskii equation in imaginary time at zero temperature in the absence of the artificial gauge potential, which is equivalent to setting δ' and Ω to zero. For this we use the split-step Crank–Nicolson method [43–46] and the solution obtained is the equilibrium ground state. To dynamically evolve the condensate, we propagate the stationary state solution in real time using Eq. (3). Furthermore, we introduce the artificial gauge potential by varying δ' from 0 to 3×10^9 Hz/m within ≈ 202 ms, but the value of Ω is kept constant throughout the evolution. Afterwards the system is evolved freely for up to $t \approx 962$ ms when it relaxes to a steady state. For the present work we consider ^{87}Rb condensate with $N = 10^5$ atoms, and the s-wave scattering length is $a_s = 99a_0$. The trapping potential parameters are chosen to be $\omega_x = \omega_y = 2\pi \times 20$ Hz, and $\lambda = 40$ which satisfies the quasi-2D condition. The Raman lasers considered for our calculations have wavelength $\lambda_{\rm L} = 790$ nm. The Rabi frequency is taken to be $\Omega = 6E_r$, where E_r is scaled with $\hbar\omega_x$. This choice of parameters is consistent with the experimental setting of Spielman et al. [8].

3.2. Harmonic potential

At the start of the real time evolution, or beginning of the dynamical evolution $t = 0$, the condensate is rotationally symmetric,

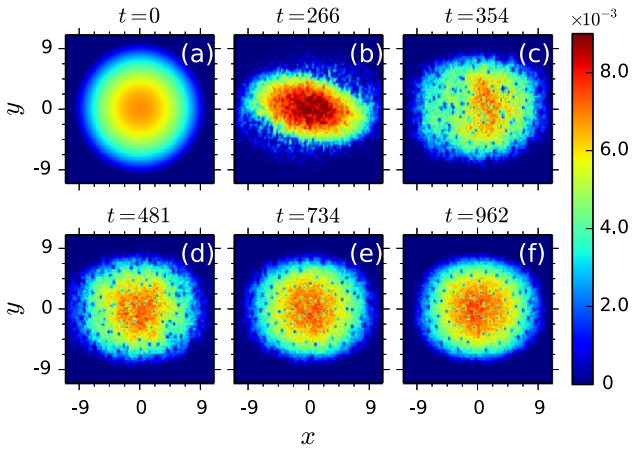

Fig. 1. Generation of vortices in the absence of dissipation. The time (in units of ms) is shown above the plots. Here x and y are measured in units of $a_{\rm osc}$. Density is measured in units of $a_{\rm osc}^{-2}$ and is normalized to unity. (For interpretation of the colours in the figures, the reader is referred to the web version of this article.)

and is devoid of any topological defects. This is shown in Fig. 1(a). As the artificial gauge potential is switched on by introducing δ' with constant Ω, the rotational symmetry of the condensate is broken since the effective frequencies along x and y directions are unequal due to the term $2C_{\rm rab}\delta'^2/E_{\rm r}$ in Eq. (3). The condensate thus departs from being circularly symmetric and acquires an elliptic structure, which is discernible from the density profiles shown in Fig. 1. Furthermore, the angular-momentum like term $i(2\pi\delta')/(\lambda_{\rm L}\Omega E_{\rm r})(y\partial\phi(x,y,t))/(\partial x)$ in Eq. (3) is non-zero and induces a deformation to the condensate. The combined effects of these two effects and an increase in the energy of the system favour the seeding of topological defects or vortices in the condensate. Initially, the vortices are generated at the periphery, where the density is low and fluctuations in phase are more prominent, and at later times the vortices migrate to the bulk of the condensate. As the system relaxes towards a steady state, the vortices acquires a spatially disordered distribution to minimize the total energy. The nature of the spatial distribution of vortices implies that the system is in a higher energy state, and this is evident from the vortex distribution as shown in Fig. 1(f). To include the effects of dissipation which may be present due to quantum and thermal fluctuations, or due to loss of atoms from the trap because of inelastic collisions in the condensate we add the dissipative term $-\gamma\partial\phi(x,y,t)/\partial t$ in Eq. (3) and examine the dynamical evolution of the condensate. Here, we set $\gamma = 0.003$ based on the results from previous work [35]. This leads to loss of energy from the condensate and the condensate dynamically evolves to it's ground state. As a consequence the vortices self organise into a vortex lattice and the evolution towards the vortex lattice is as shown in Fig. 2.

3.3. Double well potential

To study the dynamics of vortex generation and their transport in double well potential we solve time dependent GP Eq. (3) with the potential given in Eq. (4). Like in the previous case, we include a dissipative term to allow the system to relax to it's ground state, which is with a vortex lattice. For the numerical computation, we take the width of the barrier in the double well potential as $\sigma = 0.7$ μm. To obtain the initial state, like in the previous case, we again consider imaginary time ground state solution of a quasi-2D BEC of ^{87}Rb atoms without δ', Ω, and U_0. We, then evolve the solution in real time as described earlier. During the evolution in real time, we ramp up or quench the value of δ' and U_0, but keeping Ω fixed. Increment in δ' introduces artificial gauge potential in

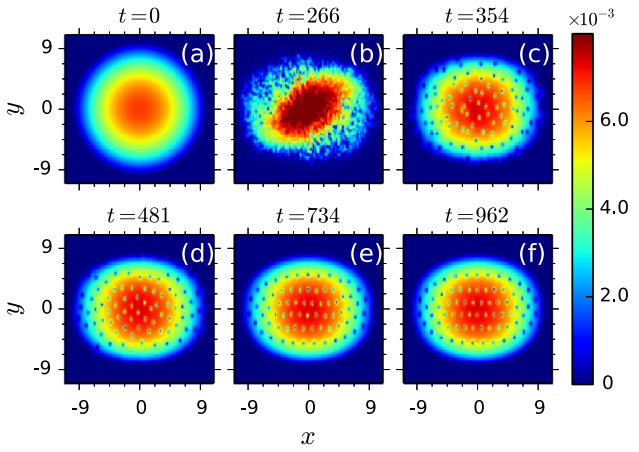

Fig. 2. Generation of vortices in the presence of dissipation. The time (in units of ms) is shown above the plots. Here x and y are measured in units of a_{osc}. Density is measured in units of a_{osc}^{-2} and is normalized to unity.

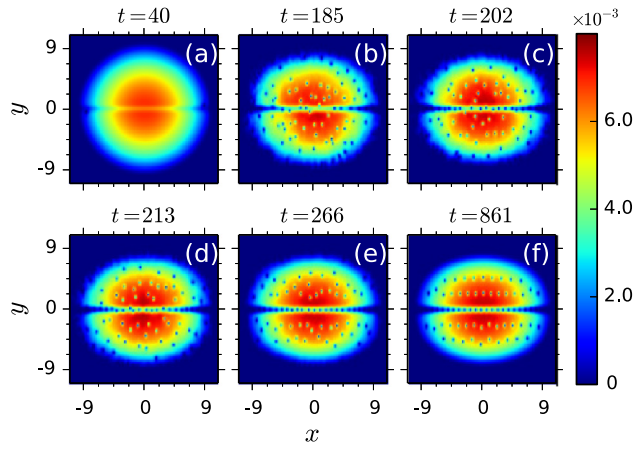

Fig. 3. Transport of vortices when laser field energy rate is less compared to the double well potential depth energy rate with dissipation. Vortices transport between the wells up to the time $t = 266$ ms, after that some vortices are settled near to the interface of the wells. The time (in units of ms) is shown above the plots. Here x and y are measured in units of a_{osc}. Density is measured in units of a_{osc}^{-2} and is normalized to unity.

the system, and vortices are generated with time. We find that the double well potential has enhanced vortex formation. The vortices are generated in the barrier region between the two wells as it is a region of low density, and the energy per vortex is lower in this regime.

The enhancement of vortex formation in the double well potential can be understood in terms of the excitation energy of a single vortex. In the case of harmonic potential the energy of the vortex located at a radial distance b from the centre in the TF approximation is $\epsilon_v \simeq (4/3)\pi R_z n(0)(\hbar^2/m)\ln(R/\xi_0)(1-b^2/R^2)^{3/2}$. Where, $n(0)$ is the density at the centre, when vortex is not present, R is the Thomas–Fermi radius, R_z is the length along z direction and ξ_0 is the healing length [42]. For the quasi-2D system R_z can be evaluated using the anisotropy parameter λ and μ in the TF approximation. Based on this expression we find that the energy of a vortex at the centre of the condensate with only the harmonic trapping potential or without the barrier is 0.028 $\hbar\omega_x$, which is lower than the value of 0.094 $\hbar\omega_x$ obtained from the numerical results. The difference could be due to deviation from the TF approximation. From the numerical results, without the barrier, the energy of a vortex located at a radial distance of 9.0 a_{osc} is 0.008 $\hbar\omega_x$. Here, the radial distance considered correspond to the peripheral region where vortices first appear. In the case of double well potential the energy of a vortex at the centre of the barrier and at the same radial distance is 0.007 $\hbar\omega_x$, which is lower than the previous case. In terms of absolute values the energy difference is not large, but as discussed latter, the presence of the barrier in the double well makes a significant difference in the dynamical evolution and generation of vortices. Since we quench two parameters of the system, δ' and U_0, we examine the system in terms of the relative quench rates. For this we define $R_1 = \lambda_{\text{L}}\partial\delta'/\partial t$ and $R_2 = \partial U_0/\partial t$ as the quench rate of the artificial gauge potential, and the barrier height between the two wells, respectively. Where λ_{L}, δ', and U_0 are the dimensionless quantities, and δ' and U_0 are ramped within a period of $t = 202$ ms. The value of δ' vary from 0 to 3×10^9 Hz/m as defined earlier. Here, R_1 affects the vortex generation, and R_2 affects the transport of vortices between the two wells. We consider three cases, depending on the relative values of R_1 and R_2.

3.3.1. $R_1 < R_2$

For this case we vary U_0 from 0 to 25.85 (in units of $\hbar\omega_x$) within a period of 202 ms, and the evolution of the density profiles are shown in Fig. 3. The inclusion of the barrier, to form a double well potential, accelerates the formation of vortices, and they appear within a short span of time ≈ 40 ms. This is much shorter than the time of ≈ 266 ms taken to generate vortices in absence of the barrier or in harmonic potential as shown in Fig. 2. The shortening is due to the modified density distribution arising from the presence of the central barrier in the double well potential. The vortices are seeded near the central region of the barrier where the density is low as shown in Fig. 3(a). During the quench, at lower values of U_0, vortices traverse from one well to the other due to the lower depth of the potential, but it stops once U_0 reaches maxima as the vortex energy is not enough for transport from one well to the other. The dynamics associated with the crystallisation of the vortices to form a vortex lattice is evident from the density patterns in Fig. 3(b)–(e). The equilibrium ground state solution of vortex lattice is obtained at ≈ 861 ms after the free evolution as shown in Fig. 3(f). One noticeable feature is the confinement of vortices along the barrier with lower spacing compared to the vortex lattice in the bulk of the condensate. In particular, the spacing between vortices is 1.43 a_{osc} and 0.87 a_{osc} in the bulk and in the barrier respectively.

3.3.2. $R_1 \geqslant R_2$

For the case of $R_1 = R_2$, the value of U_0 at the end of the quench is 18.85 (in units of $\hbar\omega_x$). During the quench vortices are generated at ≈ 45 ms of the dynamical evolution, and emerge from within the barrier region. Here, the potential depth is less compared to the case of $R_1 < R_2$, and the vortex transportation between the two wells occurs for a longer time, that is up to ≈ 304 ms. Like in the case of $R_1 < R_2$ the equilibrium ground state solution is attained at ≈ 861 ms. For illustration the condensate density profiles during the dynamical evolution are shown in Fig. 4. In the case of $R_1 > R_2$ the value of U_0 at the end of the quench is 11.85 (in units of $\hbar\omega_x$). This implies that the barrier height attained at the end of the quench is less than the two previous cases. The generation of vortices start at ≈ 50 ms, and the transportation of vortices between the two wells continues for much longer time, till ≈ 354 ms. Like in the previous cases the equilibrium ground state solution is obtained at ≈ 861 ms as shown in Fig. 5.

3.4. Uniform BEC

For uniform BEC, V_{trap} in Eq. (3) is set to zero and consider hard wall boundary. With this the BEC is uniform except at the boundary, where the density goes to zero over the length scale of

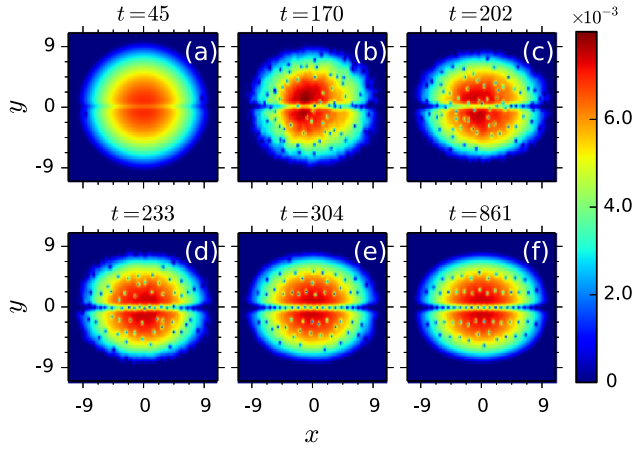

Fig. 4. Transport of vortices when laser field energy rate is equal to the double well potential depth energy rate with dissipation. Vortices cross from one well to another well up to the time $t = 304$ ms, after that some vortices are settled near the interface. The time (in units of ms) is shown above the plots. Here x and y are measured in units of a_{osc}. Density is measured in units of a_{osc}^{-2} and is normalized to unity.

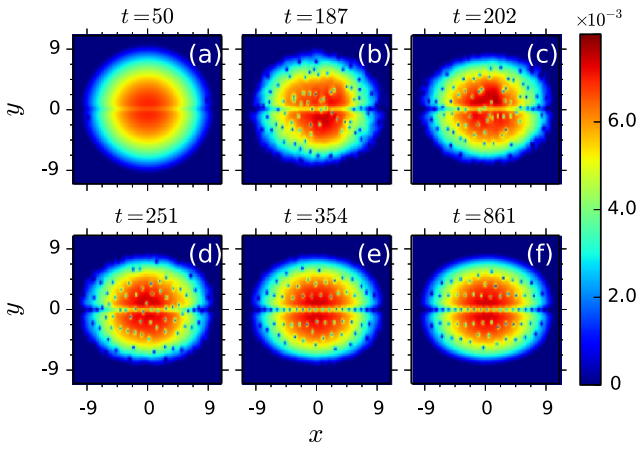

Fig. 5. Transport of vortices when laser field energy rate is high compared to the double well potential depth energy rate with dissipation. Vortices cross from one well to another well up to the time $t = 354$ ms, after that some vortices are settled near to the interface. The time (in units of ms) is shown above the plots. Here x and y are measured in units of a_{osc}. Density is measured in units of a_{osc}^{-2} and is normalized to unity.

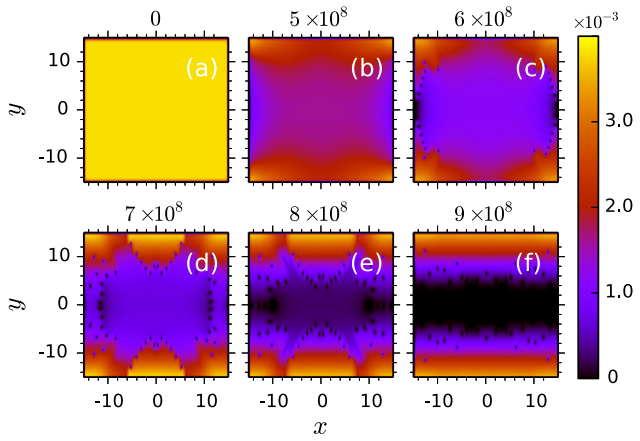

Fig. 6. Generation of vortices in the homogeneous system with the hard wall boundary with the synthetic magnetic field. The equilibrium solutions for different values of δ' (in Hz/m) are shown here and values of δ' are written above each of the plot. Vortices are generated near to the boundary and propagate into the bulk of the condensate. Here x and y are measured in units of a_{osc}. Density is measured in units of a_{osc}^{-2} and is normalized to unity.

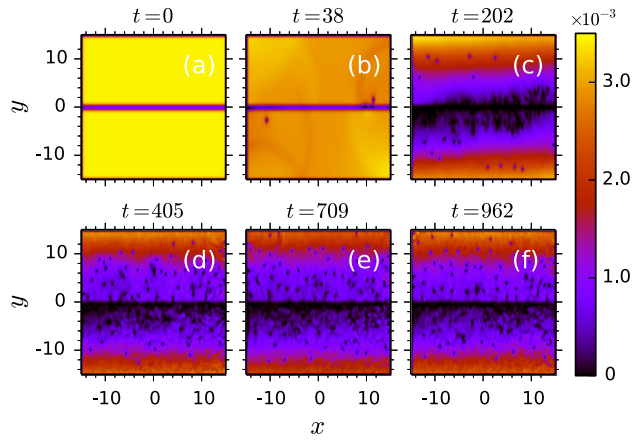

Fig. 7. Generation of vortices in the homogeneous system with the hard wall boundary. A barrier is introduced along the x direction. Vortices are generated near to the barrier and propagate into the bulk of the condensate. Here, we do not observe the vortex lattice. Here x and y are measured in units of a_{osc}. Density is measured in units of a_{osc}^{-2} and is normalized to unity.

healing length. So, the vortices enter from the edges and propagate to the bulk. We obtain the equilibrium state of the modified GP Eq. (3) with different values of synthetic magnetic field shown in the Fig. 6. We observe that condensate is fragmented at the large value of $\delta' > 9 \times 10^8$ Hz/m. In this case there is no formation of vortex lattice. We find that the vortices have higher energies in the uniform BEC $\approx 10\ \hbar\omega_x$, whereas it is $\approx 3\ \hbar\omega_x$ for BEC with harmonic confining potential. The difference can be accounted by the higher moment of inertia associated with the uniform BEC. Next, to compare with the results in presence of harmonic potential, we introduce a Gaussian barrier along x axis with $U_0 = 10$ (in units of $\hbar\omega_x$) and width of 0.7 μm. In the numerical simulation, the initial states at time $t = 0$ ms is without the synthetic magnetic field $\delta' = 0$ as shown in Fig. 7(a). Then, the magnetic field is introduced by quenching δ'. The vortices are nucleated at a critical value of δ' as shown in Fig. 7(b) at $t = 38$ ms. We increase δ' from 0 to 7×10^8 Hz/m in 0 to 202 ms time. After that, we freely evolve the system. In the uniform BEC, like in the previous case, the vortices nucleate close to the barrier and then propagate to the bulk. However, as to be expected, the dynamics of the vortices are qualitatively different from the inhomogeneous case. The dynamics of the vortices are determined by the inter-vortex interactions and remain within the bulk regions. The selected snap shots of the dynamical evolution of the vortices are shown in the Fig. 7(a)–(f).

3.5. Critical value of δ' and density

As described earlier, we take the equilibrium imaginary time solution of a quasi-2D BEC, and evolve it in real time with the introduction of a quenched artificial gauge potential. This is achieved by increasing the detuning gradient of the Raman lasers δ' and vortices are generated in the condensates when δ' reaches a critical value during the quench. In the case of a purely harmonic confining potential the critical value of δ' is 0.89×10^9 Hz/m. But, for the case of a condensate confined in double well potential the critical value of δ' is 0.26×10^9 Hz/m. Hence, the presence of the barrier in the double well potential lowers the critical value of δ', which is the measure of synthetic magnetic field in the system. To examine the generation of the vortices in more detail we examine the condensate density at the region where vortex enters in the condensate. In the case of harmonic trap, vortex enters from the peripheral region, and we use TF correction to compute the density n_c. We find that densities n_c for the two trapping poten-

tials are 0.1×10^{-3} and 0.4×10^{-3} for the harmonic and double well potential. Here, densities are measured in units of a_{osc}^{-2} and are normalized to unity. These densities correspond to the region at which vortex enters in the condensates.

4. Conclusions

We have shown that the presence of the Gaussian potential barrier enhances the generation of vortices due to the presence of artificial gauge potential. We examine this by quenching the artificial gauge potential along with the height of the barrier potential. Without the barrier potential, in the case of a harmonic confining potential, the vortices are generated at a later time and vortices are less in number as well. Like in the previous works [33–35], we observe that it is essential to introduce dissipation to obtain equilibrium vortex configuration in trapped system. The dissipation drains energy gained during the quench and allows the condensate relax to the ground state configuration by forming a vortex lattice. In case of uniform BEC, there is no formation of vortex lattice even in the presence of dissipation.

Acknowledgements

We thank Kuldeep Suthar, Sukla Pal and Soumik Bandopadhyay for very useful discussions. The numerical computations reported in the paper were carried on the Vikram-100 HPC cluster at PRL. The work of PM forms a part of Science & Engineering Research Board (SERB), Department of Science & Technology (DST), Govt. of India sponsored research project (No. EMR/2014/000644).

References

[1] K. von Klitzing, Rev. Mod. Phys. 58 (1986) 519.
[2] D.R. Yennie, Rev. Mod. Phys. 59 (1987) 781.
[3] H.L. Stormer, D.C. Tsui, A.C. Gossard, Rev. Mod. Phys. 71 (1999) S298.
[4] H.L. Stormer, Rev. Mod. Phys. 71 (1999) 875.
[5] M. König, H. Buhmann, L.W. Molenkamp, T. Hughes, C.-X. Liu, X.-L. Qi, S.-C. Zhang, J. Phys. Soc. Jpn. 77 (2008) 031007.
[6] G. Juzeliūnas, P. Öhberg, Phys. Rev. Lett. 93 (2004) 033602.
[7] S.-L. Zhu, H. Fu, C.-J. Wu, S.-C. Zhang, L.-M. Duan, Phys. Rev. Lett. 97 (2006) 240401.
[8] I.B. Spielman, Phys. Rev. A 79 (2009) 063613.
[9] K. Jiménez-García, Artificial Gauge Fields for Ultracold Neutral Atoms, Ph.D. thesis, National Institute of Standards and Technology, and the University of Maryland, Gaithersburg, Maryland, 2012.
[10] N. Goldman, G. Juzeliūnas, P. Öhberg, I.B. Spielman, Rep. Prog. Phys. 77 (2014) 126401.
[11] K.W. Madison, F. Chevy, W. Wohlleben, J. Dalibard, Phys. Rev. Lett. 84 (2000) 806.
[12] J.R. Abo-Shaeer, C. Raman, J.M. Vogels, W. Ketterle, Science 292 (2001) 476.
[13] P.C. Haljan, I. Coddington, P. Engels, E.A. Cornell, Phys. Rev. Lett. 87 (2001) 210403.
[14] T. Isoshima, M. Nakahara, T. Ohmi, K. Machida, Phys. Rev. A 61 (2000) 063610.
[15] A.E. Leanhardt, A. Görlitz, A.P. Chikkatur, D. Kielpinski, Y. Shin, D.E. Pritchard, W. Ketterle, Phys. Rev. Lett. 89 (2002) 190403.
[16] J.E. Williams, M.J. Holland, Nature 401 (1999) 568.
[17] M.R. Matthews, B.P. Anderson, P.C. Haljan, D.S. Hall, C.E. Wieman, E.A. Cornell, Phys. Rev. Lett. 83 (1999) 2498.
[18] R.M. Price, D. Trypogeorgos, D.L. Campbell, A. Putra, A. Valdés-Curiel, I.B. Spielman, New J. Phys. 18 (2016) 113009.
[19] M. Tsubota, M. Kobayashi, H. Takeuchi, Phys. Rep. 522 (2013) 191.
[20] S.K. Nemirovskii, Phys. Rep. 524 (2013) 85.
[21] J. Javanainen, Phys. Rev. Lett. 57 (1986) 3164.
[22] F. Dalfovo, L. Pitaevskii, S. Stringari, Phys. Rev. A 54 (1996) 4213.
[23] A. Smerzi, S. Fantoni, S. Giovanazzi, S.R. Shenoy, Phys. Rev. Lett. 79 (1997) 4950.
[24] F.S. Cataliotti, S. Burger, C. Fort, P. Maddaloni, F. Minardi, A. Trombettoni, A. Smerzi, M. Inguscio, Science 293 (2001) 843.
[25] M. Albiez, R. Gati, J. Fölling, S. Hunsmann, M. Cristiani, M.K. Oberthaler, Phys. Rev. Lett. 95 (2005) 010402.
[26] S. Levy, E. Lahoud, I. Shomroni, J. Steinhauer, Nature 449 (2007) 579.
[27] A. Trenkwalder, G. Spagnolli, G. Semeghini, S. Coop, M. Landini, P. Castilho, L. Pezze, G. Modugno, M. Inguscio, A. Smerzi, M. Fattori, Nat. Phys. 12 (2016) 826.
[28] M.A. Garcia-March, L.D. Carr, Phys. Rev. A 91 (2015) 033626.
[29] M.R. Andrews, C.G. Townsend, H.-J. Miesner, D.S. Durfee, D.M. Kurn, W. Ketterle, Science 275 (1997) 637.
[30] J.H.V. Nguyen, P. Dyke, D. Luo, B.A. Malomed, R.G. Hulet, Nat. Phys. 10 (2014) 918.
[31] A.L. Gaunt, T.F. Schmidutz, I. Gotlibovych, R.P. Smith, Z. Hadzibabic, Phys. Rev. Lett. 110 (2013) 200406.
[32] N. Navon, A.L. Gaunt, R.P. Smith, Z. Hadzibabic, Nature 539 (2016) 72.
[33] S. Choi, S.A. Morgan, K. Burnett, Phys. Rev. A 57 (1998) 4057.
[34] M. Tsubota, K. Kasamatsu, M. Ueda, Phys. Rev. A 65 (2002) 023603.
[35] D. Yan, R. Carretero-González, D.J. Frantzeskakis, P.G. Kevrekidis, N.P. Proukakis, D. Spirn, Phys. Rev. A 89 (2014) 043613.
[36] M.-O. Mewes, M.R. Andrews, N.J. van Druten, D.M. Kurn, D.S. Durfee, C.G. Townsend, W. Ketterle, Phys. Rev. Lett. 77 (1996) 988.
[37] D.S. Jin, M.R. Matthews, J.R. Ensher, C.E. Wieman, E.A. Cornell, Phys. Rev. Lett. 78 (1997) 764.
[38] Y.-J. Lin, R.L. Compton, A.R. Perry, W.D. Phillips, J.V. Porto, I.B. Spielman, Phys. Rev. Lett. 102 (2009) 130401.
[39] E. Hodby, G. Hechenblaikner, S.A. Hopkins, O.M. Maragò, C.J. Foot, Phys. Rev. Lett. 88 (2001) 010405.
[40] U.A. Khawaja, C.J. Pethick, H. Smith, Phys. Rev. A 60 (1999) 1507.
[41] T.P. Simula, S.M.M. Virtanen, M.M. Salomaa, Phys. Rev. A 66 (2002) 035601.
[42] C. Pethick, H. Smith, Bose–Einstein Condensation in Dilute Gases, Cambridge University Press, 2008.
[43] P. Muruganandam, S. Adhikari, Comput. Phys. Commun. 180 (2009) 1888.
[44] D. Vudragović, I. Vidanović, A. Balaž, P. Muruganandam, S.K. Adhikari, Comput. Phys. Commun. 183 (2012) 2021.
[45] B. Satarić, V. Slavnić, A. Belić, A. Balaž, P. Muruganandam, S.K. Adhikari, Comput. Phys. Commun. 200 (2016) 411.
[46] L.E. Young-S., D. Vudragović, P. Muruganandam, S.K. Adhikari, A. Balaž, Comput. Phys. Commun. 204 (2016) 209.